Theses and Dissertations   Student Graduate Works

6-16-2016

Laminar Flame Combustion Diagnostics Using Imaging Fourier Transform Spectroscopy

Michael R. Rhoby

**LAMINAR FLAME COMBUSTION DIAGNOSTICS
USING IMAGING FOURIER TRANSFORM
SPECTROSCOPY**

DISSERTATION

Michael R. Rhoby, Civilian

AFIT-ENP-DS-16-J-018

DEPARTMENT OF THE AIR FORCE
AIR UNIVERSITY

AIR FORCE INSTITUTE OF TECHNOLOGY

Wright-Patterson Air Force Base, Ohio

DISTRIBUTION STATEMENT A

APPROVED FOR PUBLIC RELEASE; DISTRIBUTION UNLIMITED.

The views expressed in this document are those of the author and do not reflect the official policy or position of the United States Air Force, the United States Department of Defense or the United States Government. This material is declared a work of the U.S. Government and is not subject to copyright protection in the United States.

AFIT-ENP-DS-16-J-018

LAMINAR FLAME COMBUSTION DIAGNOSTICS USING IMAGING FOURIER

TRANSFORM SPECTROSCOPY

DISSERTATION

Presented to the Faculty

Graduate School of Engineering and Management

Air Force Institute of Technology

Air University

Air Education and Training Command

in Partial Fulfillment of the Requirements for the

Degree of Doctor of Philosophy in Optical Sciences and Engineering

Michael R. Rhoby, MS

Civilian

June 2016

AFIT-ENP-DS-16-J-018

LAMINAR FLAME COMBUSTION DIAGNOSTICS USING IMAGING FOURIER

TRANSFORM SPECTROSCOPY

DISSERTATION

Michael R. Rhoby, MS
Civilian

Committee Membership:

Kevin C. Gross, PhD
Chair

David L. Blunck, PhD
Member

Viswanath R. Katta, PhD
Member

Glen P. Perram, PhD
Member

Marc D. Polanka, PhD
Member

AFIT-ENP-DS-16-J-018

Abstract

Combustion diagnostics is a mature field of inquiry with a host of pre-existing experimental research methods. Currently, however, no one method captures time-resolved scalar profile estimates of temperature and major species concentrations with a single instrument. Imaging Fourier transform spectroscopy (IFTS) has the potential to fill that void. IFTS offers several unique advantages for combustion diagnostics such as portability, ease of operation, and the combination of imaging and wide band spectral data. Moderate spectral resolution (up to $0.25\,\mathrm{cm}^{-1}$) across a wide band pass ($1.5\,\mu\mathrm{m}$ to $5.5\,\mu\mathrm{m}$) captures radiance from many major combustion species simultaneously. High-speed imagery existing within the interferometric measurement can be used with existing flow field analyses performed by infrared cameras. This work provides IFTS with the capability to measure time-resolved 3D imaging of scalar values in laminar axisymmetric flames. This will make IFTS a useful tool for future work in understanding combustion phenomenon, validating chemical kinetic models, verifying numerical simulations, and system performance estimate.

Using an IFTS camera, data of a partially-premixed ethylene Hencken burner flame produced at equivalence ratios of 0.8, 0.9, 1.1, and 1.3 was captured. A novel calibration methodology was developed for high-temperature flame sources. A single-layer radiative transfer model retrieved path-averaged temperature, H_2O, CO_2 and CO column densities that agreed well with previous results. For the $\Phi = 1.1$ flame, the spectrally estimated temperature for a single pixel $T = (2318 \pm 19)\,\mathrm{K}$, compared to reported laser absorption measurements, $T = (2348 \pm 115)\,\mathrm{K}$, and a NASA CEA equilibrium calculation, $T = 2389\,\mathrm{K}$. Near the base of the flame, absolute concentrations of H_2O, CO_2, and CO were $(12.5 \pm 1.7)\,\%$, $(10.1 \pm 1.0)\,\%$, and $(3.8 \pm 0.3)\,\%$, respectively. These compared

iv

favorably with CEA values of 12.8%, 9.9% and 4.1%. This work helps to establish IFTS as a valuable combustion diagnostic tool and also motivated the need for a multi-layer radiative transfer algorithm and time-resolved spectra reconstruction.

Using CFD simulations and measurements of a laminar H_2 flame, an algorithm for reconstruction of spectra as a function of the buoyancy-driven harmonic flame period is demonstrated. It is shown that the combination of a band integrated intensity value and its temporal derivative define a unique configuration of the flame's scalar fields at any time. Through selectively averaging over an ensemble of measurements, interferograms representing the scalar fields at various times can be created and converted into "snapshot" spectra. Integrated line-of-sight radiance profiles reconstructed at various times in a flame's period compare favorably to previously reported measurements. Comparisons to previously reported values of a similar flame are favorable and agree to within a maximum difference of 18.5%.

An inversion method is developed to estimate radially-resolved scalar values and is tested against several simulated laminar flames. Empirical functions estimate flame edge values, improving starting estimates for an onion-peeling process. A three-point, sliding onion-peel inversion provides a fast and flexible, yet reliable estimation of the radial scalar profiles. A global parameter minimization utilizes all data simultaneously for an optimized solution. Results of the inversion agreed with truth to within 1-10%. Flexibility for complex profile shape and sensitivity to trace species is demonstrated.

The combination of the "snapshot spectra" algorithm and the scalar field inversion method was applied to measurements of radiation from an unsteady laminar hydrogen flame. Temperature and water concentrations were resolved radially at two different "snapshot" times in the period of the flame's harmonic motion. Measured results compared favorably with previously reported values of a similar flame and CFD simulations. Temperatures agree to within 11% and water concentration values agree to within 19%.

v

This work demonstrates the ability of IFTS to make time-resolved 3-D maps of scalar

values of an unsteady, axisymmetric laminar flame.

To my father, who was and would have been very proud

And my wife, whose support was instrumental

Acknowledgements

Foremost, I would like to express my sincere gratitude to my advisor Dr. Kevin Gross for the continuous support of my study and research, for his patience, motivation, enthusiasm, and knowledge. His guidance helped me in all areas of research and writing, I could not have completing this work without him.

Michael R. Rhoby

Table of Contents

xi

List of Figures

xiii

xiv

List of Abbreviations

LAMINAR FLAME COMBUSTION DIAGNOSTICS USING IMAGING FOURIER

TRANSFORM SPECTROSCOPY

I. Introduction

In 2020, it's estimated that 62% of Unites States' energy needs will be met through
the combustion of petroleum, natural gas, liquid biofuels, and other liquid gasses [3].
With such a large portion of US energy needs being met through the burning of various
carbon fuels, the study of combustion remains an important discipline in the pure and
applied sciences. Combustion diagnostics (CD) encompasses the set of technologies
and methodologies which permit the detailed study of combustion phenomena and
remains a field of continued interest and investment. Concerns over global climate
change drive research Objectives towards improved combustion efficiency in the energy
industry. Increased efficiency and weight reduction motivates the creation of compact,
light weight combustors in the aeronautics field. Accurately characterizing the spatial
distribution of species concentrations and temperature in flames lends insight into
system efficiency, emission levels, and design optimization. Prodigious advancements
in computing power over the last 20 years have fostered research efforts toward reactive-
flow Computational Fluid Dynamic (CFD) and chemical reaction models. Despite
great advancements in the accuracy and reliability of these simulations, laboratory
measurements are still needed to validate and improve CFD models. Among these real
world techniques, those utilizing optical based diagnostics (both active and passive)
have proven the most useful.

In 1857 William Swan associated several bright emission features in the spectra of
comets with identical emissions he observed in wax candles. Concluding that these

1

emission lines originated from the carbon molecule C_2, Swan became the first to inter-twine combustion and optical diagnostic [4]. As the use of combustion systems grew, so grew a need for diagnostics. Early emission based diagnostic tools included spectro-graphs, monochromators, optical filters, photoelectric photometry, and interferometers. A complete listing of experiments in flame spectroscopy from 1800 to 1966 is available in [5]. The tools used for flame diagnostics, however, remained largely unchanged until the invention of the laser, which opened a floodgate of potential.

Use of laser measurement techniques grew rapidly. In 2005, 44% of all papers in the 30th volume of the Proceedings of the Combustion Institute incorporated laser based experimentation such as laser absorption spectrometry (LAS), laser induced florescence (LIF), and coherent anti-Stokes Raman spectroscopy (CARS) (each discussed further in Chapter II). The high degree of spatial, spectral, and temporal precision of lasers coupled with their ability to interrogate crucial minor species keeps them as the frontrunner of all diagnostic techniques. As with all measurement tools, laser systems are not without their limitations. In recent years some of these weaker points are being supplemented with a return of passive emission techniques such as IR camera diagnostics and Fourier transform infrared spectroscopy (FTIS) (both also discussed further in Chapter II). The limitations and advantages of all these techniques will be addressed later in this work, however a few are brought to light now to help motivate this research.

An ideal combustion diagnostic would provide the following capabilities:

1. Measure all relevant chemical species and temperature (*i.e.* scalar fields)

2. Resolve scalars field variations in all three dimensions

3. Track (1) and (2) over time

Most CD techniques focus on one of these goals at the expense of the other two, and a handful of methods do an excellent job at tracking two of these. At present, tech-

2

niques which simultaneously provide the spatial and temporal resolution of multiple scalars (*i.e.*, provide all three capabilities above) are generally lacking, and can be immense in size and complexity when successful [6]. In addition, many of the previous laser techniques require a large experimental footprint and are very challenging to operate, making them unattractive outside of a sophisticated optics laboratory and thus impractical for studying full-scale combustion systems under field conditions. This research brings Imaging Fourier-transform spectroscopy (IFTS) close to being a complete technique, with an ability to meet each of these three capabilities for certain combustion systems. This may represent the most comprehensive yet compact, robust, field deployable combustion diagnostic technique available. Moreover, IFTS requires only one optical port and its operation is nearly identical to a standard infrared camera. As a result, it can be set up and collecting calibrated data in about an hour, making it a very simple diagnostic to implement.

The overarching goal of this research is the development and validation of IFTS as a passive optical tool for the quantitative study of combustion systems. Specifically, this effort (1) couples a spectroscopic radiative transfer model with a tomographic reconstruction technique specifically adapted for IFTS and (2) produces algorithms which enable the transformation of an ensemble of "time-averaged" IFTS measurements of unsteady laminar flames into "instantaneous" snapshot measurements. As a result, this work enables quantitative measurements of multiple scalar fields — *both spatially and temporally* — using IFTS, a novel feat that has not been demonstrated to date. This work validates the spatial-temporal retrieval technique using well-characterized axisymmetric laminar flames, both steady and unsteady. In doing so, a foundation is laid for the application of IFTS to the study of more challenging turbulent combustion sources, which are of practical importance to the USAF and the broader combustion research community.

3

1.1 Research Objectives

This work centers around the use of a medium-wave infrared (MWIR) IFTS camera to make combustion diagnostics measurements of two variations of an unsteady laminar flame. An overall goal was the demonstration of IFTS as a viable tool for the estimation of flame scalar values in a full 4-D sense (temporal and three spatial dimensions). This was achieved through following specific objectives:

1. **Demonstrate IFTS as a viable, steady-state laminar flame CD tool.** Standard calibration techniques were found to be insufficient for use with bright, selectively-emitting radiant flames. This forced the creation of a novel calibration approach essential for the accuracy and validation of any scalar value retrieval technique. This process included the development of a gain and offset smoothing method needed to remove systematic errors due to differences in atmospheric path lengths between calibration sources and the scene, and low signal to noise ratio (SNR) at wavelengths of interest. Next, development of a single-layer, line-of-sight scalar retrieval model provided detailed CD results validated against previous measurements. These results compared favorably in the steady, nearly homogeneous region near the base of the flame, but demonstrated the need for time resolution and tomographic reconstruction models in the unsteady region well above the base. The work supporting this objective is fully developed in Chapter III.

2. **Develop algorithm to recover time-resolved spectra from ensemble measurements.** Traditional Michelson interferometer scenes are static in nature. Rapid scene changes like those in a flame introduce scene change artifacts in the measured interferograms that are not easy to overcome. The DC signal measured by IFTS (and accompanying the AC signal produced by it) encodes information about the temporal dynamics of an unsteady flame. An algorithm has been devel-

4

oped that leverages this information to produce "instantaneous" interferometric measurements corresponding to different times in the period of a harmonically unsteady flame. This is accomplished through logical sorting of DC-level signal for the entire measured data ensemble. The algorithm is validated using CFD model predictions and then applied to an unsteady hydrogen flame and compared with previous measurements [2] of a similarly-configured flame. The work in support of this objective is presented in Chapter IV.

3. **Create spectroscopic radiative transfer tomographic model for radial scalar field estimation.** Emission-based camera measurements capture line-of-sight data. To achieve spatially resolved scalar values in all three dimensions, inversion methods are required. IFTS is uniquely suited to this task as it captures all information needed by most inversion methods in a single measurement. Traditional inversion methods, however, have limitations which can be mitigated by the unique advantages of IFTS. In particular, IFTS's high spatial and spectral resolution across a wide infrared band enable simultaneous radial retrieval of multiple scalars. This objective's work is discussed in Chapter V.

4. **Demonstrate 4-D scalar retrieval in an unsteady laminar flame.** Measured data of an unsteady non-premixed hydrogen flame provided the platform to combine the algorithms developed for Objectives 2 and 3. Results compare favorably with previously reported values and CFD simulation. Temperature and water concentrations were resolved radially at two different "snapshot" times in the period of the flames harmonic motion. This work demonstrates IFTS is a viable tool for the estimation of laminar flame scalar values in a full 4-D sense. The work supporting this objective is developed in Chapter VI.

5

1.2 Document outline

Each new chapter in this dissertation contains its own introductory paragraph outlining the goals of the particular section. Here, an overview of the document is provided to aid in the understanding of how the document is organized.

Following this chapter is a background chapter, with both a literature review and a discussion of important theory (Chp. II). The literature review focuses on relevant work in the combustion diagnostics field. This includes top-level explanations of major laser and passive diagnostic methods used. Several publications will be reviewed in great detail, as their experimental setups have been used as templates, and their results as points of comparison. Next, the theory section lays out important theory including a review of laminar flames, the radiative transfer problem, the inversion problem, and an overview of IFTS.

Chapters III through VI present work supporting the stated objective. Chapter III is presented in the form of a journal article published in Optics Express (Volume 22, Number 18, Page 21600). This article discusses a novel calibration technique designed for IFTS measurements of high temperature flames. It also presents the first IFTS measurements of a laminar flame with scalars estimated using a simplified radiative transfer model for a steady, homogeneous flame and represents the fulfillment of Objective 1. Chapter IV discusses the creation of an algorithm for recovering time-resolved spectra of an ensemble of interferometric measurements of a harmonic unsteady flame. This chapter represents the fulfillment of Objective 2. Chapter V discusses the creation of a tomographic technique featuring an inhomogeneous radiative transfer model for converting line-of-sight emission measurements into radial scalar profile estimates. This chapter represents the fulfillment of Objective 3. Chapter VI presents the results of applying the algorithms developed in Chapters IV and V to estimate temporally- and

6

spatially-resolved scalar measurements in an unsteady laminar flame. This chapter represents the fulfillment of Objective 4.

After placing these results into context of current state-of-the-art CD in the Conclusions (Chapter VII), two appendices are included. First is an article published in the International Journal of Energetic Materials and Chemical Propulsion (Volume 12, Issue 1, Page 15). This article discusses IFTS and its emerging uses for studying combustion and exhaust plumes. The second appendix is a description of the computational fluid dynamics model, UNICORN, used in conjunction with the spectroscopic radiative transfer model to generate synthetic flame data.

II. Background

2.1 Literature Review

Combustion systems represent a very harsh environment, with high temperatures and often rapidly changing complex chemistry. This means that experimental retrieval can be difficult, and simultaneous retrieval of several values of importance such as temperature and species concentrations is harder still. Couple this with the fact that most real world systems have limited optical access, and it's clear why its difficult for a single measurement technique to fulfills the triangle of needs for full CD. It is also no surprise that a host of diagnostics techniques are commonly used today. This section aims to summarize only a handful of the major techniques, with specific focus on those relevant to this work. Several publications will be reviewed in great detail, as their experimental setups have been used as templates, and their results as a point of comparison. First are laser based techniques, followed by radiant emission based techniques. It should be noted that intrusive probe sampling techniques are in common use, but will not be discussed in this document.

Laser combustion diagnostics.

Current methods to determine species concentrations and temperatures in flames are dominated by laser techniques such as LIF, planar LIF (PLIF), LAS and CARS. With the majority of the available data originating from these measurements, it is prudent to provide a compressed review of these techniques. The focus will be on the unique strengths and limitations of each, and how IFTS fits into the current combustion diagnostics community. Although there are many other methods, including many variations on the three discussed here, they will not be addressed as a comprehensive review of laser techniques is not intended. Such reviews are available in the literature [4, 7–10].

www.manaraa.com

Laser-Induced Fluorescence.

LIF and PLIF have developed into the predominant detection method for trace species in flames [4]. This is largely due to the relative ease of the measurement technique, the existence of databases useful for results interpretation, and both point and planar imaging capability [4]. There are extensive reviews in the literature that cover both theory and experimentation of LIF [11, 12], so only a brief discussion of LIF is provided here. In this technique, a laser is tuned to a wavelength matching the energy transition of an atom or molecule of interest [4]. The laser excites the atom or molecule into an elevated state, from which it fluoresces to a lower energy level (still above the ground state). The input frequency of the laser is typically tuned over one or more absorption features of an atom or molecule. This fluorescent emission intensity is then detected as a function of the input laser frequency. In a PLIF system, the camera captures a 2D image of the fluorescence from a laser sheet. Fig. 1 depicts a simple energy diagram of a PLIF system, as well as a simple experimental setup.

The advantages of LIF type measurements include 2D imaging, very fast measurement rates, high spectral resolution, and good signal to noise. LIF has been used for velocity, single species concentration, temperature, and pressure measurements [4]. Flame edge location measurements are particularly suited to LIF as combustion-relevant radicals (OH, CH, C_2) indicate the reaction zone, and are readily detectable by LIF. This is an advantage over IFTS as the emission signal of these minor species is often below the SNR of the IFTS detector. Relative species location and temperature also requires little calibration. LIF temperature estimation relies on monitoring the Boltzmann population distribution of the few ro-vibrational levels interrogated by the laser, which can be done without an absolute radiometric calibration, as long as the wavelength dependent gain of the detector is known. This is something true of most Boltzmann distribution based temperature estimation methods including IFTS.

9
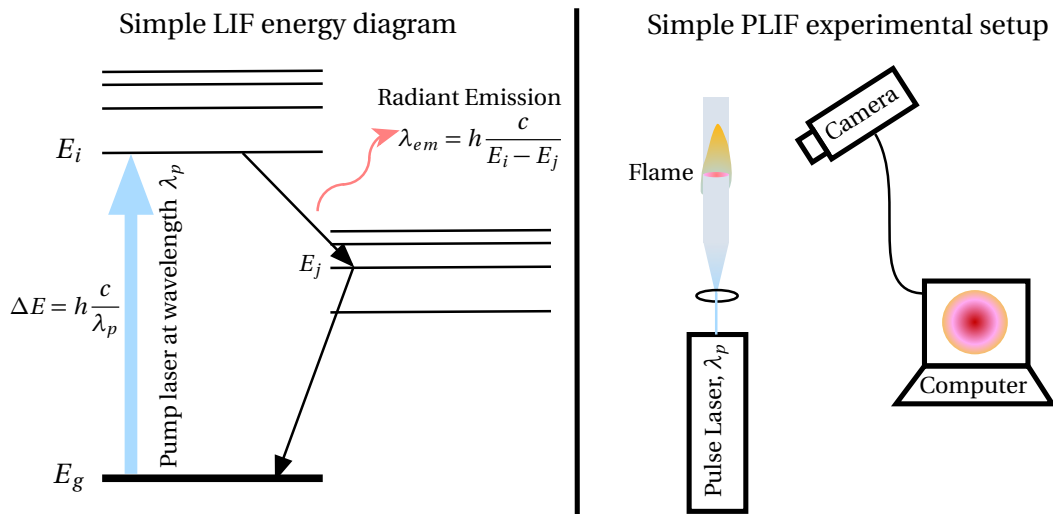
Figure 1. *Left*: **Simple LIF energy diagram.** *Right*: **Simple example of PLIF experimental setup.**

LIF is not without its limitations. The influence of level-dependent spontaneous emission, collisional transfer rates, and/or the magnitude of pre-dissociation may lead to considerable systematic errors [13]. Problems in the measured spectra can arise if one does not account for rotational energy transfer, polarization effects, quenching of the pumped energy level, and any nonlinear excitation or absorption that may occur [14, 15]. This can result in measurement uncertainty on the order of 5-7% of measured temperature values [16]. It is shown in Chapter III that IFTS is capable of uncertainties as low as 1% of temperature value measurements because of the tens of thousands of spectral features captured in each measurement. It is also no trivial matter to interrogate multiple chemical species using LIF, often requiring multiple laser sources. This adds layers of complexity and cost to an experimental setup. Again, the wide spectral band of IFTS captures information of any emitting species in that band with sufficient signal. Lastly, despite the great 2D spatial resolution PLIF provides, either the flame or the laser system must be moved for interrogation of multiple locations in the flame. This may be simple in a laboratory, but could be impractical in a real world situation.

Laser Absorption Spectrometry.

Laser absorption, at the top level, is a very straight-forward measurement technique. LAS is a predominant tool in the absolute quantitative assessment of species [17]. Again, a full review of this technique is not intended and is available in the literature [7, 12]. Laser light, usually from a tunable CW diode laser centered on a major transition energy of the species to be interrogated, is passed through a flame and the exiting attenuated signal intensity, I_{Abs}, is measured. With a knowledge of the starting laser intensity, I_0, the ratio I_{Abs}/I_0 yields the transmittance, τ, of the path traversed by the laser through Beer's law. Fig. 2 shows a simple visual of a LAS system and an experimental setup. Here, $\sigma_{12}(\lambda)$ is the absorption cross section of energy transition from ground (1) to an excited level (2) for the intended species. N_1 is the population of the ground energy state for that species. In a species that is homogeneous through the laser's line-of-sight (LOS), the population is no longer a function of position, x, and the transmittance expression simplifies to $\tau = I_{Abs}/I_0 = \exp[-\sigma_{12}(\lambda) \cdot N_1 \cdot L]$.

Similar to LIF, LAS is capable of detecting trace species in flames by actively interrogating a sample with a wavelength of light set to a specific transition of the trace species. This is again an advantage over IFTS. Unlike LIF though, absolute concentration calculations (as least in the simplicity of homogeneity) requires only a knowledge of the starting and finishing laser intensity, accurate knowledge of the path length L and the cross section of the transition, usually readily available from a database such as HITRAN [18]. This simplicity is why LAS is the predominant tool in quantitative assessment of species. LAS often uses CW lasers, providing a continuous recording of τ with time for an excellent temporal resolution into how species concentration and flame temperature are changing. This is a distinct advantage over IFTS as a single complete spectrum required for scalar value retrieval is collected on the order of 1 to 0.1 Hz.

Most flames are not homogeneous and so the ground level population N_1, among

11
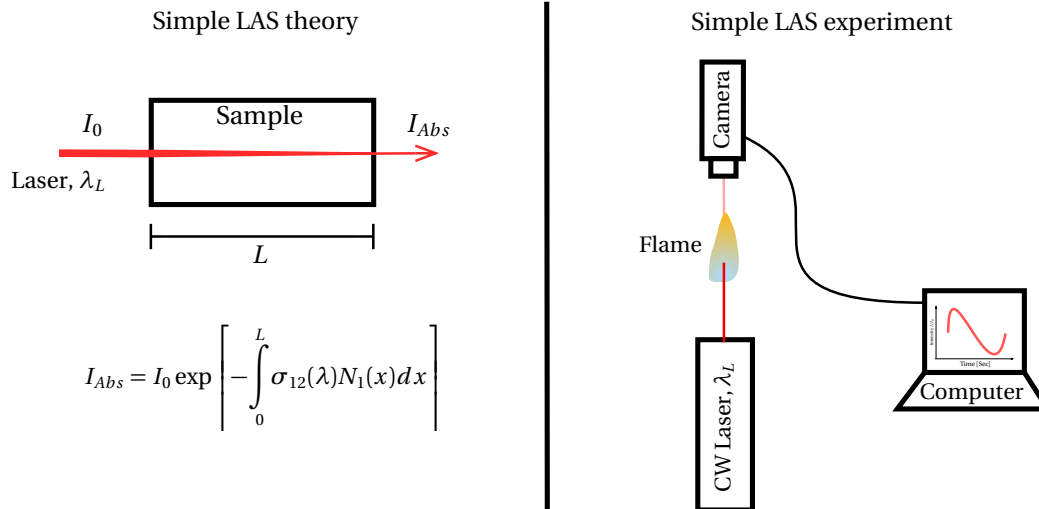
Figure 2. *Left*: **Simple LAS theory.** *Right*: **Simple example of LAS experimental setup.**

other flame conditions, is a function of x. Therefore, just like IFTS, tomographic decon-volution techniques are needed for an accurate estimation of scalar values. Furthermore, LAS takes a single LOS measurement and requires repeated measurements, moving either the flame or the laser (or incorporating many lasers), to construct 2D or 3D scalar maps. IFTS certainly improves on this, as the Telops camera can collect as many as 81920 independent LOS measurements at a single time. Lastly, LAS measures small changes in a very large signal. These small changes can often be on the same level as the noise of the detector or the laser source, making the detectivity of LAS not as high as LIF. There are several ways to improve on this issue, one being an external cavity around the flame, in effect increasing the path length of the flame. Second is the choice of energy transitions, specifically choosing only those with a very high transitional strengths. Both of these options serve to either add complexity to the measurement and post-processing, or reduce the available set of measurements.

The publication by Meyer *et al.* in 2005 [1] is an instance of a LAS experiment that has been of particular importance to this work. It provided a template for the experimental setup and was a point of comparison for the work presented in Chapter III. In Meyer's

work, LOS measurements of temperature and OH species concentration were made on a partially pre-mixed laminar ethylene/air Hencken burner flame using OH–LAS. The Hencken burner is designed to generate a near homogeneous flame close to its base making the homogeneity approximation valid. OH absorption measurements in the UV (313.5-nm) were made using sum-frequency mixing of a 763-nm and a 532-nm laser source in a beta-barium borate crystal. Temperature and OH species values are reported for a variety of flame fuel-to-air ratios (Φ), and at various heights and widths around the flame. These reports indicate that, similar to LIF, scalar values using LAS have uncertainty values on the order of 4-6% of the measured value. This can be as much as 125 K in temperature measurements and 550 ppm in OH concentration. This is due, in part, to the fact that only a single spectral feature was interrogated. IFTS improves on temperature uncertainties here by investigating many spectral features, however uncertainties in the absolute radiometric calibration of the instrument, at this time, limit the accuracy of IFTS for species concentrations to 7-10% of measured value. The reported results of Meyer *et al.* also support the need for multi-layer tomographic reconstruction even in the laboratory ideal Hencken burner flame. Results reported at heights of 40 mm above the burner and higher begin to diverge from computational results. This is attributed to, among other things, the loss of homogeneity in the flame at these heights due to the incorporation of nitrogen from the co-flow and ambient air.

An additional relevant example of a LAS experiment is that performed by Ma *et al.* in 2009 [19]. This work also used a Hencken burner but with a H_2/air flame. Distinguishing this work from that of Meyer *et al.* is the use of a hyperspectral laser source that interrogated the flame, scanning over a $250\,\text{cm}^{-1}$ range ($7250\,\text{cm}^{-1}$ – $7500\,\text{cm}^{-1}$) 200 times a second. This short-wave IR window was ideal for sampling many H_2O absorption transitions belonging to the R branch of the $\nu_1 + \nu_3$ and $2\nu_1 + 2\nu_3$ bands. Although many more lines were captured, only the 100 strongest absorption peaks

13

www.manaraa.com

were selected and used in the analysis to save time and reduce uncertainties. This work also used a tomographic reconstruction technique to develop 2D slices of scalar values. A detailed description of the reconstruction technique is available in [20]. The measurement region was discretized into seven zones by interrogating the flame with 6 beams simultaneously. This consisted of 5 zones of the flame, the N_2 co-flow around the flame and the purge flow around the co-flow. Each zone was assumed to have uniform temperature and H_2O mole fraction. Temperature and mole fraction calculations made using the tomographic reconstruction of the flame were in reasonable agreement with adiabatic flame calculations and previous CARS measurements. For a $\Phi = 1$ flame, the temperature ranged from a peak of 2308 K at flame center to 2221 K in one of the flame edge quadrants. CARS measurements of the same flame indicated a peak temperature of 2400 K and equilibrium calculations predict a peak temperature of 2379 K. Work in [19] is significant because it draws many parallels this work. It incorporates hyperspectral line-of-sight measurements at multiple locations in a flame into a tomographic 2D reconstruction of scalar values in the flame. More over it does so for a H_2/Air flame. This provided an excellent point of reference for methods and techniques for hyperspectral LOS signal as well as points of difficulty. The same inversion algorithm was not used in this work, but useful techniques for handling the hyperspectral component of the signal were implied. IFTS also suffers from having many lines in a spectrum that may be below a practical signal level, resulting in significant errors at those lines. Ma's work shows that ignoring all but the most significant lines is an acceptable way to handle this problem.

Coherent Anit-Stokes Raman Spectroscopy.

Of the three laser techniques discussed here, CARS is the most complicated. As seen in Fig. 3 CARS requires the perfect mixing of three separate laser beams to generate the

14
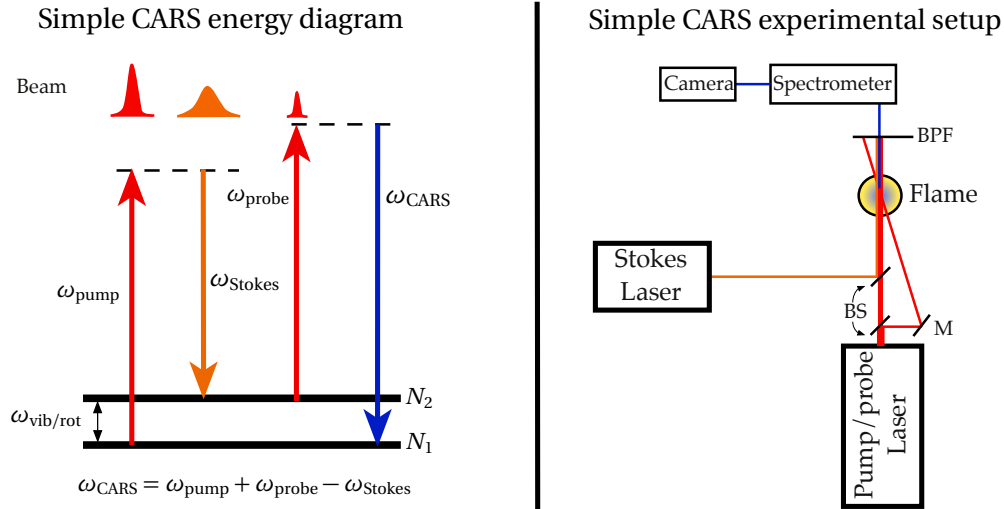
Figure 3. *Left*: **Simple CARS energy diagram. The beam profiles provided are one single example of many possible CARS arrangements.** *Right*: **Simple example of CARS experimental setup. BS = Beam Splitter, M = Mirror, BPF = Band Pass Filter.**

CARS signal. The strongest laser source is the pump laser set at ω_{pump}. This frequency is not in resonance with any transition of the interrogated molecule [4] but rather excites a virtual level. A lower intensity probe beam ω_{probe} at the same frequency is split from the pump beam. A second laser source generates the Stokes frequency ω_{Stokes}. The stokes source can be set up in two different ways. First, is a very narrow band source from a tunable laser. When the frequency difference $\omega_{\mathrm{pump}} - \omega_{\mathrm{Stokes}}$ becomes close to $\omega_{\mathrm{vib/rot}}$, the molecule will experience an oscillating polarization [21]. Because of this oscillation, the resulting CARS signal ω_{CARS}, due to the probe beam ω_{probe}, not only has a frequency of $\omega_{\mathrm{CARS}} = \omega_{\mathrm{pump}} + \omega_{\mathrm{probe}} - \omega_{\mathrm{Stokes}}$, it also is riding on top of this oscillation signal. Second, is wide band stokes source. This allows for single-shot measurements of the entire $\omega_{\mathrm{vib/rot}}$ lineshape if the CARS signal is measured though a spectrometer, as is pictured in Fig. 3 [21]. This method allows for the use of pulsed lasers sources for greater energy and very fast sampling times.

CARS has proven useful in measuring many major species of interest in combustion diagnostics, such as N_2, O_2, H_2O and CO_2 among others [4]. As the name CARS suggests,

15

the signal is coherent in nature and has a very narrow solid angle of emission. This makes signal retrieval relatively easy and provides a much improved SNR over other laser techniques. The primary function of CARS is temperature measurement. The CARS signal depends on both the population N_1 and N_2 in the energy levels that make up the frequency difference $\omega_{\mathrm{vib/rot}}$. This population is governed by the temperature dependent Boltzmann distribution and therefore the CARS signal is also temperature dependent. In fact, CARS is believed to be the most accurate estimation of temperature laser techniques can achieve, with accuracy estimated at better than 40 K [22]. It is the believe of this author that IFTS is capable of meeting this precision in temperature estimation. Concentration measurements with CARS is also possible, as long as a characteristic parameter in the measured spectrum can be distinguished above the noise level [4]. This can include peak amplitude, integrated intensity or spectral shape. Using broadband CARS and spectral line shape, CO concentration in flames has been demonstrated down to concentration levels of 0.5% – 1.0% [23, 24]. Again, because it is an active interrogation technique, CARS will be able to investigate more trace species than IFTS.

CARS does have a limit to the concentration values it can measure. When species concentrations become too low, the spectrally unstructured non-resonate background signal from the bulk of the sample can reach the level of noise in the signal. This noise is primarily made up of fluctuations in laser intensity, mode beating, spatial beam-point stability, and the fact that CARS signal is very dependent on all these values [4]. This limitation raises the major point of concern for CARS measurements – they are incredibly complicated to set up, requiring multiple lasers and any number of high-quality optics. Once set-up they are easily disturbed, often requiring realignment of the laser beams each day. This level of sensitivity to experimental setup limits CARS entirely to a laboratory test platform. IFTS can be easily setup and taking data in a few

16

hours, in the laboratory or in the field, with a relatively small footprint. Lastly, CARS is also a point sampling technique, interrogating only the point where all the beams overlap. 2D and 3D mapping of a flame takes many measurements rather than a single measurement like IFTS.

Radiant emission diagnostics.

Unlike laser based diagnostics that rely on active interrogation of a flame using external sources of radiation, radiant emission based techniques rely only on the self radiation of the chemicals in the flame. The predominant measurement techniques are IR imaging, FTIS, and the newly proposed technique of IFTS. Here we will discuss some of the advantages and disadvantages of each, again stressing how IFTS contributes to the current combustion diagnostic field.

IR Imaging.

Camera imaging in general is a very straight forward technique. A radiating flame of any kind is simply imaged using a camera sensitive to either visible light or IR radiation. The speed and ease of this type of experiment is apparent and is advantage enough if only relative LOS radiation levels are needed. Visible cameras are now capable of imaging at up to 1.4 million frames per second (Phantom v711) and IR-cameras are capable of imaging at tens-of-thousands of frames per second (Telops Fast-IR 1000, Cheetah-640CL). With this kind of temporal and spatial resolution, very fine details of flame turbulence can be measured. Introduction of seeded particles, or scene feature tracking, allows for very accurate flame velocity measurements. Also, filtering the spectral band of the camera intelligently to one dominated by a species of interest, with proper calibration, can be used for rough temperature and concentration measurements. There are many examples of combustion research done using imaging

17

systems. Most deal with the stability, velocity, and shape of flames as cameras capture this information easily. Some examples follow.

In 1969 Robson and Wilson used particle track photography to estimate flame velocity [25]. This helped them determined the stability and lift of a methane diffusion flame as a function of fuel flow rate. Flames seeded with fine aluminum particles were imaged with a camera directly. A strobe illuminated the particles at a 2400 Hz rate allowing the camera to track each particle through the flame over its 0.25 Hz exposer time. At this early date the experiment was done using film cameras and the negatives were projected to 62.5 times regular size and, on paper, the path of particles was tracked.

In 1998 Takahashi *et al.* used particle-imaging velocimetry (PIV) to perform a very similar experiment to Robson and Wilson, investigate the stability and lifting conditions of methane diffusion flames as a function of different stabilizing mechanisms and burner designs. Key advancements included two-color PIV, which allow for two-dimensional velocity flow fields, and numerical models to compare results to. With the advance of camera technology and computer models, PIV became much easier to do. Although color film was still used to capture the images, it was later digitized for analysis on a computer. Although an imaging technique, PIV often requires laser sources to illuminate the particles in the flow.

In 2007 Chung used flame imaging (in part) to investigate the propagation characteristics (speed, liftoff height, reattachment, blowout, and instability) of a more complex tribrachial flame [26]. This is a type of flame composed of a lean and a rich premixed flame wing together with a trailing diffusion flame, all extending from a single point. Such flames can be found in diesel engines, direct injection gasoline engines, premixed-charge compression ignition, and stratified-charge compression ignition engines. The need to understand the stability of these flames is apparent given the list of real world environments they are found in.

Roquemore *et al.* studied the unusual sooting structure of ethylene flames established by laminar recirculation zones of a centerbody burner [27]. Here flame photography, as well as laser sheet visualization and CFD code, helped investigate the unusual characteristic of soot. It was found that soot, entrained in the recirculation zone, followed spiral trajectories that terminated at vortex center. Photography aided in characterizing the sooting structure of the flame by locating and tracing the portion of the flame glowing yellow. A clean burning ethylene flame will glow blue at the base (dominant emission from CH and C_2 radicals), whereas soot will be yellow in the flame (dominant greybody emission). When photography was used in conjunction with sheet lasers (used to illuminate soot particles) it was discovered the soot followed discrete spirals. The photographic results, as many experimental results are intended to do, helped validate the predicted results of the CFD soot model used and showed that the simple soot model predicted the properties of these complex flames reasonably well. In a separate publication [28], the centerbody burner was again used to study sooting behavior as a function of the flame flow conditions. Photography helped discover that the sooting behavior of the flames could be dramatically altered, without changing the fluid dynamics. Under a narrow window of flow conditions, a toroidal flame could be seen near the base of a lifted flame. Interestingly, using CFD and high-speed imagery as support, it was concluded that the observed toroidal flame was an optical illusion created through the natural time-averaging of the eye.

In 2013, Denisova *et al.* published a work on emission tomography in flame diagnostics that looked to recover in-plane distributions of emission intensity measurements [29]. Final retrieval of scalar values came from a maximum entropy-based method. This was done by capturing spectral images of the flame using a CCD camera and appropriate filters to isolate emission from OH, CH, and C_2 radicals.

Additional examples showing comparisons between measured and computed flame

radiation are [30] and [31]. In 2012, Rankin *et al.* compared narrow band mid-IR radiation intensity measurements of both steady and unsteady bluff body stabilized laminar ethylene flames to computed infrared images [30]. The computed images were generated by solving the radiative transfer equation along lines-of-sight through the flame, not unlike what is done in this work. The goal of this work was insight into the flame stabilization region, and beyond, through qualitative and quantitative comparison of measured and computed imagery. Rankin *et al.* found good agreement between measured and computed images in all areas except some educational differences in the flame stabilization region. In 2013 Rankin *et al.* continued work with IR imaging, extending into the turbulent flame regime [31]. Radiation values as a function of both position and time were investigated, including mean and RMS intensities, population distribution functions, power spectral density functions of the radiation intensities, and spatial correlation of radiation intensities.

In 1999, Mungal and Lozano investigated how a jet in crossflow made from the burning plume of an unabated oil well discharge changed over time [32]. This was done directly from video footage purchased from a news network recording oil wells burning in Kuwait during the Gulf War. The footage was broken down frame-by-frame (30 frames/sec) to generate an x-y-t look at the plume. With this, it was discovered that the burning jet consisted of a series of large-scale organized structures that convect downstream, leading to a periodic flame tip burnout. The plume was much less organized, but the speed of the burning structures as they transitioned from jet to crossflow direction showed a constant speed. This suggested an underlying organization existed in the jet crossflow, in spite of its complex structure. This example of flame imaging diagnostics demonstrates combustion diagnostics where only a very limited amount of data was available, as is often the case during a war-time environment.

A secondary use for imaging combustion diagnostics is real-time condition monitor-

20

ing of combustion systems. One such example is that done by Hernandez and Ballester in 2008 [33]. In this work, three different techniques were explored for their ability in the identification of combustion states (useful for optimizing flame conditions and for use in advanced flame control techniques). First, was feature extraction, or the derivation of parameters directly from flame images. Second, was a technique using artificial neural networks to relate image features with relevant combustion parameters. This requires the development of a user designed "neural pathway" that weight, transform and compute outputs to be passed on "from neuron to neuron" given the input information of each pixel. Lastly, probabilistic pattern recognition was used to estimate relevant combustion parameters. This work shows the major advantage of CCD based imaging systems, that is real time diagnostics of 2-D flame information. More over, it proves that through some complex forethought of the processing, simple 2-D images can be interpreted into acceptably accurate, relevant combustion parameters usable in a feedback loop to optimize the combustion process.

A specific example of IR imaging used with thin filament pyrometry (TFP), that is of particular value to this work, was performed by Blunck *et al.* in 2009 [2]. In this work, an unsteady non-premixed hydrogen flame was generated using a stainless steel tapered tube with an inner diameter of 8 mm and a hydrogen flow rate of 52 mg/s. A FLIR Phoenix IR camera was used to image LOS radiation emission mostly from H_2O. A thin (15 μm diameter) silicon carbide filament was placed perpendicularly through the flame for enhanced temperature measurements. Using known emissivity and thermal properties of the filament, accurate temperature estimations were made at all points along the length of the wire. This is a well established technique because of its relative simplicity with an accomplished set of literature available for review [34, 35]. The radiation of the filament $J_{\text{fil}}^{\text{ref}}$ was calibrated first by looking at the filament in a McKenna burner at a known temperature. Future measurements of the filament in the hydrogen

21

flame were then normalized by this calibration radiance value. The temperature of the filament was determined by cross-referencing the measured ratio to a look-up table with calculated ratios at various T_{fil}. The temperature of the flame T_f was found from the temperature of the filament by correcting for radiative heat loss. Using this method yielded an overall uncertainty in T_f measurements of 7% at 1200 K and 11% at 2400 K. Measured temperature values agreed well with numerical simulations across the width of the flame. Because the filament stretched across the full width of the flame, the camera is able to capture the full radial temperature profile. Lastly, due to the rapid thermal response of the filament and the fast imaging capability of the camera, temperature measurements were gathered as a function of time, and these also agreed well with numerical simulations.

Water vapor mole fraction $\chi_{\text{H}_2\text{O}}$ was found using the spectral radiation values from the flame (not the filament). To account for the non-homogeneous nature of the flame, a narrowband radiation model called RADCAL [36], along with an onion peeling technique was used with the known temperature profile of the flame found using TFP. Additional details on an onion peeling method will be provided in Sec. 2.2, but in short $\chi_{\text{H}_2\text{O}}$ is found for the outer most ring of the flame, this value is then used to determine $\chi_{\text{H}_2\text{O}}$ for the next ring and so on to the center of the flame. Using this method $\chi_{\text{H}_2\text{O}}$ values found agreed within reason with numerical simulations of the flame. Typical uncertainties in $\chi_{\text{H}_2\text{O}}$ were found to be 21% of the value. In some instances, it was reported that calculated $\chi_{\text{H}_2\text{O}}$ values would begin to increase sharply near 0.5 cm radii due to the propagation of uncertainty. Because of this there are no reported $\chi_{\text{H}_2\text{O}}$ values within 0.5 cm. These results exemplify the most common difficulty in in the onion-peeling technique. Propagation can cause very large errors and uncertainties in the middle layers of a flame.

Fourier transform IR spectroscopy.

Similar to IR-imaging, FTIS relies primarily on the self radiation of the flame for information. There is a large set of work that uses FTIS with both emission and transmission measurements, similar to that shown in the right side of Fig. 4, which require an external radiation source and, for the purpose of this work, both will be discussed in a single group. A common technique employs the use of a Michelson interferometer to measure the constructive and destructive interference of emitted/transmitted radiation as one mirror in the Michelson is moved. One full movement of this mirror builds an interferogram that is then interpreted into a spectrum through a Fourier transformation. The length the mirror traverses determines the spectral resolution of the flame measurement. Additional details on the theory of interferograms and Fourier transforms are provided in Sec. 2.2.

This process has an advantage over all the previously discussed techniques in that a very large band of spectral information (millions of wavenumbers) can be collected in one measurement. If the spectral window is chosen carefully, information on temperature and the mole fraction of major combustion chemicals (H_2O, CO_2, CO, OH and CH_4 among others) can all be determined simultaneously. Because of the large and highly resolved spectral axis FTIS can provide, there can be millions of spectral features all governed by a temperature dependent Boltzmann distribution. This provides a highly oversampled system for temperature estimation using one of the accepted spectral databases, such as HITRAN [18]. Temperature and mole fraction estimations can therefore be very precise if the LOS is uniform. Additionally, similar to simple IR-imaging, self-radiation of the flame can be measured from great distances, making it an excellent field-deployable monitoring system.

FTIS is limited to a single LOS measurement, making it an impractical technique for mapping scalar values though the flame. Also, it is limited in its ability to detect

23
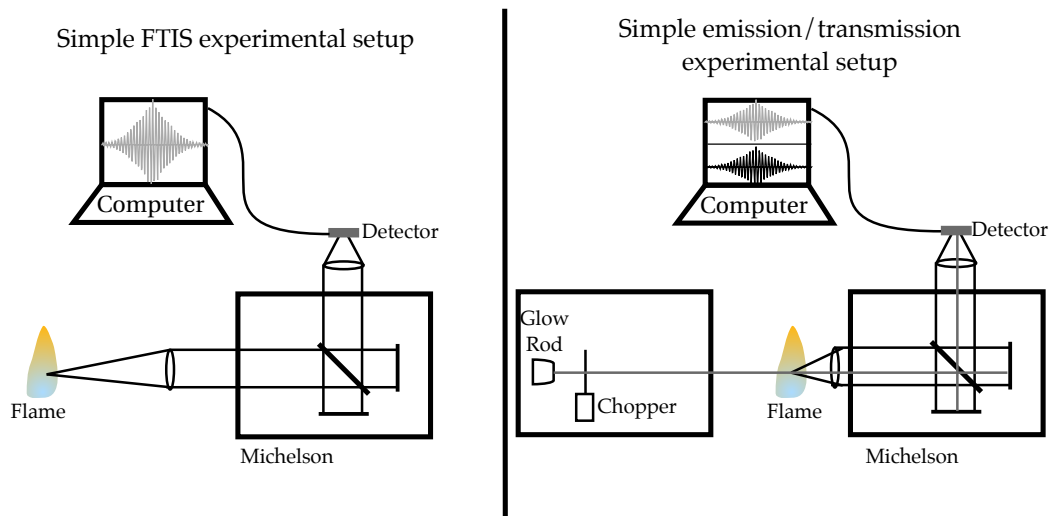
Figure 4. *Left*: **Simple setup of an emission based FTIS measurement.** *Right*: **Simple FTIS setup that includes both emission and transmission measurements.**

trace species that may have a weak signature in the spectral band of the detector. Lastly, because a spectrum is only available after a full scan of the Michelson mirror, temporal resolution of scalar values is usually in the 10 to 100-Hertz range. Any changes in the scene radiance over this scan will also severely complicate the meaning of the measured interferogram. Scanning time can be decreased, however this is usually done at the loss of spectral resolution or a decrease in the SNR of the measurement.

Early work with spectroscopic flame diagnostic measurements date as far back as at least the 1940's, where flame spectroscopy and radiation was a large topic of discussion in combustion study due to the up-tick in combustion research in the late, and post-WWII era. This literature review starts in 1966 where Tourin made static temperature and water vapor concentration profiles in non-uniform combustion gases using simple spectroscopic measurements [37].

Simmons, Yamanda and Arnold made temperature profile estimates of a non-isothermal gas in 1969 using the now popular emission/absorption technique [38]. This work utilized a hydrogen/oxygen flame generated from a seven segment burner. This ensured that the flame would have a temperature and species gradient across

24

the width of the seven burners by adjusting fuel flow through each. Using a known "general shape" of the temperature profile, the scalar profiles were approximated in terms of a simple geometric form so the profiles could be characterized in terms of a few parameters.

An excellent early work that utilized a multilayer axisymmetric approach to estimate temperature and concentration profiles is that of Brewer and Limbaugh [39]. The primary focus of this work was the development of a numerical iterative technique that solved for temperature and water vapor concentration profiles from known line strengths. This technique proved accurate when tested on a hydrogen-air flame using emission/transmission measurements. Also important in the 60's was the continued theoretical and experimental studies that yielded a fundamental basis for a H_2O and CO_2 radiation [40] and a narrow-band statistical model [41].

FTIS works earlier than the 70's are very scarce as the first commercial FTIS was not made available until 1969. The frequency of FTIS measurements in the literature does however explode in the 80's with the increase in both energy demand (through the combustion of more caustic fuels) and the desire to reduce emissions. This *catch-22* forced the industry into new and efficient combustion techniques to handle new types of coal, as well as, new techniques for *in-situ* monitoring of exhaust products. Many of these works relied on simple FTIS and emission/transmission (E/T) FTIS techniques with a focus on soot content and particle size [42–48]. The goals of these tests were usually met with a simple LOS measurement, so most work in this era did not include tomographic reconstructions. There was also some work done using FTIS in the automotive industry (Ford Motor Co.) to help characterize vehicle emissions and engine operating parameters [49, 50]. Again, because emission regulation was the predominant driving force behind these works, only emission gases were tested, which do not need to be spatially sampled.

25

In the 90's the research focus had largely switched over to laser-based techniques and the frequency of FTIS documentation began to decline. Those papers that were published did start to venture more into tomography, also in the coal fire research field [51]. Other tomographic work was being done on non-coal flames, such as laminar diffusion sooting ethylene and ethane flames [52]. In this work. line-of-sight E/T FTIS measurements were used along with a tomographic reconstruction technique to derive spectra corresponding to small volumes within the flame. From these derived spectra, scalar values were calculated resulting in temperature and species profiles throughout the flame.

FTIS research even branched out into the field of toxic waste incineration where it was used to measure chlorinated hydrocarbons in combustion [53]. In 1999, Clausen took a different approach with FTIS emission measurements by trying to estimate the temperature and concentration of low levels of CO in CO_2 by degrading the spectral resolution and thereby increasing the SNR of the detector [54]. This was a technique used later with laboratory diffusion flames [55]. Aircraft exhaust signatures are always a topic of importance, so it is no surprise that FTIS was used to measure infrared spectra of the exhaust gas of an aircraft's jet engine [56–58]. And there was also other work done that was intended for high temperature FTIS work [59].

More modern works, 2000 and later, naturally start to venture into expanded or specific applications geared toward optimizing already established systems or for understanding subtle aspects of combustion. One example looked at what affect turbulent fluctuation in flames might have on temperature retrieval and reconstruction [60]. This is important as an FTIS measures a spectrum over a time scale much slower than that of turbulence intensity and spectra generated from such measurements will have systematic errors as a result. Additional work on high temperature gases also continued [61, 62], with work aimed at validating artificially calculated data in databases such

26

as HITEMP [63]. One important article in tomographic reconstruction work is that done by Lim *et al.* [64]. In this work, a fast scheme for obtaining soot volume fraction, gas temperature, and major gas species concentrations was developed using spectral radiation intensities from a homogeneous layer. Although it is admitted that most flames will not be homogeneous, this work is an essential component for emission tomography methods that will be discussed in Sec 2.2. In 2007, Ayranci *et al.* used emission measurements to determine soot temperature, volume fractions and also refractive index [65]. These values were calculated using an inversion scheme based on tomographic reconstruction of the flame emission. The refractive index of the soot was found from spectral gradients of the emission spectra.

Imaging Fourier transform spectroscopy.

IFTS takes the advantages of FTIS and couples them with an imaging system to extend the usefulness of Michelson-based spectroscopic combustion diagnostics. Now, rather than a single point interferogram, a very fast IR imaging camera is placed behind the Michelson collecting an interferogram at each pixel simultaneously. Each of these interferograms is converted into a spectrum and the same diagnostics advantages FTIS provides are now available with up to $0.5 \times 0.5 \, \text{mm}^2$ spatial resolution. IFTS has already been demonstrated as an effective tool for measuring scalar values in a non-reacting turbulent exhaust plume exiting a coal-fired power plant [66]. In this work, measurements of temperature and typical combustion exhaust species using IFTS agreed very well with those of *in situ* measurements.

The advantages over standard FTIS are clear. The ability to image the scene provides both context to the spectra, as well as, the ability to map temperature and mole fraction measurements. Additionally, the camera does not remove the DC component of its signal, and a simple low-pass filter turns the data back into an IR video of the flame

with the ability of up to 10 kHz broad-band imaging. Chapter IV shows how this DC signal can be correlate to specific periods in a flames motion. [67] showed how the DC signal can provide turbulent statistics the flame.

Although IFTS images the flame at a high temporal rate, the full spectrum is still collected at sub-Hertz rate for most spectral resolutions desired. In fact, the added burden of such large data sets makes the full scan time of the Michelson slower than its FTIS counterpart for similar settings. Also, retaining the DC level of the signal does come with a disadvantage. Most of the cameras dynamic range is taken up with this DC level and, in bright flames, this can result in the need for ND filters, low integration times, and ultimately reduced SNR. Each pixel is still a single LOS measurement as well, so scalar values of inhomogeneous flames need to be reconstructed using tomographic techniques that may disaffirm the precision IFTS has shown in homogeneous flames. Fortunately, this is a well vetted problem in the FTIS community and previously accepted tomographic solutions are applicable, with the added advantage that IFTS collects all the needed information for most tomographic techniques in one measurement.

2.2 Theory

This section aims to lay out important theory relevant in this work. This includes a review of laminar flames and their functionality, computational fluid dynamics modeling, the radiative transfer problem, the inversion problem, and IFTS and how it works.

Laminar flames.

Although the lion's share of modern combustion diagnostics is focused on turbulent flames (and rightly so due to the turbulent nature of most real world combustion sources) there is still a need to investigate laminar flames for calibration and kinetic model verification.

28
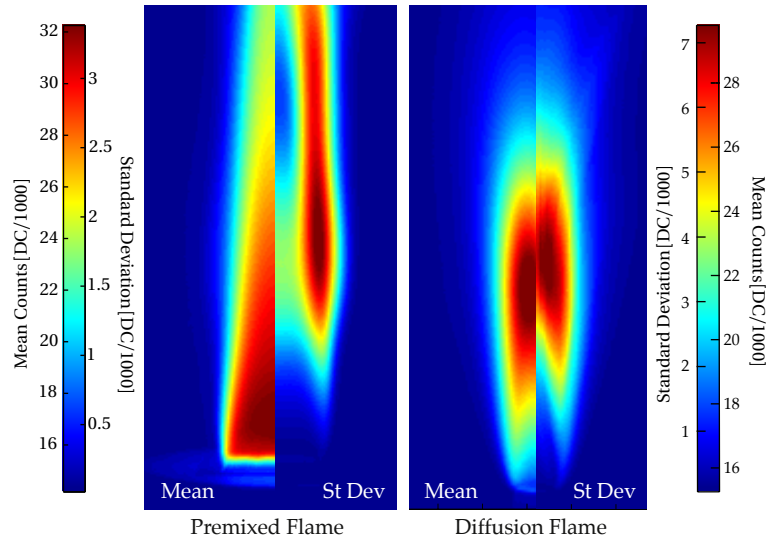
Figure 5. *Left***: Mean and standard deviation IR measurement of a laminar premixed flame.** *Right***: Mean and standard deviation IR measurement of a laminar diffusion flame.**

Laminar is defined as a fluid flow that has no disruption, or cross flow, between adjacent layers [68]. This is usually achieved through slow flow rates relative to the size of the flow field and no obstructions in the flow field. The dimensionless Reynolds number $Re = \rho V L/\mu$ is the parameter that describes whether flow conditions are laminar or turbulent in nature. Here ρ is the density of the fluid, V is the fluid velocity, L is the characteristic length of the flow (for this work L is the exit diameter of the pipe anchoring the flame), and μ is the viscosity of the fluid. There is no single Reynolds number that defines exactly the break between laminar and turbulent flow, but for $Re < 2000$, flows are normally considered laminar.

Laminar flames can be broken into two major types: premixed and diffusion. In a premixed flame, the fuel and oxidizer needed for combustion are mixed together to create a homogeneous mixture prior to ignition. This provides a uniform flame, and is the major technique used in calibration flames such as the Hencken burner or the McKenna burner. The left side of Fig 5 gives an example of mean radiant emission in the mid-IR from a laminar premixed flame. Note the uniformity in intensity across much

of the base of the flame. This is also shown in the radiant standard deviation value in the same area. In a diffusion flame, the fuel source and the oxidizer are introduced in separate locations (generally a jet of fuel flowing into ambient air). This produces a flame that is still laminar, but now has temperature and species profiles that are no longer near-homogeneous. The right side of Fig 5 gives an example of a diffusion flame. Here the mean image shows a large gradient in radiance over the radial profile. This is due to the fact that the flame is only prevalent where the correct fuel and oxidizer mixture exists, which is only at the edge of the fuel jet that is in contact with room air. The standard deviation shows that, near the center of the flame, there is little radiation or change in radiation because there is no oxidizer near the pipe exit, only the fuel jet.

During the early stages of this work, such as development of a calibration technique and when using a single-layer radiance model, a laminar premixed Hencken burner was used. This was done to help minimize any systematic errors that might have occurred due to modeling a multilayered flame using only a single model estimate. In the latter stages of this work, more complex diffusion flames were used for the development of a multilayer algorithm and a time-resolved interferogram formation algorithm.

Computational Fluid Dynamics Modeling.

Computational fluid dynamics is the use of numerical analysis to solve fluid flow problems. At the heart of all DFC models are the Navier-Stokes equations, which describe the motion of viscous fluid substances [68, 69]. In laminar flames this can be done analytically. In turbulent flows the introduction of the Reynolds stress causes a closer problem which makes analysis significantly more difficult. Turbulent CFD is, however, beyond the scope of this work. Classic applications of CFD include modeling air flow over a wing or around a car. Results can be beneficial for estimating drag and lift forces or predicting the leading-edge temperatures, and often provide bounds for

30

later experimental testing. Note that these examples do not have a reacting flow field, which greatly simplify the modeling process. A subclass of CFD, which is computational fluid dynamics with chemistry (CFDC), aims to model flow fields where species concentrations and temperature vary greatly due to chemical reactions in the flow. Laminar flames are an example of just such a flow, making CFDC very relevant to this work.

Specifically, the CFDC model entitled UNICORN (UNsteady Ignition and COmbustion with ReactioNs) was used extensively in Chapters IV and V to generate simulated data sets of flames. UNICORN is perhaps one of the most thoroughly evaluated reacting Navier Stokes based codes developed today [70]. UNICORN solves for axial- and radial-momentum equations, continuity, and enthalpy- and species conservation equations to simulate combustion in flames [70]. When written written in a cylindrical-coordinate system, the governing equations are [70]:

$$\frac{\partial \rho}{\partial t} + \frac{\partial \rho u}{\partial z} + \frac{1}{r}\frac{\partial (r \rho v)}{\partial r} = 0 \tag{1}$$

and

$$\frac{\partial (\rho \Phi)}{\partial t} + \frac{\partial (\rho u \Phi)}{\partial z} + \frac{1}{r}\frac{\partial (r \rho v \Phi)}{\partial r} = \frac{\partial}{\partial z}\left[\Gamma^\Phi \frac{\partial \Phi}{dz}\right] + \frac{1}{r}\frac{\partial}{\partial r}\left[r \Gamma^\Phi \frac{\partial \Phi}{\partial r}\right] + S^\Phi \tag{2}$$

Here, ρ, is the flow density, u and v are the axial, z, and radial, r, velocity components respectively. Eq. 1 is the continuity equation and Eq. 2 is either the momentum, species or energy conservation equation, depending on the choice of Φ. Γ^Φ are transport coefficients and S^Φ are source terms. A table of the various Φ, Γ^Φ, and S^Φ is available in [70].

In solving, momentum equations for u and v are integrated using an implicit QUICK-SET (Quadratic Upstream Interpolation for Convective Kinematics with Estimated Streaming Terms) numerical scheme [71]. Species and enthalpy is obtained using the hybrid scheme found in [72] along with upwind and central differencing. The finite-

31

difference form of the governing equations, evaluated on a staggered-grid in z and r, is written as:

$$A_P\Phi_P^{N+1} + A_{z^{++}}\Phi_{z^{++}}^{N+1} + A_{z^+}\Phi_{z^+}^{N+1} + A_{z^-}\Phi_{z^-}^{N+1} + A_{z^{--}}\Phi_{z^{--}}^{N+1} + A_{r^{++}}\Phi_{r^{++}}^{N+1}$$
$$+ A_{r^+}\Phi_{r^+}^{N+1} + A_{r^-}\Phi_{r^-}^{N+1} + A_{r^{--}}\Phi_{r^{--}}^{N+1} = S_P^\Phi + \Delta t\,\rho_P\Phi_P^N \tag{3}$$

This equation is solved over the time increment, Δt, at a point, P. N and $N+1$ are the known variables at the Nth time step and the unknown variables at the $(N+1)^{\text{th}}$ time step. z^- and z^+ are values at grid points immediately adjacent to P. A, and the terms on the right-hand side of Eq. 3 are calculated from known variables at the Nth time step. The pressure field at every time step is calculated solving a system of algebraic pressure Poisson equations at all grid points using the Lower-Upper decomposition technique. Enthalpy of all species is calculated using polynomial curve fits and are valid over the temperature range 300 to 5000 K. Viscosity, thermal conductivity, binary molecular diffusion coefficients and other such physical properties of the species are calculated using molecular dynamics. Mixture viscosity and thermal conductivity are estimated using the Wilke and the Kee expressions respectively [73]. Molecular diffusion velocity of a species is calculated according to Fick's law, using the effective-diffusion coefficient of that species [74]. The Lennard Jones potentials, effective temperatures, and coefficients for enthalpy polynomials for each species are obtained from CHEMKIN libraries. The UNICORN edition used in this work (UNICORN GRI Version 3.0) had a finite rate chemistry database that included 53 species and 650 possible chemical reactions.

This description of UNICORN only begins to describe the complex task of modeling reactive flow fields. The limiting factor in these simulations is a precise understanding of particle-particle interactions in the flow. Accurately modeling these interactions yields chemical reaction rate values and other crucial constants that are in the CHEMKIN

library. Simple monatomic and diatomic particles, such as hydrogen radicals or O_2, follow ideal gas laws closely and their interactions can be modeled with a simple kinetic theory and the billiard ball approximation [75]. With the introduction of more complex chemicals, such as hydrocarbons, the particle-particle interactions are no longer ideal and become very hard to model. Values for these more complex reaction chains found in the CHEMKIN library often come from laboratory measurements and empirical observations. Many of the chemicals in combustion, however, are very reactive and are nearly impossible to isolate to a degree sufficient for high-fidelity laboratory experimentation. Because of these limitations in the available data needed for CFDC, experimentation on simple laminar flames is still an important field of research. Measurements, such as the ones made in this work, are useful for validating CFDC predictions and isolating areas of improvement. In-fact, this interplay between CFDC and experimental measurements is a major driving force behind new discoveries in combustion phenomenon. IFTS measurements, capable of resolving major species three-dimensionally and in time, would be greatly beneficial to this effort.

Radiative transfer.

As with all passive radiation detection techniques, IFTS relies exclusively on radiation emitted by the flame. Here, we will discuss in some detail the phenomena of radiative transfer to provide insight into the measurements an IFTS camera is making.

Radiative transfer, simply defined, is how radiation born at one location is transferred to another. This process can include additional emission of radiance, absorption of radiance, and scattering. Each of these processes influence and change the total radiance that makes it to a detector. Using Modest [76], the general equation for radiative

33

transfer is an expression of the conservation of energy, and is given by

$$\frac{dL_{\tilde{\nu}}}{d\alpha} + L_{\tilde{\nu}} = (1 - \omega_{\tilde{\nu}})B(\tilde{\nu}, \alpha) + \frac{\omega_{\tilde{\nu}}}{4\pi} \int_{4\pi} L_{\tilde{\nu}}(\hat{s}_i)\Phi_{\tilde{\nu}}(\hat{s}_i, \hat{s})d\Omega_i \tag{4}$$

where here $L_{\tilde{\nu}}$ is the spectral radiant intensity, α is a dimensionless coordinate referred to as the optical depth, and is inversely proportional to the mean free path of a photon, $\omega_{\tilde{\nu}}$ is the spectral single scattering albedo, $B(\tilde{\nu}, T)$ is Planck's blackbody function at α, and $\Phi_{\tilde{\nu}}(\hat{s}_i, \hat{s})$ is the scattering phase function in the $\hat{s}$ direction. The right hand term is referred to as the source function, $S_{\tilde{\nu}}(\tilde{\nu}, \hat{s})$, for radiative transfer and represents the spectral radiant intensity in the $\hat{s}$ direction.

The solution to Eq 4 is a third-order integral equation in intensity $L_{\tilde{\nu}}$ and is quite complicated to use. There are assumptions about the flame that considerably simplify things. We will first assume the flames under investigation are free from scattering effects. That is to say $\omega_{\tilde{\nu}} \approx 0$. This greatly simplifies Eq 4, and is often a simplification used in combustion [76]. This assumption is valid because the flames under investigation in this work are clean-burning, soot-free flames. Also, the molecular size of the chemical species are far smaller than the wavelengths under investigation. The flame is, therefor, free of any particles that meet the Mie or Rayleigh scattering criteria. Without scattering, Eq 4 reduces to

$$\frac{dL_{\tilde{\nu}}}{d\alpha} + L_{\tilde{\nu}} = B(\tilde{\nu}, \alpha) \tag{5}$$

which can be solved using the integration factor $e^{-\alpha}$:

$$L_{\tilde{\nu}}(\alpha) = L_{\tilde{\nu}}(0)e^{-\alpha} + \int_0^\alpha B(\tilde{\nu}, \alpha')e^{-(\alpha-\alpha')}d\alpha' \tag{6}$$

In this form, $L_{\tilde{\nu}}(0)e^{-\alpha}$ represents any background radiance the system may have attenuated through the flame following Beer's law. As is the case in this work, this term is often ignored in the mid-wave IR as radiation from the flame dominates. It

34

should be stressed that the variable α is itself a function of position in the flame and spectral channel. This will be a very important aspect of the second half of this work, as investigations into flames that have non uniform temperature and species profiles begins. For a homogeneous source, however, there is an additional simplification that is common:

$$L_{\tilde{\nu}}(\alpha) = (1 - e^{-\alpha})B(\tilde{\nu}, \alpha) = \varepsilon(\alpha)B(\tilde{\nu}, \alpha) \tag{7}$$

which is quickly recognized as an expression of the gas emissivity $\varepsilon_{\tilde{\nu}}$ through Kichhoff's law ($\varepsilon_{\tilde{\nu}} = 1 - \tau_{\tilde{\nu}}$) where $\tau_{\tilde{\nu}}$ is the expression of the transmittance of light through a homogeneous medium following Beer's law. Eq 7 represents the radiative transfer problem in its simplest form, with the inclusion of several assumptions that will not be valid in later work. These difficulties will be further addressed in the next section and the radiative transfer equations will be readjusted to their needed forms.

Radiance model.

Understanding the radiance of the flame is key to the success of this work. As such, we will devote this section to a discussion of the radiance model used both in previous work, as well as the adaptions for future work. The equations developed in the above section will be adjusted as needed and put to use to explain what radiance the camera is measuring. With this, comes the hope that temperature and species concentrations in the flame can be worked out. Radiance models used with the IFTS have already been used successfully and reported in the literature [66].

Single layer model

It is pragmatic to discuss some of the fundamental concepts using a single layer model. This is unrealistic as most flames have some inhomogeneity in them, but the concepts are easily extended. With this assumption we can start directly from Eq 7 and

35
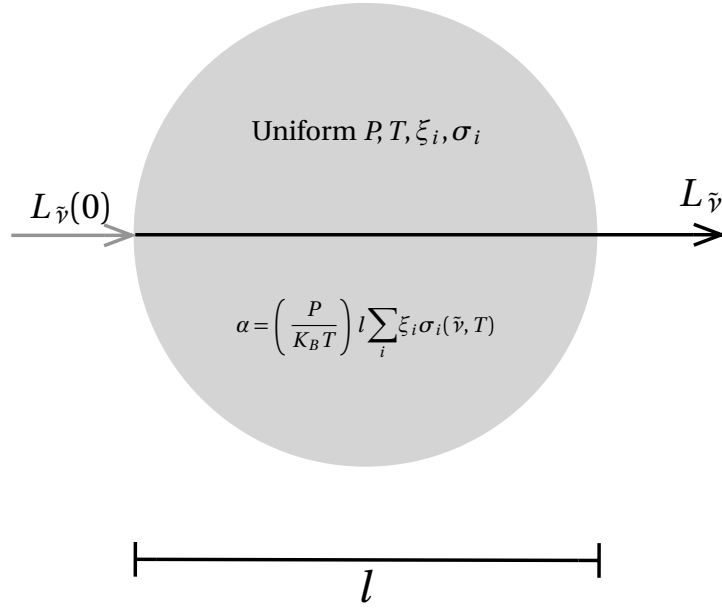
Figure 6. A schematic of a homogeneous single layer flame

define the optical depth variable as:

$$\alpha = \left(\frac{P}{K_B T} \right) l \sum_i \xi_i \sigma_i(\tilde{\nu}, T) \tag{8}$$

where we make the assumption (shown in Fig. 6) that the flame is at the same temperature T, species concentrations ξ_i, and pressure P, across the width l. Absorption cross sections $\sigma_i(\tilde{\nu}, T)$ of each species i and at each spectral channel $\tilde{\nu}$ are well defined through the various available databases such as HITRAN [18]. Again, we have assumed here that $L_{\tilde{\nu}}(0) = 0$. With this simple model, it is straight forward to equate $L_{\tilde{\nu}}(\alpha)$ with the measured radiance at the detector $L_{i,j}^{scn}$ (developed in Sec. 2.2) and adjust the independent variables T, and ξ_i until the measured radiance matches the model radiance as best as possible. In so doing, we achieve a best estimate for the temperature and species concentrations of the flame.

Multi layer model

It is not hard to see that most flames will not be homogeneous in temperature and

36
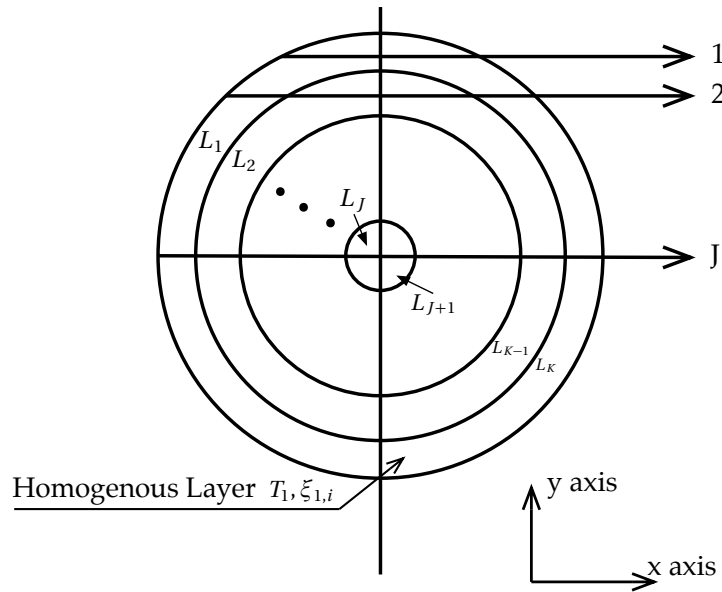
Figure 7. A schematic of a multi layer flame made up of J homogeneous layers. Note that layer $L_K = L_1$ but mathematically it is easer to number the layers from 1 to K rather than 1 to J and back to 1.

all species concentration across it's full width. This inhomogeneity complicates the estimation of scalar values and demands a multilayer model of the flame. Ideally, the flame could be treated as a continuous variable that could be integrated over, but because the IFTS camera does not have infinite resolution, it demands a discreet interpretation of the flame.

The flames that will be investigated have been carefully picked so they possess axial-symmetry. The most pragmatic way to discreetly interpret such flames is to assume it's comprised of concentric rings, each with some finite width, and each assumed to be itself homogeneous. This is depicted in Fig. 7 for a flame made up of J rings. Note that layer $L_K = L_1$ and $L_{k-1} = L_2$ and so on, but mathematically, it is easier to number the layers from 1 to K rather than 1 to J and back to 1. Now each line-of-sight radiance can be broken down into a radiative transfer equation comprised of a sum of each

37

homogeneous layer and their transmission through each successive layer. For example, LOS 1 in Fig. 7 is still simply a single homogeneous layer and can be expressed using Eq 7 and Eq 8. LOS 2, however, is comprised of two layers. The LOS radiance at layer J can be expressed as:

$$L_J = \sum_{i=1}^{K} \left(\varepsilon_i(\alpha_i) B(T_i) \prod_{j=i+1}^{K} \tau_j(\alpha_j) \right) \tag{9}$$

Perhaps a more simple way to express this is to combine Eq 6 and Eq 7 to express the accumulated radiance at each layer L_i:

$$L_i = \tau_i L_{i-1} + (1 - \tau_i) B(T_i) \tag{10}$$

where in this form we recognize that $\tau_i L_{i-1}$ is again just the background radiance that enters layer i and is attenuated through by τ_i and $(1 - \tau_i)B(T_i)$ is the radiance born in that layer. Note here again that $(1 - \tau_i)$ is the emissivity of the ith layer.

With this model, the scalar value profiles of any axisymmetric flame can be worked out given enough LOS measurements of the flame. It should be noted that this model is most effective given an optically thin flame. That is to say, when the product $\prod_{j=i+1}^{K} \tau_j(\alpha_j) \gg 0$ for all values of $\tilde{\nu}$. If this is not the case the measured radiance at some LOS L_j will not contain information from all the layers, but rather only those layers coming after the point where $\prod_{j=i+1}^{K} \tau_j(\alpha_j) \approx 0$, and an accurate reconstruction of the scalar profiles will be challenging.

Tomographic reconstruction.

Imaging techniques such as IR imaging and IFTS are capable of providing 2D information of a flame and in some cases this is sufficient. However, a flame is a three-dimensional flow field. The full 3D characterization of a flame is desirable to fully understand physical and chemical characteristics of the flame. Achieving this infor-

38

mation then requires a 3D tomographic reconstruction of the flame, using the 2D information provided in the measurement.

Although there have been recent reviews of tomography measurements in flames [77, 78], we will again review several major techniques here with a focus on how each method may be useful to IFTS measurements, or how they may be limited.

Reverse Abel transform.
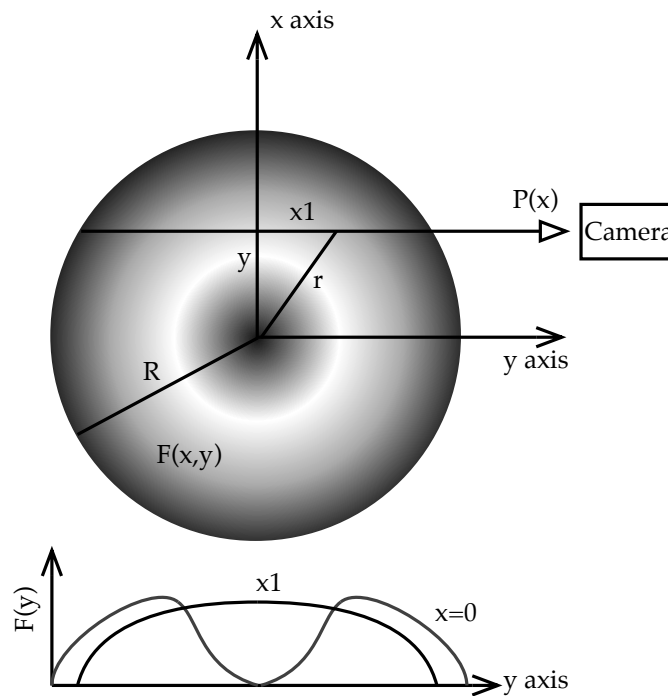
Figure 8. Depiction of a top down view of a 2D axi-symmetric function F(r). This is similar to a horizontal slice through a flame. The coordinate system and relevant information needed for an Abel reverse transformation is provided. Also provided are two example cross section profiles of F(r).

The Abel transformation is an integral transformation, named for Niels Henrik Abel, that is used in the analysis of axi-symmetric functions such as $F(r)$ pictured in Fig. 8. It is also the direct analytical solution to the axisymmetric inversion problem. This

technique is obviously limited to known axi-symmetric flames and, as it is a linear operation, to flames that are optically thin.The forward Abel transformation is used in spectroscopy to estimate integrated signal profiles $P(x)$ seen by a camera when the signal function $F(r)$ is known. This is given by:

$$P(x) = 2 \int_x^\infty \frac{F(r) r \, dr}{\sqrt{r^2 - x^2}}$$ (11)

where $r = \sqrt{x^2 + y^2}$. The reverse Able transformation is then used to recreate the signal function $F(r)$ based off the measured profile $P(x)$ and is given by:

$$F(r) = -\frac{1}{\pi} \int_r^\infty \frac{dP}{dx} \frac{dx}{\sqrt{x^2 - r^2}}$$ (12)

This technique requires measurements over the full width of the flame to be able to estimate the first derivative of intensity with x (measurements over half the flame will suffice, however the full width improves estimations in essence by sampling $F(r)$ twice). The spacing of horizontal measurements can be discrete and spaced apart, minimizing the number of projections needed. In fact, over sampling the system can lead to errors as the real difference between adjacent projections becomes comparable with the noise level [78]. IFTS has a clear advantage here as it will not only measure the full width of the flame, it will do so at all heights meaning Eq. 12 can be used along the z axis for a true 3D reconstruction. Also its 0.5 mm spatial sampling is a sufficient spatial resolution and can be artificially reduced to mittigate any oversampling issues.

There are two main problems with the Abel inversion transformation. First, is a singularity of Eq. 12 in the center of the flame where $r = x = 0$. This is an obvious setback, as it requires a linear interpolation of the center of the flame from the corresponding estimates. This is fairly insignificant for smoothly varying flames, but can be more of a

40

problem in highly structured flames. Second, is its dependence on the first derivative of $P(x)$. This causes the inversion to be very sensitive to any noise affecting $P(x)$, and often results in erroneous structure in the estimated profile. In fact, the standard Abel transform is rather infrequently used because of these two drawbacks [78], replaced instead by adaptations that work around these issues.

To counteract these shortcomings several modifications have been made to the reverse Abel transformation such as the discretization, Nestor-Olsen, and Fourier-Hankel method. For these algorithms to work, they are applied not to a continuous flame but rather a flame made up of a 2N+1 different datapoint discrete distributions $P(x)$ with axial symmetry. The Abel technique, and these modifications are reviewed, with example calculations in the literature [79, 80].

Discretization:
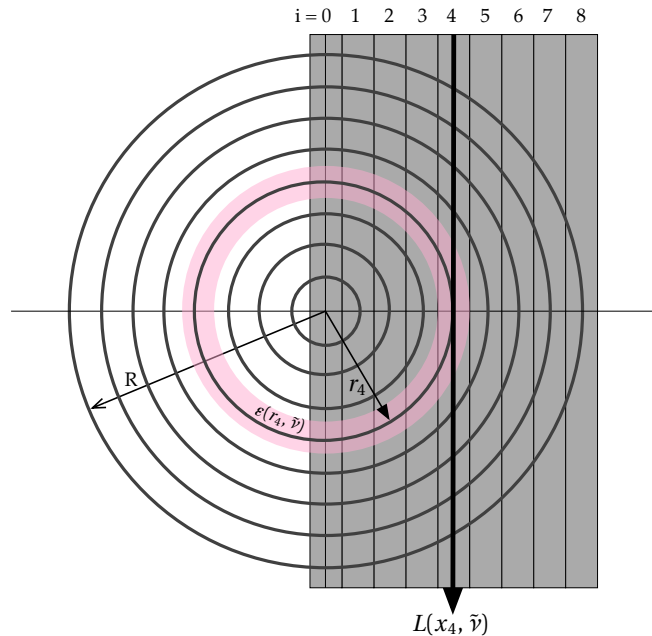
Figure 9. Depiction of a top down view of a 2D axi-symmetric function F(r). The coordinate system and relevant information needed for a discretization Abel reverse transformation is provided.

This method is based on direct discretization of Eq. 12 and by changing the denominator slightly to avoid the discontinuity:

$$F(r_j) = -\frac{1}{\pi}\sum_{i=j}^{N-1}\frac{P(x_{i+1}) - P(x_i)}{\sqrt{\left(x_i + \frac{\Delta x}{2}\right)^2 - r_j^2}} \tag{13}$$

where $x_i = r_i = i\Delta x$ and Δx is the width of each layer and $i = -N...0...N$ and $j = 0..N-1$. A depiction of this geometry is provided in Fig.9. This method is rough, but provides accurate results provided the input data $P(x_i)$ is smooth.

Nestor-Olsen:

The numerical algorithm developed by Nestor and Olsen [81] is used due to its ease of computation. The intensity profile here is given by:

$$F(r_j) = -\frac{2}{\pi\Delta x}\sum_{i=j}^{N-1}P(x_i)B_{j,i}\begin{cases} B_{j,i} = A_{j,i-1} - A_{j,i} & \text{for } i \geq j+1 \\ \\ B_{j,i} = -A_{j,i} & \text{for } i = j \end{cases} \tag{14}$$

where

$$A_{j,i} = \frac{[i^2 - (j-1)^2]^{1/2} - [(i-1)^2 - (j-1)^2]^{1/2}}{2i-1}$$

The major advantage for this algorithm is its ease of computation. It also has a reduced sensitivity to noise and was shown to better estimate a sample $F(r)$ than the discretization method [80].

Fourier-Hankel:

The derivation of the Fourier-Hankel transformation is not shown here but is available in the literature [80]. In short the Abel, Fourier, and Hankel transforms form an integral operator cycle. For example, applying the Abel transform to a 1D function and then applying the Fourier transform to the result is the same as applying the Hankel transform to the original 1D function. So rather than directly applying the reverse Abel

42

transform, here the combination of a Fourier transform and a Hankel transform are applied. In its final form, the intensity profile is given by:

$$F(r_j) = \frac{1}{2\pi\Delta x(2N+1)^2} \sum_{i=-N}^{N} P(x_i) \sum_{k=0}^{N} \cos\left[\left(\frac{i}{2N+1}\right)k\right] k \, J_0\left(\frac{jk}{2N+1}\right) \qquad (15)$$

where J_0 is the zero-order Bessel function. This method clearly adds some complexity to the equation, but also is claimed to be the method least sensitive to noise and therefore gives better accuracy [80].

Onion peeling.
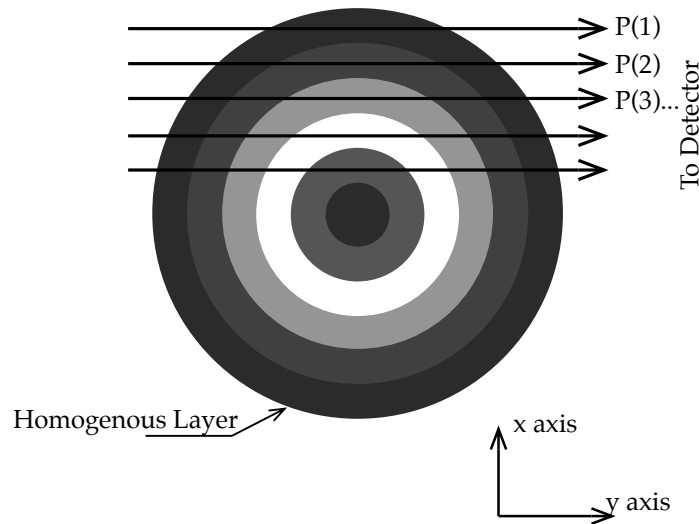
Figure 10. Depiction of a top down view of 2D axi-symmetric concentric rings. This is similar to a horizontal slice through a flame that has been divided into homogenous layers. The coordinate system and relevant information needed for an onion peeling transformation is provided.

As the name implies, and similar to the Abel transform, this method divides the

43

flame into concentric layers, like those of an onion, that are each assumed to be homogenous. Then, the flame is reconstructed one ring at a time, starting with the outside most ring. Then, using information gained from the previous ring, the next layer is solved. For example, in Fig. 10, the outer layer has a measured spectrum represented by P(1). Because it is assumed that this layer is homogenous, and there is only one layer contributing, it is straight-forward to measure the scalar values using a single layer model that is well established (discussed in Sec. 2.2) and used extensively in Sec. III The second layer, however, is now a combination of layer 2 in the middle and layer 1 in the back and front. Fortunately, all the information about layer 1 has already been solved for so there is again only one unknown layer left. This can be solved for using prior knowledge of flame geometry and a multi layer radiation model (also discussed in Sec. 2.2). This is continued layer by layer keeping fixed the information about the layers already solved for, until the full flame is vetted.

Dasch provides one mathematical example of 1-D onion-peeling for an axi-symmetric medium [78]. In this work, the flame is approximated by rings of constant property between $r_j - \Delta r/2$ and $r_j + \Delta r/2$ for each data point r_j projected data $P(x_i)$ is expressed as:

$$P(x_i) = \Delta r \sum_{j=i}^{\infty} \mathbf{W}_{i,j} F(r_j) \qquad (16)$$

where

$$\mathbf{W}_{i,j} = \begin{cases} 0 & j < i \\ [(2j+1)^2 - 4i^2]^{1/2} & j = i \\ [(2j+1)^2 - 4i^2]^{1/2} - [(2j-1)^2 - 4i^2]^{1/2} & j > i \end{cases} \qquad (17)$$

to express this deconvolution in matrix form it is simple to state that

$$\mathbf{D}_{i,j} = (\mathbf{W}^{-1})_{i,j} \qquad (18)$$

44

Onion-peeling is the most commonly used process to reconstruct flames, because of its simplicity [78]. Despite its popularity, a downside of this technique is immediately clear. Each successive estimation relies entirely on the last, making any systematic errors compound near flame center. A way to minimize this is by coupling this technique with some other measurement, such as that done by Blunck *et al.* [2]. As discussed above, this work coupled a TFP temperature measurement with onion peeling, giving an accurate temperature profile, which is a huge aid to the onion peeling estimation of the water concentration.

Imaging Fourier transform spectroscopy.
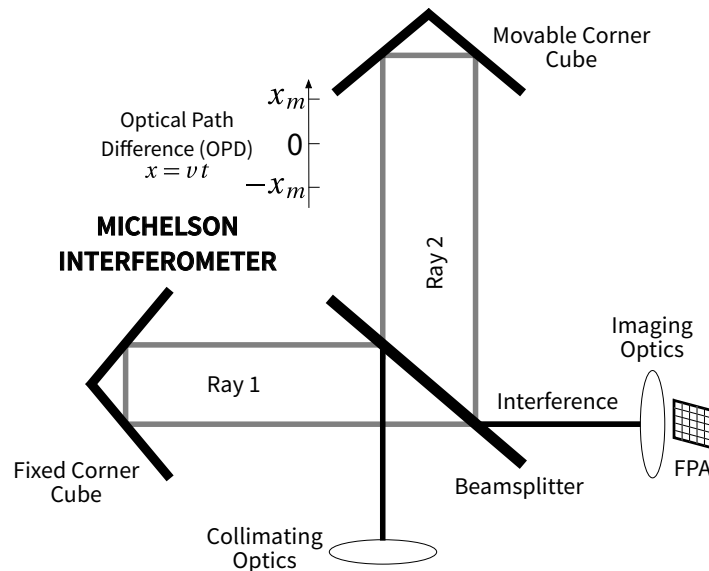
Figure 11. A schematic of a typical corner-cube style Michelson interferometer

45

The term Fourier transform spectroscopy is applied to any technique that requires a Fourier transform to turn raw data into the desired spectrum, however this work will focus on the predominant techniques that rely on continuous wave Michelson interferometers. A schematic example of a Michelson interferometer is provided in Fig. 51. As the incident radiation enters the camera, it strikes a beamsplitter, ideally sending equal parts toward each corner cube. The radiation is reflected back through the beamsplitter and recombines before it's imaged onto the detector. One of the corner cubes is moveable, and continuously scans over a range ($\pm x_m$ in Fig. 11), creating an optical path difference (OPD) between the two rays. This results in interference (either constructive or destructive) between the recombined rays due to the phase difference of the radiation. This interference pattern, referred to as an interferogram, is then imaged by the detector as a function of both time and the optical path difference of the two rays. Unlike standard Fourier transform spectrometers, imaging FTS has the unique advantage of a multi-element focal plane array (FPA). This results in an interferogram at each pixel of the detector that directly maps back to a unique line-of-sight in object space. A typical interferogram is pictured in grey in Fig. 12. Applying a Fourier transformation to the interferogram and the proper calibration (and also some time averaging if the scene is not steady) yields the information rich spectrum of the scene, shown in black in Fig 12.

46
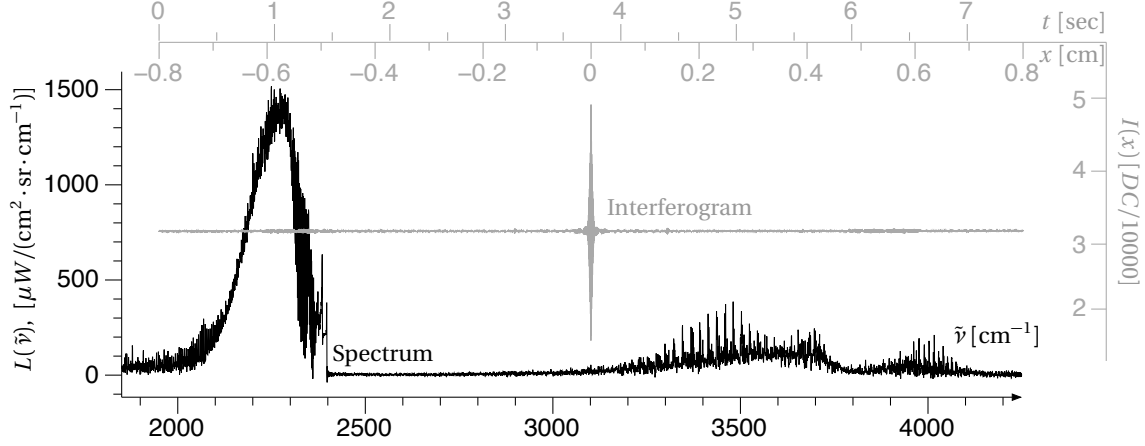
Figure 12. An overlay of a time averaged interferogram and its corresponding calibrated spectrum.

Mathematically, this process can be described as follows. The measured intensity $I_{i,j}(x)$ at each pixel (i,j) of the FPA is given by:

$$I_{i,j}(x) = \frac{1}{2}\int_0^\infty [1 + \cos(2\pi\tilde{\nu}x)]G_{i,j}(\tilde{\nu})L_{i,j}(\tilde{\nu})\mathrm{d}\tilde{\nu} = I_{i,j}^{DC} + I_{i,j}^{AC}(x) \tag{19}$$

Here, $G_{i,j}(\tilde{\nu})$ represents the spectral response of the instrument (this includes the quantum efficiency η of the FPA as well as transmission/reflection losses within the instrument and optics) to the radiance $L_{i,j}(\tilde{\nu})$ that makes it to the detector. This radiance is composed of both the atmospheric attenuated scene radiance and the self-emitted radiance of the sensor. This total scene intensity $I_{i,j}(\tilde{\nu})$ can be thought of as a composition of a constant offset $I_{i,j}^{DC}$ and a modulated component $I_{i,j}^{AC}(x)$. For a steady scene (such as a gas cell set at a constant temperature), the DC term never changes and is a waste of detector response. I^{DC} is usually removed through AC coupling the detector. When viewing a dynamic scene such as flames, however, the DC signal, driven by changes in temperature and species concentrations, is a strong function of time and position and therefore cannot be ignored. In fact, it can be an asset, as the camera records changes

47

in the DC component at each pixel very rapidly, which can be leveraged into high speed IR imagery of the flame. The modulated component $I_{i,j}^{AC}(x)$ is the change in intensity associated with the effects of interference of the Michelson, the cosine transform of the gain-weighted measured radiance.

A raw, uncalibrated spectrum is calculated through the Fourier transform of the modulation intensity at each pixel $I_{i,j}(x)$:

$$Y_{i,j}^{scn}(\tilde{\nu}) = \mathscr{F}\left\{I_{i,j}^{AC}(x) - I_{i,j}^{DC}\right\}(\tilde{\nu}) \tag{20}$$

Then with proper calibration, discussed in detail in Chapter III , the apparent radiance of the scene is worked out:

$$L_{i,j}^{scn}(\tilde{\nu}) = \frac{Y_{i,j}^{scn}(\tilde{\nu})}{G_{i,j}(\tilde{\nu})} - L_{i,j}^{ins}(\tilde{\nu}) \tag{21}$$

Note that this radiance is actually a convolution of the actual scene radiance (described in Sections 2.2 and 2.2) and the instrument line shape, ILS:

$$L_{i,j}^{scn}(\tilde{\nu}) = \int L_{i,j}(\tilde{\nu})\text{ILS}(\tilde{\nu} - \tilde{\nu}')d\,\tilde{\nu}' \tag{22}$$

where $\text{ILS}(\tilde{\nu}) = 2x_m\text{sinc}(2\pi x_m \tilde{\nu})$ and x_m is the maximum optical path difference of the Michelson. This ILS convolution serves to limit the spectral resolution of the camera and is adjustable with x_m. Additional details on the camera calibration are provided in Chapter III.

48

III. Mid-IR hyperspectral imaging of Laminar flames for 2-D scalar values

The following is a published submission in Optics Express presented in its entirety [82]. The focus is on calibration and validation of IFTS as a tool for basic combustion diagnostics of a partially-premixed laminar ethylene flame. Authors of this article include Michael Rhoby, Dr. David Blunck, and Dr. Kevin Gross. The work is significant for the following reasons:

- It presents a novel mid-IR, IFTS calibration technique for use with high temperature flame sources.

- It presents a detailed approach for uncertainty estimation in calibration

- It presents a new emission-based measurement which permits quantification of two-dimensional scalar distributions in laminar flames.

As first author I was responsible for data capture, reduction, and analysis, and the initial draft of the document. Dr. Kevin Gross contributed in data analysis and was the primary editor of the document. Dr. David Blunck acted as a secondary editor and analysis for the viewpoint of the combustion community. This chapter represents the satisfaction of objective 1.

3.1 Abstract

This work presents a new emission-based measurement which permits quantification of two-dimensional scalar distributions in laminar flames. A Michelson-based Fourier-transform spectrometer coupled to a mid-infrared camera (1.5 μm to 5.5 μm) obtained 256×128 pixel hyperspectral flame images at high spectral ($\delta\tilde{\nu} = 0.75\,\mathrm{cm}^{-1}$)

and spatial (0.52 mm) resolutions. The measurements revealed line and band emission from H_2O, CO_2, and CO. Measurements were collected from a well-characterized partially-premixed ethylene (C_2H_4) flame produced on a Hencken burner at equivalence ratios, Φ, of 0.8, 0.9, 1.1, and 1.3. After describing the instrument and novel calibration methodology, analysis of the flames is presented. A single-layer, line-by-line radiative transfer model is used to retrieve path-averaged temperature, H_2O, CO_2 and CO column densities from emission spectra between 2.3 µm to 5.1 µm. The radiative transfer model uses line intensities from the latest HITEMP and CDSD-4000 spectroscopic databases. For the $\Phi = 1.1$ flame, the spectrally estimated temperature for a single pixel 10 mm above burner center was $T = (2318 \pm 19)\,$K, and agrees favorably with recently reported laser absorption measurements, $T = (2348 \pm 115)\,$K, and a NASA CEA equilibrium calculation, $T = 2389\,$K. Near the base of the flame, absolute concentrations can be estimated, and H_2O, CO_2, and CO concentrations of $(12.5 \pm 1.7)\,$%, $(10.1 \pm 1.0)\,$%, and $(3.8 \pm 0.3)\,$%, respectively, compared favorably with the corresponding CEA values of 12.8%, 9.9% and 4.1%. Spectrally-estimated temperatures and concentrations at the other equivalence ratios were in similar agreement with measurements and equilibrium calculations. 2-D temperature and species column density maps underscore the Φ-dependent chemical composition of the flames. The reported uncertainties are 95% confidence intervals and include both statistical fit errors and the propagation of systematic calibration errors using a Monte Carlo approach. Systematic errors could warrant a factor of two increase in reported uncertainties. This work helps to establish IFTS as a valuable combustion diagnostic tool.

3.2 Introduction

Scalar measurements in flames are needed for understanding combustion phenomenon, validating chemical kinetic models, and verifying numerical simulations.

www.manaraa.com

Intrusive measurements, such as temperature sensing via thermocouples or gas sampling, are straightforward to implement at discrete locations. Measurements at multiple locations or simultaneous determination of temperature and species (at a location) are more challenging and further disturb the flow field. Laser-based methods provide highly effective, non-intrusive means to interrogate both laminar and turbulent flow fields, and are the cornerstone of combustion diagnostics [4]. These techniques often require sophisticated experimental arrangements with multiple optical access points. Simultaneous measurement of multiple scalar quantities (i.e., temperature and mole fractions of various flame species) typically requires multiple laser sources, and mapping these with high spatial resolution can be arduous.

Flame emission measurements are another class of nonintrusive diagnostics that complement laser-based techniques. Multiple line-of-sight Fourier-transform spectrometer (FTS) measurements, when paired with appropriate tomographic deconvolution algorithms, can be used to simultaneously determine temperature and mole fractions of major flame species [45, 52]. High-speed infrared cameras with various band-pass filters have been used to map spatial and temporal variations in radiant intensity and relate these to the spatial distribution of scalar values [2] and to various measures of turbulence (e.g. integral length and time scales) [31, 83].

A new flame emission technique using an imaging Fourier-transform spectrometer (IFTS) can provide spatially resolved, detailed (e.g. $\delta \tilde{\nu} = 0.25\,\mathrm{cm^{-1}}$) wide-band (e.g. the mid-IR, 1.5 μm to 5.5 μm) spectra in a single measurement. Such highly resolved spectral measurements across the mid-IR can be used to monitor rotation-vibration emissions from fuels, intermediates, and major combustion products. High-resolution spectra are valuable for tomography algorithms (e.g. [19]) since variations in different scalar values (i.e., temperature and species concentrations) produce distinct and nearly unambiguous changes in the observed spectral emissions. Previously, IFTS

51

has been used to identify pollutants and quantify species concentrations in the non-reacting turbulent exhaust plume from a coal-fired power plant smokestack [66]. More recently, IFTS has been employed in the measurement and qualitative assessment of a turbulent jet flame [67] and to study plumes arising from laser-material interactions [84]. Tomography techniques have not yet been adapted to IFTS flame measurements. This is significant because the high-resolution spectra, collected simultaneously at multiple lines-of-sight, have the potential to allow significantly improved accuracy in determining scalar values compared to other infrared emission based techniques.

Considering the value of nonintrusive emission-based measurement techniques, and the potential for using an IFTS to determine multiple scalar values in three-dimensions, this paper lays the groundwork for such efforts through the study and analysis of a laminar flame. More specifically, the objectives of this work are as follows: (1) collect spectral information from a laminar flame produced by a canonical burner; (2) develop a novel calibration technique needed for mid-IR flame measurements; (3) pair the latest high-temperature spectroscopic databases with a line-by-line radiative transfer model to estimate two-dimensional scalar values from the spatially-resolved spectra; (4) apply Monte Carlo techniques to understand systematic calibration errors on spectrally-retrieved scalars; (5) compare scalar estimates to those reported in the literature to assess capabilities and limitations of this new technique. This work is a key step in the development of IFTS for three-dimensional scalar estimation and should serve as a benchmark for future applications of IFTS to the study of reacting flows.

3.3 Experimental

In this work, a well-characterized, partially-premixed ethylene (C_2H_4) flame was studied to allow comparisons with scalar values reported in the literature. The flame was produced by a Hencken burner, which has a 25.4 mm × 25.4 mm square burner with

an array of fuel tubes arranged within a honeycomb mesh through which the oxidizer flows. Immediately surrounding this is a similar honeycomb arrangement 6.4 mm wide consisting of tubes which carry an inert co-flow gas (N_2) to improve flame stability. The fuel and oxidizer mix shortly above the burner, resulting in a partially premixed flame. Additional details regarding the burner can be found in the literature [1, 85]. The Hencken burner was placed in a three-sided enclosure to minimize room disturbances. A schematic of the experimental set-up and detailed view of the Hencken burner is provided in Fig. 13. The flame was produced by flowing 12.21 SLM of air and 0.69 SLM to 1.11 SLM of ethylene (C_2H_4) through the burner. This produced equivalence ratios between 0.8 and 1.3. Temperature and OH mole fractions from a similarly configured Hencken burner were previously measured via laser absorption measurements [1]. 12.0 SLM of N_2 co-flow was used to minimize entrainment of lab air and matched the conditions reported in the literature. Flow rates were controlled using MKS 1480A ALTA mass flow controllers which have an accuracy of ±1% of the set point flow rate. Laboratory conditions were steady with a temperature of 297 K, pressure of 976 hPa, and an 18.5% relative humidity.

A Telops Hyper-Cam MW-E imaging Fourier-transform spectrometer (IFTS) was used to capture mid-infrared (MWIR, 1.5 μm to 5.5 μm) hyperspectral radiation emitted by the Hencken burner flame. The IFTS features a traditional Michelson interferometer
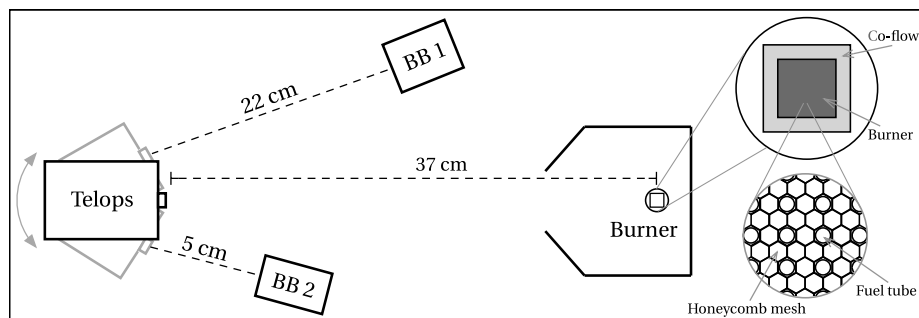
Figure 13. Schematic of the experimental arrangement. Important relative distances are provided as the image is not to scale. The Telops camera was placed on a rotation platform for fast and accurate transitions between the flame and calibration sources. An expanded view of the burner surface is provided to show the fuel tube and honeycomb mesh arraignment.

53

coupled to a high-speed 320×256 Indium Antimonide staring focal-plane array (FPA) via $f/2.5$ imaging optics. The pixel pitch is $30\,\mu m$ and the optics produce a mean RMS spot size of $14\,\mu m$ across the array. Instrument details can be found in the literature [67, 86, 87]. An external $0.25\times$ telescope expanded the field-of-view and provided an effective focal length of $21.5\,mm$. The IFTS was located a distance $d = 373\,mm$ from the center of the flame with its optical center located approximately $u_0 = 60\,mm$ above the burner. The spatial resolution of each pixel was $0.52\,mm \times 0.52\,mm$ at the flame (the image plane). Under the paraxial, thin-lens approximation, the depth of focus is $43\,mm$. This exceeds the detectable flame width, and due to its symmetry, indicates that each pixel's signal corresponds to photons emitted along the full line-of-sight through the flame. For this experiment, the FPA captured the two-dimensional data with a $40\,\mu s$ integration time on a 256×128 pixel sub-window. The spectral resolution was set to $\delta \tilde{v} = 0.75\,cm^{-1}$ where $\delta \tilde{v}$ is the full-width at half-maximum of the instrument line shape (ILS). Symmetric interferograms were obtained by continuously scanning the Michelson interferometer at a uniform speed ($0.21\,cm\,s^{-1}$) to a maximum optical path difference of $x_m = 0.8\,cm$, with images captured every $632.8\,nm$. This corresponds to a *camera frame rate* of $3.4\,kHz$. Each interferometric "cube" consisting of 25,278 images was acquired in $7.5\,s$, and corresponds to an *interferometric cube rate* of $0.13\,Hz$. Each cube requires more than $1.5\,GB$ of storage. To balance the needs of capturing a statistically sufficient sampling of the flame and efficiently storing and processing a large data set, 50 interferometric cubes of each flame were acquired and averaged.

Data for radiometric calibration was collected using 2 in and 6 in square CI Systems blackbody sources placed at distances of $5\,cm$ and $22\,cm$, respectively, from the camera. This ensured each over-filled the instrument's field-of-view (FOV). A standard [88] two-point calibration—modified for noise suppression (see Sec. 3.4)—was performed to remove both system response and instrument self-emission from the raw signal by

measuring the 2 in and 6 in blackbodies at 200 °C and 580 °C, respectively. Correction of the spectral axis due to dispersion in the imaging system was performed as previously described [86]. Temperatures for the 2 in and 6 in are accurate to within ±0.3% and ±1.0%, respectively, of the set-point temperatures. Spectral emissivities for the 2 in and 6 in blackbodies are reported to be 0.980 ± 0.004 and 0.96 ± 0.02, respectively. The manufacturer-reported blackbody uncertainties were taken to represent 95% confidence intervals (CIs), and were used to perform a Monte Carlo error analysis of both the calibrated radiances and spectrally-retrieved scalar values. This analysis is presented in a later section. Calibrated radiance spectra $L_i(\tilde{\nu})$ are reported at each pixel (i) with units $\mu W/(cm^2\, sr\, cm^{-1})$. The spectral variable $\tilde{\nu} = \lambda^{-1}$ is expressed in wavenumbers (reciprocal wavelength, cm^{-1}).

3.4   Radiation Model

Interferogram Formation.

Here, great care is taken in describing the modeling, approach, and calibration of data since this work develops a new technique that will serve as a benchmark for future studies. A Michelson imaging interferometer splits the incident radiation into two beams and then recombines them so that an interference pattern is produced at the focal plane array (FPA). The measured signal at each pixel (i) of the FPA, $I_i(x)$, varies with the optical path difference, $x = \nu t$, as the interferometer scans in time, t, at a constant speed, ν. For a *static* scene with a radiance spectrum $L_i(\tilde{\nu})$, the measured signal after passing through an ideal interferometer is given by

$$I_i(x) = \int_0^\infty (1 + \cos(2\pi\tilde{\nu}x))\, G_i(\tilde{\nu}) \big(L_i(\tilde{\nu}) + L_i^I(\tilde{\nu}) \big) \, d\tilde{\nu} \tag{23}$$

$$= I_i^{\mathrm{DC}} + I_i^{\mathrm{AC}}(x). \tag{24}$$

55

$G_i(\tilde{\nu})$ accounts for the spectrally-dependent response of the instrument, and includes factors such as the quantum efficiency of the detector, as well as transmission and reflection losses within the optics. Note that $G_i(\tilde{\nu})$ rapidly approaches 0 as $\tilde{\nu}$ approaches the band-gap of the photodetector material (InSb, $\tilde{\nu}_{\text{b.g.}} \simeq 1855\,\text{cm}^{-1}$). The at-detector radiance is a combination of both the source radiation and the thermally-generated photons within the instrument, $L_i^I(\tilde{\nu})$, and thus requires at least two unique calibration measurements to determine the scene radiance spectra, $L_i(\tilde{\nu})$. The total scene intensity is comprised of a constant offset I_i^{DC} — the unmodulated, spectrally-integrated signal — and a modulated component, $I_i^{\text{AC}}(x)$, which encodes the spectral information via the cosine transform. The raw spectrum is obtained by Fourier-transformation of the AC term, and application of standard calibration techniques [88] produces $L_i(\tilde{\nu})$. An important modification to the standard calibration approach is required for high-temperature flames and is described in the next section.

In the present work, the flame becomes unsteady about 20 mm above the burner due to buoyancy effects. This caused substantial, systematic variation in scene radiance so that $L_i = L_i(\tilde{\nu}, t)$ with a fluctuation timescale much shorter than the interferometric measurement time scale. The DC term is no longer a constant, but captures the broadband radiance fluctuations caused by buoyancy effects in the flame. Furthermore, the AC term is no longer the cosine transform of a static spectrum, and its Fourier-transformation is difficult to interpret quantitatively. If the dynamic source is ergodic and a statistically sufficient number of data cubes are acquired, then the mean interferogram corresponds to the mean source radiance. The Fourier-transform is a linear transform mapping the interferogram to the spectrum and thereby preserves this association. However, the radiance spectrum is a nonlinear function of the flame scalar values, so interpretation of the flame radiance must be performed carefully.

There is significant information content about the unsteady fluctuations encoded

in a single interferogram. To appreciate this, note that the Michelson encodes spectral information by modulating the intensity at frequencies above $f_{\text{b.g.}} = v\,\tilde{v}_{\text{b.g.}}$. In these measurements, the mirror velocity was $v = 0.21\,\text{cm}\,\text{s}^{-1}$ yielding $f_{\text{b.g.}} \simeq 390\,\text{Hz}$. Thus, at frequencies below $f_{\text{b.g.}}$, the intensity fluctuations can be attributed to radiance fluctuations. Application of an appropriate low-pass filter removes the intensity modulations caused by the action of the Michelson, thereby yielding a high-speed infrared intensity images (i.e., a movie) of the unsteady flow. This will facilitate interpretation of the spectra presented in this work, and more generally enables flow field analysis similar to what is currently performed by infrared cameras [2, 31].

Instrument Calibration.

Radiometric calibration of FTS is well established for low temperature participating media [66, 86, 88]. However, high flame temperatures required the development of a new calibration approach. We first review the standard FTS calibration methodology, which starts by assuming the instrument responds linearly to incident radiation. Observation of a blackbody source at two distinct temperatures affords the pixel-wise (i) determination of the system response ($G_i(\tilde{v})$, gain) and self-emission ($L_i^I(\tilde{v})$, offset) which define the linear transform mapping scene radiance $L_i^S(\tilde{v})$ to instrument response $Y_i(\tilde{v})$:

$$Y_i(\tilde{v}) = G_i(\tilde{v})\big(L_i(\tilde{v}) + L_i^I(\tilde{v})\big). \tag{25}$$

This calibration approach has practical limitations for this work. The flame of interest has a nominal temperature of ~2400 K and exhibits strong, selective emission between $2100\,\text{cm}^{-1}$ to $2400\,\text{cm}^{-1}$ and between $3100\,\text{cm}^{-1}$ to $4200\,\text{cm}^{-1}$. Elsewhere, the flame emission is negligible, and the integrated radiance across the IFTS's bandpass produces a signal comparable to that produced by a 550 °C blackbody. Thus, to ensure the flame integrated radiance is bracketed by the calibration integrated radiances, the

57

higher-temperature blackbody should exceed this temperature. However, the integrated radiance corresponding to this blackbody temperature is constrained by the upper limit of the camera's dynamic range. In the present work, a wide-area blackbody set to 580 °C was used, and filled ~90% of the FPA dynamic range at the zero path difference (ZPD, $x = 0$). For comparison, the brightest part of the flame used ~85% of the dynamic range at ZPD. Between $3250 \, \mathrm{cm}^{-1}$ and $4250 \, \mathrm{cm}^{-1}$, the signal-to-noise ratio (SNR) of a typical flame measurement can exceeded the SNR of the high-temperature blackbody by a factor of three. The blackbody curve at this temperature monotonically decreases with $\tilde{\nu}$ across the IFTS bandpass. Moreover, the number of photons per unit energy emitted by the blackbody decreases as $1/\tilde{\nu}$ across the detector bandpass. These effects reasonably limit the achievable SNR of the gain term at higher wavenumbers. Since the calibrated scene radiance is obtained via division by $G_i(\tilde{\nu})$, a low-SNR gain can introduce errors in $L_i(\tilde{\nu})$ that are non-normally distributed, complicating the quantitative interpretation of flame spectra.

The InSb quantum efficiency, optics transmittances, and other factors affecting system response are such that $G_i(\tilde{\nu})$ exhibits a smooth, slow variation with $\tilde{\nu}$. A possible exception to this is the effect that the atmospheric transmittance profile would have on $G_i(\tilde{\nu})$, if it is not accounted for when modeling the at-sensor radiance from a distant blackbody source. Our calibration methodology accounts for atmospheric absorption, and leverages the expectation of smoothness of the resulting gain term. A least-squares smoothing spline is then applied to each pixel's gain term. It was determined via graphical inspection that fifteen spline points adequately captured the variation in $G_i(\tilde{\nu})$ without fitting to the noise.

Single-pixel gain curves obtained via the standard calibration method and our modified approach are compared in Fig. 14. The gain determined from the standard calibration without atmospheric compensation is shown in grey. Overlaid with this

58
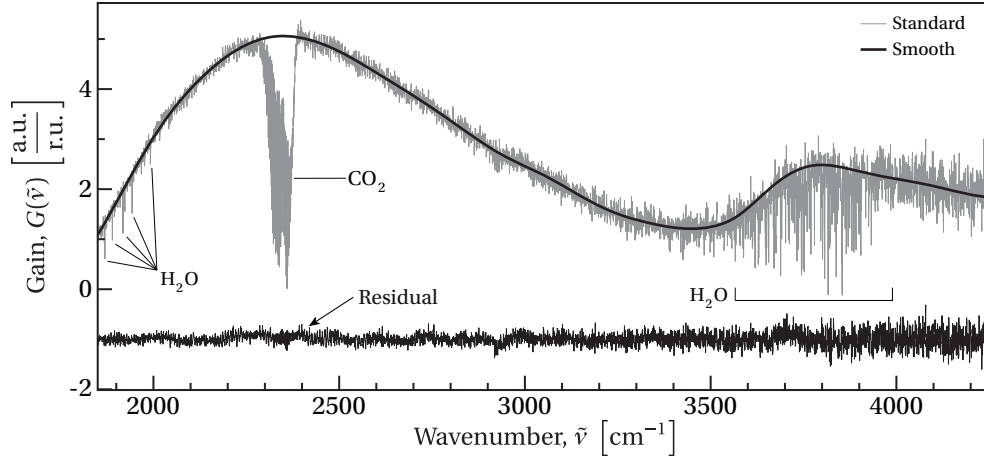
Figure 14. Representative single-pixel gain curve computed from standard calibration method (grey) compared with the gain curve obtained after atmospheric correction and spline smoothing (black). Residual difference between standard gain curve and the product of the smooth gain curve with atmospheric transmittance function is provided, offset by −1 a.u./r.u.. Atmospheric absorption features are annotated. Here, a.u. represents arbitrary units and r.u. represents radiometric units.

curve is the modified gain obtained using atmospheric compensation and a spline fit. The residual difference between the standard gain and the smooth gain, multiplied by the atmospheric transmittance profile, is also shown. The largely unstructured residuals are dominated by noise, indicating the effectiveness of the atmospheric compensation and spline smoothing.

Spectral Radiation Model for Determining Scalar Values.

A simple model describing the apparent line-of-sight flame radiance was used to estimate temperature and relative species concentrations from the measured spectra. The spectral radiance $L_i(\tilde{\nu})$ from a non-scattering source in local thermodynamic equilibrium (LTE) can be approximated by

$$L_i(\tilde{\nu}) = \tau(\tilde{\nu}) \, \varepsilon(\tilde{\nu}, T, \vec{\xi}) \, B(\tilde{\nu}, T) * \text{ILS}(\tilde{\nu}) \tag{26}$$

where $\varepsilon(\tilde{\nu}, T, \vec{\xi})$ is the gas emissivity, which is a function of gas mole fractions $\vec{\xi}$, and $B(\tilde{\nu}, T)$ is Planck's blackbody radiance distribution at temperature T. Here, $\tau(\tilde{\nu})$ repre-

59

sents the transmittance of the atmosphere between the flame and instrument. Measured meteorological conditions were used to estimate $\tau(\tilde{\nu})$. $\text{ILS}(\tilde{\nu})$ represents the instrument line shape of a Fourier-transform spectrometer with which the "monochromatic" flame spectrum is convolved. No apodization of the interferograms was performed, thus $\text{ILS}(\tilde{\nu}) = 2\pi x_m \text{sinc}(2\pi x_m \tilde{\nu})$ [86, 89]. In a non-scattering medium, the spectral emissivity is related to the scalar values via

$$\varepsilon(\tilde{\nu}, T, \vec{\xi}) = 1 - \exp\left(-lN\sum_i \xi_i \sigma_i(\tilde{\nu}, T)\right) = 1 - \exp\left(-\frac{l}{l_{\text{MFP}}}\right) \tag{27}$$

where the number density $N = P/(k_B T)$, l is the path length through the flame, ξ_i is the ith species mole fraction, and $\sigma_i(\tilde{\nu}, T)$ is its corresponding absorption cross-section. The product $\vec{q} = \vec{\xi}l$ is denoted the fractional column density. The reciprocal of the number density and sum over mole-fraction weighted cross-sections defines the photon mean-free-path, l_{MFP}, in the model flame.

The phenomenological absorption cross-section σ_i for the ith species represents a sum over discrete spectral emission lines, each with its own line intensity, S_{ij}, and line shape, $\phi_{ij}(\tilde{\nu})$, via:

$$\sigma_i(\tilde{\nu}, T) = \sum_j S_{ij}(T)\phi_{ij}(\tilde{\nu} - \tilde{\nu}_j, T). \tag{28}$$

The line shape term is dependent on the partial pressures of the various species. In this work, the Voigt profile is used and a constant pressure of $P = 976\,\text{hPa}$ is assumed throughout the flame. In computing the Voigt profile, species are assumed dilute so that only broadening rates for dry air are used. Line mixing and continuum effects on the line shape were not included. Parameters to compute absorption cross-sections for H_2O and CO were computed using the HITEMP spectroscopic database [63], and cross-sections for CO_2 were computed using the CDSD-4000 spectroscopic database [90]. The phenomenological cross section includes the weighting of internal state

populations via Boltzmann statistics (assuming LTE), and the temperature dependence is computed (see the appendix in Ref. [91]) using the appropriate partition function data accompanying the HITEMP and CDSD-4000 databases. Cross-sections for each species were pre-computed at temperatures between 300 K to 3000 K every 50 K, and quadratic interpolation was used to compute cross-sections at arbitrary temperatures.

Spectral estimates of the flame temperature and fractional column densities were determined at each pixel by fitting Eq. 26 to the corresponding measured spectrum. This was accomplished by minimizing the sum of squared differences between the data and model parameters, T and $\vec{q} = (q_{H_2O}, q_{CO_2}, q_{CO})$, using a Nelder-Mead direct search followed by a Levenberg-Marquardt gradient-based error minimization. Atmospheric H_2O and CO_2 concentrations were also model parameters to ensure the best possible estimate of τ. In the $\Phi = 0.8$ and $\Phi = 0.9$ flames, a small baseline oscillation was observed in spectral regions absent of line emission from the combustion gases. As discussed later, this only occurred in certain flame locations and is likely the result of insufficient temporal averaging over the flame unsteadiness. To mitigate the impact of the baseline oscillation on the spectral fit results, a 4th-order polynomial was added to the model for the $\Phi = 0.8$ and $\Phi = 0.9$ measurements. The spectrum at each pixel contains 3000 unique radiance values, ensuring the six-parameter or eleven-parameter nonlinear model is highly over-determined.

This model makes a few notable simplifications to the actual radiative transfer problem, the most significant being the assumption of flame homogeneity along each pixel's line-of-sight. This is a reasonable approximation near the base of the Hencken burner where—as supported by flame images presented in the next section—the mixing layer is a small fraction of the total line-of-sight. This assumption is also made in the analysis of OH laser absorption measurements of the similarly configured Hencken flame against which the present results will be compared [1]. The width of the mixing layer

61

steadily increases with height above the flame, and the homogeneity approximation above ~20 mm breaks down. As the mixing layer grows, temperature and density gradients become non-negligible and will systematically bias the fit parameters due to the variation in T and ξ_i along the line-of-sight. Given these limitations, this model can only be used to estimate core flame temperature and concentrations near the base of the burner and along lines-of-sight that are not dominated by the mixing layer, i.e., $u < 20$ mm and $|v| < 10$ mm. Here u and v represent the flame coordinate system, and are defined in Fig. 31. A multi-layer deconvolution approach can be developed for flames or regions where mixing is significant, as discussed previously. Within this region, absolute concentrations are determined via $\xi_i = q_i/l$ where $l = 25.4$ mm$/\cos(\theta(u))$ and $\theta(u) = \tan^{-1}\left((u_0 - u)/d\right)$ is a small angle which accounts for the line-of-sight through the flame for rays a distance $y_0 - y$ from the optical center of the camera. Elsewhere in the flame, the biased estimates, due to mixing, of T and $\vec{q}$ are to be interpreted as path-averaged quantities. Note that they are not true path-averaged quantities due to the nonlinear dependence T and ξ_i have on measured radiance. A multilayer deconvolution method is being developed to estimate 3-D distributions of temperature and species mole fractions.

Other model simplifications include neglecting the transport of background radiation through the plume and atmospheric path radiance generated between the flame and sensor. However, these quantities are negligible compared to the flame radiance. The impact of neglecting collisional self-broadening in the Voigt profile has not been assessed, however its impact is expected to be small since typical line widths are narrower than the width of the instrument line shape, ILS($\tilde{\nu}$).
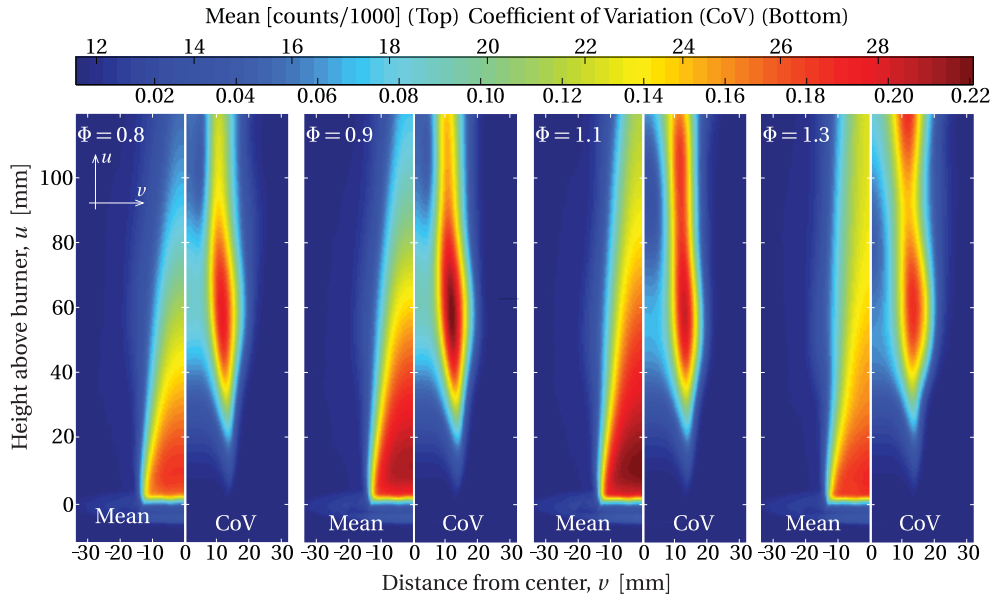
Figure 15. Split imagery of the symmetric flame for each of the four Φ values tested. Mean camera intensity values are on the left and coefficient of variation values are on the right. The top and bottom of the color bar correspond to the mean intensity in 1,000's of counts and CoV values, respectively.

3.5 Results

Data overview.

Fig. 15 compares the broadband imagery captured by the IFTS in a single interferometric measurement at each equivalence ratio. The imagery was obtained by applying a low-pass filter along the OPD dimension with a cut-off frequency below $f_{\text{b.g.}}$. The left half of each image corresponds to the time-averaged intensity in raw camera counts. Near the base of each burner, the intensity rapidly increases with height, peaking at about 10 mm, and then decaying more gradually with increasing distance from the burner. The most fuel lean trial with $\Phi = 0.8$ exhibits the swiftest decay in intensity with height and the fuel rich trial with $\Phi = 1.1$ shows the slowest intensity decay with height. Traversing each flame axially, the transition from flame emissions to background occurs near $v = \pm 13$ mm near the base of the burner. This mixing layer remains small up to about $u = 10$ mm. Due to the symmetry of the burner, it follows that the mixing layer represents a small contribution to the measured line-of-sight radiance near the

63

www.manaraa.com

burner. The mixing layer increases in size with additional height above the burner due to entrainment of the N_2 co-flow.

The right half of each image shows the intensity coefficient of variation (COV), which is the standard deviation of intensity normalized by the mean intensity. Near the base of the burner, each flame is steady, yielding intensity values on the order of 25,000 to 30,000 counts with minimal variations (CoV < 2%). Around 20 mm above the burner, buoyancy effects produce unsteady flow, causing intensity variations which increase with height and are more than 15% of the mean intensity by 40 mm. Unsteady intensity fluctuations were largest for the $\Phi = 0.9$ trial with CoV values exceeding 22% in the mixing layer near 60 mm above the burner. Interestingly, CoV values between 40 mm $\leq u \leq$ 90 mm and $v = 0$ were substantially larger for the fuel lean-flames compared with the fuel-rich flames.

Center-flame spectra at 10 mm, 60 mm and 100 mm above the burner are presented in Fig. 16. The largest emission feature near 2250 cm^{-1} is from the asymmetric stretching mode of CO_2, as well as combination bands at nearly resonant frequencies. Careful inspection of the region between 2000 cm^{-1} to 2150 cm^{-1} reveals the P-branch of CO (see inset plot). The R-branch overlaps with the strong CO_2 emission and becomes difficult to discern. The line emission between 3000 cm^{-1} to 4200 cm^{-1} is primarily due to H_2O rotational fine structure associated with transitions between several vibrational states. Also within this region is weaker broadband emission from CO_2, and very weak spectral emission from OH. The spectral radiance decreases with height due to cooling brought on by mixing with the N_2 co-flow and surrounding air. The entrainment of air enables oxidation of CO to occur with increasing distance from the burner, and by 100 mm CO emission lines are substantially diminished.
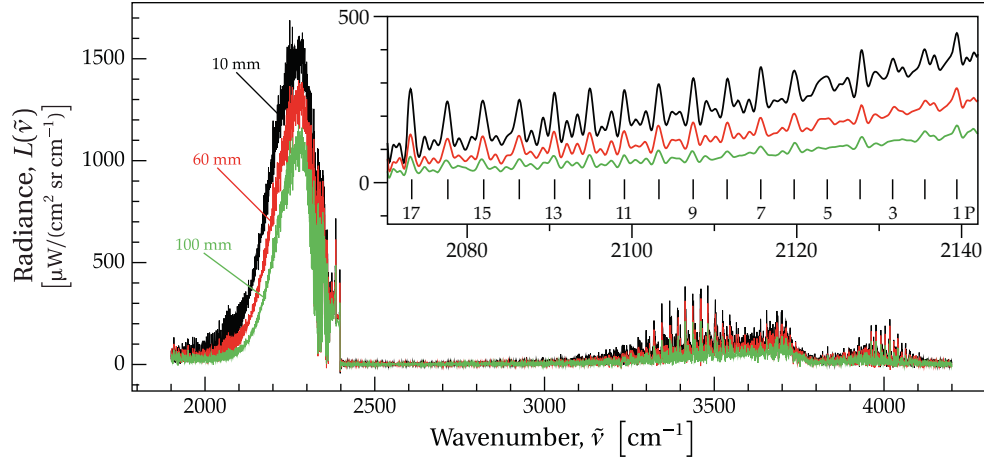
Figure 16. Three center-flame spectra corresponding to heights 10 mm**,** 60 mm **and** 100 mm **above the base of the** $\Phi = 1.1$ **flame. The inset plots presents a detailed view of the P-branch corresponding to the fundamental** $1 \rightarrow 0$ **emission from CO. Odd numbered rotational levels are marked.**

2-D spectral estimates of scalar values.

Single pixel results.

Fitting Eq. 26 enables simultaneous retrieval of T and mole fractions ξ_{H_2O}, ξ_{CO_2} and ξ_{CO}. In the top panel of Fig. 17, the emission spectrum between 1975 cm^{-1} to 4225 cm^{-1} is shown for a single pixel at location $(u, v) = (10\,\text{mm}, 0\,\text{mm})$ for the $\Phi = 1.1$ trial. Also provided is the model prediction corresponding to the best-fit parameters of $T = (2318 \pm 19)\,\text{K}$, $\xi_{H_2O} = (12.5 \pm 1.7)\,\%$, $\xi_{CO_2} = (10.1 \pm 1.0)\,\%$ and $\xi_{CO} = (3.8 \pm 0.3)\,\%$. The measured temperature compares favorably with recent laser diagnostics results [1], $(2348 \pm 115)\,\text{K}$, as well as with NASA CEA [92] equilibrium flame temperature of 2389 K. H$_2$O, CO$_2$ and CO mole fractions are in good agreement with the CEA equilibrium values of 12.8%, 9.9% and 4.1% respectively. We are not aware of other experimental determinations of these same species mole fractions for a similarly configured Hencken burner to compare against.

Reported fit parameter errors are the 95% CIs due to measurement noise and the propagation of calibration uncertainties. They do not account for systematic errors in the model. Details on the computation of parameter uncertainties is postponed

65
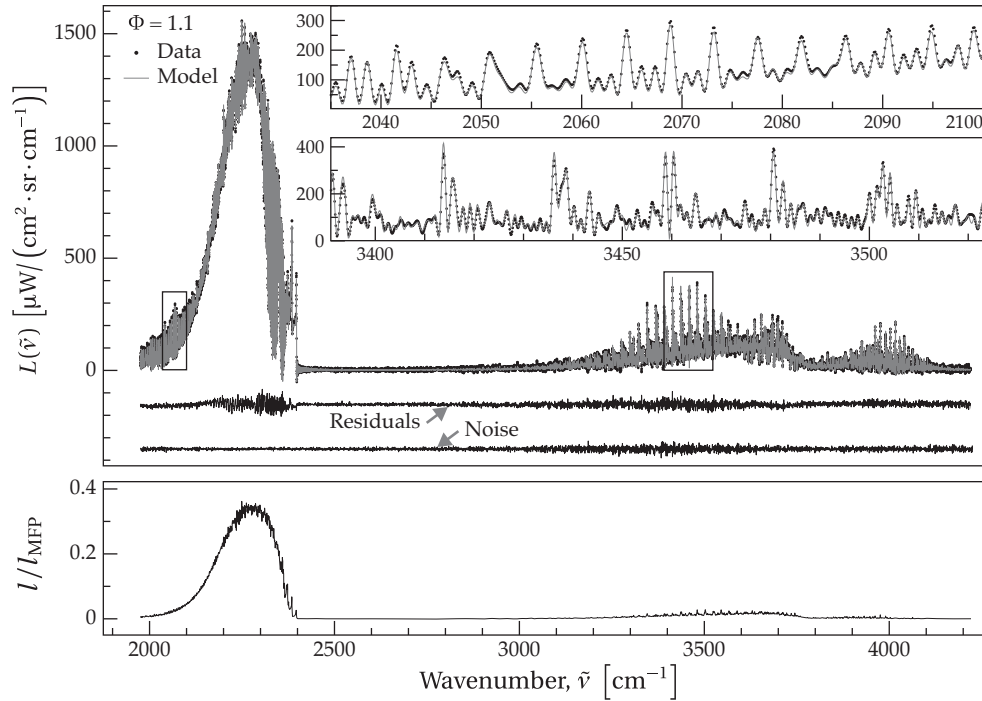
Figure 17. *Top*: **Ethylene $\Phi = 1.1$ center-flame spectrum** 10 mm **above burner (· black) is compared with a model fit (– gray). Fit residuals, offset by** $-150\,\mu\mathrm{W}/(\mathrm{cm}^2\,\mathrm{sr}\,\mathrm{cm}^{-1})$**, and instrument noise level, offset by** $-350\,\mu\mathrm{W}/(\mathrm{cm}^2\,\mathrm{sr}\,\mathrm{cm}^{-1})$**, are provided.** *Bottom*: **Ratio of the flame path length,** l**, to the calculated mean free path of a photon,** l_{MFP}**, under the conditions estimated by the model fit.**

until Sec. 3.5. The difference between the data and model are also presented in Fig. 17, denoted Residuals, and compared with the imaginary part of the spectrum, denoted Noise. The fit residuals are mostly unstructured with a root-mean-square (RMS) value of $10.1\,\mu\mathrm{W}/(\mathrm{cm}^2\mathrm{sr}\mathrm{cm}^{-1})$. The RMS value of the fit residuals is only 1.5 times larger than the RMS value of instrument noise, indicating that the model describes the flame spectrum well overall. However, some systematic errors are present. This is most evident from the observed structure in the residuals between $2150\,\mathrm{cm}^{-1}$ to $2400\,\mathrm{cm}^{-1}$. Within this range, the fit residual RMS value is 5.9 times larger than the instrument noise RMS value. However, the noise in this region is small, and the RMS fit residual in this band is only 3.5% of the RMS signal. The quality of this single pixel spectral fit is representative of the fit quality across the hyperspectral image.

Mixing layer effects may contribute to the systematic fitting errors observed between $2150\,\mathrm{cm}^{-1}$ to $2400\,\mathrm{cm}^{-1}$. The bottom panel of Fig. 17 shows the ratio of the flame path

66

length, l, and the calculated mean free path of a photon, l_{MFP} (Eq. 27), under the conditions estimated by the model fit. This ratio is less than 3% across most of the spectrum, but approaches 40% within the strong CO_2 asymmetric-stretch emission band. This suggests that while the plume is optically thin across most of the spectrum, some optical trapping occurs within this CO_2 band. It follows that emission from the mixing layer will have a larger effect within this band in comparison with the optically thin spectral regions. This interpretation is consistent with the observation that fit residual magnitudes relative to the signal increase with height (i.e. mixing layer width). While the homogeneous assumption is adequate across most of the spectrum and yields spectral retrievals in good agreement with experimental and theoretical predictions, the high fidelity measurements may contain information about small mixing layer effects.

A second contributing factor for systematic fit errors may be associated with limitations of the spectroscopic databases used in this work. Recent measurements [93, 94] of high-temperature (2000 K to 5000 K) CO_2 produced via microwave discharge suggests that systematic errors in the spectral radiance between $2100\,\text{cm}^{-1}$ to $2450\,\text{cm}^{-1}$ can be up to 10–30%. Similarly, in a recent study involving laser irradiation of graphite targets [95], an empirical emissivity correction factor was needed to adequately reproduce the observed spectral emissions from the hot, CO_2-rich plume above the target within this same spectral region. However, in both of these recent experiments, CO_2 temperatures were much larger than the flame temperatures observed in this work and, in some cases, exceeded the useful temperature range of the CDSD-4000 database. Moreover, the radiative transfer models required to accurately describe the data were considerably more complicated than what is needed to model the Hencken burner flame. Thus, while limitations of the spectroscopic databases cannot be ruled out, their effect on the scalar estimates is likely small given both the good fit quality and the excellent agreement

between spectrally-retrieved scalar values with Meyer's results and CEA thermodynamic calculations.

Finally, the point-spread function of the instrument causes subtle mixing of spectral emissions from nearby pixels, and our instrument model does not yet account for these effects. As our future efforts will focus on three-dimensional scalar field reconstruction, these small effects will need to be properly modeled. Given the possible systematic errors due to instrumentation, model simplifications, and limitations of high-temperature spectroscopy databases, actual scalar value uncertainties may exceed those presented here by an additional factor of two. Despite this important caveat, the small fit uncertainties exemplify the benefit of a highly-resolved emission spectrum across a wide band pass for temperature estimation. 3000 unique data points between $1975\,\text{cm}^{-1} \leq \tilde{\nu} \leq 4225\,\text{cm}^{-1}$ sample myriad H_2O, CO_2 and CO emission lines, each representing a transition between pairs of internal energy levels. When local thermodynamic equilibrium prevails, the population of each internal energy level is governed by the same temperature via the Boltzmann distribution.

Radial and axial fit results.

Spectrally-estimated scalars were uniform across the flame near the base of the burner. Fig. 18 shows the results for the $\Phi = 1.1$ trial at $u = 10\,\text{mm}$. The mean temperature obtained for all pixels within 5 mm of flame center was $T = 2317\,\text{K}$ with a standard deviation of 2 K. Note that the pixel-to-pixel temperature variance is approximately ten times smaller than the fit errors associated with the individual spectral estimates (nominally 20 K). For comparison, the corresponding laser-based temperature measurement is also provided. The transition to lines-of-sight dominated by radiance from the mixing layer occurs around $\pm 10\,\text{mm}$ from the center of the burner; beyond this, the retrieved temperature rapidly decays with distance. While the H_2O and CO_2 mole fraction profiles

68
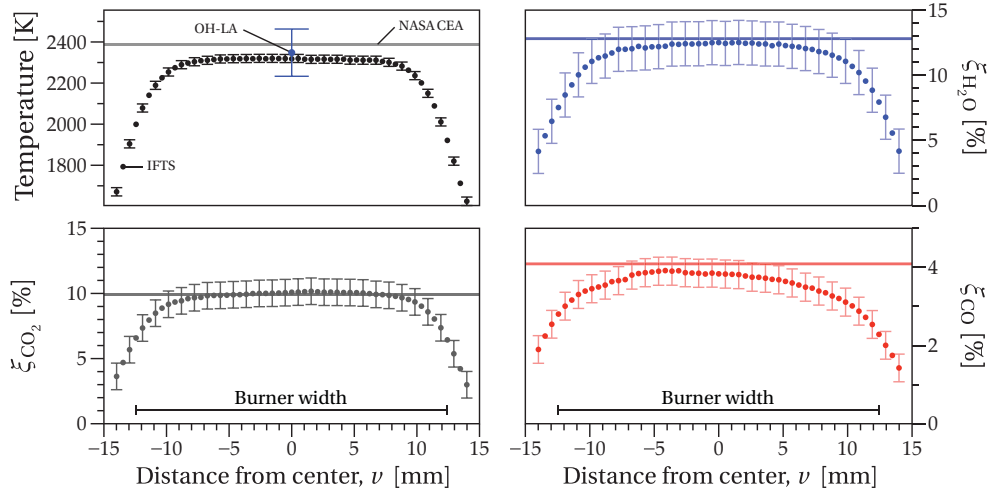
Figure 18. Spectrally-retrieved scalar values of ethylene flame 10 mm **above the burner for the** $\Phi = 1.1$ **condition. Error bars indicate the 95% confidence interval and only every other bar is shown for clarity. For comparison, the temperature value obtained by OH-laser absorption measurements (●) and the NASA CEA equilibrium values (— , — , —) are provided.**

are qualitatively similar in shape to that of temperature, the CO profile is less flat across the center of the flame. Mean values within 5 mm of flame center for H_2O, CO_2, and CO were 12.5% and 10.1%, and 3.8%, respectively. Pixel-to-pixel standard deviations (0.1%, 0.08%, and 0.08%, respectively) were much smaller than measurement uncertainties. The reduction in both temperature and mole fraction in the mixing layer result in SNRs too low to support spectral retrievals beyond $v = \pm 15$ mm.

Temperatures estimated at $u = 10$ mm for each equivalence ratio are compared with
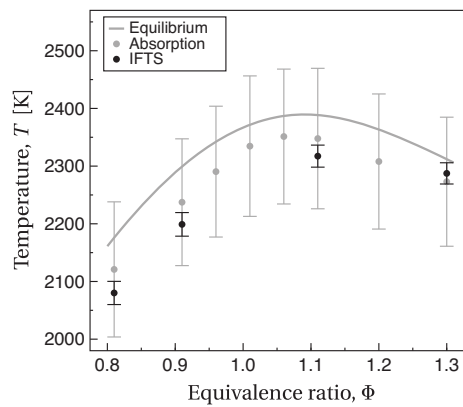
Figure 19. Variation of spectrally-retrieved average temperature with equivalence ratio in ethylene flame at a height of 10 mm **above the burner. Comparison values of temperature measured with OH-laser absorption and chemical equilibrium analysis are taken from Meyer** *et al.* **[1].**

69

the laser absorption measurements [1] and equilibrium calculations in Fig. 19. The results are in very good agreement. IFTS temperature estimates are well within the error bars of the laser-based measurements [1], and don't differ by more than 30 K. However, with the exception of the $\Phi = 1.3$ case, spectrally-estimated temperatures are lower than those reported by Meyer.

The left panel of Fig. 20 presents the spectrally-estimated temperature profiles for all pixels with a sufficient signal-to-noise ratio at heights of 5 mm, 10 mm, 20 mm and 40 mm above the burner for the $\Phi = 0.9$ flame. Error bars are not displayed to improve visualization, but errors are nominally $\pm 1\%$. The temperature profiles at heights of 5 mm and 10 mm are flat and rapidly decay within the thin mixing layer near $v = \pm 12.5$ mm. This nearly top-hat profile is consistent with the approximation of the flame as a single, homogeneous layer. However, at $u = 20$ mm, the mixing layer has widened slightly, and by $u = 40$ mm, the flame core only spans $|v| \leq 4$ mm. The right panel of Fig. 20 compares spectrally-retrieved temperature of the $\Phi = 0.9$ flame traversing vertically through the centerline ($v = 0$) with Meyer's OH absorption [1] results. Temperature increases rapidly above the base of the flame and peaks near 10 mm. The spectrally-estimated results are in good agreement with the laser measurements at each height investigated in Meyer's work.

The variation in scalar values with distance from the burner is presented for all equivalence ratios in Fig. 21. The results should be interpreted as path-averaged scalar values to recognize the significance of temperature and concentration gradients along the line-of-sight which become more prominent with increasing height. The cooler, outer edge of the flame contributes less to the path-integrated signal, so path-averaged temperatures will be lower than the center flame temperature. Additionally, the increasing size of the mixing layer makes it difficult to estimate absolute concentrations, so col-

---

[1]The error bars provided by Meyer *et al.* are not clearly defined and may not represent 95% CIs.

70
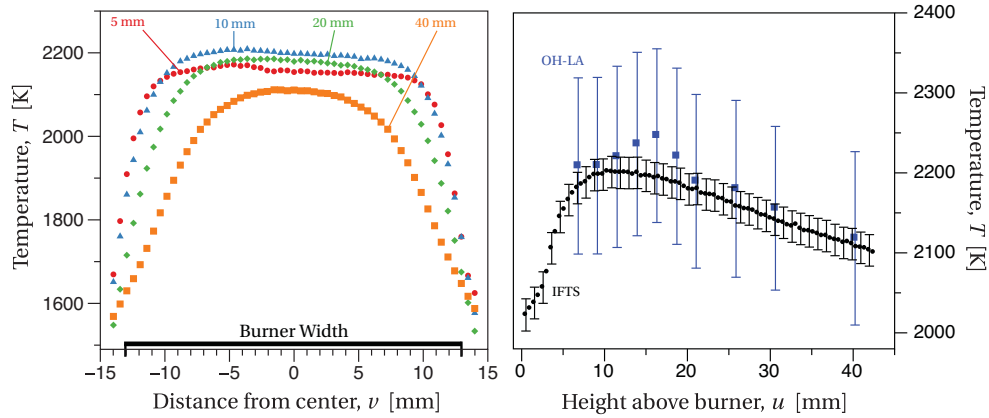
Figure 20. *Left panel*: **Spectrally-retrieved temperature of ethylene flame at heights of** 5 mm**,** 10 mm**,** 20 mm **and** 40 mm **above the burner for the** $\Phi = 0.9$ **condition. Error bars are not shown for clarity but have nominal half-widths of approximately** 20 K**.** *Right panel*: **Comparison of the spectrally-estimated temperatures (IFTS) with laser absorption measurements (OH-LA) at various heights along the centerline of the** $\Phi = 0.9$ **flame. Error bars are omitted at every other point for clarity.**

umn densities are reported instead. While the current two-dimensional path-averaged results are valuable, retrieving three-dimensional scalar fields using a deconvolution technique is the ultimate goal of this effort.

Of particular interest is the variation in scalar values with equivalence ratio. All scalar values immediately increase with u. At each equivalence ratio, temperature, $q_{H_2O}(u)$, and $q_{CO_2}(u)$ rapidly increase and peak between $9 \, \text{mm} \leq u \leq 12 \, \text{mm}$. The initial behavior of $q_{CO}(u)$ is similar, but it reaches a maximum between $2 \, \text{mm} \leq u \leq 4 \, \text{mm}$. After reaching their peak values, the scalar quantities exhibit a gradual decay with u in a manner that is highly dependent on Φ. In the fuel lean flames ($\Phi = 0.8, 0.9$), the oxygen rich environment enables quick conversion of CO to CO_2, and the CO_2 profiles follow an axial profile similar to H_2O. In the fuel rich flames ($\Phi = 1.1, 1.3$), the oxygen lean environment results in much larger CO concentrations near the burner and a more gradual conversion of CO to CO_2. While the N_2 co-flow limits diffusion of surrounding air into the flame, above $u = 30 \, \text{mm}$, the buoyancy forces lead to flame unsteadiness, and the entrainment of atmospheric O_2 is likely. (Recall the CoV map in Fig. 15.) It is reasonable that this increases the rate of $CO \rightarrow CO_2$ conversion, as evidenced by a slight increase in slope of the $q_{CO_2}(u)$ curve for $\Phi = 1.1$ and a substantial increase in slope

71
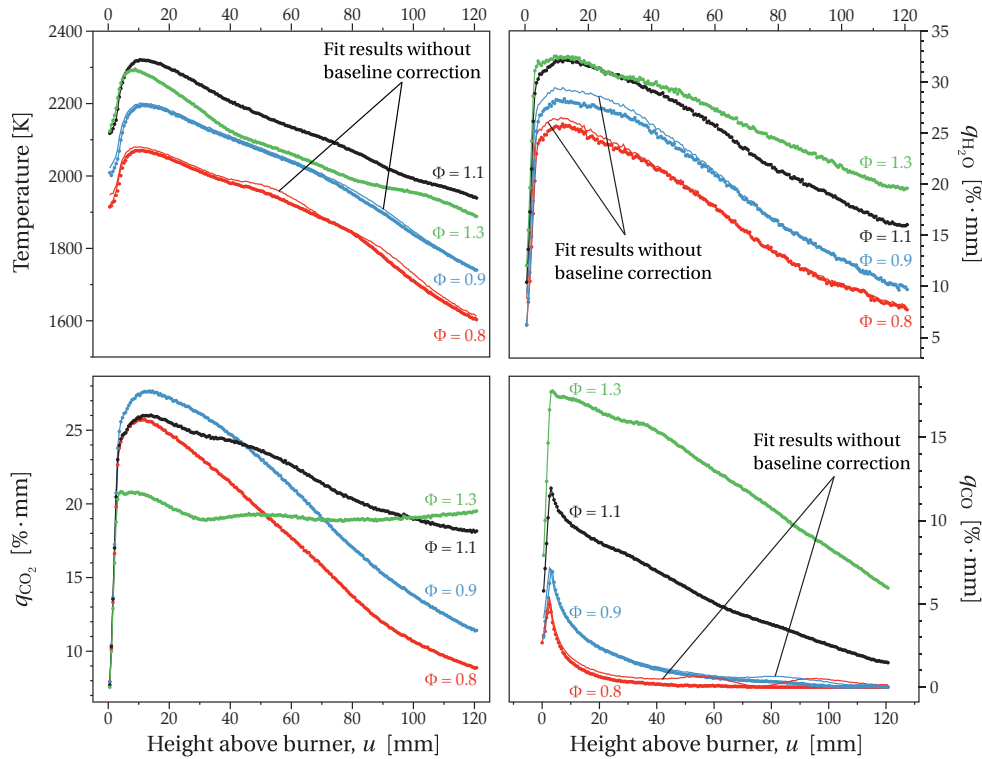
Figure 21. Spectrally-retrieved scalar values of the C_2H_2/air flame, along the centerline ($v = 0$), for $\Phi = 0.8$ (• red), $\Phi = 0.9$ (• blue), $\Phi = 1.1$ (• black), and $\Phi = 1.3$ (• green). Error bars are omitted for clarity. Fit results obtained without the polynomial baseline correction for $\Phi = 0.8$ (— red) and $\Phi = 0.9$ (— blue) are annotated.

for $\Phi = 1.3$. The enhanced oxidation of CO at this height may be responsible for the observable change in the corresponding $T(u)$ curve. Between $10\,\mathrm{mm} \leq u \leq 30\,\mathrm{mm}$, the $T(u)$ slope is $-3.9\,\mathrm{K/mm}$ and $-5.5\,\mathrm{K/mm}$ for $\Phi = 1.1$ and $\Phi = 1.3$, respectively. Between $40\,\mathrm{mm} \leq u \leq 70\,\mathrm{mm}$, the slopes increase to $-3.4\,\mathrm{K/mm}$ and $-3.3\,\mathrm{K/mm}$ for $\Phi = 1.1$ and $\Phi = 1.3$, respectively.

As mentioned briefly before, spectra between $40\,\mathrm{mm} \leq u \leq 90\,\mathrm{mm}$ for $\Phi = 0.8$, and to a lesser extent for $\Phi = 0.9$, exhibit a subtle, low-frequency baseline oscillation. This oscillation produced a small bias in the T and q_{CO} fit parameters, and prompted the pragmatic addition of the 4th-order polynomial to the model for the fuel-lean flames. This was the minimum order needed to visually account for the baseline oscillation; however, polynomials up to 7th-order did not significantly affect the fit results. The baseline oscillation is a small fraction of the total signal and the polynomial never

72

represented more than 1.5% of the peak spectral radiance. The baseline oscillation is likely a result of insufficient averaging over the intensity fluctuations arising from unsteady behavior in this flame region. It was not perceptible in the fuel-rich cases, and this is consistent with the smaller CoV values at $\nu = 0$ observed in Fig. 31. For comparison, the fit results obtained without using the 4th-order polynomial to model the baseline are provided in Fig. 21 for context. The difference in $q_{CO_2}(u)$ is imperceptible. While the baseline polynomial removes anomalous behavior in $q_{CO}(u)$ and $T(u)$ within the unsteady region, it also systematically lowers the $q_{H_2O}(u)$ column density where the flame is highly stable ($u < 40\,mm$).

Scalar maps.

Fig. 22 compares two-dimensional (2-D) maps of temperature and column densities obtained from the $\Phi = 0.8$ and $\Phi = 1.1$ flames. These maps represent the most complete, spatially resolved, line-of-sight scalar value measurements of Hencken burner ethylene flames to date, and demonstrate the utility of IFTS for combustion diagnostics. The 2-D scalar profiles reveal the differences in combustion under fuel-lean and fuel-rich conditions. Most notable is the rapid conversion of CO to CO_2 in the $\Phi = 0.8$ flame, because of the abundance of available oxygen. This quick conversion of CO yields near identical H_2O and CO_2 maps in the $\Phi = 0.8$ flame. The $\Phi = 1.1$ flame has a large concentration of CO near the base. Diffusion and entrainment of surrounding air enables the gradual conversion of CO to CO_2, and the corresponding exothermicity of this reaction reduces the rate at which the path-averaged temperature decays with height, u.
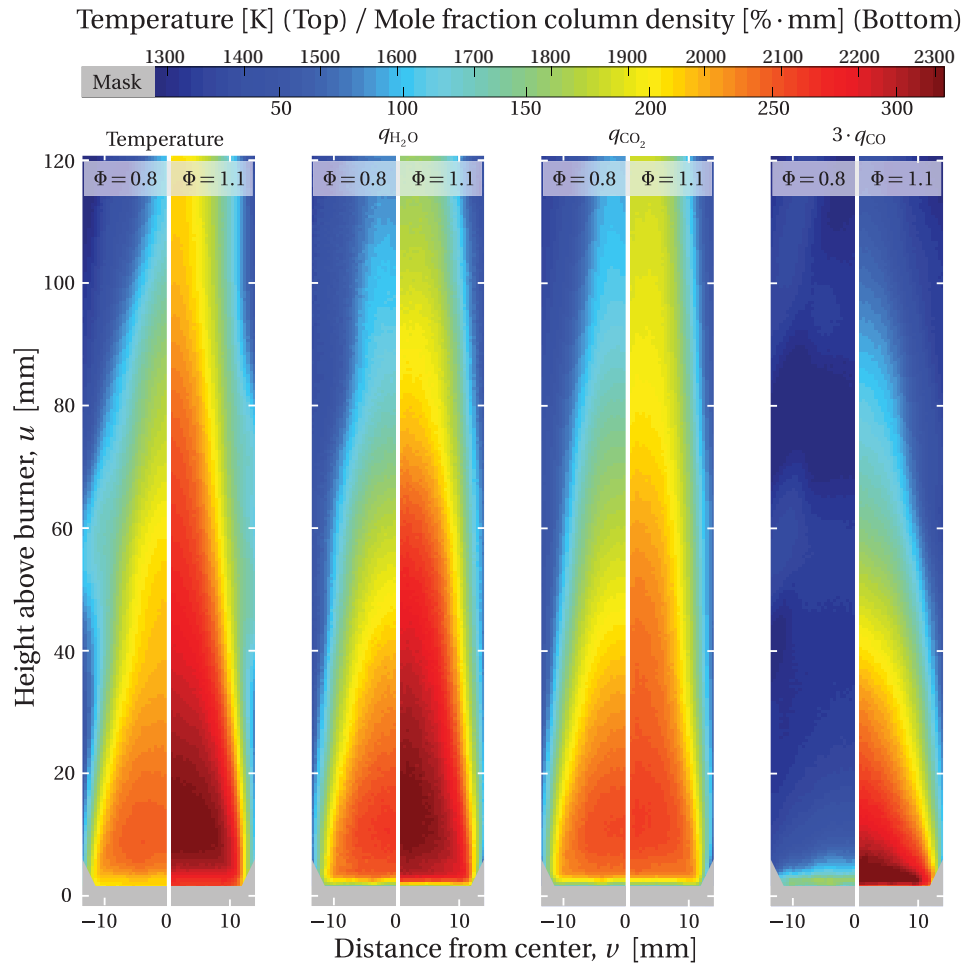
Figure 22. Split imagery comparison of path-averaged scalar values for $\Phi = 0.8$ **(left) and $\Phi = 1.1$ (right).** *Left panel*: **Temperature.** *Center-left panel*: **H_2O column density.** *Center-right panel*: **CO_2 column density.** *Right*: **Scaled CO column density. CO values are tripled to use the full range of the common color axis. The top and bottom color bar scales represent temperature and column density, respectively.**

Uncertainty estimation.

An important source of systematic error in the spectrum, and consequently the estimation in scalar values, arises from imperfections in the calibration blackbody sources. High-temperature, wide-area blackbodies are necessary for calibrating flame measurements, but these are not as accurate as smaller blackbodies designed for calibrating lower temperature scenes. To assess the impact of absolute temperature and spectral emissivity uncertainty on the spectrally-retrieved scalar values, a Monte Carlo error analysis was performed. The manufacturer-specified 95% CIs for set-point tem-

peratures and emissivities defined normal distributions from which random values were drawn. 2,000 iterations were performed, each time calibrating using blackbody temperatures and emissivities drawn from their respective uncertainty distributions. With each iteration, the spectral fits were performed leading to a distribution of scalar values which capture the the uncertainty due to calibration. In general, these systematic calibration errors (δ_cal) were larger than the statistical uncertainty determined from the non-linear regression (δ_nlr). In this work, scalar value uncertainties represent the root quadrature sum of these two sources, i.e. $\delta_\text{total} = \sqrt{\delta_\text{nlr}^2 + \delta_\text{cal}^2}$.

The uncertainty distributions of T, ξ_{H_2O}, ξ_{CO_2} and ξ_{CO} obtained from the Monte Carlo error analysis of the $\Phi = 1.1$ flame spectrum at $(u, v) = (10\,\text{mm}, 0\,\text{mm})$ are presented in Fig. 23. Continuous probability distribution functions were estimated via kernel density estimation using the Epanechnikov kernel. The 95% CI for temperature spans 2307 K to 2326 K, which is more than 5 times larger than the regression uncertainty of 3.5 K. Adding in quadrature both the statistical fit error and the calibration systematic error yields a spectrally-estimated temperature of $T = (2318 \pm 19)\,\text{K}$. Calibration errors had a much larger impact on the uncertainty of concentrations. For example, the H_2O mole fraction 95% CI (11.85 % to 13.64 %) is 15 times larger than the statistical fit uncertainty (0.12 %). Quadrature addition yields $\xi_{H_2O} = (12.6 \pm 0.8)\,\%$. The impact on the other flame species was similar and is reported in Fig. 23. Uncertainties of a few percent in blackbody temperature and emissivity affect the absolute radiometric accuracy much more than the relative spectral shape. Since the spectrally-retrieved temperature is strongly influenced by the relative line heights, whereas the column densities are dominated by the absolute line heights, the relative errors in temperature are much smaller than relative errors in column density.

75
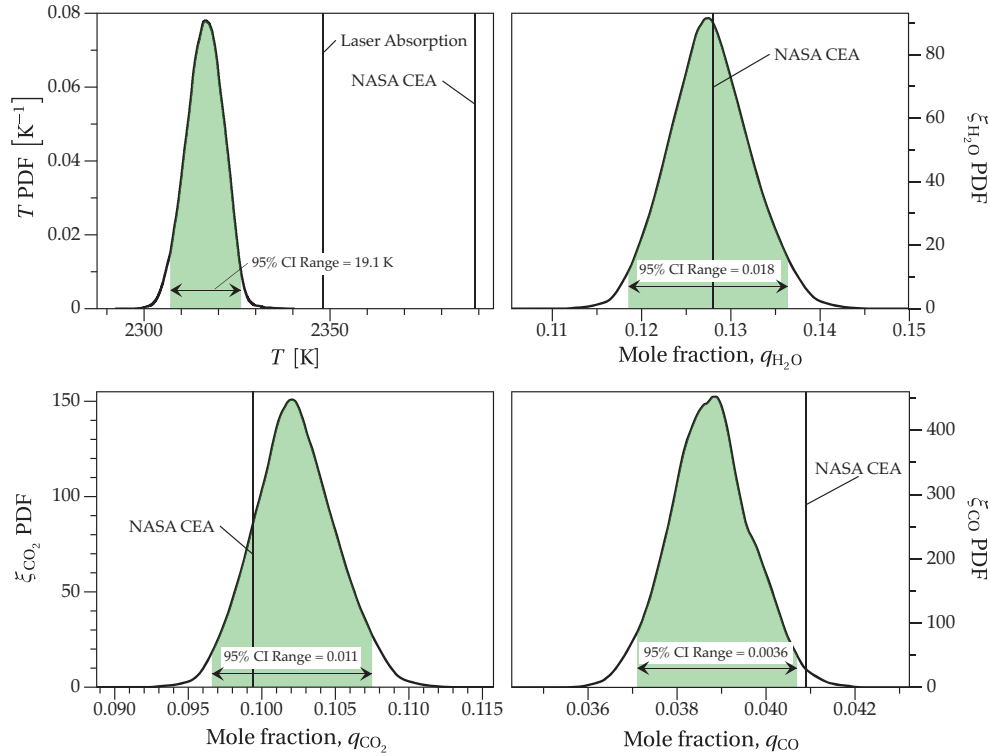
Figure 23. Uncertainty distributions estimated from a 2,000 iteration Monte Carlo analysis to propagate calibration source uncertainties to the spectrally-retrieved scalar values. The shaded areas are centered at the mean value and correspond to the 95% confidence interval. Previous experimental and equilibrium results are provided for context.

3.6 Conclusions

This investigation of an ethylene flame ($\Phi = 0.8 - 1.3$) sought to establish IFTS as a useful combustion diagnostic. Spectrally-determined temperatures at all Φ values agree with previous laser absorption flame measurements of a similarly-configured Hencken burner. The large number of ro-vibrational emission lines and band structures arising from multiple species lead to statistical temperature uncertainties less than 50 K. Additionally, the retrieved H_2O, CO_2 and CO mole fractions are in excellent agreement with equilibrium predictions. The 2-D scalar fields obtained enable both the visualization and quantitative comparison of the Φ-dependent chemistry throughout the flame.

IFTS offers several unique advantages for combustion diagnostics. First, it is portable and can be set up and collecting calibrated spectral imagery in about an hour. Second, it

76

enables the measurement of a moderate resolution spectrum (up to $0.25\,\mathrm{cm}^{-1}$) across a wide band pass ($1.5\,\mu\mathrm{m}$ to $5.5\,\mu\mathrm{m}$). This represents highly constraining data which can be used to benchmark computational fluid dynamics simulations. As demonstrated, the spectra are readily interpreted in terms of 2-D path-averaged temperature and column density maps. Moreover, the adaptation of existing deconvolution algorithms to the high-fidelity hyperspectral flame images may enable the retrieval of the 3-D scalar fields. The high-speed imagery existing within the interferometric measurement enables visualization of flame dynamics, and this enhances interpretation of 2-D scalar fields derived from the time-averaged spectra. Additionally, existing flow field analyses currently performed by infrared cameras can be readily adapted to the broadband imagery captured within the IFTS measurement. However, as a passive measurement, IFTS does not have the same sensitivity to trace species that lasers enjoy, and homonuclear diatomic molecules (e.g. H_2) cannot be observed. Additionally, the slow speed ($0.1\,\mathrm{Hz}$ to $10\,\mathrm{Hz}$) at which typical IFTS measurements are captured requires statistically significant numbers of observations (100–1000) to properly average over temporal fluctuations in the scalar fields.

IV. Time-resolved IFTS for Harmonic Unsteady Laminar Combustion

The following is a research paper, in its entirety, intended for publication in Optics Express. The focus is on reconstruction of instantaneous line-of-sight interferograms from an ensemble of time varying data cubes. Authors of this article include Michael Rhoby, and Dr. Kevin Gross. The work is significant for the following reasons:

- It presents a novel technique for reconstructing spectra at various instants in time from an ensemble of interferometric measurements of a harmonic combustion system.

- It lays groundwork for translating line-of-sight camera imagery into radial information that will yield scalar value maps in a full 4-D sense.

As first author I was responsible for data capture, reduction, and analysis, and the initial draft of the document. Dr. Kevin Gross contributed in data analysis and was the primary editor of the document. This chapter represents the satisfaction of objective 2.

4.1 Abstract

Combustion studies can benefit from spatially-resolved wide-band spectra, such as those achievable using an imaging Fourier transform spectrometer (IFTS). However, such measurements are often temporally averaged, complicating the interpretation of dynamic combustion sources due to nonlinearity in the radiative transfer problem. Using both CFD simulations and measurements of an unsteady, nonpremixed H_2 flame, we demonstrate an algorithm for reconstruction of "snapshot spectra" at arbitrary times in the flame's period from an ensemble of IFTS measurements. The method assumes that the band integrated intensity (I^{DC}) and its temporal derivative (dI^{DC}) define a unique configuration of the flame's scalar conditions. Measurements with

I^{DC} and dI^{DC} values corresponding to a specific time within the flame's period are selectively averaged, producing a snapshot interferogram and corresponding spectrum. The snapshot reconstruction algorithm is validated using simulated interferometric measurements of time-varying spectra generated from CFD-generated scalar fields. Then, snapshot spectra from an actual H_2 flame are compared with previously reported measurements of a similarly configured hydrogen flame. Comparison are least favorable at $t = 53$ ms with a mean difference of 30.1 W/m^{2}sr or 18.5% and are most favorable at $t = 12$ ms with a mean difference of 8 W/m^{2}sr or 3.8%.

4.2   Introduction

Combustion diagnostics is a field of continued interest, with active research in areas such as combustion efficiency [96], soot formation [27], fuel droplet mixing [97], and validation of computer modeling [71, 98–100]. An extensive review of combustion diagnostics prior to 2002 is available in [97]. The ability to simultaneously determine multiple scalar fields (*e.g.*, temperature and species concentrations) three-dimensionally with high temporal resolution is highly desired and the focus of current experimental efforts [19, 31, 67, 82]. These measurements are desirable, yet difficult to achieve. Flame scalar value measurements reveal key combustion phenomenon, enable validation of chemical kinetic models, and benchmark numerical simulations. Laser-based methods—the cornerstone of combustion diagnostics [97]—provide highly selective, sensitive, non-intrusive means to interrogate laminar and turbulent flow fields under a variety of flame conditions. However, three-dimensional mapping of multiple scalar fields typically requires a complicated optical set-up with raster scanning multiple lasers. Flame emission measurements are another class of nonintrusive diagnostics, complementing laser-based techniques, and are often easier to implement. High-speed infrared cameras with various band-pass filters have been used to map spatial and

79

temporal variations in radiant intensity. These can be related to spatial distributions of scalar values [2] and to various measures of turbulence (*e.g.* integral length and time scales) [31, 83]. Broadband imaging, however, is limited in its ability to discriminate the influence of multiple scalars, since, e.g., both temperature and species concentrations influence band-integrated intensity. Fourier-transform spectrometer (FTS) measurements, when paired with appropriate tomographic deconvolution algorithms, can simultaneously determine temperature and mole fractions of major flame species [45, 52].

Imaging Fourier-transform spectrometer (IFTS), a type of hyperspectral imager (HSI), has recently been used to measure the spatial and spectral characteristics of both laminar and turbulent laboratory flames [67, 82]. These time-averaged measurements capture information related to the steady-state scalar fields. However, when scalar fluctuations are large, quantitative interpretation of the time-averaged HSI data is complicated due to the non-linearities inherent in radiation transport. In instances when the frequency of the spectral emission is fast compared to the scalar fluctuations, time-resolved Fourier transform spectroscopy (TR-FTS) using step-scan techniques have been successful [101–105]. Step-scan techniques arrest the moving mirror in an FTS to a set position- referenced by a metrology laser-and kept stationary while the scalar fluctuations progress. Data is collected and averaged and the process is repeated at the next mirror position [101, 104]. A complete, averaged interferogram is obtained in one mirror sweep. TR-FTS using step-scan is often used in biophysics and chemical rate reaction research and has demonstrated spectral resolution of $0.25\,\mathrm{cm^{-1}}$ and temporal resolution on the order of ns [101, 102]. At present, imaging with TR-FTS requires raster scanning similar to most laser techniques because no imaging FTS with step-scan capability is commercially available. An additional drawback to step-scan FTS is uncertainty in the absolute position of the moving mirror. Fluctuations in the

80

mirror position when it should be arrested, even movement of several nm, can introduce systematic errors in the average interferogram.

The creation of a time-resolved measurement technique for the study of laminar flame dynamics, combined with the spatial and spectral resolution of IFTS would further improve its utility as a combustion diagnostic. In this paper, an alternative algorithm to step-scan sampling is presented for TR-IFTS. Spectra are reconstructed at various instants in time from an ensemble of interferometric measurements of a harmonic combustion system acquired by a continuously-scanning IFTS. The algorithm is developed and tested by constructing "measurements" of a simulated buoyancy-driven unsteady hydrogen diffusion flame [2]. The algorithm is then applied to real IFTS measurements of a hydrogen diffusion flame and compared with recent measurements [2].

4.3 Michelson interferometry for dynamic flames

For a system in local thermodynamic equilibrium, and for a non-scattering medium, the discretized solution to the radiative transfer problem through n homogenous layers is given by
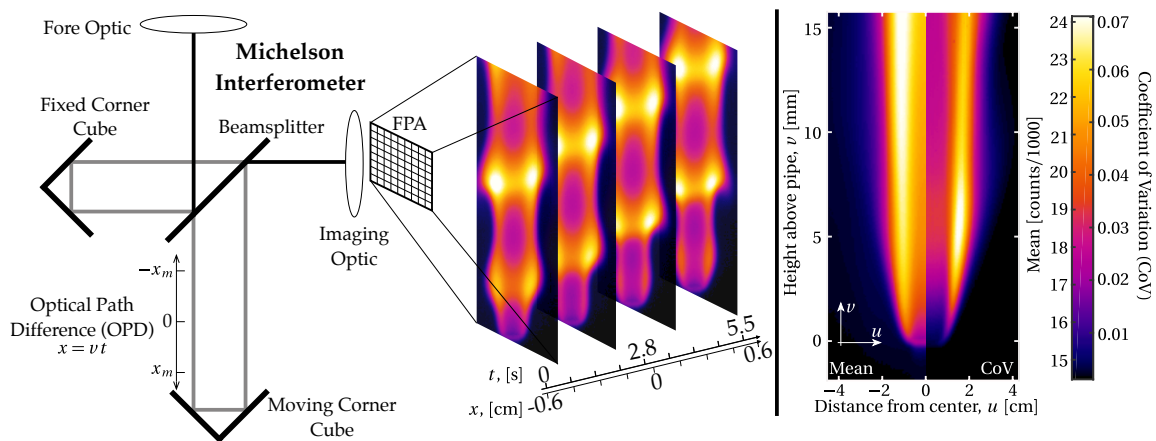
Figure 24. *Left*: Depiction of a Michelson interferometer and several sequential images captured by the FPA. *Right*: Split imagery of a symmetric flame. Mean camera intensity values are on the left and coefficient of variation (CoV) values are on the right.

81

$$L(\tilde{\nu}) = L_0 \prod_{i=1}^{n} \tau_i(\tilde{\nu}) + \sum_{i=1}^{n} \left(B(\tilde{\nu}, T_i)(1 - \tau_i(\tilde{\nu})) \prod_{j=i+1}^{n} \tau_j(\tilde{\nu}) \right). \tag{29}$$

Here, $L(\tilde{\nu})$ is the line-of-sight (LOS) scene radiance spectra, and L_0 is any background radiance prior to layer $i = 1$. The emissivity of the ith layer is given by $(1 - \tau_i(\tilde{\nu}_i))$, where

$$\tau(\tilde{\nu}) = e^{-N \cdot l \cdot \sum_k \xi_k \sigma_k(\tilde{\nu}, T)}. \tag{30}$$

Here, $N = P/(k_B T)$ is the number density, l is the layer path length, ξ_k is the kth species mole fraction, $\sigma_k(\tilde{\nu}, T)$ is its corresponding absorption cross-section, and $B(\tilde{\nu}, T)$ is Plank's blackbody radiation at temperature T.

The Telops measures $L(\tilde{\nu})$ through the coupling of a Michelson interferometer with a high-speed 320×256 pixel Indium Antimonide (InSb) focal-plane array (FPA). A depiction of a Michelson interferometer is provided in the left side of Fig. 24. This process results in constructive and destructive interference values, $I_i(x)$, at the ith pixel which vary with optical path difference (OPD), or mirror scan distance, $x = \nu t$, and time t, assuming a constant scan speed, ν. After a full mirror scan, an interferogram at each pixel of the FPA is formed, which is a composition of FPA images (also pictured in Fig. 24) captured at a fixed OPD spacing, which in this work is $\Delta x = 632.8$ nm corresponding to the HeNe metrolog laser wavelength. Additional instrument details are available in [82]. For a *static* scene, $I_i(x)$, is given by

$$
\begin{aligned}
I_i(x) &= \int_0^\infty (1 + \cos(2\pi \tilde{\nu} x)) G_i(\tilde{\nu})(L_i(\tilde{\nu}) + L_i^I(\tilde{\nu})) d\tilde{\nu} \\
&= I_i^{\text{DC}} + I_i^{\text{AC}}(x).
\end{aligned} \tag{31}
$$

Here, $G_i(\tilde{\nu})$ is the spectral response of the camera, and $L_i^I(\tilde{\nu})$ is the instrument self emission. Because the scan time of the Michelson can be on the order of seconds, traditional scenes for this instrument are static in nature (insignificant changes in the scalar values

82

T, ξ_k, and N) to avoid changes in $L_i(\tilde{\nu})$ over a scan. In this case the unmodulated, spectrally-integrated signal, I_i^{DC}, is a constant value and is often removed leaving only the modulated component, $I_i^{\text{AC}}(x)$. Scene spectra are easily obtained through Fourier transformation of $I_i^{\text{AC}}(x)$ and high-temperature scene calibration techniques [82].

In buoyancy driven harmonic flames the measurement scene is decidedly *non-static* with changes in $L(\tilde{\nu})$ occurring faster ($f_F \sim 10\,\text{Hz}$) than the scan speed of the Michelson ($f_M \sim 0.18\,\text{Hz}$ in this work), but much slower than the detector cut-off modulation frequency ($f_d \sim 385\,\text{Hz}$; the product of the mirror scan speed, $\nu = 0.214\,\text{cm/s}$, and the detector cut-off frequency, $1800\,\text{cm}^{-1}$). The Fourier transformation of a single measurement of $I_i^{\text{AC}}(x)$ is no longer a representation of the flame's emission. Averaging over many independent scans of the Michelson is a common way to mitigate changes in $I_i^{\text{DC}}(x)$. However, an average over an ensemble of spectral measurements that have an unsteady, pulsating scalar field with period τ has a fundamental limitation

$$\langle L_i(\tilde{\nu}, T(t), \xi_k(t)) \rangle = \frac{1}{\tau} \int_0^t L_i(\tilde{\nu}, T(t), \xi_k(t))\, dt \neq L_i(\tilde{\nu}, \langle T(t) \rangle, \langle \xi_k(t) \rangle). \qquad (32)$$

The non-equality arises from the nonlinear dependence of L on T and ξ_k. This inequality makes one unable to determine the temporal behavior of scalar fields from a time-averaged spectrum. Also, such a spectrum is likely an unphysical representation of the flame's radiance so accurate average scalar value retrievals is unlikely as well. It is for this reason that a method to determine the scene spectrum at instantaneous points in time is needed.

4.4 Methods

Simulated Flame Data.

To better use the information captured in a measurement ensemble, we now consider the interferometric measurement of a time-varying source like that pictured in Fig. 25. The flames of interest have a harmonic frequency, $f_F \sim 10\,\text{Hz}$, which is well below the detector cut-off modulation frequency, $f_d \sim 385\,\text{Hz}$. Thus, $I_i^{\text{DC}}(x)$ can be separated, via low-pass filter, from $I_i^{AC}(x)$ caused by the action of the Michelson. If the time scale of flame motion approaches that of the detector cut-off frequency, a separation of $I_i^{\text{DC}}(x)$ and $I_i^{\text{AC}}(x)$ becomes difficult, limiting this proposed method to harmonic flame motion that has a frequency, $f_F \lesssim 200\,\text{Hz}$.

Additionally, observed in the flame measured here, I_i^{DC} and the sign of its slope are uniquely associated with a single configuration of the flame's scalar fields. To develop an algorithm that leverages these flame properties, a simulated flame data set was generated. The computational fluid dynamics model (CFD) titled UNICORN [27, 71, 99, 100, 106] was used to simulate a hydrogen diffusion flame data set modeling the flame presented in [2]. This data set satisfies two key assumptions: (1) the flame is harmonic with a well-defined period; (2) its $I^{\text{DC}}(t)$ and slope are uniquely associated with a single flame configuration. Fig. 26 shows a representation of a single radial cross section of this flame as it changes over one cycle of its period. Using Eq 29, and the scalar values provided from the CFD mode, theoretical LOS integrated spectra were created, and from these spectra, interferograms were generated using Eq 31. Before the conversion to an interferogram, each spectra was given a random amount of noise governed by a Gaussian distribution of zero mean and an RMS signal-to-noise ratio (SNR) of 25, compared to the peak RMS signal. These interferograms, therefore, closely model what would be seen from an IFTS instrument interrogating the theoretical flame.

84
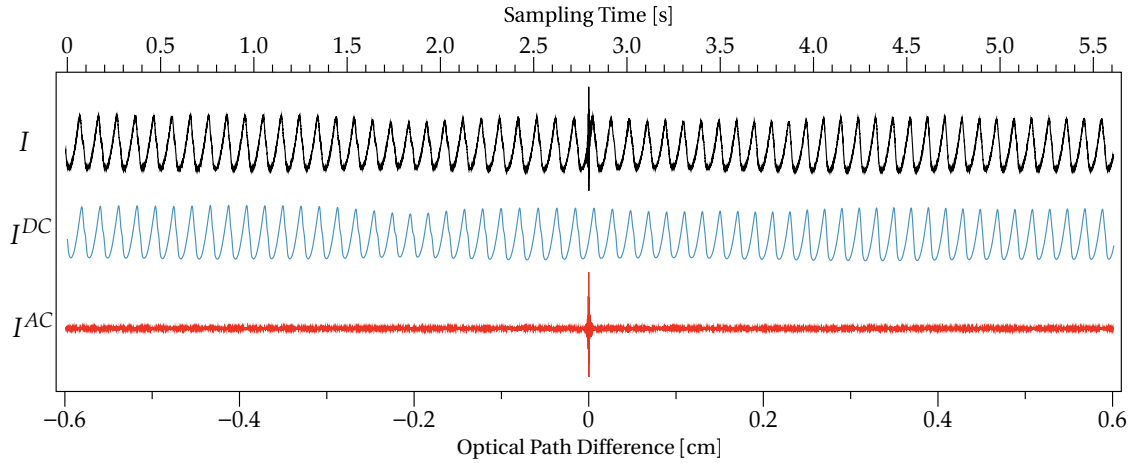
Figure 25. A single measured interferogram $I_i(x)$ that has been broken into its unmodulated, $I_i^{\mathrm{DC}}(x)$, and modulated, $I_i^{\mathrm{AC}}(x)$, components through low- and high-pass filtering, respectively.

Measured Flame Data.

In addition to the simulated flame data set, an unsteady hydrogen (H_2) diffusion flame, similar to the flame used in [2], was setup and measured. The flame was produced by flowing 34 ± 1 standard liters per minute (SLM) of pure H_2 through a simple stainless steel pipe 34.3 cm in length with an inner diameter of 8 mm. The pipe setup was placed in an enclosure to minimize room disturbances. The enclosure was made of a diffuse black material to minimize reflections and background radiation. The flow rate was controlled using MKS 1480A ALTA mass flow controllers which have an accuracy of $\pm 1\%$ of the set point flow rate. Laboratory conditions inside the enclosure varied throughout testing due to the effects of the flame. Air temperature ranged from 308 K to 320 K, relative humidity ranged from 30.0% to 40.0%, and the pressure held constant at 988 hPa. A depiction of the experimental setup is provided in Fig. 27.

A Telops Hyper-Cam MW-E IFTS was used to capture mid-infrared (MWIR, 1.5 μm to 5.5 μm) hyperspectral radiation emitted by the hydrogen flame. A detailed description of the Telops camera is available in the literature [67, 82, 86, 87] and only a brief description is given here. The IFTS features a traditional Michelson interferometer coupled to a high-speed Indium Antimonide staring focal-plane array (FPA) via $f/2.5$ imaging optics. An

85
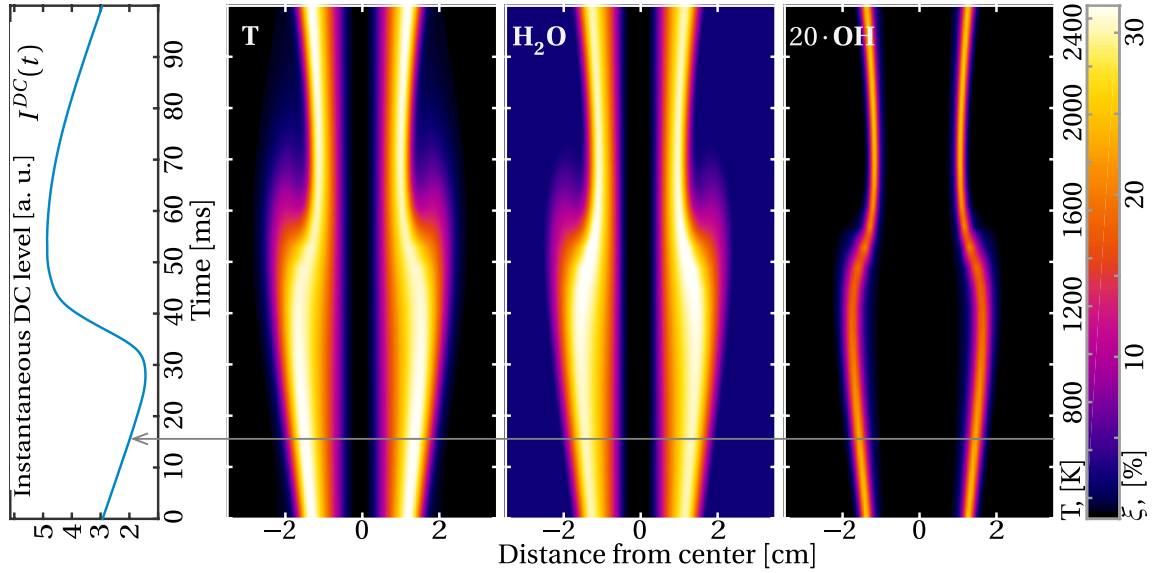
Figure 26. A single radial cross-section of a CFD-generated hydrogen diffusion flame over one flame flicker period. The value, $I^{DC}(t)$, that would be expected from this flame is also shown.
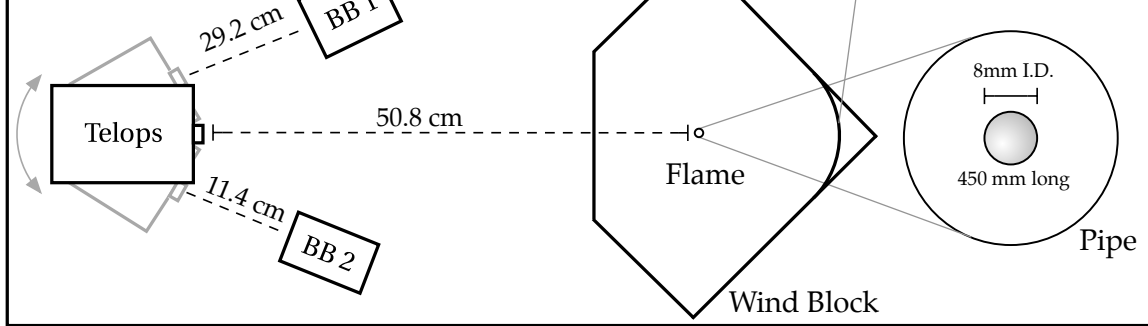
Figure 27. Schematic of the experimental arrangement. Important distances are provided as the image is not to scale. The Telops camera was on a rotation platform for fast and accurate transition between the calibration sources. An expanded view of the pipe used as a burner is provided with dimensions.

external $0.25\times$ telescope was used and the IFTS was located a distance $d = 50.8$ mm from the center of the flame with its optical center located approximately $u_0 = 6.8$ mm above the burner. For this experiment, the FPA captured imagery with a $40\,\mu$s integration time. The interferograms had a maximum OPD of 0.6 cm corresponding to an unapodized spectral resolution of $1\,\text{cm}^{-1}$.

Data for radiometric calibration, outlined in [82], was collected using 2 in and 6 in square CI Systems blackbody sources placed at distances of 11.4 cm and 29.2 cm, respectively, from the camera. This ensured each over-filled the instrument's FOV. The

calibration sources were set at 200 °C and 425 °C, respectively. A standard [88] two-point calibration—modified for noise suppression (see Sec. 3.4)—was performed to remove both system response and instrument self-emission from the raw signal. Correction of the spectral axis due to dispersion in the imaging system was performed as previously described [86]. Temperatures for the 2 in and 6 in are accurate to within ±0.3% and ±1.0%, respectively, of the set-point temperatures. Spectral emissivities for the 2 in and 6 in blackbodies are reported to be 0.980 ± 0.004 and 0.96 ± 0.02, respectively.

Algorithm for TR-IFTS.

An algorithm has been developed to retrieve an approximation to the instantaneous interferogram at any time, t_0, in the period of a flame from an ensemble of interferometric measurements. If a sufficient number of interferograms are collected, then each configuration of the periodic flame will have been measured at each OPD. The retrieval task amounts to extracting the subset of interferograms matching the flame at a specific point in its period, at each OPD. In the following development, the reconstructed interferograms are denoted $y_r(x, t)$, the DC level over a single period is denoted $I^{\text{DC}}(t)$, and is estimated from a low-pass filtered interferometric measurement, the slope of the DC level over a single period is denoted $dI^{\text{DC}}(t)$, and the measured ensemble data is denoted $y_m(x)$ with its DC component denoted $y_m^{\text{DC}}(x)$.

The following algorithm is used to estimate the instantaneous interferogram value at OPD x_i and time t_0:

1. Determine DC-level intensity and slope value at a given time t_0 via the $I^{\text{DC}}(t)$ and $dI^{\text{DC}}(t)$ curves.

2. Define a Gaussian distribution weighting value, w_{DC}, centered at $I^{\text{DC}}(t_0)$ and a FWHM defined by $I^{\text{DC}}(t_0 + \Delta t)$ and $I^{\text{DC}}(t_0 - \Delta t)$, where Δt is an uncertainty in t_0.

87

3. Define a Gaussian distribution weighting value, w_{Slope}, centered at $d I^{\text{DC}}(t_0)$ and a FWHM defined by $d I^{\text{DC}}(t_0 + \Delta t)$ and $d I^{\text{DC}}(t_0 - \Delta t)$.

4. Form the ith OPD value, $y_r(x_i)$, by taking a weighted mean of $y_m(x_i)$ with weights $w = w_{\text{DC}} \cdot w_{\text{Slope}}$.
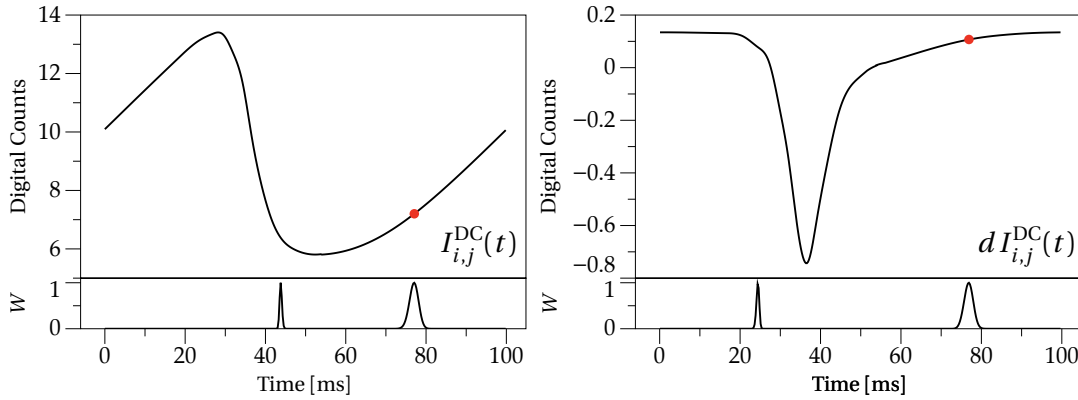
Figure 28. Depiction of the mean DC-level intensity and slope curves for the center LOS of the simulated data set. Weighting values shown are for a time reconstruction of $t_0 = 76\,\text{ms}$.

The first three steps of the above algorithm are depicted in Fig. 28. Here it can be seen that $I^{\text{DC}}(t)$ and $d I^{\text{DC}}(t)$ act as maps correlating measured values to points in the periodic motion of the flame. Using this weighing map, every sampled value in the ensemble of interferograms is assigned a weighting value. Recreation of the "snapshot" interferogram consists of taking the weighted mean of all measured values at each OPD. The weighting values shown in Fig. 28 correspond to a desired reconstruction at $t_0 = 76\,\text{ms}$. Note that the desired value of $I^{\text{DC}}(t)$ and $d I^{\text{DC}}(t)$ both occur twice over the full motion of the flame. The additional points in the flame motion where $I^{\text{DC}}(t)$ and $d I^{\text{DC}}(t)$ match do not, however, occur at the same time. The total weighting value $w = w_{\text{DC}} \cdot w_{\text{Slope}}$, then, ensures that only the measurement values corresponding to when the flame was in the desired configuration will be weighted highly.

88

4.5 Simulation Results

In total, 1000 time varying interferograms, each with a random starting phase in the flame period, were generated to represent the ensemble of flame measurements y_m. Fig. 30 (A) demonstrates the reconstruction algorithm for period times $t_0 = 29\,\text{ms}$ and 76 ms. Five randomly selected measured interferograms are shown for $x < 0$. The periodic nature of the flame is visible, and multiple periods are recorded in a single scan. The reconstructed interferograms corresponding to $t_0 = 29\,\text{ms}$ and 76 ms are shown for $x > 0$. Here it is seen that the reconstruction removes all variation in I_i^{DC} leaving only the desired I_i^{AC} component. The reconstructed interferograms were converted to spectra and are compared with the true instantaneous spectra in Fig. 30 (B). The mean absolute error in these reconstructions are 3.8% and 6.4% for $t_0 = 29\,\text{ms}$ and 76 ms, respectively. This reconstruction error scales exponentially with N where N is the number of interferograms used. To determine the number of interferograms to use in the ensemble, the recreation algorithm was performed using a variable value of N. For each N the reconstruction was run 20 times, pulling N random interferograms from a total set of 5000. The rms difference between spectra reconstructed using 5000 interferograms and the reconstructed spectra, at $t_0 = 29\,\text{ms}$, as a function of N and Δ_t is shown in Fig. 29. The difference decays exponentially with N and approaches the asymptotic limit near $N = 200$. The error bars shown in Fig. 29 indicate the standard deviation of the 20 trials performed at each N. Changing the value of Δ_t does not change the number of interferograms needed to a degree greater than the error bars. Fig. 29 shows that additional measurements past 200 may not be cost effective, as they provide little improvement in the reconstructed interferograms. When switching to measured data, rather than this ideal simulated data however, variations in the stability of the flame will occur. These variations may reduce the number of interferograms that

89

match the desired I_i^{DC} and $dI^{\mathrm{DC}}(t)$ values, effectively reducing the ensemble sample size. For this reason 1000 interferograms are used to ensure an adequate sample size.

When the flame is at an extremum, such as $t = 29\,\mathrm{ms}$, an increase in Δt will incorporate a small range in values compared to $t = 35\,\mathrm{ms}$. A change in Δt, however, translates to a large range of values in the corresponding point of W_{Slope}. It is this interplay between W_{DC} and W_{Slope} that ensures only the desired data is averaged together for a given time, t_0. Similar to any harmonic motion there is more data points to sample from at the extrema of I_i^{DC}. This is because the flame spends more time in these configurations. As a result of this, reconstructions taken at the extrema tend to have less uncertainty.

4.6 Measured Results

Data Overview.

Fig. 31 (A) shows the broadband imagery captured by the IFTS in a single interferometric measurement. The left half corresponds to the time-averaged intensity in raw camera counts. Laterally, the intensity peaks around ±1.5 cm, with less intensity approaching the flame centerline. This suggests a ring of combustion surrounding a smaller fuel rich core. The right half of Fig. 31 shows the intensity coefficient of variation (CoV), which is the standard deviation of intensity normalized by the mean intensity. The time steps shown in Fig. 31 (B) match those reported in [2]. It should be noted that this imagery is integrated over the entire spectral response of the camera, nominally $1800\,\mathrm{cm}^{-1}$ to $6667\,\mathrm{cm}^{-1}$, whereas in [2], a filter was used to limit the bandwidth of the measurement to $3460\,\mathrm{cm}^{-1}$ to $3774\,\mathrm{cm}^{-1}$. This, along with natural variations in the flame, and color scale differences may contribute to any variations in comparing data here to [2]. Buoyancy effects and shear forces produce necks and bulges causing the vortical structures seen in Fig. 31(B). The CoV map shows these pulsations are a factor throughout the flame, except directly above the pipe exit.

90
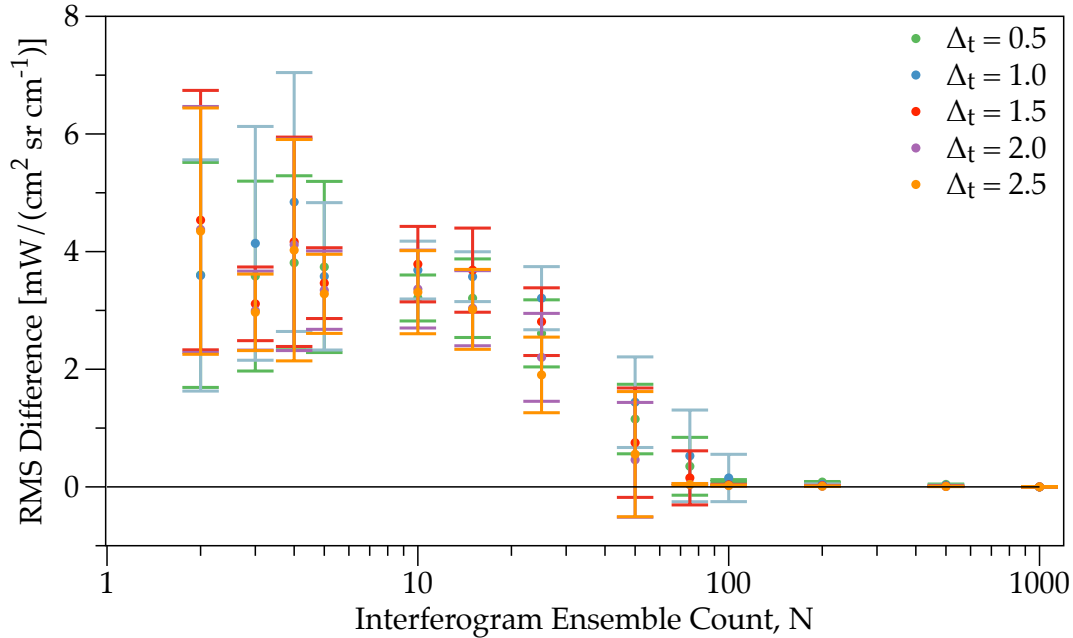
Figure 29. RMS difference between spectra reconstructed using 5000 interferograms and reconstructed spectra as a function of both N and Δ_t. Error bars are the standard deviation of 20 trials using random interferogram selection at each N.

In total, 780 interferometric cubes of the flame were acquired. Fig. 32 (A) shows five randomly selected interferograms, taken at a $(u, v) = (1.0\,\text{cm}, 4.5\,\text{cm})$ for $x < 0$. By measuring the mean time between all peaks in I^{DC} for each interferogram, the flame period was found to be $94.90 \pm 0.09\,\text{ms}$ ($10.54 \pm 0.01\,\text{Hz}$). The mean DC intensity profile for a single pixel, $I^{DC}(t)$, is shown in the top left inset of Fig. 32. This profile is the average shape between successive peaks of all y_m^{DC} measured at a height of 4.5 cm above the pipe and along the centerline. The reported uncertainty range represents one standard deviation of the mean value, $\sigma_{I^{DC}(t)}$. The mean slope profile for a single pixel, $dI^{DC}(t)$, is shown in the top right inset of Fig. 32. This profile is the derivative of $I^{DC}(t)$ measured at a height of 4.5 cm above the pipe and along the centerline. The reported uncertainty range also represents one standard deviation of the mean value, $\sigma_{dI^{DC}(t)}$.

91
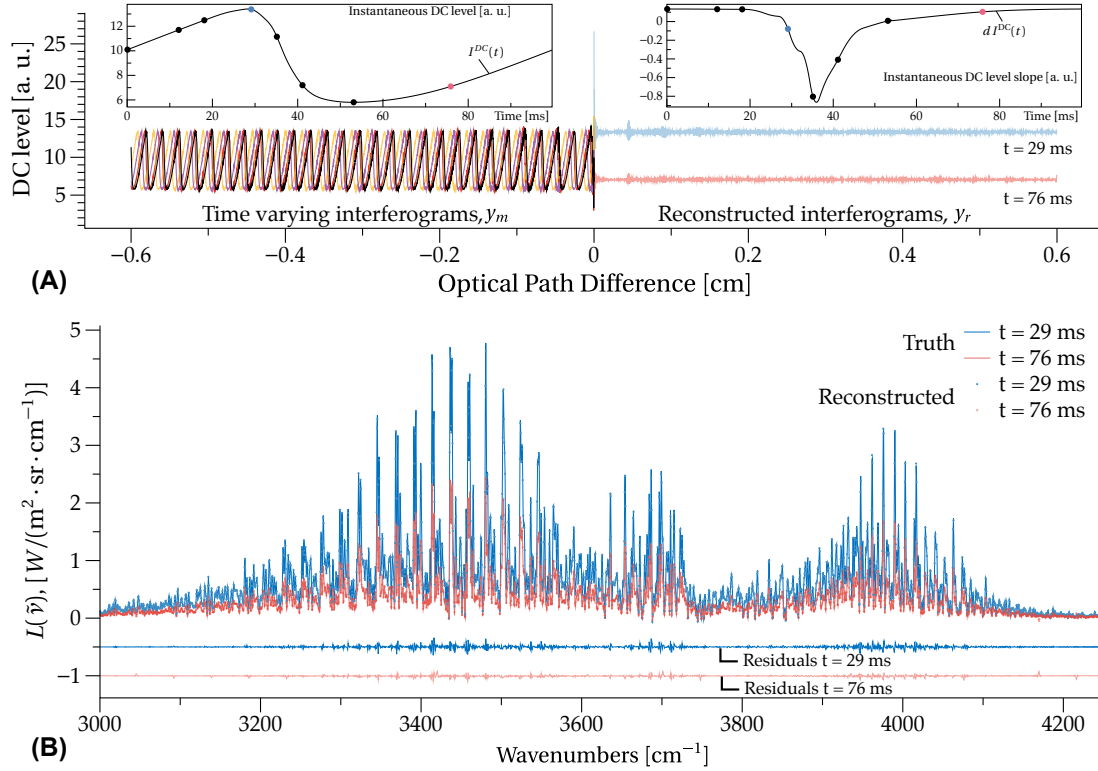
Figure 30. (A) *Center-Left*: **Time varying interferograms,** $y_m(x)$**, taken at** $(u, v) = (1\,\text{cm}, 4.5\,\text{cm})$ **of which 5 of 1000 are shown.** *Center-Right*: **Reconstructed instantaneous time interferograms,** $y_r(x, t)$**, at** $t = 4\,\text{ms}$ **and** $40\,\text{ms}$**.** *Top-Left*: **DC level as a function of flame period,** $I^{\text{DC}}(t)$**.** *Top-Left*: **Slope of DC level as a function of flame period,** $I^{\text{Slope}}(t)$**(B) Spectra associated with the truth and reconstructed interferograms at** $t = 4\,\text{ms}$ **and** $40\,\text{ms}$**. Residual differences are offset for clarity.**

Radiance profiles.

Using the algorithm outlined in Sec. 4.4 with $\Delta t = 5\,\text{ms}$, interferograms corresponding to each time in Fig. 31 (B) were recreated for every pixel in the full width of the flame, $4.5\,\text{cm}$ above the pipe. Two of these interferograms, corresponding to $t = 29\,\text{ms}$ and $76\,\text{ms}$ and $u = 1\,\text{cm}$ are shown in Fig. 32 (A) for $x >= 0$. The corresponding spectra are shown in Fig. 32 (B).

Measured integrated LOS radiance profiles of the flame periodic motion are shown in Fig. 33 and are compared with infra-red camera measurements reported in [2], as well as UNICORN simulated results. The reported uncertainty represents the one standard deviation confidence interval and was calculated by performing the algorithm in Sec. 4.4 twice again, first with $I^{\text{DC}}(t) + \sigma_{I^{\text{DC}}(t)}$ and $dI^{\text{DC}}(t) + \sigma_{dI^{\text{DC}}(t)}$, and secondly with

92
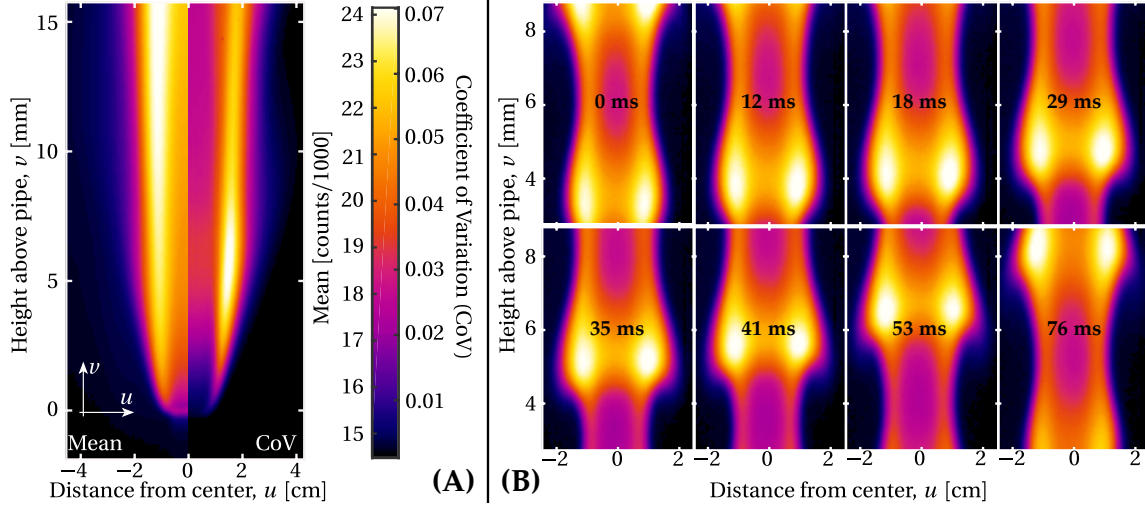
Figure 31. *(A)*: **Split imagery of the symmetric flame. Mean camera intensity is on the left and coefficient of variation (CoV) values are on the right.** *(B)*: **Instantaneous sequential imagery showing a complete period of the flame motion. The labels correspond to times between images in ms.**

$I^{\mathrm{DC}}(t) - \sigma_{I^{\mathrm{DC}}(t)}$ and $dI^{\mathrm{DC}}(t) - \sigma_{dI^{\mathrm{DC}}(t)}$. This provided a range in reconstructed spectra at a given time t_0 and therefore an indication of the uncertainty in the LOS integrated radiance. Error bars do not include any uncertainty due to systematic effects that may be introduced through uncertainty in the Δt value, calibration, camera optics, or the read-out circuitry of the detector.

In [2], radiation from the flame was recorded with a camera measuring radiation over the spectral band $3460\,\mathrm{cm}^{-1}$ to $3774\,\mathrm{cm}^{-1}$. Data over a 0.17 cm range about $v = 4.5\,\mathrm{cm}$ was averaged and data from $u < 0$ was averaged with $u > 0$ to improve SNR and to help mitigate any variations in the symmetry of the flame. In comparing to [2] then, only the spectral band from $3460\,\mathrm{cm}^{-1}$ to $3774\,\mathrm{cm}^{-1}$ (indicated in spectral axis of Fig. 32 (B)) was integrated over. Additionally, data from 4.48 cm to 4.62 cm (3 pixels) above the pipe was averaged and data about the centerline was also averaged.

Visually, IFTS results compare well with [2] at times 0 ms, 12 ms, 18 ms and 35 ms with mean differences of 15.5 W/m²sr, 8.1 W/m²sr, 9.7 W/m²sr and 12.7 W/m²sr respectively. These equate to 7.7%, 3.8%, 4.5% and 7.8% mean difference respectively. Time $t = 29$ ms shows the largest mean difference of 30.1 W/m²sr or 18.5%. Results at

93
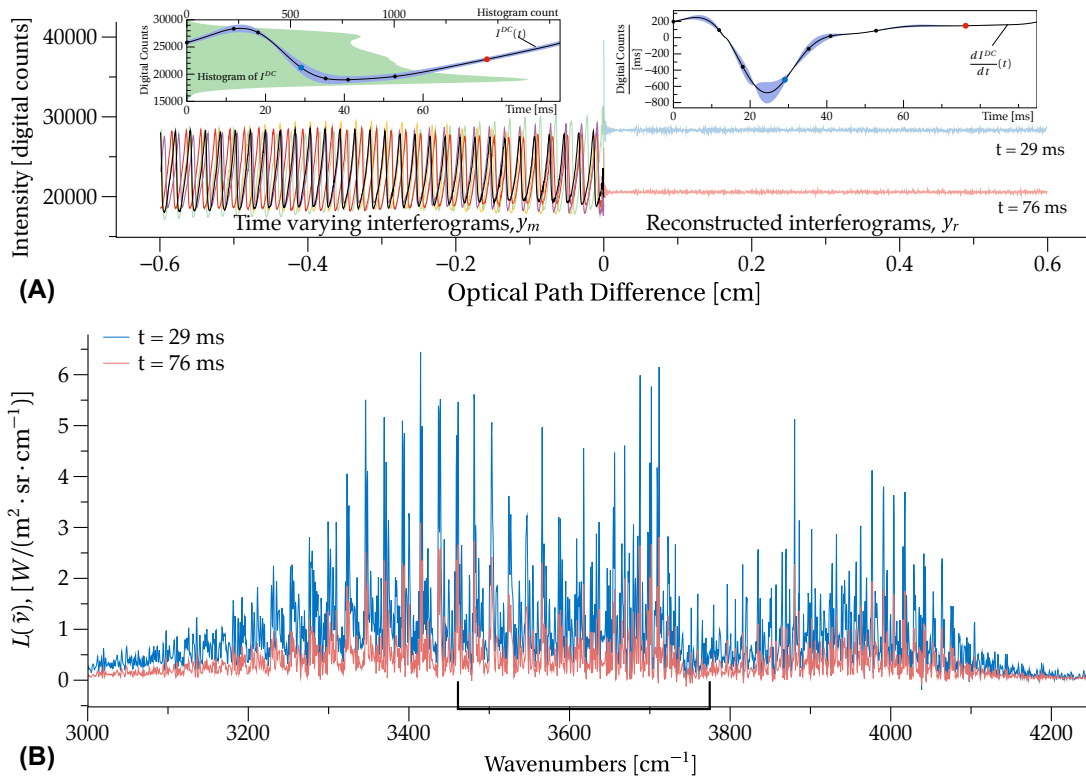
Figure 32. (A) *Center-Left*: **Time varying interferograms,** $y_m(x)$**, of which 5 of 780 are shown.** *Center-Right*: **Reconstructed instantaneous time interferograms,** $y_r(x, t)$**, at** $t =$29 ms **and** 76 ms**.** *Top-Right*: **DC level as a function of flame period,** $I^{DC}(t)$**. The highlighted range indicates the** $\pm 1\sigma$ **uncertainty range of the DC profile. (B) Spectra associated with the reconstructed interferograms at** $t = 29$ ms **and** 76 ms**.**

time $t = 29$ ms, however, compare more favorably to simulation results than the IR camera values. Measurements at times 18 ms, 29 ms, and 35 ms are systematically high for $x < 1$ cm, with a maximum deviation of 27.5 W/m^{2}sr (11.1%) at $(u, t) = 0.35$ cm, 29 ms. Measurements at all times except 18 ms, 29 ms are systematically lower for $x > 1$ cm, with a maximum deviation of 54.3 W/m^{2}sr (35.6%) at $(u, t) = 1.1$ cm, 53 ms. These systematic deviations suggest a difference in overall amplitude of the integrated radiance between the two experimental data sets. There could be multiple factors contributing to the observed difference, for example inconsistencies in the fuel flow rate, flame period or uncertainties in reconstructed sample time. Differences in the atmospheric conditions and path-length of the two experiments could also contribute to the differences. It should also be noted that data reported in [2] represent a single flame period, whereas

94
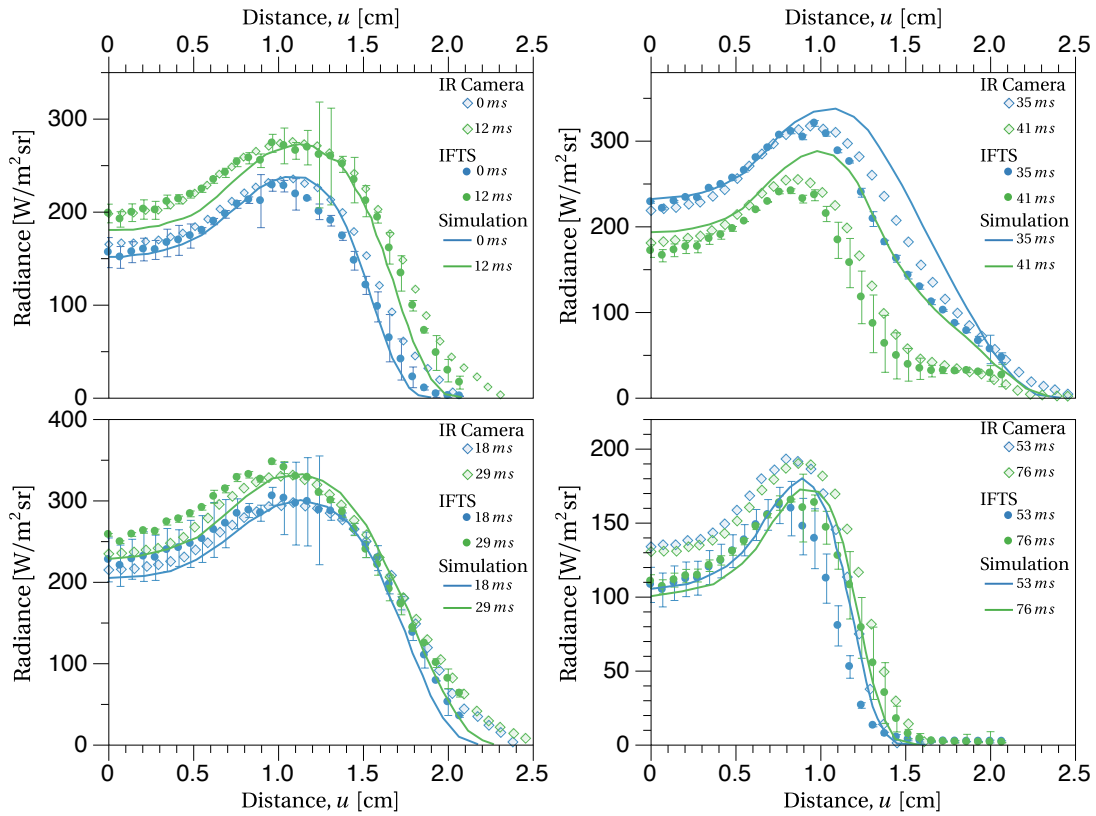
Figure 33. Comparison of reconstructed, previous experimental [2], and simulated LOS flame radiance profiles for several times in a single flame period at a height of $v = 4.5\,\mathrm{cm}$. Error bars represent the one standard deviation confidence interval.

the reconstructed snapshot spectra represent selective averaging of 780 interferometric measurements capturing more than 39,000 flame periods.

Note values at 29 ms and 35 ms show the narrowest uncertainty ranges. The I^{DC} profile in Fig. 32 (A) shows that these times are near the extrema in flame radiation. Extrema points like these are best reconstructed by the outlined algorithm as these times often have the most data points to draw from. This can be seen by the peak in the histogram of data measured for the pixel at $(u, v) = 1\,\mathrm{cm}$, 4.5 ms, shown in Fig. 32 (A). This added data has the benefit of a stronger weighted mean when rebuilding $y_r(x_i)$ at theses values in t. Uncertainties at all times are greatest near the flame edge. This is primarily due to lateral movement in the flame and natural variations in the width of the vortical structures seen in Fig. 31 (B).

95

4.7 Conclusions

Results of the reconstruction algorithm generated from theoretical data agree to 7% of truth values, demonstrating the validity of the algorithm. When applied to measurements of a real hydrogen flame, reconstructed lateral LOS radiance values agree at worst to within 18%, and at best to within 4% of previously reported values. There is a systematic difference in the amplitude of the radiance profiles as a function of the flame period. These differences may be due, in part, to differences in the flame setup or natural variations in the flame motion. The reconstruction algorithm, however, was able to recreate instantaneous radiance measurements that follow the same trends as previous values, both laterally and temporally. This shows great promise moving forward. Now, this reconstruction algorithm can be used in future IFTS measurements of any unsteady laminar flames with a repeatable periodic motion that is well below the detector cut-off frequency. Rather than simply averaging over many instrument scans to remove the effects of I^{DC}, the method described can utilize information available in an ensemble of measurements to reconstruct interferograms representative of instantaneous flame configurations. These recreations will lead to "snapshot" spectra that, when paired with an inversion process translating line-of-sight camera imagery into radial information, will yield scalar value maps in a full 4-D sense. Future research would also include a comparison of this TR-IFTS method to a step-scan IFTS when reliable step-scan IFTS instrumentation is available.

96

V. Inversion algorithm for retrieval of 3D scalar profiles in laminar flames using IFTS: Development and simulation

The following is a research paper, in its entirety, intended for published in Optics Express. It focuses on the development and validation of a retrival algorithm capable of reconstructing radial scalar values in laminar flames. Authors of this article will include Michael Rhoby, and Dr. Kevin Gross. The work is significant for the following reasons:

- It presents a novel technique for reconstructing radial scalar values in axisymmetric flames. A technique that uses all measured data simultaneously to improve on established methods.

- It lays groundwork for translating line-of-sight camera imagery into radial information that will yield scalar value maps in a full 4-D sense.

As first author I was responsible for data capture, reduction, and analysis, and the initial draft of the document. This chapter represents the satisfaction of objective 3.

5.1 Abstract

Inversion methods of emissions data for the axisymmetric scene case are in common use. Most, however, suffer from optically thin scene limitations, or compounding error that make flame-center estimates difficult. By capturing spatially resolved 2D spectra of a scene, IFTS is well suited for tomographic inversion techniques of emission measurements. Here, a method is described that uses these advantages to measure radially resolved scalar values in simulated laminar flames. Empirical functions describe the scalar value decay to atmospheric conditions, improving starting estimates for an onion-peeling process. A three-point, sliding onion-peel inversion provides a fast and flexible, yet reliable estimation of the radial scalar profiles. A global parameter

minimization uses all available LOS data. Three test profiles, simulating the time-averaged radial scalars of a premixed ethylene and non-premixed hydrogen flame, were created from CFD calculations. The inversion model was tested and validated against these simulated flame profiles. Results of the inversion agreed with truth to within 10% at worst, and at best to within 1%. The inversion successfully recreated the complex radial profiles of a diffusion flame. Additionally, it demonstrated sensitivity to trace species with low signal. Reconstructions of flame center were accurate, but uncertainties were still highest there. This work allows IFTS measurements to be extended from 2D spectra into 3D scalar values of all major combustion species.

5.2   Introduction

Laminar and axisymmetric flames are a common configuration used for instrument calibration, computer model development, and some practical engineering applications [27, 97]. Accurate radial scalar profiles of these flames are important for understanding combustion phenomenon, validating chemical kinetic models, verifying numerical simulations, and system performance estimate. Intrusive techniques such as thermo-couple and gas sampling [107, 108] can be used to obtain point value measurements. But this sampling interrupts the flow field, and mapping the full flame can be difficult. Laser techniques are effective, and are the current leader in combustion diagnostics [10, 97]. Laser techniques such as Raman scattering [109], coherent anti-Stokes Raman scattering (CARS) [110], and laser-induced fluorescence [109, 111] provide single species values at a point or a planar cross-section. Here again, mapping the full flame is difficult and multiple chemical species information requires several laser sources or a tunable laser [111]. Optical access for all the needed components can become challenging in an engineering application, and their delicate setups make them impractical beyond the laboratory environment.

98

Simpler emission and absorption techniques, both active such as LAS [19, 52] and passive such as IR-imaging [2, 30, 31, 112–114], are also common mapping techniques that are easier to implement. Here, an inversion process is required to retrieve radial scalar profiles from line-of-sight (LOS) emission or absorption measurements. The majority of inversions use variations on three methods [77, 78]. First are integral calculations, such as the inverse Abel transform, that compute radial emission of a flame given lateral, LOS projections (i.e. an image) [80, 113, 115]. While this method is the direct analytical solution to the cylindrically symmetric inversion problem, it is rare for emission data to be inverted by the Abel transform. This is largely due to the method's limitation to optically thin emission only, and its sensitivity to noise [78]. Second, and the most common method, is emission tomography with inverse analysis, commonly referred to as onion-peeling [2, 52, 112, 114]. Here the flame domain is divided into homogeneous, concentric rings. Starting with the outer ring, a radiation model is optimized to fit the measured emission by adjusting that layer's temperature and species concentrations. This process is repeated for each successive layer, holding all previous layers fixed. Onion-peeling is a straight-forward technique and is capable in both optically thin and opaque flames. However, each successive layer measurement is dependent on the previous, and the outermost starting layers is often where SNR is the worst. Retrieval uncertainty due to noise and systematic errors is compounded with each layer making the flame center (often the point of most interest) difficult to estimate. The third method is computed tomography (CT) using measured data from a number of different look angles [19]. Using the Radon transform, the different projections can be reconstructed into an image of a flame cross-section. This technique has the advantage of working on asymmetric flames, but is sensitive to the total number of look angles used. Ma *et al.* [19] utilized CT methods and hyperspectral laser absorption spectroscopy to reconstruct temperature estimates of a flame cross-section. With six

projection angles, the reported cross-sections are represented by five averaged zones rather than a continuous distribution. To reconstruct a cross-section with high fidelity, a large number of projection angles is required and in engineering systems, more than one look-angle may be unfeasible.

A new emission spectroscopy combustion diagnostics (CD) technique using an imaging Fourier-transform spectrometer (IFTS) is being developed [67, 84, 116]. IFTS has been shown to effectively retrieve scalar value profiles in a steady, top-hat like, Hencken burner flame [82] where near homogeneity renders an inversion process unnecessary. In that work, the single-layer flame assumption was adequate near the base of the flame. This assumption, however, broke down higher in the flame and near the flame edge where it was concluded a multi-layer scalar profile was needed.

This work advances from [82] by developing a multi-layer retrieval algorithm for the estimation of radial scalar values in axisymmetric flames. Here, a variation on a traditional onion-peeling inversion is developed for IFTS data and validated agains computer simulated data sets. More specifically, the objectives of this work are as follows: (1) develop a computational fluid dynamics (CFD) generated lateral LOS hyperspectral data set for algorithm testing and validation; (2) detail the inversion retrieval process; (3) investigate the sensitivity and limitations of the retrieval process. This work is a key continuing step in the development of IFTS for reacting flow measurements and should serve as a benchmark for future applications of IFTS to study unsteady and turbulent flows.

5.3 Theory

In [82], homogeneous single-layer radiative transfer equations were used to describe the apparent LOS flame radiance, $L(\tilde{\nu})$. Here those equations are extended to the multi-layer radiative transfer problem. Under the assumption of a non-scattering source in

100

local thermodynamic equilibrium (LTE), the apparent LOS radiance along any path is given by

$$L(\tilde{\nu}, s) = L_0(\tilde{\nu}, T)e^{-\int_0^l \alpha(\tilde{\nu}, s)ds} + \int_0^l B(\tilde{\nu}, T(s'))\alpha(\tilde{\nu}, s')e^{-\int_{s'}^l \alpha(\tilde{\nu}, s')ds'} \tag{33}$$

where L_0 is any background radiation, $\alpha(\tilde{\nu}, s)$ is the wavelength dependent absorption coefficient and $B(\tilde{\nu}, T)$ is Plank's blackbody radiation at temperature T. Under the assumption of radial axis symmetry, the cross-section of a flame can be broken into a series of n concentric rings of uniform spacing, Δr, like that pictured in Fig. 34. Measured radiance at a LOS, m, is then described by a discrete form of Eq. 33

$$L_m(\tilde{\nu}, s) = L_0 \prod_{i=1}^n \tau_i(\alpha_i) + \sum_{i=1}^n \left(B(\tilde{\nu}, T_i)(1 - \tau_i(\alpha_i)) \prod_{j=i+1}^n \tau_j(\alpha_j) \right) \tag{34}$$

where the transmissivity, $\tau(\alpha)$, of the ith layer is governed by Beer's Law:

$$\tau(\alpha) = e^{-N \cdot l \cdot \sum_k \xi_k \sigma_k(\tilde{\nu}, T)} \tag{35}$$

Here, $N = P/(k_B T)$ is the number density, l is the layer path length, ξ_k is the kth chemical species mole fraction, and $\sigma_k(\tilde{\nu}, T)$ is its corresponding absorption cross-section, described below. Modeling LOS flame radiance under these assumptions is now a matter of accurately choosing values for T_i and ξ_i^k for all layers. For simplicity, the remainder of this work will refer to T_i and ξ_i^k jointly as the scalar profiles, S.

The absorption cross-sections of the gas-phase molecular species, k, are described by

$$\sigma_k(\tilde{\nu}, T) = \sum_j s_{k,j}(\tilde{\nu}_j, T)f_j(\tilde{\nu}) \tag{36}$$

where $s_{k,j}$ is the spectral line intensity of the jth rovibartional transition of the kth species.

101

f_j is a Voigt profile line shape term associated with the jth absorption line. Line width and a slight shift away from $\tilde{\nu}_j$ are dependent on temperature, pressure, and relative concentrations of gas species parameters. In computing the Voigt profile, pressure was held constant at 1 atm, and species are assumed dilute so that only broadening rates for dry air are used. Line mixing and continuum effects on the line shape were not included. In this work, the latest edition of the HITEMP extension of the HITRAN spectral database was used to compute the absorption cross-sections for H_2O, OH, and CO [18, 63]. Absorption cross-sections for CO_2 were calculated using the the latest CDSD-4000 database [90].

5.4   Simulated flame data

Radial profiles.

In this study a total of three radial scalar profiles were explored and are pictured in the inset images of Fig 35. All profiles were generated using a computational fluid dynamics (CFD) model, UNICORN. This is a time-dependent, axisymmetric mathematical model that solves the full Navier-Stokes equations written in a cylindrical-coordinate system. Further details on the UNICORN model and its many applications is available in the literature [27, 71, 99, 100, 106]. Profile sets 1 and 2 represent the time-averages radial scalar profiles of a pre-mixed, $\Phi = 2$, ethylene/air flame with a total flow rate of 8 standard liters per minute (SLM) issuing from an 8 mm inner diameter pipe. Set 1 is taken at a height of 10 cm above the pipe and set 2 is taken at a height of 3 cm above the pipe. Profile 3 shows the time-averaged radial scalar profile of a diffusion hydrogen flame simulating 34 SLM of H_2 issuing from a 8 mm inner diameter pipe at a height of 4.5 cm.

These data sets provide realistic scalar profiles on which to validate the retrieval. Profile 1 has high temperature and scalar values at the flame center and relatively

102
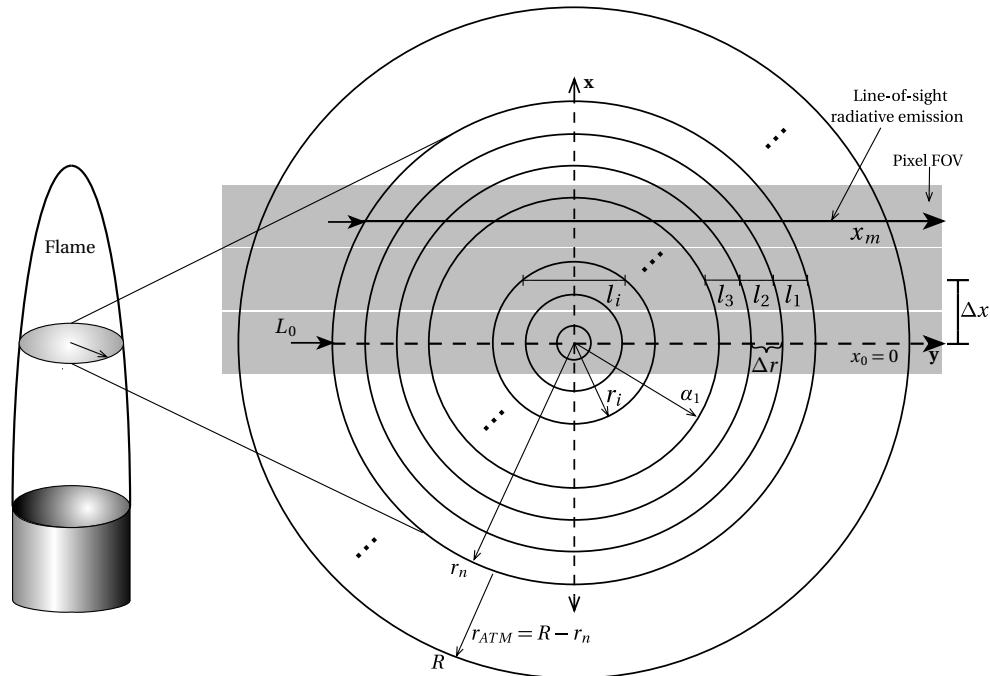
Figure 34. Multi-layer radiative transfer parameters on a horizontal cross-section of an axisymmetric flame. Note that $R >> r_n$

simple scalar profile shapes. Profile 1 is, therefore, a benchmark test subject. Profile 2 challenges the retrieval with a flame center where the temperature and major species concentrations are very low. This is a difficult retrieval situation for any emission based inversion, as radiation born at the flame center is minimal and is attenuated by the rest of the flame. Also, the complex shape is a complicated profile to reconstruct. Profile 3 is free of carbon emission species such as CO_2 and CO. These species have a relatively short mean free path of a photon making estimations of flame center difficult. Without them, estimations of concentration and temperature at the flame center are more probable. The mean free path of a photon in a given homogenous layer is given by

$$l_{\text{mfp}} = \frac{1}{N \sum_k \sigma_k(T, \tilde{\nu})\xi_k} \tag{37}$$

and provides a value for the mean distance a photon at wavenumber $\tilde{\nu}$ will travel before being absorbed. If this value is less than the half-width of the flame, then photons born

103
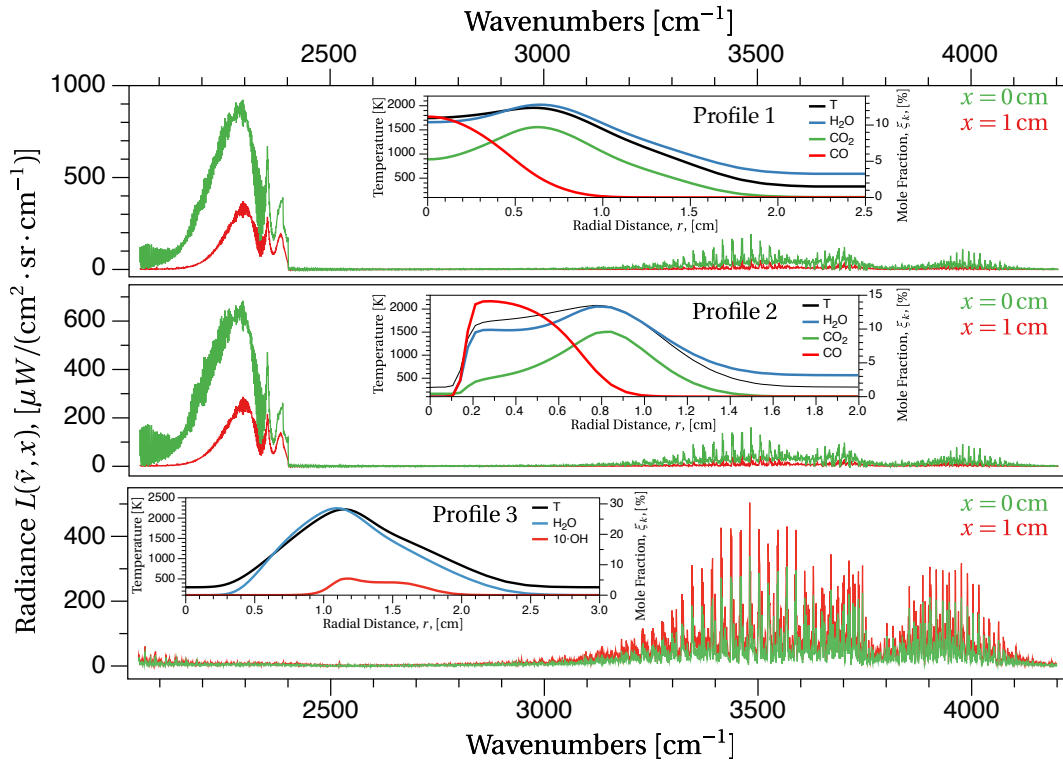
Figure 35. Simulated spectra of the three test profiles. Spectra shown are taken at $x = 0\,\text{cm}$ and $x = 1\,\text{cm}$. **Radial scalar values of the three test profiles are also provided in the inset figures.**

in the center of the flame will likely never reach the detector in quantities sufficient for a retrieval inversion. Eq. 37 shows that the mean free path is inversely proportional $\sigma(T, \tilde{\nu})$. Fig. 36 shows values of $\sigma(T, \tilde{\nu})$ at $T = 2000\,\text{K}$ for H_2O, CO_2, and CO. It is clear that the mean free path of H_2O emission will be much longer than those of CO_2 and CO emission under flame conditions. Note this is only a demonstration that the mean free path of H_2O emission is longer than CO_2 emission, and not an actual calculation of l_{mfp}. Profile 3 has the trace species, OH, which contributes very little to the overall radiance of the flame. Profile 3, therefore, tests how the retrieval handles emission without a great diversity in optical depth, as well as the ability to capture trace species. It is the intent that, with this diverse group of theoretical yet realistic test profiles, any conclusions should be applicable to other smooth radial profiles.

104
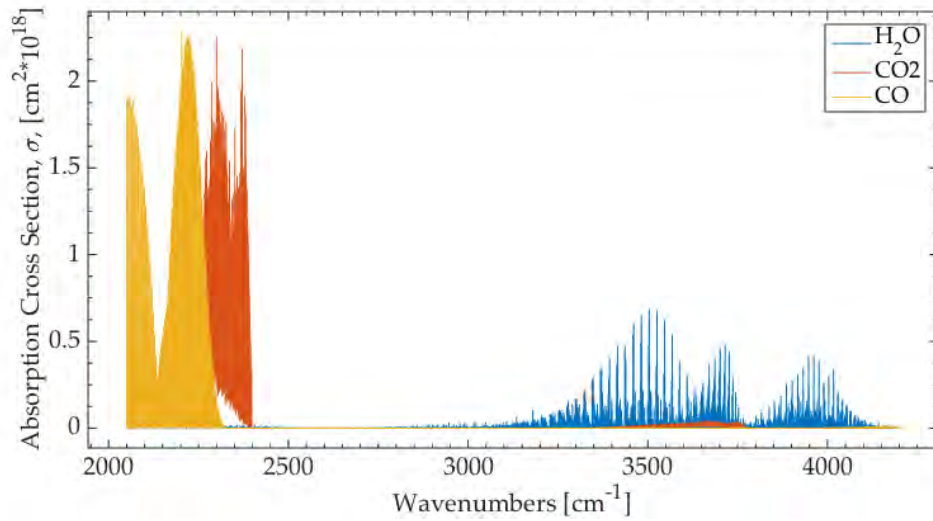
Figure 36. Absorption cross sections of H$_2$O, CO$_2$, and CO taken at 2000 K.

Line-of-sight spectra.

Using the radial profiles in Fig. 35, together with Eq. 34 and the conventions estab-

lished in Fig. 34, simulated line-of-sight spectra were generated. Spectra at $x = 0$ cm

and $x = 1$ cm for each profile are shown in Fig. 34. For each profile set, 1800 radial layers

were used. A large number of layers has the effect of minimizing any discretization

error associated with the transition from the integral form, Eq. 33, to the discrete form

radiative transfer equation. The first 1500 layers extend from flame center to $r_n = 12$ cm,

for a Δr of 0.08 mm. The final 300 layers extend from $r_n = 12$ cm to $R = 50$ cm, for a Δr

of 1.26 mm and represent the atmospheric path between the flame and a detector. Note

that, as seen in Fig. 34, $r_1 = \Delta r/2$ and $r_2 = 3\Delta r/2$ etc. The spacing of the line-of-sight

spectra, $\Delta a = \Delta x$, was set at 0.07 cm, a realistic at-scene, single-pixel, field-of-view of

an IFTS camera with a 50 cm stand-off distance. In total, 65 line-of-sight spectra were

generated starting at $x = 0$ cm and extending out to $\pm x = 2.3$ cm. Differing amounts of

Gaussian noise were added to each LOS spectra producing SNR values of 300, 250, and

60 for Profiles 1, 2, and 3 respectively. SNR here is defined by the RMS of the data divided

by the RMS of the noise. These values were chosen to match real IFTS measurements of

105

www.manaraa.com

similar flame conditions. After the addition of noise, data from $x < 0$ was averaged with data $x > 0$, resulting in a final total of 33 LOS spectra ranging from $x = 0\,\text{cm} - 2.3\,\text{cm}$. Also, the simulated radiance is convolved with, $\text{ILS}(\tilde{\nu}) = 2\pi a\,\text{sinc}(2\pi a \cdot \tilde{\nu})$, which represents the instrument line shape function of a Fourier-transform spectrometer [86, 89]. A spectral resolution of $1\,\text{cm}^{-1}$ was used, which is the full-width at half-max of the convolved sinc function and is set using a value of $a = 0.6\,\text{cm}$. This was chosen for its balance between computational speed and the ability to resolve rotational structure in the spectra.

5.5 Inversion Algorithm

Here, the inversion algorithm for estimating radial scalar profiles from hyperspectral lateral radiation is outlined. The algorithm is based on a combination of a variation on onion peel inversion, followed by a direct optimization of all scalar parameters simultaneously. The description of the algorithm is broken into sections, representing the major steps in the retrieval process.

Defining radial layers.

As stated in Sec. 5.4, the number of layers, n, used to define the flame has a substantial impact on the retrieval process. As $n \to \infty$ the discretization error approaches zero removing systematic error. The total number of layers used, however, is a large driving factor in the computational time needed to solve Eq 34. A balance between minimizing discrete sampling error and system performance is, therefore, important. Note that the distance from $r = 0$ to R can, and ideally should, be broken into two sections with different value of Δr, with smaller evaluation point spacing in regions where the scalars exhibit large radial variation. It is clear from the radial profiles in Fig. 35 that, for $r > 3.5\,\text{cm}$, the scalars have decayed to their atmospheric conditions,
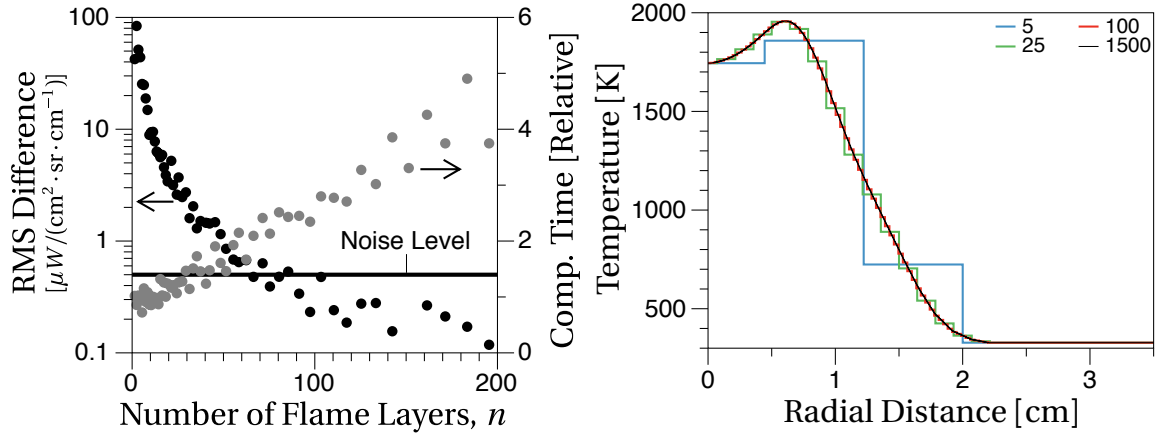
Figure 37. *Left*: **Comparison of the RMS difference between a spectra generated with $n = 1500$ layers, and spectra generated with increasing values of n. The relative computational time needed to generate one LOS spectra is also shown as a function of n. The RMS value of a typical noise value is shown for comparison.** *Right*: **The radial temperature scalar values of Profile 1 as best represented by 5, 25, 100 and 1500 layers.**

S^{ATM}. In the remainder of this work this portion will be referred to as the atmospheric layers and $r <= 3.5\,\text{cm}$ as flame layers.

The left half of Fig. 37 shows that, for Profile 2, the RMS difference between the highly layered "truth" spectra ($n = 1800$) and spectra generated with fewer layers drops below the noise level near $n = 100$. The computational time is over twice that of a single layer, but is on the order of $0.5\,\text{s}$ for a single LOS. The right half of Fig. 37 shows visually that $n = 100$ can adequately reconstruct the radial temperature of Profile 2.

Owing to these results, during the reconstructions presented here, each profile set is modeled with 100 flame layers and 3 atmospheric layers. The flame layers extend from flame center to $r_n = 3.5\,\text{cm}$, for a Δr of $0.35\,\text{mm}$. The final 3 layers extend from $r_n = 3.5\,\text{cm}$ to $R = 50\,\text{cm}$, for a Δr of $15.5\,\text{cm}$.

Atmosphere and flame edge.

A fundamental drawback of the onion-peeling technique is the need to start at the outer edge of the flame, r_n, where the SNR is often poor. Systematic error in the estimate of these layers will propagate inwards, limiting the likelihood of a successful

retrieval at areas of more interest. To mitigate this problem, the algorithm presented here initiates the onion-peeling process at an evaluation point, $r_i < r_n$. This point will be referred to as α_1 henceforth. Initially, α_1 is set by locating a point where the SNR of $L(\tilde{\nu})$ exceeds a desired level; an SNR of of 5 is used in this work (in a later step, each scalar profile will have its own optimized α_1). This approach utilizes the empirical observation that $S(r)$, in laminar flames, decay smoothly and asymptotically to S^{ATM}, something demonstrated in Fig. 35. All layers that comprise the decay of the flame to atmospheric conditions, $r_i > \alpha_1$, are modeled using a Logistic function for each scalar. This function is an empirical approximation to the shape of the flame edge, but was found to be a better approximation than an exponential or Gaussian decay. The Logistic function for each scalar, $S(r)$, is given by:

$$S(r_i > \alpha_1) = \frac{S^{Max}}{1 + \exp(\kappa \cdot (r_i - r_0))} + S^{\text{ATM}} \tag{38}$$

Here, κ is the steepness of the decay, r_0 is the r value of the sigmoid's midpoint. S^{Max} is the upper asymptotic limit of the curve and is solved for directly using the scalar value estimates at $r_i = \alpha_1$

$$S^{Max} = \frac{S(\alpha_1) - S^{\text{ATM}}}{1 + \exp(\kappa \cdot (\alpha_1 - r_0))} \tag{39}$$

By fixing $r_0 = \alpha_1$ and by fixing S^{ATM} to known values, the edge of the flame can be modeled through only two parameters, κ and $S(\alpha_1)$, for each scalar value. The choice to fix $r_0 = \alpha_1$ is not mandatory, but allowing r_0 to be an adjustable parameter adds additional computational time and was found to have little benefit to the fidelity of the reconstruction.

To solve for these parameters, all LOS measurements where $x \geq r_s$ are modeled using Eq. 34 and the scalar values at each layer defined by Eq. 38. Parameters are optimized

by minimizing the sum of squared differences between the simulated data ("observed" data), $L_{obs}(\tilde{\nu}, x)$, and modeled data, $L_{mdl}(\tilde{\nu}, x)$. This is done by first using a bounded Nelder-Mead search followed by a Jacobian based Levenberg-Marquardt search.

Onion Peel.

Once the flame edge has been modeled, the algorithm reverts to a more traditional onion peel approach. Moving inward along r from α_1, a new evaluation point, α_2, is chosen for interrogation. Now, all LOS spectra where $x \geq \alpha_2$ and $x \leq \alpha_1$ are used, and the parameter set includes $S(\alpha_2)$ and $S(\alpha_1)$. The starting estimate for $S(\alpha_2)$ are set at the values of $S(\alpha_1)$. Parameter optimization is now done using only a Levenberg-Marquardt search. Note that this process includes parameters that have been previously solved. This is done to minimize the chance of a parameter settling to a local minima in the search. Also note that the spacing, $\alpha_2 - \alpha_1 = \Delta\alpha$ needs to be $\geq \Delta x$, or no additional LOS spectra would be included and the new measurement would be redundant. Any radial layers that fall between evaluation points are assigned values using piecewise cubic Hermite polynomial interpolation (PCHIP). Here it is important to emphasize that the evaluation points, α_i, are locations where the scalar field values $S(\alpha_i)$ are directly estimated as fitting parameters. Locations between $S(\alpha_i)$ are estimated through interpolation. α_i locations do not need to correspond to LOS measurement locations, x_i, but the spacing $\Delta\alpha \geq \Delta x$.

Moving inward, the next evaluation point is defined as $r_i = \alpha_3$. For the purposes of this test $\Delta\alpha$ is fixed, but this condition is not a requirement. At this next location the parameter set includes $S(\alpha_3)$, $S(\alpha_2)$ and $S(\alpha_1)$ with the starting estimate of $S(\alpha_3)$ set to the previous results of $S(\alpha_2)$. Again, a Levenberg-Marquardt search is used to optimize the parameter values using all LOS data where $x \geq \alpha_3$ and $x \leq \alpha_2$.

This process is repeated for m evaluation points such that $\alpha_m = 0$ and the full radial

109

profile of the flame is defined. Note each inward step includes the parameters of the new evaluation location as well as the previous two locations, i.e the final optimization includes the parameters $S(\alpha_m)$, $S(\alpha_{m-1})$ and $S(\alpha_{m-2})$. This process is referred to here as a three-point sliding onion-peel. It was observed that using more than three sliding points unnecessarily added to the computational time of the inversion and using less than three sliding points may result in parameter solutions that succumb to a local minima solution.

Full parameter optimization.

The final results of the three-point sliding onion-peel are used as the starting estimate for a final error minimization step. First the location of α_1 is optimized for each radial scalar profile, α_1^S. Profile 1 in Fig. 35 shows that the point where a Logistic function adequately describes the decay to atmosphere for temperature may be around $\alpha_1 = 1.25\,\mathrm{cm}$. At this point, however, the concentration of CO has already reached atmospheric conditions and $\alpha_1 = 0.6\,\mathrm{cm}$ would be more appropriate. Without *a priori* knowledge of the radial profiles it is difficult to assign a unique α_1 value to each scalar. With the results of the three-point sliding onion-peel, however, α_1^S can be set to where $S(r)$ reaches some fraction of its maximum value. In this work, that value is set to 25%.

Once all α_1^S are set, a Levenberg-Marquardt search is done over all parameters simultaneously; those of the Logistic edge estimation included. This has the advantage of utilizing all the measured data for a global solution of the radial scalar profiles.

5.6 Results and discussion

Profile 1.

Fig. 38 show the comparison of the true and reconstructed radial scalar values of Profile 1. Here, a spacing of $\Delta\alpha = 2\Delta x$ was used. Overall, the retrieval agrees well with

110
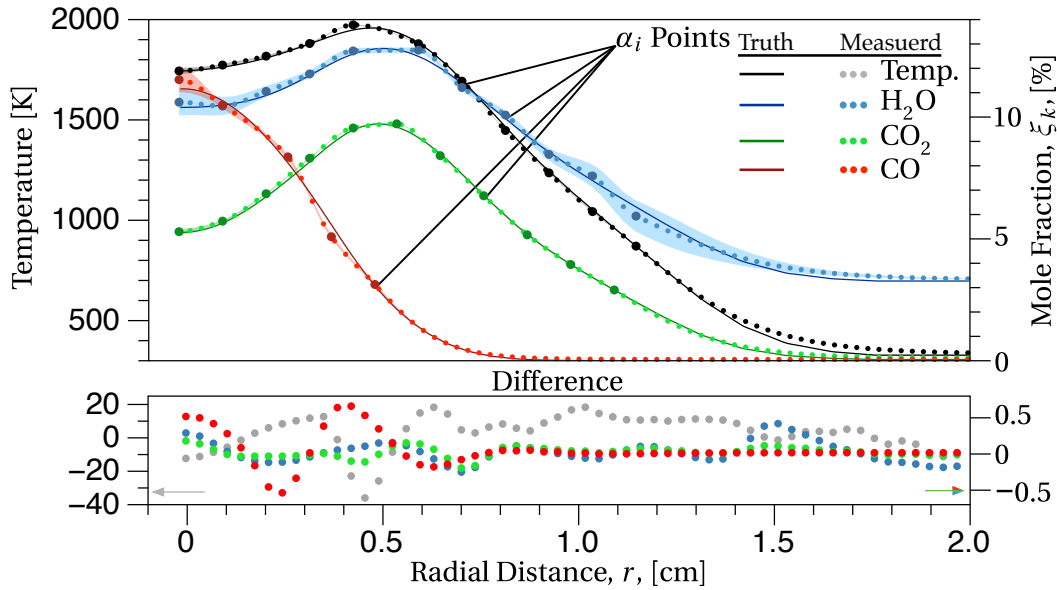
Figure 38. Results of the inversion algorithm for Profile 1. In this trial, $\Delta \alpha = 2 \Delta x$ was used. Shaded regions represent the 95% confidence interval of the retrieval.

truth values. The largest deviation, 8%, occurs at $r = 0.5$ cm in the CO profile. The average difference is 1.5%, 1.5%, 0.8%, and 2.8% for temperature, H_2O, CO_2, and CO respectively. Note that, seen most notably in the temperature and H_2O reconstruction, the Logistic function may be incapable of capturing the exact shape of the decay to atmosphere. In the H_2O profile, the Logistic function has a less-sharp curvature than the truth profile. Despite this, the residual difference between truth and modeled spectra, pictured in Fig. 39, shows no structure. This suggests that either the model is insensitive to the fitting parameter κ; or the edge region of the H_2O profile has less effect on the total radiance, and the difference between the truth and measured profile is below the noise of the data. This second possibility is a trend supported by the estimated uncertainties also pictured in Fig. 38.

Uncertainties were calculated by adjusting each fitting parameter individually until the difference of the modeled radiance, $L(\tilde{\nu}, x)$, and the adjusted model radiance $L'(\tilde{\nu}, x)$ exceeds 2σ at any $(\tilde{\nu}, x)$. Here, 2σ is twice the RMS value of the noise in each LOS measurement. These ranges for each α_i were treated as the 95% confidence interval and were used to build a Gaussian distribution of possible values at each α_i. Then a Monty

111

www.manaraa.com
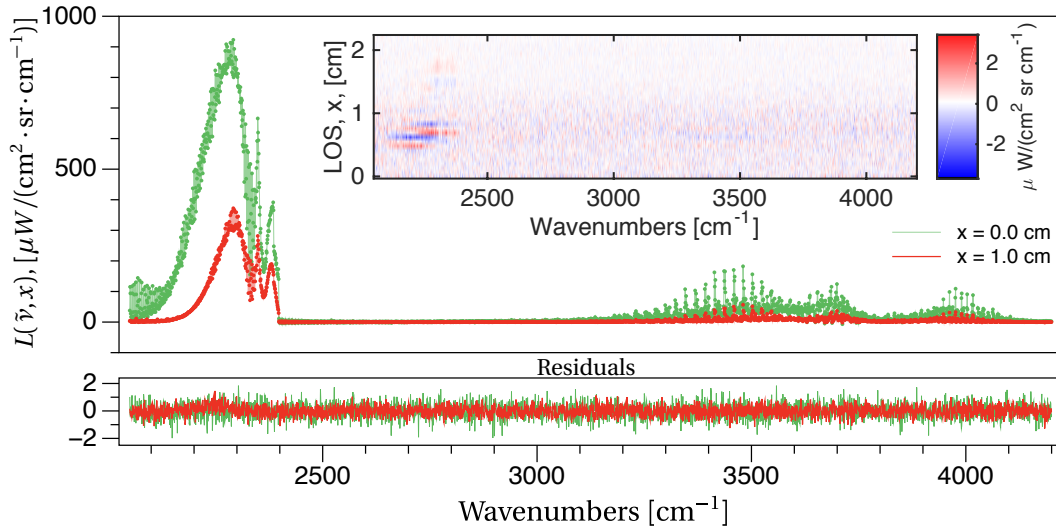
Figure 39. Comparison of simulated truth spectra and modeled LOS spectra for LOS $x = 0\,\mathrm{cm}$ and $x = 1\,\mathrm{cm}$ for Profile 1. The residual differences between truth and model for the selected LOS's is provided. A complete map of the residuals is also provided in the inset image.

Carlo method was used to randomly generate 1000 $S(r)$ profiles. The shaded regions shown in Fig. 38 represent twice the standard deviation of the $S(r)$ ensemble at all r. This method finds the point where an adjustment in a parameter makes a significant change to the modeled spectra. Note that it does not account for any correlation in error between parameters. The overall uncertainty, is therefore, likely higher at every point. Using a Levenberg-Marquardt search does generate a covariance matrix. This, however, provides the statistical certainty in each parameter which is a function of the total data points available. With 33 LOS spectra each composed of over $8,000$ spectral points, the confidence interval estimated using the covariance matrix is on the order of $\delta T \sim 0.5\,\mathrm{K}$ and $\delta \xi_k \sim 10^{-4}$ and is not a realistic estimate of uncertainty. Any coarseness in the uncertainty estimate profiles is a result of the PCHIP interpolation between α_i, and the true uncertainty is likely smoother.

The uncertainty is highest overall for H_2O. This is primarily due to the high 3% composition of H_2O in the simulated atmosphere. This generates more atmospheric absorption than the other chemical species making H_2O less detectable in general. As noted before, the edge of the H_2O profile has the lowest effect on the radiance of the

flame. The center of the flame is a point of high uncertainty in H_2O, a trend also seen in the rest of the scalars. This is primarily due to the attenuation of signal as it passes through the rest of the flame.

Uncertainty in temperature is lower relative to the chemical species. Radiance increases with temperature following Plank's law. An increase in temperature from 1500 K to 1600 K, a 6.7% increase, will increase the radiance of a greybody by a factor of 30% at 4200 cm^{-1}. With the error estimation method described, this non-linear relationship between temperature and radiance contributes to tight error estimates on the temperature profile. Additionally, the relative line heights of the rotational fine structure seen in the spectra is governed by temperature through the Boltzmann distribution. The wide spectral band at a high spectral resolution measured by IFTS captures emission from millions of such rotational lines, each governed by a single temperature. This yields a very overdetermined system and also contributes to the precision in temperature measurements.

Fig. 40 shows the comparison of the true and reconstructed radial scalar values of Profile 1, now using LOS generated with a SNR of 500 . The change in SNR does impact the fits overall, now with average differences of 0.8%, 0.9%, 0.7%, and 2.5% for temperature, H_2O, CO_2, and CO respectively. Fig. 41 shows the reconstructed radial scalar values using a SNR of 125. The average differences in this trial is 1.7%, 1.4%, 0.8%, and 2.5% for temperature, H_2O, CO_2, and CO respectively. For both these trials, the largest deviations occur again at $r = 0.5$ cm in the CO profile and in the temperature and H_2O Logistic function. The small variation in the retrieved scalar profiles over this range in SNR suggests that the retrieval algorithm is, to an extent, insensitive to changes in Gaussian noise. As a direct result of the definition used here for uncertainty, the uncertainly in each scalar profile does change with SNR. Note, however, that for all three trials the uncertainty range fails to encompass truth for the CO scalar at $r = 0.5$ cm. This

113
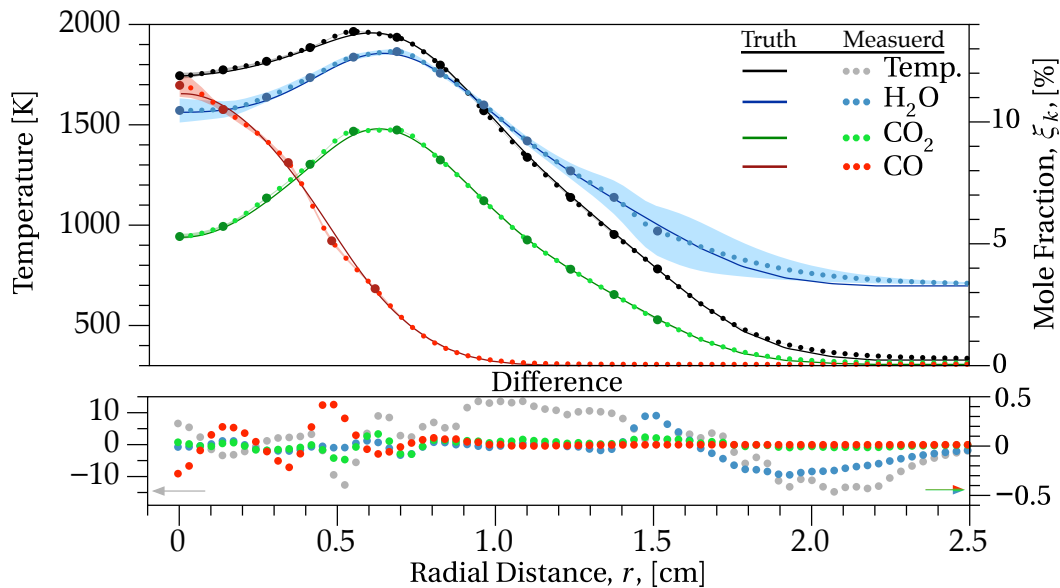
Figure 40. Results of the inversion algorithm for Profile 1. In this trial, the simulated data was given an SNR of 500. Shaded regions represent the 95% confidence interval of the retrieval.

indicates a systematic limitation in the retrieval that is most likely associated with the inability of either the Logistic function, or the PCHIP interpolation, to capture the true curvature of the profile.

Profile 2.

Fig. 42 show the results of the retrieval of Profile 2. Here, a spacing between evaluation points of $\Delta\alpha = 2\Delta x$ was used. The retrieval captures the shape of the radial scalar profiles very well for $r > 1.0$ cm. The sharp drop-off near $r = 0.1$ cm, however, is not reconstructed well for all scalars. The retrieval has a tendency to decay near-linearly to the center conditions rather than follow the true sigmoid shape of the drop-off. This deviation near the center is evident by structure in the residuals of the $x = 0$ cm spectra, shown in Fig. 43. Note there are no structured residuals in the $x = 1$ cm spectra. This spectra is defined using only scalar values of $r \geq 1$ cm, where the retrieval agrees well with truth. This is very useful, as the point where residuals first show structure can be used to locate where the retrieval is diverging from truth; something that is easily seen in the inset residual map in Fig. 43. The average difference between the reconstructed

114
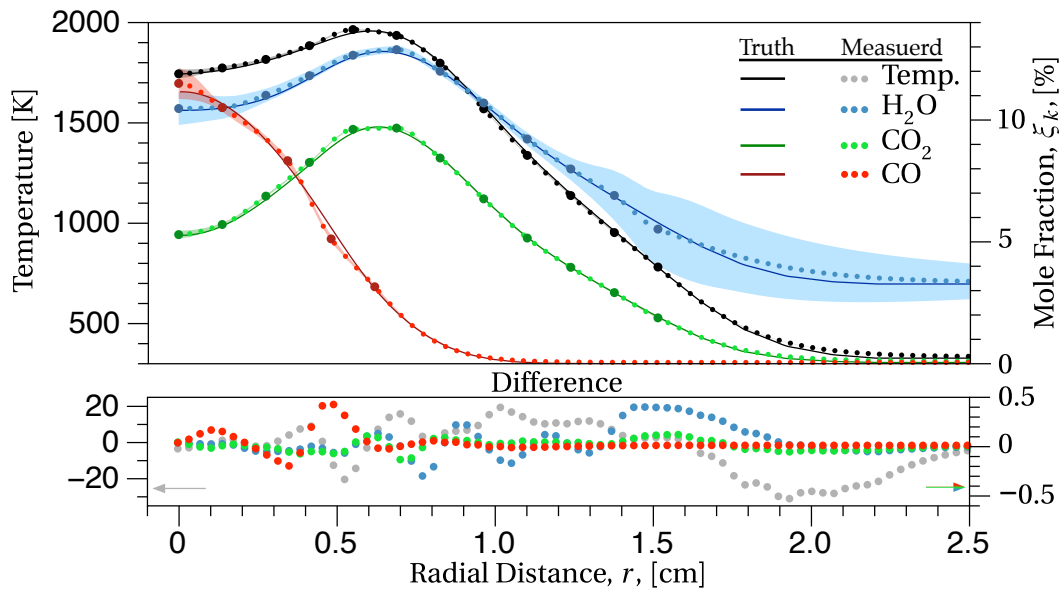
Figure 41. **Results of the inversion algorithm for Profile 1. In this trial, the simulated data was given an SNR of 125. Shaded regions represent the** 95% **confidence interval of the retrieval.**

and truth values for this profile are 4.5%, 6.9%, 7.9%, and 16% for temperature, H_2O, CO_2, and CO respectively.

The uncertainty at the center of the flame is again higher than elsewhere. The estimate in H_2O, for example, can be increased by over a factor of 8 before there is a noticeable change in the modeled radiance. This is a result of the combination of low temperature and low scalar values here. These atmospheric-like conditions ensure that most photons created in the flame center will be absorbed prior to reaching the detector. The uncertainty in CO_2 and CO, however, are relatively low at flame center. This is a result of how the uncertainty is determined. This is likely do, in-part, to the very low to zero concentration of these chemicals in the long atmospheric path.
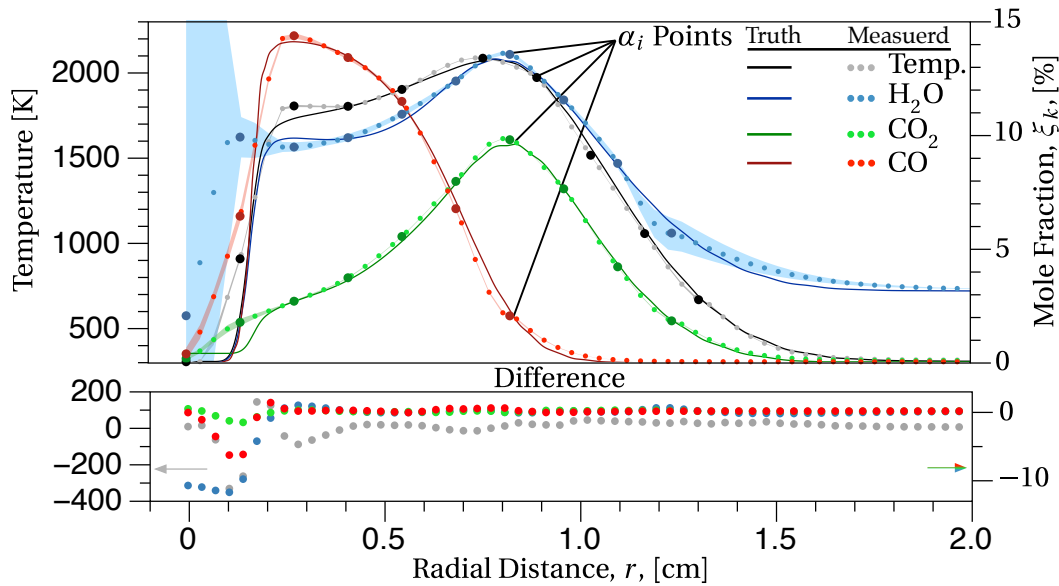
Figure 42. Results of the inversion algorithm for Profile 2. In this trial, a evaluation point spacing of $\Delta\alpha = 2\Delta x$ was used. Shaded regions represent the 95% confidence interval of the retrieval.
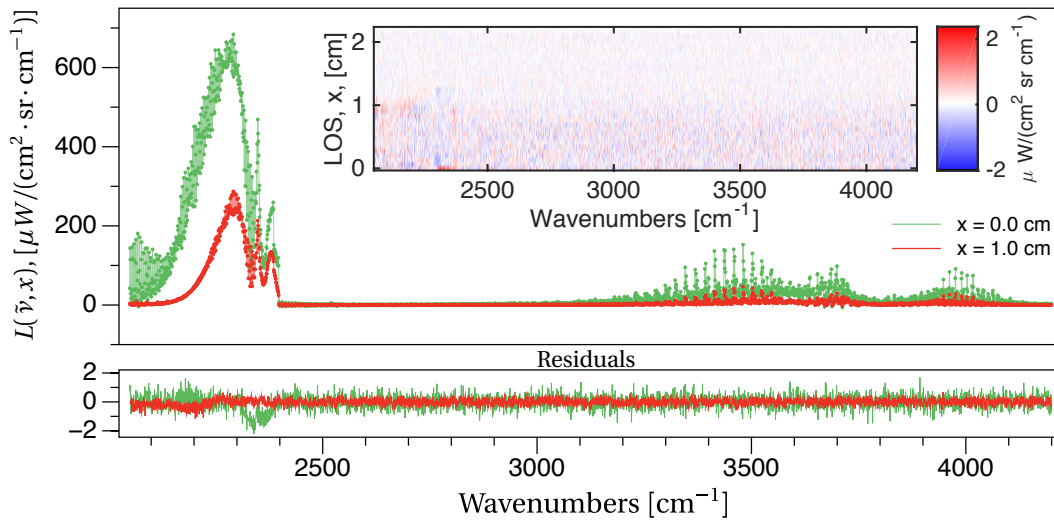
Figure 45. Comparison of simulated truth spectra and modeled LOS spectra for LOS $x = 0\,\text{cm}$ and $x = 1\,\text{cm}$ for Profile 2. The residual differences between truth and model for the selected LOS's is provided. A complete map of the residuals is also provided in the inset image.

To improve the retrievals ability to capture the true shape of the profile, more evaluation points can be used. Fig. 44 show the results of the retrieval of Profile 2 with a spacing between evaluation points of $\Delta\alpha = \Delta x$. Additional sampling shows a sig-

116
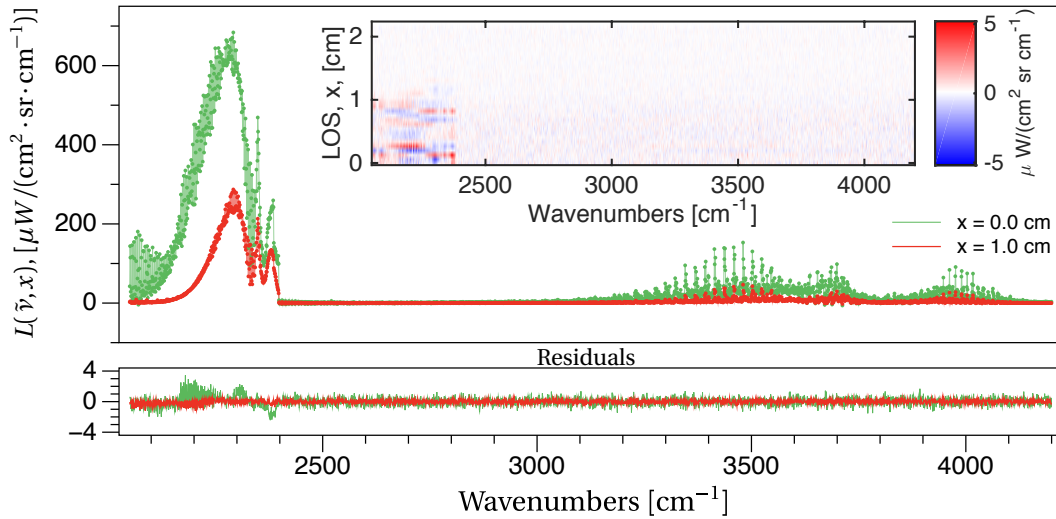
Figure 43. Comparison of simulated truth spectra and modeled LOS spectra for LOS $x = 0\,\mathrm{cm}$ and $x = 1\,\mathrm{cm}$ for Profile 2. The residual differences between truth and model for the selected LOS's is provided. A complete map of the residuals is also provided in the inset image.

nificant improvement in the retrieval in general, and in particular at $r \leq 0.1\,\mathrm{cm}$. The improvement is also evident in the reduction of structured residuals, seen in Fig. 45. The average difference is now 0.8%, 1.8%, 2.0%, and 6.7% for temperature, H_2O, CO_2, and CO respectively. This improvement does come at a cost. By decreasing the evaluation point spacing, the total number of testing locations, m, increased from 10 to 18, translating to an increase in computation time of 57% in the onion-peel stage. The total number of parameters being fit in the final stage of the algorithm increased from 45 to 80, equating to an increase in computation time of 263%. This is a total increase in computational time of 200%. A trade-off between the number of evaluation points and the desired accuracy of the retrieval is, therefore, important. Also, with more parameters to fit, the uncertainty in any one parameter becomes larger. This is evident in the increase in uncertainty of all profiles despite the better fit results. Note that the location and spacing of evaluation points can be changed as needed. Ideally, one or two additional evaluation points can be allocated to each scalar around $r = 0.1\,\mathrm{cm}$ to improve the sampling's spatial resolution where it is needed most. This prevents the need to add in many additional points needlessly at $r > 0.1\,\mathrm{cm}$. With no *a priori* knowledge of the

117
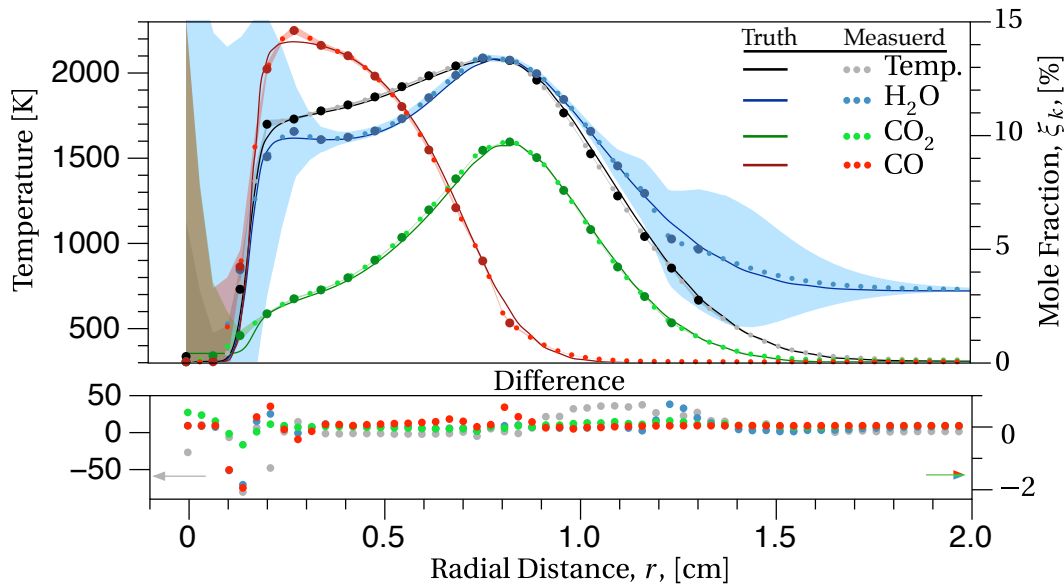
Figure 44. **Results of the inversion algorithm for Profile 2. In this trial, a evaluation point spacing of** $\Delta\alpha = \Delta x$ **was used. Shaded regions represent the** 95% **confidence interval of the retrieval.**

correct solution, however, choosing specific sampling locations is difficult. The use of an adaptive process to choose an ideal sampling point distribution would be beneficial, but is beyond the scope of this research.

Profile 3.

Fig. 46 show the results of the retrieval of Profile 3. Here, a spacing between evaluation points of $2\Delta\alpha = 2\Delta x$ was also used. The retrieval is able to captures the shape of the radial scalar profile of H_2O and the trace species, OH. Values of temperature at $r < 0.5$ cm, however, diverge from truth. With little chemical species at the flame center that have spectral emission in the measured band, an increase in temperature has little effect on the radiance. Fig. 47 shows that once again the difference between the truth and model spectra shows no structure. The average difference between the truth and modeled profiles is 9.1%, 2.9%, and 3.8% for temperature, H_2O, and OH respectively.
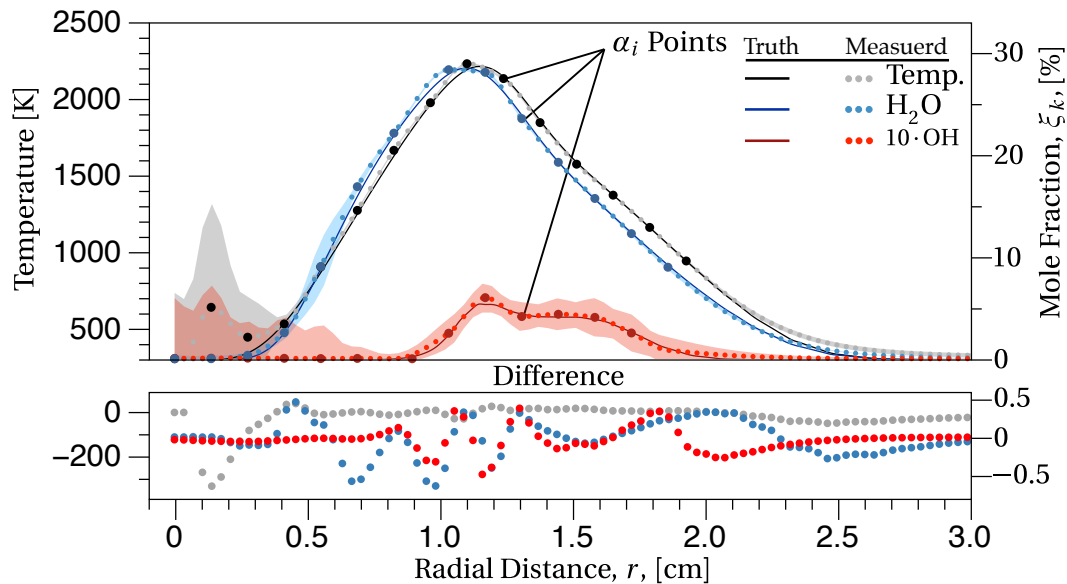
Figure 46. Results of the inversion algorithm for Profile 3. Shaded regions represent the uncertainty in the retrieval.

5.7 Conclusions

This investigation of simulated data has established a novel method to estimate radially resolved scalar values from lateral IFTS measurements in a subclass of flames. An empirical function was used to describe the scalar value decay to atmospheric conditions. This improves the starting estimate for an onion-peeling process and reduces the compounded uncertainty moving inward. A three-point sliding onion-peel provides a fast and flexible, yet reliable estimation of the radial scalar profiles. Finally, the addition of a global parameter minimization optimizes the shape of the radial profiles using all available data simultaneously. This is a significant advantage over a traditional onion-peel inversion.

Results of the inversion agreed with truth to within 10% at worst, and at best to within 1%. The inversion algorithm was able to recreate the complex radial shape of Profile 2 and was able to accurately retrieve the trace species OH in Profile 3. The inversion model does reconstruct the conditions of the flame center in all three profiles. But the uncertainty there shows the insensitivity of emission-based techniques to penetrate

www.manaraa.com
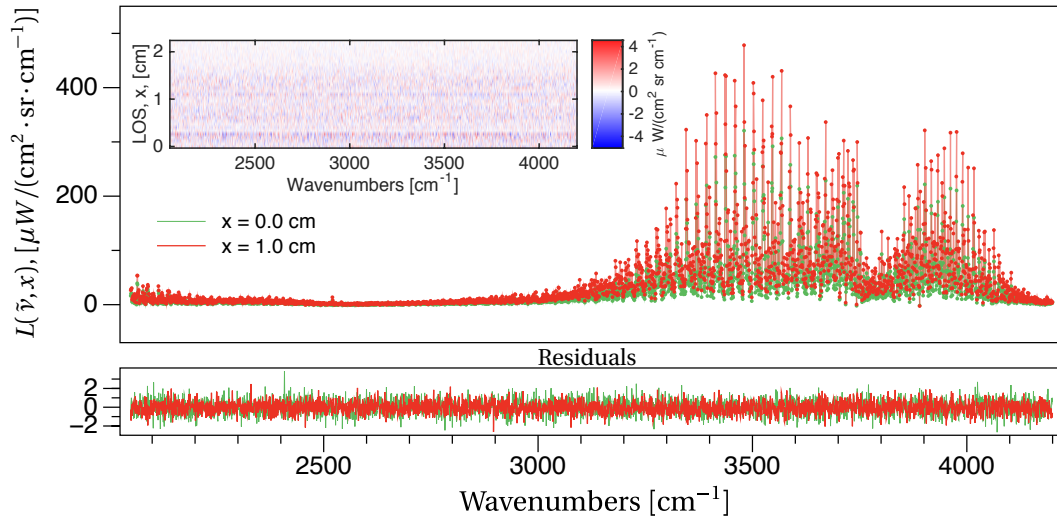
Figure 47. Comparison of simulated truth spectra and modeled LOS spectra for LOS $x = 0\,\text{cm}$ and $x = 1\,\text{cm}$ for Profile 3. The residual differences between truth and model for the selected LOS's is provided. A complete map of the residuals is also provided in the inset image.

to the center of a flame. Results also show that the Logistic function used to estimate the edge of the flame may not be the best choice and further investigation of other options is needed. Also, the automation of evaluation point locations would be a helpful improvement to the algorithm. Additionally, the uncertainty estimates of the radial profiles needs to be updated to a process that incorporates covariance of the fitting parameters.

This work is a major step forward in the use of IFTS as a viable combustion diagnostics tool. Rather than being limited to line-of-sight integrated scalar values. IFTS can now provide radially resolved scalar values of axisymmetric scenes. When paired with an algorithm that creates time-resolved spectra, future IFTS measurements of harmonically unsteady laminar flames can provide scalar value maps in a full 4-D sense.

VI. Time Resolved Radial Scalar Profiles of a Laminar Hydrogen Flame

6.1 Introduction

Chapters IV and V presented work that are key precursors to meeting the ultimate objectives of this work: (1) reconstructing instantaneous LOS spectra from an ensemble of IFTS measurements Chapter IV, and (2) recreating radial dependance of various scalars from LOS spectra in Chapter V. In this chapter, the two techniques are married together and applied to measured data of a pure hydrogen diffusion flame. Results here are presented in a more traditional manner and not as a document prepared for a journal. As such, and as much is previously covered, the fundamental theory and methodology are not explicitly outlined here. The focus in this chapter is presenting a successful demonstration of measured instantaneous scalar fields in a laminar unsteady flame using IFTS. This chapter is significant for the following reasons:

- It demonstrates that previously outlined techniques, developed using simulated data, are effective on real measurements.

- It shows IFTS is capable of providing instantaneous and spatially-resolved scalar fields in laminar flames.

- It solidifies IFTS is a useful diagnostic tool even for rapidly changing, yet harmonic scenes.

This chapter represents the satisfaction of all research objectives.

6.2 Methods

The results presented here combine the experimental data set of a H_2 flame, and time-resolved interferogram reconstruction algorithm described in Chapter IV with

121

the inversion algorithm described in Chapter V. therefore, only a brief review of the relevant points of each method and the data are repeated here.

First, the 780 measured data cubes were processed using the algorithm descried in Sec. 4.4; achieving time resolved interferograms of the flame. Again, the algorithm was applied to all data from the rows at 4.48 cm to 4.62 cm (3 pixels) above the pipe. When doing this time resolved reconstruction, note that the mean period of the flame motion is very important. As stated in Sec. 4.4, this profile is the average shape between successive peaks of all y_m^{DC} for a given pixel. This results in a mean period of the flame where the point of peak radiance is always defined to be $t = 0$. Fig. 48 (A) shows this by comparing measured $I^{DC}(t)$ for three different pixels. Shown in black is $I^{DC}(t)$ corresponding to the pixel $(u, v) = (0\,\text{cm}, 4.5\,\text{cm})$. In red is $I^{DC}(t)$ for pixel $(u, v) = (0.9\,\text{cm}, 4.5\,\text{cm})$ and green shows $I^{DC}(t)$ for $(u, v) = (1.6\,\text{cm}, 4.5\,\text{cm})$. It is clear that, even though the overall amplitude and shape of each $I^{DC}(t)$ may be different, they are all starting with their peak intensity at $t = 0$.

What is not stated in Sec. 4.4, is that each location u in the flame does not pass through its point of peak radiation in phase. This phase difference between the center-line $I^{DC}(t)$ motion and any other lateral $I^{DC}(t)$ profile is due, in part, to the diffusion of the fuel into the oxidizer and the sheer forces in the flame. Fig. 48 (B) shows this phase difference as a function of u. Note that positive values of the phase shift mean
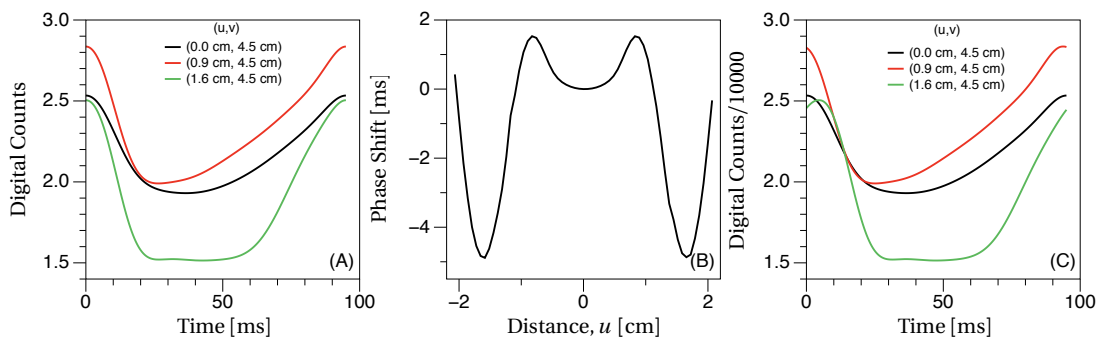
Figure 48. (A) Mean $I^{DC}(t)$ at three different values of u. (B) Phase shift in $I^{DC}(t)$ as a function of u. (C) Corrected mean $I^{DC}(t)$ at three different values of u.

122

that the point of peak radiation lag behind the center point, and negative values mean that the point of peak radiation come before the center point in time. Knowing and accounting for this phase shift is very important for a successful recreation of time resolved interferograms across the width of a flame. Fig. 48 (C) shows the same three $I^{DC}(t)$ now with their appropriate phase shifts added. Note that a phase shift of 1.2 ms does not make a large visible difference in the $(u, v) = (0.9\,\text{cm}, 4.5\,\text{cm})$ profile. A phase shift of -4.75 ms, however, makes a noticeable shift in the $(u, v) = (1.6\,\text{cm}, 4.5\,\text{cm})$ profile. Even when this shift is small it is vital in reconstructing interferograms at times where the slope, $dI^{DC}(t)$ is large. For example, the shift in $(u, v) = (0.9\,\text{cm}, 4.5\,\text{cm})$ moved the value at $t = 11\,\text{ms}$ by 3.6% compared to only 0.2% at $t = 0\,\text{ms}$. Once the relative phase shift between each u location is accounted for, the global phase can be changed to meet any convention. Note in Fig. 48 (c) that $t = 0$ was defined to match the point where the center of the flame passed through its point of peak radiance. In [2], however, $t = 0$ was defined to match the point where the flame's bulging motion was just beginning. To compare the reconstructed interferograms to [2] in Chapters V and later in this chapter, a phase shift of 29.89 ms was added to each $I^{DC}(t)$.

Following the reconstruction of time-resolved interferograms, the data was converted to spectra and calibrated using the method outlined in Sec. 3.4. The calibrated data from all three rows was then averaged together, and data from $u < 0$ was averaged with $u > 0$ to improve SNR and enforce symmetry. An estimation point spacing of $\Delta\alpha = 2\Delta x$ was used in the inversion process where here $x = 0.07\,\text{cm}$. The radial layers used match those described in Sec. 5.5, 100 flame layers extending out to $r = 3.5\,\text{cm}$ for a $\Delta r = 0.35\,\text{mm}$. The final 3 layers extend from $r_n = 3.5\,\text{cm}$ to $R = 50\,\text{cm}$, for a Δr of 15.5 cm.
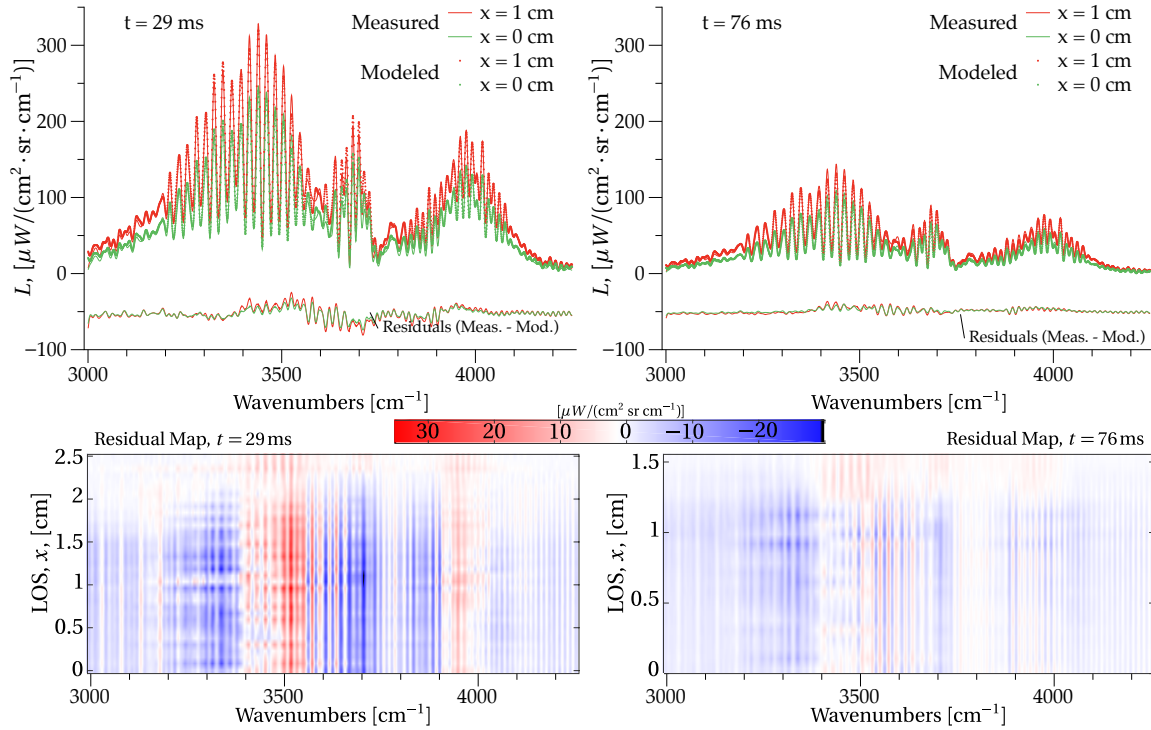
Figure 49. **Reconstructed (measured) and modeled spectra at** $r = 0\,\text{cm}$ **and** $r = 1\,\text{cm}$ **for the** $t = 29\,\text{ms}$ **and** $t = 76\,\text{ms}$ **inversions. The residual differences between truth and model for the selected LOS's is provided and are offset from zero for clarity. Complete maps of the residuals are also provided below.**

6.3 Results and Discussion

Fig. 49 shows the comparison of reconstructed (measured) and modeled spectra at $x = 0\,\text{cm}$ and $u = 1\,\text{cm}$ for both $t = 29\,\text{ms}$ and $t = 76\,\text{ms}$. The presence of structure in the residuals indicates that the reconstructed spectra is not fully modeled by the simulated data. There are several possible causes for this. (1) Note that Fig. 30 shows small but noticeable structure in the residuals of the simulated data results. This high-frequency structure results from improper reconstruction of interferogram ends. The process employed in finding the DC profile, I^{DC}, of each interferogram is viable except at the ends of the interferograms. There, edge effects present themselves as sharp peaks or drops in the estimated I^{DC}. Not only does this have an adverse effect on I^{DC}, but it also has a major effect on the estimation of the slope, dI^{DC}, which is calculated directly from I^{DC}. To minimize the impact on reconstructed interferograms, I^{DC} and dI^{DC} are

124

always artificially truncated by 2% of the number of sampling points after generation. If any edge-effects are still present during the reconstruction, Fig. 30 shows that they cause small, sharp features in the data. Note in this chapter the reconstructed spectra have been artificially convolved down to a spectral resolution of $8\,cm^{-1}$. This reduction in resolution is done by truncating the interferograms from a maximum optical path difference of 0.6 cm to just 0.075 cm. This is primarily done to help improve the SNR of the reconstructed data, but also helps remove edge effects in the reconstruction. (2) The absolute radiometric calibration of the data is key in retrieving quantitative estimates of scalar values, as outlined in Chapter III. Improper calibration will result in a baseline shift of spectra. To mitigate any chance of this, a 4th order polynomial baseline correction was used when fitting the data. It is unlikely, however that calibration would cause structured residuals, as the detector gain is a smoothly varying function and instrument self-radiation is negligible in the spectral region of interest here.(3) Any difference in the line-shape of the measured and modeled data can have a dramatic impact on retrieval values and will often present as "ringing" in the residuals. The residuals seen in Fig. 49 do seem to show this ringing. The model line-shape, however, is set by the maximum optical path difference of the measured interferogram and as this data is artificially truncated to a known value, the measured and modeled line-shapes should be in agreement. The model line-shape was included as a fitting parameter, so the residuals are likely not from a line-shape issue. (4) Additionally if the atmospheric absorption modeling is not accurate, residual differences will appear structured and this will have an effect on all LOS's which is something seen in the residual maps in Fig. 49. This is most likely the cause of the residuals seen here and more concerning this is discussed below.

Fig. 50 shows the retrieved radial temperature and water concentration profiles measured at a height of 4.5 cm above the burner and for times $t = 29\,ms$ and $t = 76\,ms$

125
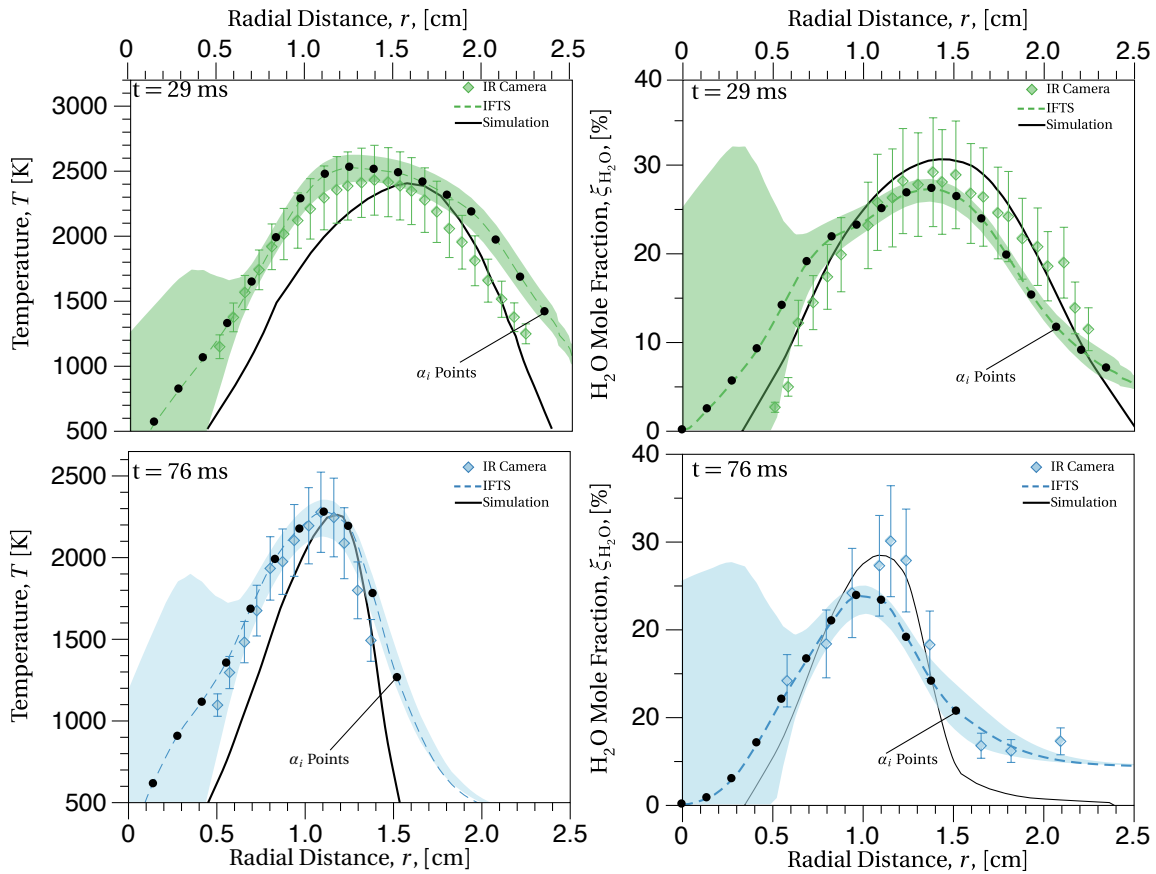
Figure 50. Temperature and H_2O concentration results of the inversion algorithm performed on the $t = 29\,\text{ms}$ and $t = 72\,\text{ms}$ time-resolved spectra. Shaded regions represent the confidence interval of the retrieval. Results are compared to previous IR band-pass measurements [2] and UNICORN simulation.

in the flame motion. Here again the confidence intervals do not include correlation between sampling points, and as a result are likely higher overall. Results are compared to previously measured results of a similar flame using IR band-pass imagery and thin-filament pyrometry [2] and a UNICORN simulation. The IFTS retrieved temperature results compare well, showing the same trends as the IR camera and simulation results. Temperatures for $t = 29\,\text{ms}$ at $r < 1\,\text{cm}$ are higher compared to previous results, with a maximum difference of 50% at $r = 0.5\,\text{cm}$. This, however, is self-consistent with results shown in Fig. 33. There, integrated radiance values for $t = 29\,\text{ms}$ at $r < 1\,\text{cm}$ were also greater than previous results, a trend now explained by the difference in measured temperature. Temperatures for $t = 29\,\text{ms}$ at $r > 1.5\,\text{cm}$ are also higher compared to pre-

vious results, with a maximum difference of 25% at $r = 2.2$ cm. Temperatures compare well between $r = 1$ cm and $r = 1.5$ cm with an average difference of 2%. Neither experimental results compare favorably with the simulated temperature profile for $t = 29$ ms. Temperatures for $t = 76$ ms at $r < 1.1$ cm are lower compared to previous results, with a maximum difference of 35% at $r = 0.5$ cm. This is again self-consistent with results shown in Fig. 33. There, radiance values for $t = 76$ ms were particularly lower than previous results at $r < 1$ cm. IFTS measurements do compare well, however, with the simulated temperature for $t = 76$ ms at $r < 1$ cm. A trend again seen in the integrated radiance values in Fig. 33. Values after $r = 1$ cm compare well with an average difference of 0.75%. Uncertainties were calculated using the method described in Sec. 5.6. Note that as seen in Chapter V, uncertainty in the temperature increases near flame center and flame edge.

The IFTS retrieved water concentrations also compare well with IR camera and simulation results. Note that the UNICORN simulation did not include an atmospheric concentration value and so ξ_{H_2O} decays to zero. ξ_{H_2O} for $t = 29$ ms at $r > 1$ cm are low compared to previous results, with a difference of 20%. Fig. 33, however, shows an excellent comparison in integrated radiance for $t = 29$ ms at $r > 1$ cm. The combination of a higher temperature and lower ξ_{H_2O} values accounts for this correct integrated radiance comparison. The estimated value of ξ_{H_2O} near $r = 1$ cm in the $t = 76$ ms profile is lower than previous estimations and simulation. It, however, shows a slightly flattened peak which may suggest the PCHIP interpolation is not able to adequately reconstruct ξ_{H_2O}. If sampling points fall on either side of a peak, the result is often a flattened estimate.

At both times evaluated, the IFTS retrieved atmospheric temperature and water concentrations were about 400 K and 4% respectively. These are higher than weather measurements taken during experimentation, 340 K and 3% respectively. It is noted

127

that the flame was fully contained inside a wind-block and that during testing the vent above the flame was turned off to remove disturbances in the air flow. Weather measurements were taken inside the shroud periodically but this required opening the shroud. Because of this, the true atmospheric conditions, S^{ATM}, are likely higher than weather measurements, and also likely changed significantly throughout the course of the measurements. This has the possibility of introducing scene change artifacts, even in the time-resolves interferograms, that could account for the residuals seen in Fig. 49.

The two times reconstructed here represent two distinct points in the flame motion. At $t = 29$ ms, the flame is bulging and at $t = 76$ ms the flame is in a stretched state. These changes in the shape of the flame are due to vortices that form around the flame [117]. The fast moving fuel jet combined with the rapidly expanding gasses from combustion produce a shear-layer with the stagnant atmospheric air. The measured results show that the temperature and water concentration vary significantly in width between these two conditions, but do not vary greatly in their peak temperature and concentration values. There is a small difference, however, in the peak temperature and the drop-off in temperature on the fuel side of the flow. At $t = 29$ ms the peak temperature is 2413 K and at $t = 76$ ms the peak temperature is 2181 K, a difference of 232 K. This difference in temperature is due to the flame-vortex interactions and a system Lewis number (Le) that is less than 1^1. As the shearing forces create a vortex, lab air rich in oxygen is entrained into the flow providing a local increase in reaction and subsequently a higher temperature. In the stretched regions, there is less entrained oxygen. This slows the reaction and the low thermal diffusion rate results in cooling of the flame on the fuel side of the flow. Previous estimations of this temperature difference in necked and bulged regions were found to be 222 K [2] and ~ 150 K [118].

Despite the difference in temperature and the gradient in temperature at the flame

---

[1]The Lewis number is the ratio of thermal diffusivity to mass diffusivity.

128

center, the decay in ξ_{H_2O} at flame center are similar for both times. At locations $r > 1\,\text{cm}$, however, they are very different. This is again due to the flame-vortex interactions. The ratio of the binary diffusion coefficient of water over hydrogen is less than one. This means that in areas where the flame is bulging, the diffusion of hydrogen into the flame-front is dominating. With the increase of available fuel, coupled with an ample supply of entrained oxygen, more water is produced [117].

6.4 Conclusions

This chapter combines two major algorithms developed for this work to measure scalar values of an unsteady laminar flame in a full 4D sense. Results are good in comparison with previously reported results [2], and CFD simulation. Temperature values for $t = 29\,\text{ms}$ and $72\,\text{ms}$ have an average difference of 10% and 11% respectively. Water concentration values differ by an average of 19% and 15% respectively. Structured residuals in the modeled spectra do suggest additional improvements may be needed. Automated sampling point locations and improvement to the empirical edge function are the most important areas of future research.

This work demonstrates IFTS is a viable combustion diagnostics tool in harmonic laminar flames. Only one row of the flame and two periods in the flame motion were reconstructed here. But full scalar value maps in a full 4-D sense could be made if desired. Continued research toward adapting these techniques to turbulent and asymmetric scenes is still needed. This work, however, brings IFTS even closer to practical use on modern engineering applications of combustion.

VII. Conclusions

This work has demonstrated the usefulness of a Telops Hyper-Cam Midwave Infrared camera to make combustion diagnostics measurements of unsteady laminar flames. This was achieved through the successful recovery of scalar values in a full 4-D sense. The completion of specific research objectives were met through the following:

1. **Demonstrate IFTS as a viable, steady-state laminar flame CD tool.**

   Through the investigation of a laminar premixed ethylene flame, IFTS demonstrated initial promise as a useful combustion diagnostic. This first required the creation of a novel calibration technique that minimized the negative effects of low SNR gain measurements. Spectrally-determined temperature and species concentrations agreed with previous laser absorption flame measurements. The large number of ro-vibrational emission lines and band structures arising from multiple species lead to statistical temperature uncertainties less than $50\,\mathrm{K}$. The 2-D scalar fields achieved through a simple single-layer model agreed well at the base of the flame. Results higher in the flame, however, motivated the need for a multi-layer and time-resolved retrieval algorithm.

2. **Develop algorithm to recover time-resolved spectra from ensemble measurements.**

   By utilizing the one-to-one relationship between flame configuration and a measured DC-signal level and slope, an algorithm to recreate instantaneous "snapshots" of a flame spectra was achieved. Results of the algorithm agree to within 7% of truth values, demonstrating the merit of the algorithm on a simulated data set. When applied to measurements of a real hydrogen flame, reconstructed lateral LOS radiance values agree to within 18% of previously reported values. The reconstruction algorithm was able to recreate instantaneous radiance measurements

130

that follow the same trends as previous values, both laterally and temporally. Now, simply averaging over many instrument scans to remove the effects of I^{DC} is not needed and all information available in an ensemble of measurements can be used.

3. **Create spectroscopic radiative transfer tomographic model for radial scalar field estimation.** A traditional onion-peel inversion was improved upon through three additions. First an empirical function is used to describe the scalar value decay to atmospheric conditions. This improves the starting guess at the outer-most flame layers. Second, a three-point sliding onion-peel provides a fast and flexible, yet reliable estimation of the radial scalar profiles. Finally, the addition of a global parameter minimization optimizes the shape of the radial profiles using all available data simultaneously. Using simulated data sets, the inversion agreed with truth to within 10%. The inversion showed flexibility in recreating various flame shapes, and sensitivity to even trace species. The inversion model is even capable of reconstructing the flame center in all three profiles tested.

4. **Demonstrate 4-D scalar retrieval in an unsteady laminar flame.** Measured data of an unsteady non-premixed hydrogen flame was used to combine the algorithms developed for Objectives 2 and 3. Results compare well with previously reported values and CFD simulation. Temperature and water concentrations were resolved radially at two different "snapshot" times in the period of the flame's harmonic motion. Measured temperature values have an average difference of 10% and 11% respectively. Water concentration values differ by an average of 19% and 15% respectively. This work demonstrates full scalar value maps in a full 4-D sense could be made if desired.

IFTS offers several unique advantages for combustion diagnostics. Its portable

131

and compact, field-deployable design makes it a fast and rugged measurement tool. Capturing moderate resolution spectrum (up to $0.25\,\mathrm{cm}^{-1}$) across a wide band pass ($1.5\,\mu\mathrm{m}$ to $5.5\,\mu\mathrm{m}$) provides resolved information of many major combustion species simultaneously. The high-speed imagery existing within the interferometric measurement enables visualization of flame dynamics, and this enhances interpretation of 2-D scalar fields derived from the spectra. Existing flow field analyses performed by infrared cameras can be readily adapted to the broadband imagery captured within the IFTS measurement. With the completion of this work, IFTS now has the advantage of time-resolved 3D imaging of scalar values in laminar axisymmetric flames. This will make IFTS a useful tool for understanding combustion phenomenon, validating chemical kinetic models, verifying numerical simulations, and system performance estimate. Continued research toward adapting these techniques to turbulent and asymmetric scenes is still needed. This work, however, brings IFTS even closer to practical use on modern engineering applications of combustion.

Appendix A. Imaging Fourier-Transform Spectroscopy for Combustion Diagnostics and Code Validation

The following is a research paper, in its entirety, published in the International Journal of Energetic Materials and Chemical Propulsion (Volume 12, Issue 1, Page 15). This article discusses IFTS and its use with plume diagnostics and code validation. It is held to an appendix as it is only partially relevant to the focus of this research. Authors of this article include Michael Rhoby, Jacob Harley, Kevin Gross, Pierre Tremblay, and Martin Chamberland. This appendix further meets the requirements of objective 1.

As first author I was responsible for data capture, reduction, and analysis for the section of the paper pertaining to laminar flame combustion diagnostics.

1.1 Abstract

Laminar and turbulent flow fields found in smokestacks, flames, jet engine exhaust, and rocket plumes are of practical and academic interest and could greatly benefit from spatially-resolved spectral measurements. Key physical flow field parameters such as temperature and species concentrations can be extracted from spectral observations. Spectral images of flow fields produce rich information for plume diagnostics and could be used to validate next-generation plume codes. Laser-based diagnostics are typically used to measure temperatures, concentrations, and flow velocities. Unfortunately, these laser-based techniques are largely confined to a laboratory environment, and tracking multiple species concentrations is complicated due to the limited bandwidth of tunable laser sources. The advantage of a passive sensor with high resolution across a broad bandwidth would make an imaging Fourier-transform spectrometer (IFTS) an attractive instrument for flow diagnostics, particularly when the flow field of interest cannot be studied in a laboratory. In this paper, we present an overview of IFTS and its

uses for flow visualization and combustion diagnostics in various plumes. Examples from recent measurements of laminar flames and jet engine exhaust will be presented.

1.2   Introduction

Laminar and turbulent flow fields emanating laboratory flames, jet engines, and rockets are of practical and academic interest and could benefit from spatially-resolved spectral measurements. Spectral emissions encode important flow field parameters such as temperature, density, and species concentrations. Laser-based diagnostics are typically used to measure these parameters [4]. However, such techniques are a challenge to set up and are limited to a laboratory environment. The limited bandwidth of tunable laser sources makes tracking multiple species concentrations difficult. The advantage of a passive sensor with high resolution across a broad bandwidth would make imaging Fourier-transform spectrometry (IFTS) an attractive instrument for flow diagnostics, particularly when the flow field of interest cannot be studied in a laboratory. In this paper, we present an overview of IFTS and its uses for flow visualization and combustion diagnostics in various plumes. Examples from recent measurements of a laminar flame [82] and jet engine exhaust [66, 119–122] will be presented.

Laminar and turbulent flow fields emanating laboratory flames, jet engines, and rockets are of practical and academic interest and could benefit from spatially-resolved spectral measurements. Spectral emissions from a flow field are a function of scalar fields such as temperature, density, and species concentrations. Thus, proper interpretation of the spectrum can simultaneously reveal multiple scalar flame properties. The ability to determine multiple scalar fields three-dimensionally and with high temporal resolution is difficult yet highly desired since it reveals key combustion phenomenon, enables validation of chemical kinetic models, and is useful for benchmarking numerical simulations. Laser-based methods—the cornerstone of combustion diagnostics—

134

provide highly selective, sensitive, non-intrusive means to interrogate laminar and turbulent flow fields [4]. However, three-dimensional mapping of multiple scalar fields often requires raster scanning multiple lasers in a sophisticated experimental arrangement. Moreover, most laser-based measurement techniques are limited to a laboratory environment unless substantial effort and cost are expended to harden and make portable the diagnostic system. Flame emission measurements are another class of nonintrusive diagnostics which complement laser-based techniques and are easier to implement. High-speed infrared cameras with various band-pass filters have been used to map spatial and temporal variations in radiant intensity and relate these to the spatial distribution of scalar values and to various measures of turbulence (e.g. integral length and time scales). Broadband imaging, however, is limited in its ability to discriminate the influence of multiple scalars. Fourier-transform spectrometer (FTS) measurements, when paired with appropriate tomographic deconvolution algorithms, can be used to simultaneously determine temperature and mole fractions of major flame species.

Imaging Fourier-transform spectrometer (IFTS) represents a new combustion diagnostic which combines the advantages of studying flames with spectroscopy and infrared imaging in a simultaneous fashion. In this paper, we present an overview of IFTS and its uses for flow visualization and combustion diagnostics in various plumes. Examples from recent measurements of a laminar flame [82] and jet engine exhaust [66, 119–122] will be presented.

1.3 Instrumentation

We have looked at various high-temperature laminar and turbulent flow fields using a Telops Hyper-Cam interferometer [87, 123]. This IFTS features a high-speed 320 × 256 pixel InSb (1.5—5.5 µm, 2 kHz full-frame) focal-plane array (FPA). Sequential scene imagery focused on the FPA is collected while looking through a scanning Michelson

interferometer. The interferogram cube is thus a stack of broad-band infrared images collected at fixed optical path differences (OPDs). Acquisition rate depends on spectral resolution and mirror speed, which in turn is affected by spatial resolution and camera integration time.

An ideal Michelson-based IFTS produces (at each pixel) an interferogram $I(x)$ represented by

$$I(x) = \frac{1}{2} \int_0^\infty (1 + \cos(2\pi x \tilde{\nu})) G(\tilde{\nu})(L_s(\tilde{\nu}) + L_i(\tilde{\nu})) \, \mathrm{d}\tilde{\nu} = I_{DC} + I_{AC}(x)$$

where x is the optical path difference, $L_s(\tilde{\nu})$ is the scene spectrum, $L_i(\tilde{\nu})$ are spectral emissions from within the instrument, and $G(\tilde{\nu})$ is the spectral system response which includes the quantum efficiency of the detector. Here, I_{DC} represents the integrated intensity and $I_{AC}(x)$ is the cosine transform of the (uncalibrated or raw) spectrum. Fourier-transformation of $I(x) - I_{DC}$ yields the raw spectrum. This implicitly assumes the source spectrum is static over the course of the measurement. For laminar flow, this is typically true. However, the case of turbulent flow in which $L_s(\tilde{\nu})$ may rapidly and stochastically change throughout an interferometric measurement is addressed in Section 1.4.

Two on-board blackbodies permit linear calibration to remove the effects of detector response $G(\tilde{\nu})$ and instrument self-emission $L_i(\tilde{\nu})$. A schematic of an IFTS is presented in Figure 51. Also shown are an example interferogram for a single pixel and its corresponding spectrum upon Fourier-transformation.

136
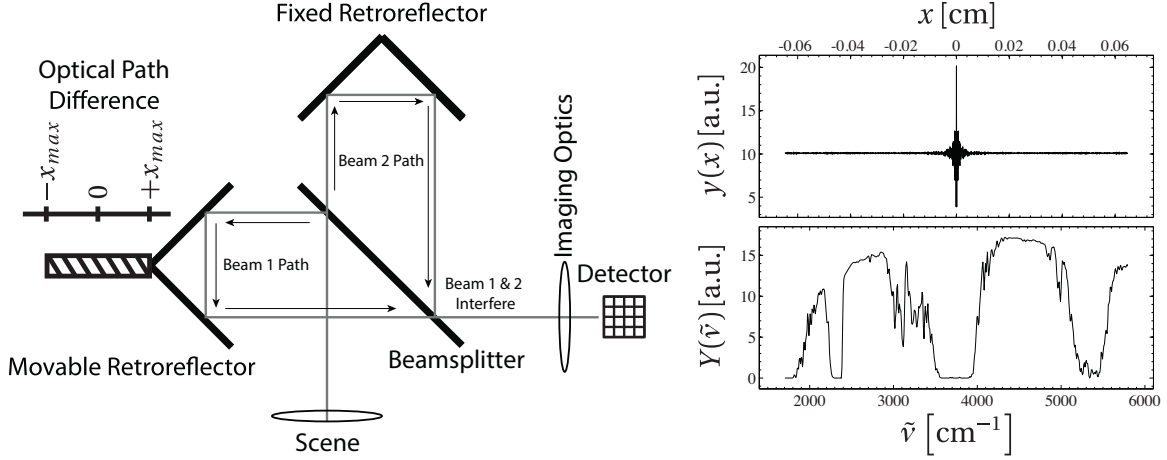
Figure 51. *Left panel*: Schematic of an imaging Fourier-transform spectrometer. An interference pattern is measured at the focal-plane array detector by varying the phase between the two light beams via the movable retroreflector. *Right panel*: Illustration of an single-pixel interferogram (top) and its corresponding spectrum (bottom) upon Fourier-transformation.

1.4 Theory

Radiative transfer for ideal turbulent flow.

The spectral radiance $L(\tilde{\nu})$ from a non-scattering source in local thermodynamic equilibrium along a length l line-of-sight (LOS) can be expressed as [124]

$$L(\tilde{\nu}) = \int_0^l e^{-\tau(s)} \kappa(\tilde{\nu}, s) B(\tilde{\nu}, T(s)) \, \mathrm{d}s \tag{40}$$

where $\tau(s) = \int_s^l \kappa(\tilde{\nu}, s') \, \mathrm{d}s'$ is the optical depth, $\kappa(\tilde{\nu}, s)$ is the absorption coefficient, and $B(\tilde{\nu}, T)$ is Planck's blackbody distribution at temperature T. The term $\kappa(\tilde{\nu}, s) B(\tilde{\nu}, T(s))$ accounts for photons "born" at the point s along the LOS, and $e^{-\tau(s)}$ accounts for the fraction of those photons absorbed as they travel through the remaining plume towards the source. The dependence of κ on both $T(s)$ and species concentrations $\vec{\xi}(s)$ was suppressed. For an ideal, high-temperature, two-dimensional flow field which is homogeneous along the LOS, Eq. 40 can be approximated by

$$L(\tilde{\nu}, T) = \tau(\tilde{\nu}) \varepsilon(\tilde{\nu}, \vec{\xi}, T) B(\tilde{\nu}, T) \tag{41}$$

137

where the source emissivity ε is defined by $\varepsilon(\tilde{\nu}, \vec{\xi}, T) = 1 - e^{-\kappa(\tilde{\nu})l}$ and $\tau(\tilde{\nu})$ represents the transmittance of the material (atmosphere) between the source and instrument. This model assumes the plume radiance dominates all other sources (e.g., photons emitted behind or in front of the plume).

In this work, spectra are modeled using the Line-by-Line Radiative Transfer Model (LBLRTM) [125] in conjunction with the high-temperature extension (HITEMP [63]) to the HITRAN database [18] of spectroscopic line parameters.

Note that at all wavenumbers $\tilde{\nu}$, Planck's distribution $B(\tilde{\nu}, T)$ monotonically increases with temperature. Additionally, for many gas-phase systems in local thermodynamic equilibrium, this monotonicity is preserved, so we assume $T_2 > T_1$ implies $L(\tilde{\nu}, T_2) > L(\tilde{\nu}, T_1)$ for all $\tilde{\nu}$.

In a non-reactive turbulent flow field, the instantaneous temperature T fluctuates about a mean temperature $\langle T \rangle$ according to a probability distribution $P(T)$[?]. Uncorrelated fluctuations in $\vec{\xi}$ may also occur, but are ignored[1]. For an ergodic flow field, the average of an ensemble of spectral measurements yields

$$\langle L(\tilde{\nu}, T) \rangle = \int L(\tilde{\nu}, T) P(T) \, dT \neq L(\tilde{\nu}, \langle T \rangle) \tag{42}$$

where the non-equality arises due to the nonlinear dependence of L on T. To properly interpret $\langle L(\tilde{\nu}, T) \rangle$, *a priori* knowledge of $P(T)$ would be required and simply fitting a single-T model to it necessarily results in biased temperatures and species concentrations. To address this problem we now consider flow measurement made by an interferometer.

---

[1]If concentration fluctuations are significant, the one-to-one mapping of quantile spectra to unique temperatures to be described may not be valid. However, multiple quantile spectra do contain information complementary to and different from the mean spectrum.

Quantile interferogram analysis for a two-dimensional turbulent flow field .

Dynamic scenes are often considered problematic for IFTS as changes in scene radiance during the interferometric scan produce scene-change artifacts (SCAs) in the spectrum. While time averaging can minimize the effects of this "source noise," an alternate method is presented which, in addition to minimizing SCAs, can provide additional information about the fluctuation statistics in the flow field. In the case of two dimensional turbulent flow which is dominated by temperature fluctuations and is homogeneous along the instrument's line of sight, temperature fluctuation statistics can be recovered.

To simplify the presentation, we assume an instrument response of unity and ignore instrument self emission. Under these conditions, an ideal Michelson produces an interferogram $I(x_i, T_i)$ at each OPD x_i of the turbulent flow via

$$I(x_i, T_i) = \int (1 + \cos(2\pi x_i \tilde{\nu})) L(\tilde{\nu}, T_i) \, d\tilde{\nu} \qquad (43)$$

where T_i represents a random sample from $P(T)$ and is assumed constant over the short FPA integration time. With a FPA, the DC component is preserved, and this is key to the following development. Recall that $L(\tilde{\nu}, T)$ is a monotonic function of temperature at all $\tilde{\nu}$. Since $1 + \cos(2\pi x_i \tilde{\nu}) \geq 0$ for any x_i and all $\tilde{\nu}$, it follows that $T_2 > T_1 \rightarrow I(x_i, T_1) > I(x_i, T_2) \forall x_i$. If an ensemble of interferometric measurements of the ergodic flow field are captured, then at each x_i, a range of temperatures weighted by $P(T)$ will have been observed. As the chain of probabilities demonstrates, the monotonicity of $L(\tilde{\nu}, T)$ permits sorting the ensemble of measured $I(x_i)$'s into various quantiles

$$q = \mathbb{P}\left\{T \leq T_q\right\} = \mathbb{P}\left\{L(\tilde{\nu}, T) \leq L(\tilde{\nu}, T_q)\right\} = \mathbb{P}\left\{I(x_i, T) \leq I(x_i, T_q) \equiv I_q(x_i)\right\} \forall x_i \qquad (44)$$

where T_q is the qth quantile, $\mathbb{P}\{\_\}$ denotes probability of the argument, and $I_q(x_i)$ defines

139

the "quantile interferogram". So long as a sufficient number of measurements are made to enable robust quantile estimates, $I_q(x_i)$ is a valid interferogram corresponding to the spectrum $L_q(\tilde{\nu}) \equiv L(\tilde{\nu}, T_q)$.

The limitation to an unrealistic two-dimensional flow field may appear to limit the utility of this technique. However, the sorting of interferograms can still be performed to yield quantile spectra. These quantile spectra contain information which is complementary to and distinct from the mean spectrum. An example from an axisymmetric jet is presented in Section 1.5 and demonstrates this point.

Extraction of moderate-speed imagery from interferometric measurements .

The Michelson interferometer encodes spectral information via intensity variations (as represented by the cosine term in Equation 43). These variations occur at a frequency greater than $f = v_m \tilde{\nu}_d$ where v_m is the mirror scan velocity and $\tilde{\nu}_d$ is the lowest frequency photon ($\tilde{\nu}_d \sim 1700\,\text{cm}^{-1}$) that the camera detects. Thus, a temporal low-pass filter can be applied to the interferogram cube yielding moderate-speed imagery. Also, if there are broad regions in which no spectral emissions are observed, a temporal band-pass filter can be applied to recover imagery (with no DC level) at higher frame rates. The mirror scan velocity varies with spatial resolution and camera integration time.

A specific example illustrates the differences between camera and spectral image acquisition rates. For a window size of 48×156 pixels and an integration time of $5\,\mu\text{s}$, the camera in the IFTS acquires images at nearly $10\,\text{kHz}$ as the Michelson assembly continuously varies the optical path difference (OPD) between interfering beams. Each image corresponds to a change in OPD of $632.816\,\text{nm}$ [2], and in this instrument configuration, the mirror speed is $0.64\,\text{cm}\cdot\text{s}^{-1}$. To achieve spectral images at $1.5\,\text{cm}^{-1}$ between $1700\,\text{cm}^{-1} < \tilde{\nu} < 6667\,\text{cm}^{-1}$ requires approximately $12{,}500$ sequential images

---

[2]A HeNe reference laser is used to trigger the camera to capture images at regular OPD intervals.

collected between $-0.4\,\text{cm} < \text{OPD} < 0.4\,\text{cm}$. The spectral image is thus acquired at $0.8\,\text{Hz}$. While the camera frames at $10\,\text{kHz}$, intensity modulations at frequencies greater than $f = 1700\,\text{cm}^{-1} \times 0.64\,\text{cm}\cdot\text{s}^{-1} = 1088\,\text{Hz}$ could occur due to the action of the Michelson, thus the effective frame rate after low-pass imagery is approximately $1\,\text{kHz}$. Broadband infrared imagery at these rates permits characterization of many types of turbulent flow.

1.5 Results & Discussion

Laminar flame.

To demonstrate the utility of IFTS for combustion diagnostics, measurements of a Hencken burner were recently acquired [82] and the key results are summarized here. A Hencken burner produces a nearly ideal adiabatic flame and is routinely used as a calibration standard for testing new combustion diagnostics. In a series of experiments, an ethylene (C_2H_4) / air flame was produced at various equivalence ratios [3] (Φ). Total volumetric flow rates were between $10.9\,\text{SLM}$ and $17.1\,\text{SLM}$. The instrument collected 1000 spectral images at $1\,\text{cm}^{-1}$ resolution on a 200×64 pixel array.

The observed spectra are dominated by broadband emission from CO_2 between $2150\,\text{cm}^{-1}$ and $2400\,\text{cm}^{-1}$. Emission from H_2O are spectrally structured and are found between $3000\,\text{cm}^{-1}$ and $4200\,\text{cm}^{-1}$; weaker emissions can be found below $2000\,\text{cm}^{-1}$. Spectra from fuel-rich ($\Phi > 1$) flames exhibited CO emission lines on either side of the $2143\,\text{cm}^{-1}$ band center. The CO line intensities increased with Φ. An example spectrum is presented in Figure 52.

High-speed imagery was extracted from the interferometric cubes (see Section 1.4) and revealed that the flame was steady up to approximately $30\,\text{mm}$ above the burner. Within this region, the flame is stable and nearly homogeneous with a very thin mixing

---

[3]The equivalency ratio is defined by the actual fuel:air ratio relative to the stoichiometric fuel:air ratio.
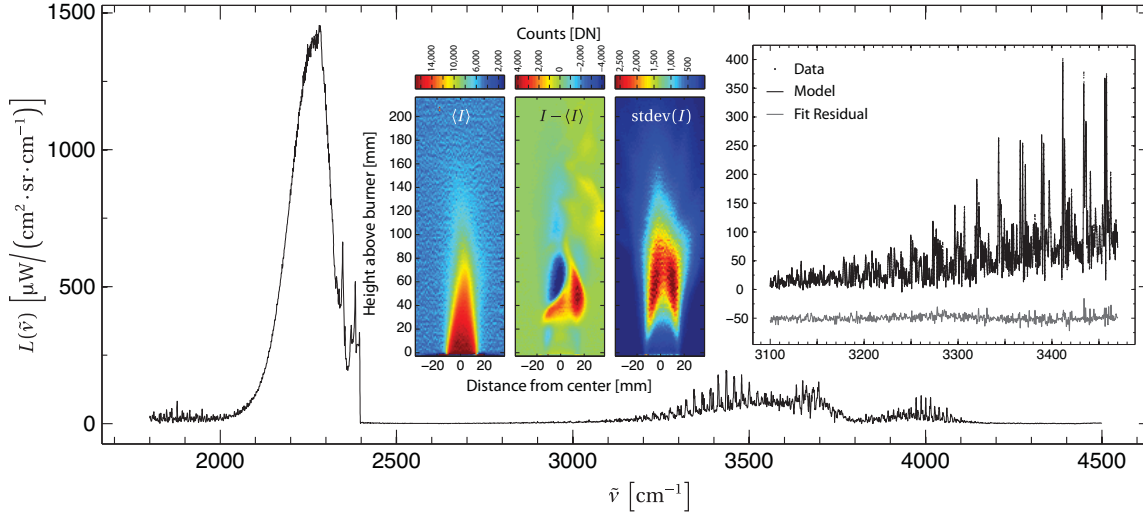
Figure 52. Mean single-pixel spectrum of an ethylene flame centered $20\,\text{mm}$ **above the burner. The large peak at** $2250\,\text{cm}^{-1}$ **is due to** CO_2 **and the structured emission between** $3000\,\text{cm}^{-1}$ **and** $4200\,\text{cm}^{-1}$ **is primarily due to** H_2O. **The inset color panels present (1) the time-averaged broadband infrared image (left), difference between an instantaneous and the mean flame image (middle), and the standard deviation of the flame intensity (right). The inset spectrum compares an ethylene center flame spectrum at** $10\,\text{mm}$ **with a model fit. Fit quality can be judged by the residuals offset by** $50\,\mu\text{m}/(\text{cm}^2 \cdot \text{sr} \cdot \text{cm}^{-1})$.

layer. However, above $30\,\text{mm}$ unsteady behavior was observed as revealed by the inset imagery in Figure 52. The left panel provides the time-averaged flame intensity and characterizes the mean flow field. The middle panel shows the difference between an instantaneous flame intensity and the mean flame intensity. Variations up to 50% of the mean signal are evident. The standard deviation of each pixel's intensity are provided in the right panel.

Within this homogeneous portion of the flame, the radiative transfer model (Equation 41) can be used to simultaneously retrieve temperature and species concentrations from the observed spectrum. To validate this approach, an ethylene flame measurement was taken corresponding to $\Phi = 0.91$ via fuel and air flow rates of $0.78\,\text{SLM}$ and $12.2\,\text{SLM}$, respectively. This was to permit comparison with measurements of an identical flame studied using a tunable diode laser absorption[4] technique [1]. Flame temperature and

---

[4]The laser-based diagnostic measured the shape of a single hydroxy radical (OH) line to extract temperature

mole fractions of H_2O and CO_2 were estimated by a nonlinear least-squares fit of Equation 41 to the the IFTS spectrum at 10 mm above flame center. These fit parameters were adjusted using a Levenberg-Marquardt algorithm to minimize the sum of squared differences between the measured and model spectrum. The fit results were good as demonstrated in the inset spectrum of Figure 52. The spectrally estimated temperature of $T = 2172 \pm 28$ K was in excellent agreement with the OH laser absorption temperature of $T = 2226 \pm 112$ K. Optimal concentrations for H_2O and CO_2 were $13.7 \pm 0.6\%$ and $15.5 \pm 0.8\%$, respectively, exceeding expected results by 20% according to equilibrium calculations. Relative line heights determine the gas temperature, whereas absolute line heights determine species concentrations. The good agreement in temperature suggest the relative instrument spectral calibration is good. However, the poor agreement in concentration could be caused by a systematic error in the absolute calibration.

Jet engine .

Having demonstrated the applicability of IFTS to a laminar flame, we now consider the highly turbulent flow field produced by a jet engine. Rapid temperature fluctuations in the flow field produce substantial changes in the instantaneous scene spectrum during the course of an interferometric measurement. The SCAs associated with the spectrum from a single interferometric cube appear as noise. Time-averaging reduces this "source noise" and produces a recognizable spectrum. However, the quantile analysis discussed in Section 1.4 is evaluated for its utility in reducing SCAs as well as providing information on temperature fluctuation statistics.

The exhaust plume from a Turbine Technologies SR-30 turbojet was imaged by the IFTS. The SR-30 is a small turbojet designed for educational laboratory work. A single-stage centrifugal compressor operating between 39,000–87,000 rpm delivers air to the 27 cm long × 17 cm diameter engine designed for combusting various fuels including

143

Jet-A, JP-8, diesel, and kerosene. Maximum thrust of the SR-30 is approximately 178N with a nominal exhaust temperature of 720 °C. 800 spectra at $25\,\text{cm}^{-1}$ were collected on a 48×156 pixel window.

The collection of interferometric measurements were sorted into quantiles $I_q(x_i)$ corresponding to $q \in \{0.159, 0.5, 0.841\}$. These quantiles correspond to the $m - \sigma$, median, and $m + \sigma$ of a normal distribution characterized by mean m and standard deviation σ. Quantile interferograms were converted to apparent radiance spectra. Plume spectra at all quantiles feature weak broadband emission between $2000-2800\,\text{cm}^{-1}$ with large emission features arising from thermally excited CO_2. A map of brightness temperature[5] $T_B(L_q(\tilde{\nu}))$ at $\tilde{\nu} = 2278\,\text{cm}^{-1}$ from the median quantile is presented in the top of Fig. 53. The plume appears fairly symmetric and spans nearly the full width of the FPA. The low-emissivity, polished metal engine appears substantially cooler. The median-quantile spectrum $L_{q=0.5}(\tilde{\nu})$ for a center pixel near the jet is also shown. The imaginary part of the spectrum is also provided and appears as noise, indicating SCAs have been minimized. (In a properly-calibrated FTS measurement of a static scene, the signal is contained in the real part and noise is equitably distributed among the real and imaginary parts. SCAs can be detected by examination of the imaginary part.) Kinetic temperatures could be retrieved from the spectrum using an appropriate radiative transfer model which properly accounts for the three-dimensional flow field.

At each pixel, the magnitude of temperature fluctuations can be characterized by estimating the standard deviation by differencing two brightness temperature quantiles, i.e. $\sigma_B^+(\tilde{\nu}) = T_B(L_{q=0.841}(\tilde{\nu})) - T_B(L_{q=0.5}(\tilde{\nu}))$. A map of $\sigma_B^+(\tilde{\nu})$ at $\tilde{\nu} = 2278\,\text{cm}^{-1}$ is provided in the bottom panel of Fig. 53.

While the map represents fluctuations in brightness temperature and not the gas kinetic temperature, the two are connected through the effective spectral emissivity of

---

[5]Brightness temperature is defined by $T_B(L(\tilde{\nu})) = c_2\,\tilde{\nu}/\log\big(1 + c_1\,\tilde{\nu}^3/L(\tilde{\nu})\big)$ where c_1 and c_2 are the first and second radiation constants.

144
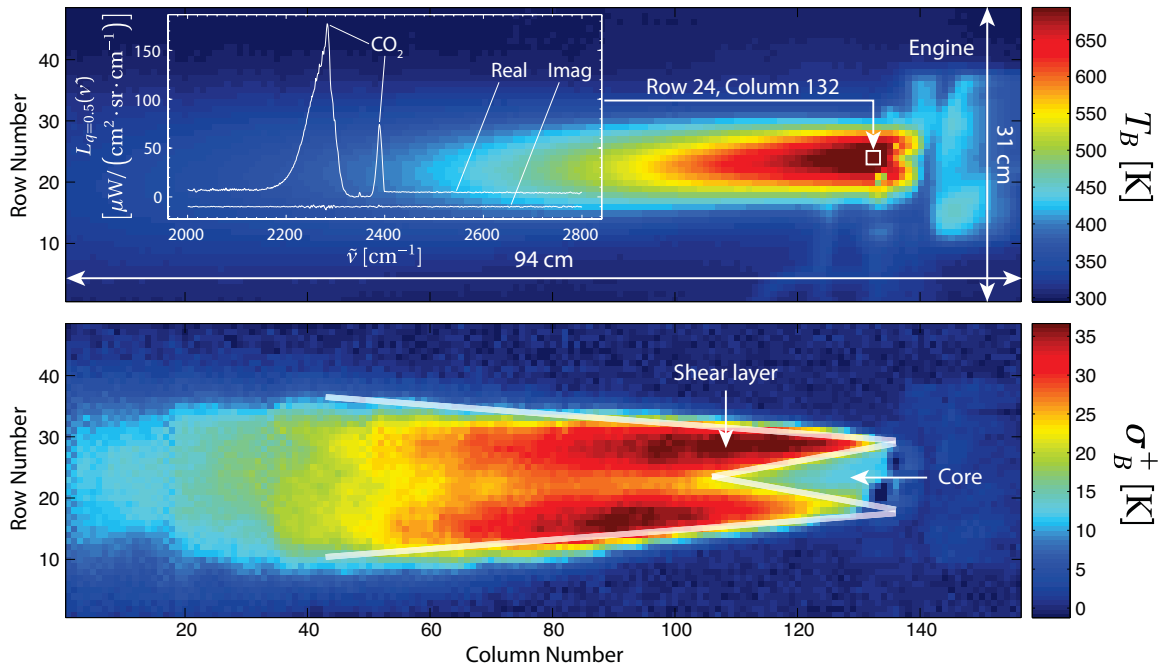
Figure 53. *Top panel*: **Brightness temperature** T_B **at** $\tilde{v} = 2278\,\text{cm}^{-1}$ **from the median quantile** ($q = 0.5$) **spectrum. The inset figure presents the spectrum for a center pixel at engine exit.** *Bottom panel*: **Brightness temperature standard deviation** σ_B^+ **estimated by differencing brightness temperatures from the** $q = 0.841$ **and** $q = 0.5$ **quantile spectra. Translucent lines are overlaid to distinguish the core and shear layers.**

the plume. Thus, this image indicates qualitatively the strength of temperature fluctuations throughout the plume and reveals asymmetry in the spatial distribution. The fluctuations are strongest at the shear layer where the hot exhaust gases turbulently mix with the cold ambient air. The wedge shaped core is also evident, and while turbulent, appears less so than at the shear layer as expected. While non-uniformities along the LOS complicate quantitative interpretation, we've demonstrated that IFTS can be used to study turbulent flows and have presented a novel method to estimate temperature fluctuation statistics.

Bulk flow field characterization is also possible as demonstrated in a separate experiment. Recently, exhaust from an F109 turbofan engine was imaged with the IFTS [122]. Examination of the time-averaged spectra from the exhaust plume indicated that the spectral region above $4200\,\text{cm}^{-1}$ was free of spectral emissions. Since the Michelson mirror was scanned at a speed of $0.18\,\text{cm} \cdot \text{s}^{-1}$ in this experiment, intensity variations at

145

frequencies above 756 Hz could be attributable to fluctuations in the flow field. A temporal high-pass filter (Butterworth, 756 Hz cut-off) was applied to the stack of images comprising a single interferometric cube. A sequence of images is provided in Figure 54 and reveals the dynamic flow. Turbulent eddies are observed to move down stream at a nearly constant velocity. Since the camera frame rate (2860 Hz) and pixel dimensions ($0.26 \times 0.26\,\mathrm{cm}^2$) are known, frame-by-frame tracking of one eddy provides a bulk flow velocity estimate of $181\,\mathrm{m\cdot s}^{-1}$. This compares well to the exit velocity of $176\,\mathrm{m\cdot s}^{-1}$ computed using measured fuel/air mass flow rates and a thermocouple temperature measurement at the exhaust exit [122].

1.6 Conclusions

In this paper, we've summarized recent efforts at developing IFTS for combustion and flow field diagnostics. The IFTS enables highly resolve spectra across a wide bandwidth to be captured at each pixel in an image. We've demonstrated how this enables simultaneous retrieval of temperature and multiple species concentrations. Moreover, the DC information captured by the focal-plane array in the IFTS yields high-speed, broad-band imagery "for free" enabling characterization of the bulk flow in a dynamic plume. This was used to successfully estimate bulk flow velocity from a jet engine. Additionally, the DC information permits the estimation of spectra at various total-intensity quantiles. These quantile spectra complement the information found in the mean spectrum and enable qualitative estimates of temperature fluctuation statistics. The wealth of information that can be extracted from IFTS measurements of flow fields establishes it as a useful diagnostic tool. In particular, IFTS measurements could be used to validate predictions from next-generation plume codes.

146

256 pixels, 0.26 cm/pixel   Camera frame rate: 2860 Hz
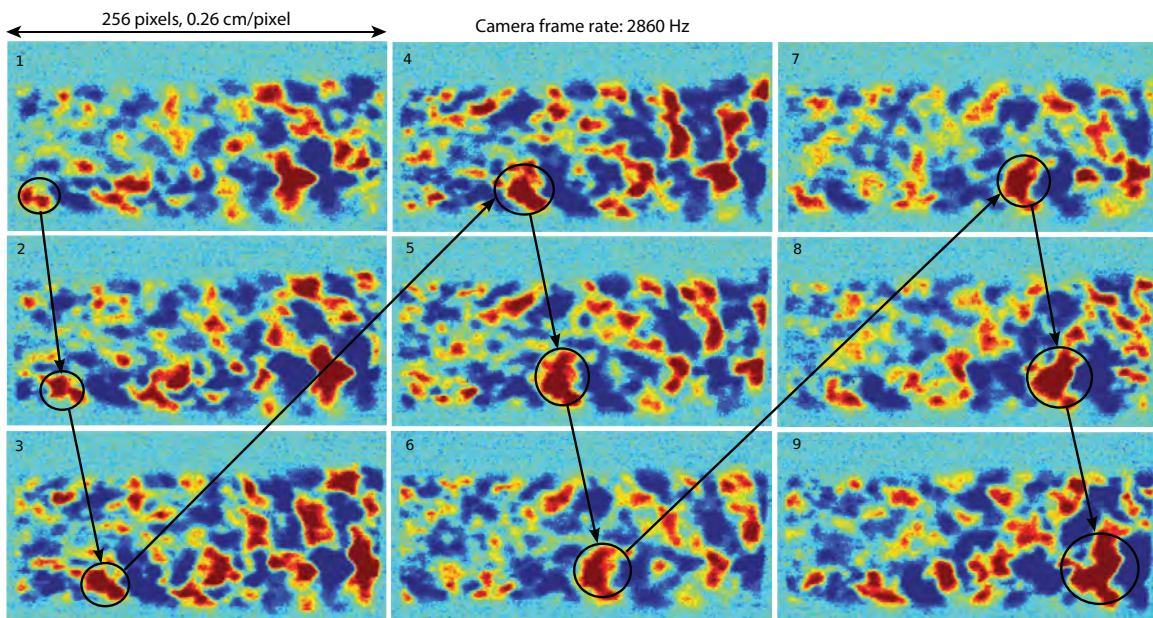
Figure 54. Tracking turbulent eddies enables bulk flow velocity estimation as demonstrated in this sequential imagery of F109 engine exhaust. A Butterworth temporal high-pass filter with cut-off frequency of $756\,\mathrm{Hz}$ was applied to the imagery.

147

Appendix B. Using UNICORN

This appendix presents a description of the computational fluid dynamics model, UNICORN. This description is intended to be a guide in using UNICORN for future AFIT students to simulate laminar flames, and is presented as such. This includes some repeated material from Sec. 2.2. It includes an explanation of each relevant input variable, how to run UNICORN, how to export the data into MatLab, and how to visualize and use the results in MatLab. Also included are examples input files for several flame configurations setups. Note that the detailed guide makes use of a UNICORN input file used in the research for Chapter III and input files used in the simulations of Chapters 4 and 5 are also provided.

2.1   What is UNICORN

In short, UNICORN (UNsteady Ignition and COmbustion with ReactioNs) is a time-dependent computational fluid dynamics with chemistry (CFDC) model that is perhaps one of the most thoroughly evaluated Navier Stokes based codes developed today [70]. UNICORN solves for axial- and radial-momentum equations, continuity, and enthalpy- and species conservation equations to simulate combustion in flames [70]. When written written in a cylindrical-coordinate system, the governing equations are [70]:

$$\frac{\partial \rho}{\partial t} + \frac{\partial \rho u}{\partial z} + \frac{1}{r}\frac{\partial (r\rho v)}{\partial r} = 0 \tag{45}$$

and

$$\frac{\partial (\rho \Phi)}{\partial t} + \frac{\partial (\rho u \Phi)}{\partial z} + \frac{1}{r}\frac{\partial (r\rho v \Phi)}{\partial r} = \frac{\partial}{\partial z}\left[\Gamma^\Phi \frac{\partial \Phi}{dz}\right] + \frac{1}{r}\frac{\partial}{\partial r}\left[r\Gamma^\Phi \frac{\partial \Phi}{\partial r}\right] + S^\Phi \tag{46}$$

Here, ρ, is the flow density, u and v are the axial, z, and radial, r, velocity components respectively. Eq. 1 is the continuity equation and Eq. 2 is either the momentum, species or energy conservation equation, depending on the choice of Φ. Γ^Φ are transport co-

148

efficients and S^Φ are source terms. A table of the various Φ, Γ^Φ, and S^Φ is available in [70].

In solving, momentum equations for u and v are integrated using an implicit QUICK-SET (Quadratic Upstream Interpolation for Convective Kinematics with Estimated Streaming Terms)) numerical scheme [71]. Species and enthalpy is obtained using the hybrid scheme found in [72] along with upwind and central differencing. The finite-difference form of the governing equations, evaluated on a staggered-grid in z and r, is written as:

$$A_P\Phi_P^{N+1} + A_{z^{++}}\Phi_{z^{++}}^{N+1} + A_{z^+}\Phi_{z^+}^{N+1} + A_{z^-}\Phi_{z^-}^{N+1} + A_{z--}\Phi_{z--}^{N+1} + A_{r^{++}}\Phi_{r^{++}}^{N+1}$$
$$+ A_{r^+}\Phi_{r^+}^{N+1} + A_{r^-}\Phi_{r^-}^{N+1} + A_{r--}\Phi_{r--}^{N+1} = S_P^\Phi + \Delta t \rho_P \Phi_P^N \tag{47}$$

This equation is solved over the time increment, Δt, at a point, P. N and $N+1$ are the known variables at the Nth time step and the unknown variables at the $(N+1)^{\text{th}}$ time step. z^- and z^+ are values at grid points immediately adjacent to P. A, and the terms on the right-hand side of Eq. 3 are calculated from known variables at the Nth time step. The pressure field at every time step is calculated solving a system of algebraic pressure Poisson equations at all grid points using the Lower-Upper decomposition technique. Enthalpy of all species is calculated using polynomial curve fits and are vallid over the temperature range 300 to 5000 K. Viscosity, thermal conductivity, binary molecular diffusion coefficients and other such physical properties of the species are calculated using molecular dynamics. Mixture viscosity and thermal conductivity are estimated using the Wilke and the Kee expressions respectively [73]. Molecular diffusion velocity of a species is calculated according to Fick's law, using the effective-diffusion coefficient of that species [74]. The Lennard Jones potentials, effective temperatures, and coefficients for enthalpy polynomials for each species are obtained from CHEMKIN libraries. The UNICORN edition used in this work (UNICORN GRI Version 3.0) had

149

a finite rate chemistry database that included 53 species and 650 possible chemical reactions.

2.2 Build an input file

This may be the most important aspect of using UNICORN. Understanding each line of the input will save hours of computation and the potential for false results. Below is an example of an actual input file used to simulate a partially premixed ethylene flame with an N_2 co-flow (This is an input that models the Hencken burner as closely as possible). Take the time to review each line and what each variable represents, you may even learn something you need to worry about.

After you have reviewed all the variables used, you can build an input file using the MatLab wrapper function "Build_Unicorn_Input_Files.m"

Example input.

This is the input file for modeling the 1" Hencken burner with a 0.25" co-flow (if the burner was round) flowing an ethylene/air mixture at a rate of 2 m/s with a $\Phi = 1.1$ fuel-to-air ratio.

```
1,-CH4-Air Premixed Flame Phi 1.1 (Hencken Burner) - (Global & Finite Rate Chemistry Model)----------
1, 0, 0 / ISYM,IREAD,IGNIT
1, 0, 0.01,0.0625,0.001,-40.0,0,4*0.0/ISTDY,INOISE,(X,Y,A,F of noise)
0.00,0.0500,0.250  / RTOT,ALENG
1.0, 294.0,1.0133D+05, 1.225,1.0,10.0,0.233, 5, 07, 08, 09/ Reference Values
1, 0, 1, 1, 1,  1/  IFLOW,ISWIRL,ITHRM,ICHEM,IPROP,IGRAV
6  / No. of cards describing the boundaries >=4
1,2, 0.2500, 0.0, 11*0.0/ J=1  Axis
2,0, 0.2500, 0.0, 0.01000,0.0,0.0,300.0, 1.0,10.0, 0.000000,0.231371,0.006991,0.00,0.00/J=1 ambient N2
3,0, 0.0125, 2.0, 2.00000,0.0,0.0,300.0, 1.0,10.0, 0.069697,0.215258,0.006459,0.00,0.00/J=1 FuelJet
3,0, 0.0189, 0.0, 0.25000,0.0,0.0,300.0, 1.0,10.0, 0.000000,0.000000,0.000000,0.00,0.00/J=1 N2 Jet
3,0, 0.0100, 0.0, 0.01000,0.0,0.0,300.0, 1.0,10.0, 0.000000,0.231371,0.006991,0.00,0.00/J=1 ambient N2
4,3, 0.0500, 0.8, 11*0.0/  I=LI  Exit
0/NBODY
0/NFINJ
7, 20,0.002,  50,0.0070, 50,0.0120, 50,0.0200, 50,0.0350, 50,0.0700, 20,0.0600/NI,I,X
3, 62,0.0248, 10,0.0050, 10,0.0090/ NJ,(J(N),Y(N))
1000, 0,  0.50, -100, 0/  ITEND,ISECS,CFLNO,ISTORE,ISTB
1 ,  1 /  ITPRNT,IPRES
'PNT','PNT', 'PNT',  'PNT',   'PNT',   'PNT' / N-Scheme- U,V,W, H,Sp,KE
100,100, 100,  100,   100,  100 / No.of Relaxations- U,V, H,  Species
0.9,0.9, 0.99, 0.99, 0.99, 0.99/RELX-U,V,W, H,Sp,K
1.0D-08,1.0D-08, 1.0D-08, 1.0D-08, 1.0D-08, 1.0D-08/Tolerance
1000.0,1.0D+15,100000*1/Rxns.
00,2,0,0.04,0.08,0.12,0.15/IBEVOL,ISEVOL,NEVOL,(XEVOL(N),N=1,NEVOL)
0,0,6,11,26/IBDRV,NDRV,IDRV(1;10)
0,0/IBDRG,ISDRG
0,10,5,0,02.000,1000.0,01.0,1.0/NOPT,IBINJ,ITINJ,IEINJ,PDIA,PDEN,PTHR,PVEL
15000,100,1,00,0.0,0.084,0.0,0.025,0,2/IBANM,ISANM,KSYM,IPANM,X1,X2,Y1,Y2,NF,KORNT
15000,01/NBAVE,NEAVE
'FLAME.DATA'/---- INPUT DATA -----
'FLAMEA.DATA'/---- STORE THE FINAL DATA -----
'TIME.DATA'/----- Time Evolution------
'DRIVE.DATA'/------- Driving History-----
'DRAG.DATA'/------- DRAG Data ---------
'TRACK.DATA'/------ Particle Data-------
'MOVIE.DATA'/------- Movie Data------------
'FLAVE.DATA'/------- Average Data --------
'output'/---- WRITE THE DATA -----
CCCCCCCCCCCCCCCCCCCCCCCCCCCCCCCCCCCCCCCCCCCCCCCCCCCCCCCCCCCCCCCCCCCCCC
DRIVE-1 (Low Speed)
0,-30, 0.01,0.0625,0.001,-40.0/ISTDY,INOISE,(X,Y,A,F of noise)
   0.0,0.0,0.0,0.00,0.1,0.2,0.30,0.50,0.80,0.8/ANOISE(1-10)
   0.80, 0.80, 0.60,0.40,0.2,0.1,0.0,0.0,0.0,0.0,0.0/ANOISE(11-20)
   0.00, 0.00, 0.00,0.00,0.0,0.0,0.0,0.0,0.0,0.0,0.0/ANOISE(21-30)
DRIVE-2 (High Speed)
0,-30, 0.01,0.0625,0.001,-40.0/ISTDY,INOISE,(X,Y,A,F of noise)
   0.0,0.0,0.0,0.00,0.1,0.2,0.40,0.80,1.20,1.2/ANOISE(1-10)
   1.20, 0.90, 0.60,0.40,0.2,0.1,0.0,0.0,0.0,0.0,0.0/ANOISE(11-20)
   0.00, 0.00, 0.00,0.00,0.0,0.0,0.0,0.0,0.0,0.0,0.0/ANOISE(21-30)

1000.0,1.0D+14,20*0,686*1,0,0,8*1,0,0,2*1,0,0,736*1,0,0,2000*1/Rxns.
```

Line-by-line breakdown.

Here each line is broken down into its variables, pointing out what each does and what variables are most important. Each variable is color coded to its description.

Wherever possible, pictures have been provided to aid in the understanding of what each variable does.

> 1,- C2H4-Air Premixed Flame Phi 1.1 (Hencken Burner) - (Global & Finite Rate Chemistry Model)-

This line is simply the file name line. Change this to reflect the flame you are setting up to help keep things organized. Remember, you can not change the actual name of the file (this will always be input.uni) so its important to keep a unique name here.

> 1, 0, 0/ ISYM,IREAD,IGNIT

Here we define whether the flame is axisymmetric or a 2D flow as well as some information the code uses to start.

ISYM

0 for 2D flows;

1 for an axisymmetric flow

*For most laminar flame research, axisymmetric will be the best setting. Using the axisymmetric setting means the calculations will only be performed from flame center outward with the assumption of a mirrored boundary at flame center. Also the calculations will only be performed in a plane, this greatly speed up the calculations.

IREAD

0 will start the calculation from scratch with no inputs needed

1 will start the calculation from a provided file titled "FLAME.DATA" however the grid system used will still be the one specified in the input file

2 is the same as 1, however the data will be transferred from the grid used in

152

the "FLAME.DATA" onto the one specified point-by-point irrespective of the coordinates.

* If a file "FLAME.DATA" is available it is best to keep this setting at 1. However if you have generated a brand new flame, "FLAME.DATA" may not exist yet so 0 is needed here. Note that this may add to computation time because the code has no good starting guess. If you have already run the code for a wile and you would like to start up again where the code last left off, be sure to copy the output results stored in "FLAMEA.DATA" to "FLAME.DATA".

IGNIT

This variable allows the user to define an ignition source. This is needed when starting the code without a "FLAME.DATA" file. This input does not include an example of ignition but one is provided below.

```
1,0,0.01,0.0625,0.001,-40.0,0,4*0.0/ISTDY,INOISE,(X,Y,A,F of noise)
```

This line sets the steadiness of the flame and the addition of artificial sources of noise.

ISTDY

1 for steady-state simulations

0 for unsteady simulations

* In all cases where starting from initial guesses it is best to have this set to 1. This will allow the code to come to a steady-state solution quickly, providing a good starting point for an unsteady calculation. If you know the flame is unsteady, run the steady-state code for 1000 or so iterations and start the code up again from the steady-state solution with this now set to 0. Again this requires replacing the input results stored in "FLAME.DATA" with the results from "FLAMEA.DATA"

0 for no artificial noise

*This value will turn on artificially introduced noise, i.e. a speaker putting waves into the fuel stream. This level of complication is most likely not something AFIT will need and so this value should be left 0.

ALL OTHERS

This will adjust the artificial noise's position, frequency and amplitude. Because the previous value is left to 0, these values are inactive.

0.00,0.0500,0.250 / RTIN, RTOT,ALENG

This line sets the dimensions of the calculation domain
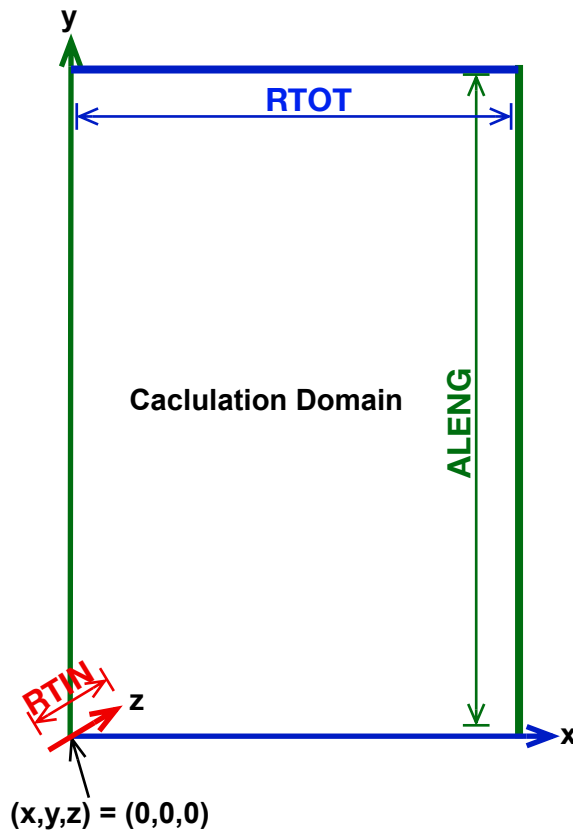
RTIN

0.00 - inner line (or plane) of the computational domain, [m]

* If the flame is defined above to be axisymmetric, this value should be kept 0. There is no need to do calculations outside of a singe plane because it would add no unique solutions.

RTOT

0.05 - width of the computational domain, [m]

* Here the value is set to 5 cm but this value should be changed to accommodate each flame AND enough space around the flame for any ambient air around it that may be affected. Remember, if the flame is axisymmetric the calculation domain only needs to accommodate half the flame width. If the flame is closely surrounded by an encasement, the width of the encasement should be used.

ALENG

0.25 - height of the computational domain, [m]

* The height setting is more open to change depending on the desired results. It should be set to as high a value as possible as this will provide the maximum information in the results. The tradeoff however is a decrease in spatial resolution if the number of grid points used are fixed, or an increase in calculation time if more grid points are added. It is, therefor, prudent to understand how high of a flame calculation you will NEED and not go much further than that. The height of the calculation domain does not directly affect the flame chemistry, just the window of results you will get.

1.0, 294.0,1.0133D+05, 1.225,1.0,10.0,0.233, 5, 07, 08, 09/ Reference Values

155

In this line the reference values for some of the physical constants are set. Also the fuel(s) used in the setup are defined.

Velocity

1.0 - Reference velocity for the system U, [m/s]

* This value does not set the flow velocity of the fuel, but is rather a reference value. For most flames, a value between 1 m/s and 10 m/s is recommended. Note, though, if the code does not run and the U-RESID value shown in the terminal window is very large, say 1E100+ then the reference value is set improperly.

Temperature

294.0 (Room temperature)- Temperature of the ambient air, [K]

* Set this value to the measured atmospheric conditions measured in the experiment you are comparing against. Otherwise keep fixed at room temperature.

Pressure

10133D+05 (Atmospheric pressure) - Pressure of the system p, [Pa]

* Set this value to the measured atmospheric conditions measured in the experiment you are comparing against. Otherwise keep fixed at standard pressure.

Density

1.225 (Density of air at sea level) - Reference density of the system ρ, in [kg/m^3]

* Set this value to the density of the free-stream conditions measured in the experiment you are comparing against. Otherwise keep fixed at standard density.

Turbulence kinetic energy

1.0 - Reference turbulence kinetic energy value k in units of energy/mass, [J/kg]

* Turbulence kinetic energy is defined as $\frac{1}{2}\langle \mathbf{u} \cdot \mathbf{u} \rangle$ where $\langle \mathbf{u} \cdot \mathbf{u} \rangle$ is the trace of the Reynolds stress tensor. This value is not active for laminar flames.

10.0 - Reference turbulence kinetic energy dissipation rate ϵ, $[\text{m}^2/\text{s}^3]$

* Turbulence kinetic energy dissipation rate is defined as $\epsilon = \nu \langle s_{i,j} s_{i,j} \rangle$ where ν is the kinematic viscosity and $s_{i,j}$ is the fluctuating rate-of-strain tensor. This value is not active for laminar flames.

Oxygen

0.233 (mass fraction of oxygen in air) - Reference oxygen MASS fraction, no units

* This sets the mass fraction of oxygen in the ambient air conditions

Primary Fuel

5 - Ethylene is set as the primary fuel by putting the number 5 here.

* To change the primary fuel, simply replace 5 with one of these preset fuel choices:

C——————————————————————————————

C FUEL: 1 - H2, 2–CH4, 3–CH3OH, 4–C2H2, 5–C2H4, 6–C2H6,

C 7–C3H8, 8–C3H6, 9–CH2O, 10–CO, 11–C7H16

C——————————————————————————————

Additions to the primary fuel

07, 08, 09 - This example shows the possible addition of HCO, CO_2, and CO

* Note here that the numbering convention of the primary fuel above and the additional chemicals is not the same. Also note that all additions put in here DO NOT need to be used in the calculation. They will be ignored in the calculation if their mass fraction is set to 0 in a later line. The chemicals to choose from are:

157

```
C*********************************************************************
C
C                    Combustion of methane Fuel
C            GRI Version 3.0 Mechanism 53 species and 650 reactions
C
C
C     1-CH4                    2-O2                    3-CH3
C     4-CH2                    5-CH                    6-CH2O
C     7-HCO                    8-CO2                   9-CO
C    10-H2                    11-H                    12-O
C    13-OH                    14-H2O                  15-HO2
C    16-H2O2                  17-C2H                  18-C2H2
C    19-C2H3                  20-C2H4                  21-C2H5
C    22-C2H6                  23-HCCO                  24-C
C    25-CH2(S)                26-CH2OH                 27-CH3O
C    28-CH3OH                 29-CH2CO                 30-HCCOH
C    31-C3H7                  32-C3H8                  33-CH2CHO
C    34-CH3CHO                35-N                     36-NH
C    37-NH2                   38-NH3                   39-NNH
C    40-NO                    41-NO2                   42-N2O
C    43-HNO                   44-CN                    45-HCN
C    46-H2CN                  47-HCNN                  48-HCNO
C    49-HOCN                  50-HNCO                  51-NCO
C    52-AR                    53-N2
C
C                      FINTE-RATE CHEMISTRY
C
C*********************************************************************
```

1, 0, 1, 1, 1, 1/ IFLOW,ISWIRL,ITHRM,ICHEM,IPROP,IGRAV

This line is very important even though most of it will likely remain unchanged.

Here is where a turbulent or a laminar calculation is chosen

IFLOW

0 - Does no flow calculation

1 - Does a laminar-flow calculation

2 - Does a turbulent-flow calculation

* The functionality of this value is straightforward. Check a calculation of your

flame's Reynolds number to see if it falls into the laminar or turbulent category.

Reynolds numbers $\sim< 2000$

ISWIRL

0 - Does not perform swirl calculation

158

1 - Includes a swirl component to the velocity in the calculations

* Here swirl is defined as a deliberate swirl to the fluid flow before ignition, i.e. if the pipe flowing the chemicals has a swirling device. This will probably never be the case so this value should remain 0.

ITHRM

0 - Does not perform temperature calculations

1 - Does perform temperature calculations

* Temperature calculations should always remain on

ICHEM

0 - Does not perform species transport calculations

1 - Does perform species transport calculations

* Species transport calculations should always remain on

IPROP

0 - Transport properties will be held constant

1 - Transport properties will be a function of concentrations and temperature

* This should always remain on

IGRAV

0 - Gravity is not included in the calculation

n **- Gravity is included in the calculation.** If $n > 0$ then the gravitational constant used will be $n * g$, where $g = 9.8\ m/s^2$. If $n < 0$ then the gravitational constant used will be g/n

* Unless we are working on the moon, this should always remain 1

6 / No. of cards describing the boundaries >=4

159

This value sets the number of lines, immediately following, that describe the boundaries of the system. There is a minimum of 4 because you must at least define the top, bottom, left and right side of the calculation domain. For an axisymmetric flame with no co-flow this value should be set to 5 (top, bottom, left and right side of the domain and one more for the edge of the fuel pipe). In this example, the flame is axisymmetric and has a co-flow so 6 lines are needed. Additional examples of various flame setups are provided in Section 2.5.

```
1, 2, 0.2500, 0.0, 11*0.0/ J=1 Axis
2, 0, 0.2500, 0.0, 0.01000, 0.0, 0.0, 300.0, 1.0,10.0, 0.000000, 0.231371, 0.0005,0.00,0.00/J=1 ambient air
3, 0, 0.0125, 1.0, 2.00000, 0.0, 0.0, 300.0, 1.0,10.0, 0.069697, 0.215258, 0.0005,0.00,0.00/J=1 FuelJet
3, 0, 0.0189, 0.0, 0.25000, 0.0, 0.0, 300.0, 1.0,10.0, 0.000000, 0.000000, 0.0000,0.00,0.00/J=1 N2 Jet
3, 0, 0.0500, 0.0, 0.01000, 0.0, 0.0, 300.0, 1.0,10.0, 0.000000, 0.231371, 0.0005,0.00,0.00/J=1 ambient air
4, 3, 0.0500, 0.8, 11*0.0/ I=LI Exit
```

These lines are the most important of the entire input file. Here is where the flame size, flow rates and starting conditions are defined.

ISIDE

    1 - Bottom side of the grid system

    2 - Top side of the grid system

    3 - Left side of the grid system

    4 - Right side of the grid system

    * When defining the edge of the flame or a co-flow, use ISIDE = 3

0 - Specified flow boundary

1 - A wall boundary

2 - An axis of symmetry boundary

3 - A free flow boundary

* The bottom of the system should be set to an axis of symmetry. If the flame was previously defined as axisymmetric, the program will automatically treat the far left side (the first line with ISIDE $= 3$) of the system as the point of symmetry for the calculation. If the flame is in a small enclosure (small enough to where the flame flow-field would be affected by the walls) then a value of 1 may be needed for the right and top sides. Additional examples of various flame setups are provided in Section 2.5.

LENGTH

Length of boundary, [m]

*Set the length of each boundary with this value. If the boundary is the bottom or top, the length should match the value specified in ALENG above. If the boundary is the right side of the grid the length should match the value specified in RTOT above. The length of all the specified "left" boundaries should add to match RTOT as well. In this example a 2.5 cm flame is surrounded by a 0.64 cm co-flow. Because the flame has been set to axisymmetric we only need to specify half the flame width, thats why the third line here has a length of 0.0125 m. This means that from $x = 0$ to $x = 0.0125$ the system is described by the flow settings in the third line. Line 4 has a length of 0.0189 because the length of this section adds to the end of the previous section, i.e. $0.0189 = 0.0125 + 0.0064$. Lastly, line 5 shows that the remainder of the calculation domain (from 0.0189 to 0.05) is defined by the flow settings in the 5th line.

An extrapolation constant or a profile definition depending on what ITYPE is

If ITYPE is 2, or 4 then this should be a value between 0 and 2. Values closer to 0 represent an extrapolation that is more stable but less accurate. Values closer to 2 are more accurate but can be unstable. A value of 1.2 to 0.8 is usually ok.

If ITYPE is 3, then this value describes the exit velocity profile. 0 is a top hat exit velocity profile. 1 is a perfect parabolic exit profile and any value in between is somewhere between a top hat and a parabola.

Flow velocity

(u, v, w) - Velocity of the fluid in each direction, [m/s]

* This is where the pipe exit velocity is set. In the cases where you have knowledge of the fuel flow rates in units of volume/time, you will need to divide out the area of the pipe exit to get to m/s. Note also that this example has a small velocity value for the "top" line. This is intended to mimic a hood vent used in the experimental setup. A velocity of 0 is okay if no vent is used.

The v and w components of the velocity should be 0 for most flames if the pipe is vertically placed.

Temperature

300 - Temperature of the flow described in that line, [K].

* This should match the ambient air temperatures measured during experimentation if you are trying to match a laboratory test.

k and ϵ

1.0 - k value for this boundary, [J/kg]

10.0 - ϵ value for this boundary in [m^2/s^3]

* These values only represent starting guesses and need not be changed. Again they are inactive for laminar flames

Fuel mass fraction

0.069 - Fraction of the flow that is the primary fuel by mass

Oxygen mass fraction

0.215 - Fraction of the flow that is oxygen (O$_2$) by mass

Fuel addition mass fractions

0.0065 - Fraction of the flow that is each of the additions to the primary fuel by mass

www.manaraa.com
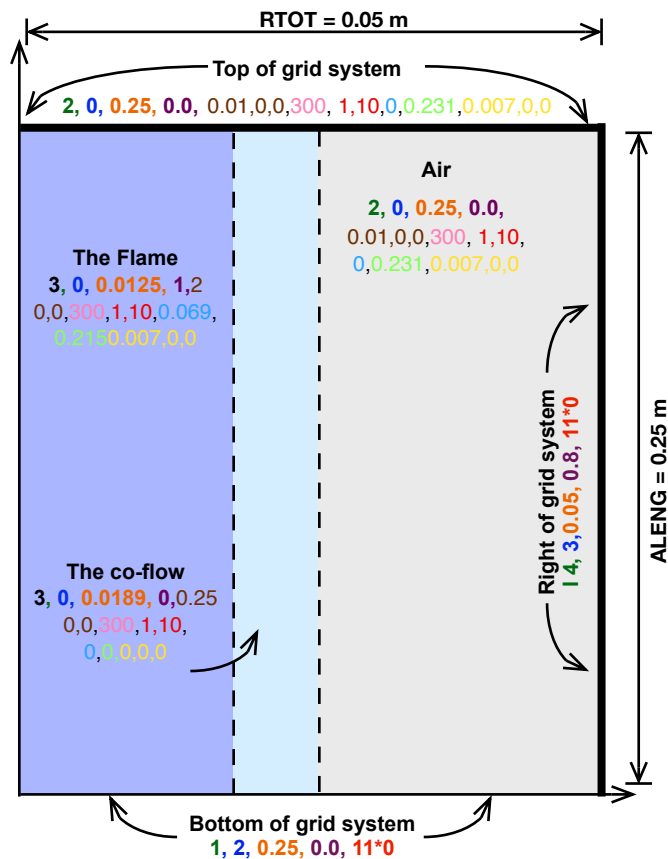
Example mass fraction calculations.

The Flame

In this input example, the flame was set up to be a $\Phi = 1.11$ ethylene/air pre-mixed flame. This means the fuel and air flow in together in a ratio of fuel to oxygen of 1.1 compared to the stoichiometric ratio. There are any number of ways to achieve this Φ valaue but in this example the air needed to have a flow rate of 12.2 SLM. Given this it is straightforward to calculate the needed fuel flow rate. First, start with the balanced reaction equation:

$$C_2H_4 + 3O_2 \rightarrow 2CO_2 + 2H_2O$$
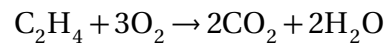
From this we can see that there is a 3/1 oxygen to fuel ratio for a perfect stoichiometric reaction to occur. In other words, if a $\Phi = 1$ flame was desired, the fuel flow rate would need to be $\frac{12.2*0.21}{3} = 0.86$ SLM, where here we account for the fact that air is only 21% oxygen by volume. With this value it is easy to get to the needed flow rate of any Φ value desired:

$$\text{Fuel Flow Rate} = \frac{\text{Air Flow Rate} * 0.21}{3} * \Phi = 0.85 * \Phi$$

And so for a $\Phi = 1.1$ flow we see we need about 0.95 SLM of fuel.

To get from flow rates to the values seen in the input files requires a bit more math. Remember, the values in the input are total flow MASS fractions, not volume fractions. Because of this, we first need to calculate the total mass of the flow. The molecular mass of ethylene is 28 and the molecular mass of air is roughly 28.97

164

so, given the flow rates, the molecular mass of the total flow is:

$$\frac{0.95}{0.95 + 12.2} * 28 + \frac{12.2}{0.95 + 12.2} * 28.97 \rightarrow 28.9$$

With this value we can finally get the mass fractions needed for the input file. First the fuel:

$$\frac{0.95}{0.95 + 12.2} * \frac{28}{28.97} \rightarrow 0.069$$

or in words, its the fraction of the total flow that has a mass of 28.

The total mass that is oxygen:

$$\frac{12.2}{0.95 + 12.2} * 0.21 * \frac{32}{28.9} \rightarrow 0.21$$

This example has the addition of CO_2 in the flow. This is added just to account for the presence of atmospheric CO_2. Its mass fraction is calculated in the same way as the oxygen, knowing that the atmosphere is about 0.04% CO_2.

$$\frac{12.2}{0.95 + 12.2} * 0.0004 * \frac{44}{28.9} \rightarrow 0.0005$$

The Co-Flow

The co-flow is a pure flow of N_2 making it very easy to describe. UNICORN is setup in such a way that the fraction of flow that is not specifically described by the fuel, O_2, or additions is automatically set to N_2. That means, to get a pure N_2 flow you need simply set all mass fraction values to 0.

The Ambient Air

It is important here, and in all previous calculations, to measure as best as possible the atmospheric conditions at the time of the experiment. It is straightforward to

165

describe this using the standard mass fractions of the components of air. Note that the top of the grid system and the ambient air usually have the same setup.

```
0/NBODY

0/ NFINJ
```

These two lines will most likely not be needed. NBODY sets the number of "bodies" that will be in the calculation domain. If this value is greater than 0, additional lines below 0/NBODY and before 0/NFINJ will be needed. These bodies are things such as the fuel pipe if you want the calculation domain to extend below the bottom, or an object in or above the flame. Most flames will be perfectly described without the fuel pipe included in the calculation. Only when flame liftoff is a possibility is this truly needed. An example of a fuel pipe body is provided in Sec. 2.5.

NFINJ

This should remain 0.

```
7, 20, 0.002, 50, 0.0070, 50, 0.0120, 50, 0.0200, 50, 0.0350, 50, 0.0700, 20, 0.0600/NI,I,X
```

Here is where the axial component of the grid system is setup. Grid sampling should be thought out carefully to maximize resolution in areas where combustion events are most prevalent.

NI

7 - Number of sections to divide the grid into along the axial direction

* Note here that in this example 7 sections are chosen and so there are 7 pairs of numbers that follow.

I

20 - Number of grid points to be used in this section.

166

* Note that the total number of grid points available in the axial direction is fixed to 500 in the code.

0.002 - length of this grid section, [m].

* Note that the total length of all sections needs to be equal to or less than the total width of the system RTOT. If the sum of all grid sections equals RTOT then the sum of all grid numbers, I, should equal 500 also. If $\sum X <$ RTOT and $\sum I < 500$, the remaining grid points will be distributed exponentially over the remaining distance.

3, 62, 0.0248, 10, 0.0050, 10, 0.0090,/NJ,J,Y

Here is where the vertical component of the grid system is setup. Again, grid sampling should be thought out carefully.

NJ

3 - Number of sections to divide the grid into along the vertical direction

* Note here that in this example 3 sections are chosen and so there are 3 pairs of numbers that follow.

I

62 - Number of grid points to be used in this section.

* Note that the total number of grid points available in the vertical direction is fixed to 200 in the code.

Y

0.0248 - length of this grid section, [m].

* Note that the total length of all sections needs to be equal to or less than the

total height of the system ALENG. If the sum of all grid sections equals ALENG then the sum of all grid numbers, J, should equal 200 also. If $\sum Y < $ ALENG and $\sum J < 500$, the remaining grid points will be distributed exponentially over the remaining distance.

1000, 0, 0.50, -100, 0/ ITEND,ISECS,CFLNO,ISTORE,ISTB

This line allows you to adjust how many iterations the code runs for, and how the output file is saved.

ITEND

1000 - Total number of iterations to be performed

*The code does not shut off until this number of iterations is reached, even if a consistent solution is reached, so choose this value wisely. If you are starting from initial conditions then this may need to be quite a large value. Starting from a previous solution may only need 1000 iterations. If you are running with ISTDY set to 1 with the intention of stopping the code and staring it again with ISTDY set to 0, this value should be around 1000-5000. A good tip, though, is to set this to a very large value always, 100000+, and let the code run. You can always stop it early with no consequences.

Here is an example of how many iterations to include for this input file: Each iteration represents 0.00002 seconds of real time. If you want information on one period of a flame that flickers at a rate of 90 ms per flicker then 5000 iterations would represent 100 ms, or about 1 flame period.

ISECS

0 - Allowed cpu time in seconds

* Keeping this value at 0 will not restrict the cpu

168

CFLNO

0.50 - non-dimensional time-step * Change this to change the iteration time value for each step of the code. Here 0.5 represents a time step of 0.2 ms each code iteration. A value of 0.8 would represent a time step of 0.4 ms.

ISTORE

-100 - Number of iterations between each output file save

* If this value is positive, the code will save every n iterations and keep each saved file, growing "FLAMEA.DATA" each save. If the value is negative the code will save every n iterations and overwrite the same file each time. Setting this value to 0 will provide no output files until the last iteration.

Note that a code used later to convert the output file into a format MatLab can read is only capable of handling the first 99 instances saved to the FLAMEA.DATA file. Choose ITEND and ISTORE so that ISTORE is about 1/100 of ITEND.

1, 1,/ ITPRNT, IPRES

ITPRNT

0 - No final output file

1 - Final output file

* You should always want the final results, so keep this a 1

IPRES

1 - Prints the residuals in the terminal screen as the code is running every n iterations

* In this example the code will show the residuals every iteration. This does not represent any change in computational time so staying with 1 is best

```
'PNT','PNT', 'PNT', 'PNT', 'PNT', 'PNT' / N-Scheme- U,V,W, H,Sp,KE
100,100, 100, 100, 100, 100 / No.of Relaxations- U,V, H, Species
0.9,0.9, 0.99, 0.99, 0.99, 0.99/RELX-U,V,W, H,Sp,K
1.0D-08,1.0D-08, 1.0D-08, 1.0D-08, 1.0D-08, 1.0D-08/Tolerance
1000.0,1.0D+15,100000*1/Rxns.
00,2,0,0.04,0.08,0.12,0.15/IBEVOL,ISEVOL,NEVOL,(XEVOL(N),N=1,NEVOL)
0,0,6,11,26/IBDRV,NDRV,IDRV(1;10)
0,0/IBDRG,ISDRG
0,10,5,0,02.000,1000.0,01.0,1.0/NOPT,IBINJ,ITINJ,IEINJ,PDIA,PDEN,PTHR,PVEL
```

This block of code deals with numerical schemes, relaxations, tolerances, reactions used and particle injections and is best left alone

```
15000, 100, 1, 00, 0.0, 0.084, 0.0, 0.025, 0, 2/IBANM,ISANM,KSYM,IPANM,X1,X2,Y1,Y2,NF,KORNT
```

This line gives you the option of outputting a figure as the code runs to help visualize the code progress.

IBANM

15000 - Sets the iteration where the figure is first generated

* Set this to a low value if you want a figure quickly to check the setup of a flame.

ISANM

n - A new figure will be saved every n iterations after IBANM

-n - A figure will be saved every n iterations after IBANM overwriting the previous figure

KSYM,IPANM,X1,X2,Y1,Y2,NF,KORNT

These allow you to change the shape of the figure and should not be changed

```
15000, 01, /NBAVE,NEAVE
```

This line gives you the option of saving an average results file in addition to the standard output

NBAVE

15000 - Sets the iteration where averaging will begin

* Make sure that the flame has come to a steady solution before turning this on.

NEAVE

0 - No averaging is done

1 - Average from NBAVE to the end

n > NBAVE - only average from NBAVE to n

*With regards to averaging, it is best done in MatLab later, when it can be controlled more.

```
'FLAME.DATA'/—- INPUT DATA —–

'FLAMEA.DATA'/—- STORE THE FINAL DATA —–

'TIME.DATA'/—– Time Evolution——

'DRIVE.DATA'/——– Driving History—–

'DRAG.DATA'/——- DRAG Data ———

'TRACK.DATA'/——– Particle Data——-

'MOVIE.DATA'/——- Movie Data————

'FLAVE.DATA'/——- Average Data ——–

'output'/—- WRITE THE DATA —–
```

These lines define the names of all the files that will be saved and they should be left alone.

```
CCCCCCCCCCCCCCCCCCCCCCCCCCCCCCCCCCCCCCCCCCCCCCCCCCCCCCCCCC
```

171

This line sets the end of the input file. Anything after this line is not active, so store any notes or different flame setups here

2.3   Run the input file

To run the input file you must first have all the correct files in the directory. This includes:

1. **input.uni**

   The input file. Take care not to change the file format of this document from a "Plane Text" file or the code will not run.

2. **FLAME.DATA**

   The starting dataset. This is not 100% necessary but is highly recommended. Again, here file format is very important. When working with a Mac computer, this file will often end up with the wrong line ending delineator. This especially occurs when copying data from "FLAMEA.DATA" to "FLAME.DATA". If the code does not run try the following command in the Terminal:

   sed -e 's/$/\r/' FLAME.DATA > FLAME.DATA

3. **FLAMEA.DATA**

   The final dataset.

4. **output**

   A file that stores run output information

5. **unicornd-griv3.out**

   This is the UNICORN executable

With all these files in the same directory, open a Terminal window and set the terminal path to the same directory with these files.

172

To run UNICORN, enter: **./unicornd-griv3.out** into the Terminal window and hit enter. If UNICORN is running correctly, you should see the following appear in the Terminal window:

```
     ---FINITE-RATE MODEL FOR H2 AND HYROCARBON FUELS--
            ----(SANDIEGO MECHANISM)----
        ----( 53 SPECIES &  325 X 2 REACTIONS)----
      --- (FUEL USED IN THIS CALCULATION IS H2     ) ---
        NO. OF REACTIONS USED IN THIS CALCULATION=  634
        NO. OF REACTIONS IN FALL-OFF REGION =  29 X 2

  BETA-X=  0.577900    BETA-Y=  0.599706
       IREAD = 1; READING DATA FROM   FLAME.DATA
   IT CONTAINS--605301   201  71 1 1 0 1 1 1 0100000 0.0000200

                    ---GRID SYSTEM 201X 71---
             ---DXMIN =  0.500 mm; DYMIN =  0.500 mm---
             ---Time Step =  0.000020000000 seconds---

 ------------ ITERATIONS FROM    1 TO    20  (DT = 0.020000 ms) ------------
  U-RESID           M-RESID   HT-RESID    CHEM-RES     K & EPS-RESID
  2.0E-03( 6, 5, 0)  1.2E-15  5.0E-01( 8)  5.8E-07( 6)  0.0E+00 & 0.0E+00( 0)
```

2.4 Bringing results into MatLab

The file "FLAMEA.DATA" stores the UNICORN results, but it needs to undergo a few changes first before MatLab can read it correctly.

- First the raw, unstructured UNICORN output must be converted from a staggered mesh to a regular mesh and (depending on the input variable ISTORE) FLAMEA.DATA needs to be broken into each saved file. This is done with the executable "unicorn-to-tecplot-multi.out". In a Terminal window, with **FLAMEA.DATA** and **unicorn-to-tecplot-multi.out** in the same directory, type **./unicorn-to-tecplot-multi.out** and hit enter. You will immediately be prompted with the question "HOW MANY FIES YOU HAVE IN FLAME.DATA?". Type in the number of files (1 to 99) that are saved in FLAMEA.DATA and hit enter. If FLAMEA.DATA has more than 99 files then only the first 99 will be used. This will immediately start

173

exporting files titled **flame**##**.dat** where ## is 01, 02 ... 99 depending on how many files FLAMEA.DATA had.

- Next the flame##.dat files need to be switched to a CSV format for the Matlab "importdata" function to handle. A MatLab wrapper function, **Change_flame_to_flame_csv.m** is available to do this cleanly. It loops over each flame##.dat file to create a flame##_csv.dat file, deleting the old flame##.dat.

- Lastly, the files "flame##_csv.dat" need to be imported into MatLab and interpolated onto a uniformly-spaced grid. The Matlab wrapper function **Import_Unicorn _Data.m** has been written to help with this. Note that these files can be large, and interpolating 4 or more variables over 99 files and then saving the results can take over an hour.

2.5   Additional input file examples

Provided here are additional examples of input files. These examples show some of the variation in the input values described in Sec. 2.2 including a pipe style flame and a flame with a body.

Hydrogen diffusion flame example input.

This example simulates the flame tested in [2]. It is a laminar, pure hydrogen diffusion flame exiting an 8 mm pipe. This code was used in the simulation of data for Chapters IV and V.

```
1,———H2-Air Diffusion Flame(Global & Finite Rate Chemistry Model)————————
1,0, 10, 20, 1700.0, 010, 020 / ISYM,IREAD,IGNIT,IGKEEP,IGTEMP,IGC,JGC
1,0,0.01,0.0625,0.001,-40.0,0,4*0.0/ISTDY,INOISE,(X,Y,A,F of noise)
0.000,0.150,0.400/ DEPTH,WIDTH,HEIGTH
10,313,098700,1.225,1.0,10.0,0.233,01,08,14,03,04,05,07,06,09,/ Reference Values
1, 0, 1, 1, 1, 1, 1/IFLOW,ISWIRL,ITHRM,ICHEM,IPROP,IGRAV
05 / No. of cards describing the boundaries >=4
1,2,0.4000,0.0, 16*0.0/  J=1  (Bottom-axis)
2,0,0.4000,0.0,0.010,0.000,0.000,313.0,1.0,10.0,0.00000,0.23300,0.00000,0.006500,6*0.00000/J=LJ Air Jet
3,0,0.0040,1.0,12.40,0.000,0.000,294.0,1.0,10.0,1.00000,0.00000,0.000000,7*0.00000/J=LJ Air Jet
3,0,0.1500,0.0,0.000,0.000,0.000,313.0,1.0,10.0,0.00000,0.23300,0.00000,0.006500,6*0.00000/J=LJ Air Jet
4,3,0.1500,1.2, 16*0.0/  J=1  (Right-axis)
0/NBODY
0/NFINJ
7,60,0.0150,40,0.0150,20,0.0120,20,0.0200,20,0.0400,20,0.0800,10,0.0860/NI,I,X
5,25,0.0050,12,0.0060,10,0.0120,10,0.0300,08,0.0500/NJ,J,Y
2000,0,0.8,-0100,0/  ITEND,ISECS,CFLNO,ISTORE,ISTB
1,1/  ITPRNT,IPRES
'PNT' 'PNT', 'PNT', 'PNT', 'PNT', 'PNT' / N-Scheme- U,V,W, H,Sp,KE
100,100, 100,  100,  100,  100 / No.of Relaxations- U,V, H,  Species
0.9,0.9, 0.99, 0.99, 0.99, 0.99/RELX-U,V,W, H,Sp,K |
1.0D-08,1.0D-08, 1.0D-08, 1.0D-08, 1.0D-08, 1.0D-08/Tolerance
1000.0,1.0D+11,10000*1/Rxns.
00,2,0,0.04,0.08,0.12,0.15/IBEVOL,ISEVOL,NEVOL,(XEVOL(N),N=1,NEVOL)
0,0,6,11,26/IBDRV,NDRV,IDRV(1;10)
0,0/IBDRG,ISDRG
0,10,5,0,00.020,1000.0,01.0,1.0/NOPT,IBINJ,ITINJ,IEINJ,PDIA,PDEN,PTHR,PVEL
1,-10,1,01,0.0,0.100,0.0,0.020,0,2/IBANM,ISANM,KSYM,IPANM,X1,X2,Y1,Y2,NF,KORNT
0,0/NBAVE,NEAVE
'FLAME.DATA'/---- INPUT DATA -----
'FLAMEA.DATA'/---- STORE THE FINAL DATA -----
'TIME.DATA'/----- Time Evolution------
'DRIVE.DATA'/------ Driving History-----
'DRAG.DATA'/------- DRAG Data ---------
'TRACK.DATA'/------ Particle Data-------
'MOVIE.DATA'/------- Movie Data------------
'FLAVE.DATA'/------- Average Data --------
'output'/---- WRITE THE DATA -----
CCCCCCCCCCCCCCCCCCCCCCCCCCCCCCCCCCCCCCCCCCCCCCCCCCCCCCCCCCCCCCCCCCCCCCCCCC
```

Ignition Source Set

Fuel now H2

No Co-Flow

New Sampling Grid

10,20, 1700, 010, 020/IGNIT, IGKEEP, IGTEMP, IGC, JGC

Note that in this example, an ignition source is used. The variables that define this ignition are as follows:

IGNIT

0 - No ignition is used

N > 0 - Ignition will start at the Nth iteration

* Set this to a low value if you want the flame to start quickly.

IGKEEP

N > 0 - Ignition will stay on for N iterations

IGTEMP

N - Temperature of the ignition source

* This needs to be set higher than the ignition temperature of your fuel mixture obviously.

IGC

N - Location of the ignition along the J axis

IGC

N - Location of the ignition along the I axis

Hydrogen diffusion flame with body example input.

This example simulates the same flame tested in [2]. Now, however, there is a 1 mm thick body (a circular disk) placed 2 mm above the pipe exit and extending out with a radius of 3 mm. This is an example of a type of bluff body. Note here that the XM, YM, XP, YP naming convention seems to have the X and Y labels reversed.

```
1,------H2-Air Diffusion Flame with body(Global & Finite Rate Chemistry
Model)-----------
1, 1, 0, 0, 1700.0, 250, 054 / ISYM,IREAD,IGNIT,IGKEEP,IGTEMP,IGC,JGC
1,0, 0.01,0.0625,0.001,-40.0,0,4*0.0/ISTDY,INOISE,(X,Y,A,F of noise)
0.00,0.150,0.400  / RTOT,ALENG
20.0, 294.0,1.0133D+05, 1.225,1.0,10.0,0.233, 01, 01,20,32,14,08,11,12,13/ Reference
Values
1, 0, 1, 1, 1,  1/  IFLOW,ISWIRL,ITHRM,ICHEM,IPROP,IGRAV
05 / No. of cards describing the boundaries >=4
1,2, 0.4000, 0.0, 16*0.0/ J=1  (Bottom-axis)
2,0, 0.4000, 0.0,00.010,0.0,0.0, 294.0, 1.0,10.0, 0.00000,0.23300,8*0.0/J=LJ Air Jet
3,0, 0.0040, 0.0,12.400,0.0,0.0, 294.0, 1.0,10.0, 1.00000,0.00000,0.0,7*0.0/I=1 Fuel
Jet
3,0, 0.1500, 0.0,00.010,0.0,0.0, 294.0, 1.0,10.0, 0.00000,0.23300,8*0.0/I=1 Ambient
air
4,3, 0.1500, 1.2, 16*0.0/  I=LI  Exit
1/NBODY
0.0020,0.0000,0.0030,0.0030, 500.0/XM,YM,XP,YP--BODY1
0/NFINJ
5, 40,0.020, 40,0.032, 40,0.060, 40,0.120, 20,0.080/ NIREGN,IREGN(N),XREGN(I)
5, 20,0.010, 12,0.010, 10,0.018, 10,0.028, 10,0.040/ NJREGN,JREGN(N),YREGN(I)
100, 0,  0.8, -10, 0/  ITEND,ISECS,CFLNO,ISTORE,ISTB
1 ,  1 /  ITPRNT,IPRES
'PNT','PNT', 'PNT',  'PNT',  'PNT',  'PNT' / N-Scheme- U,V,W, H,Sp,KE
100,100, 100,  100,  100,  100 / No.of Relaxations- U,V, H,  Species
0.9,0.9, 0.99, 0.99, 0.99, 0.99/RELX-U,V,W, H,Sp,K
1.0D-08,1.0D-08, 1.0D-08, 1.0D-08, 1.0D-08, 1.0D-08/Tolerance
1000.0,1.0D+11,10000*1/Rxns.
00,2,0,0.04,0.08,0.12,0.15/IBEVOL,ISEVOL,NEVOL,(XEVOL(N),N=1,NEVOL)
0,0,6,11,26/IBDRV,NDRV,IDRV(1;10)
0,0/IBDRG,ISDRG
0,10,5,0,00.020,1000.0,01.0,1.0/NOPT,IBINJ,ITINJ,IEINJ,PDIA,PDEN,PTHR,PVEL
001,05,1,01,0.0,0.100,0.0,0.020,0,2/IBANM,ISANM,KSYM,IPANM,X1,X2,Y1,Y2,NF,KORNT
000,00/NBAVE,NEAVE
'FLAME.DATA'/---- INPUT DATA -----
'FLAMEA.DATA'/---- STORE THE FINAL DATA -----
'TIME.DATA'/----- Time Evolution------
'DRIVE.DATA'/------ Driving History-----
'DRAG.DATA'/------- DRAG Data ---------
'TRACK.DATA'/------ Particle Data-------
'MOVIE.DATA'/------- Movie Data------------
'FLAVE.DATA'/------- Average Data --------
'output'/---- WRITE THE DATA -----
CCCCCCCCCCCCCCCCCCCCCCCCCCCCCCCCCCCCCCCCCCCCCCCCCCCCCCCCCCCCCCCCCCCCCCCCCC
```

1 Body added

Ethylene premixed pipe flame.

This example simulates the same flame tested in Chapter V.

```
1,Ethylene pipe flame Start(Global & Finite Rate Chemistry Model)------------
1,0, 10, 20, 1700.0, 010, 020 / ISYM,IREAD,IGNIT,IGKEEP,IGTEMP,IGC,JGC
1,0,0.01,0.0625,0.001,-40.0,0,4*0.0/ISTDY,INOISE,(X,Y,A,F of noise)
0.000,0.150,0.400/ DEPTH,WIDTH,HEIGTH
10,308,098700,1.225,1.0,10.0,0.233,05,08,14,03,04,05,07,06,09,/ Reference Values
1, 0, 1, 1, 1, 1, 1/IFLOW,ISWIRL,ITHRM,ICHEM,IPROP,IGRAV
05 / No. of cards describing the boundaries >=4
1,2,0.4000,0.0, 16*0.0/  J=1  (Bottom-axis)
2,0,0.4000,0.0,0.010,0.000,0.000,308.0,1.0,10.0,0.00000,0.23300,0.00000,0.0200,6*0.00000/J=LJ Air Jet
3,0,0.0040,1.0,2.646,0.000,0.000,294.0,1.0,10.0,0.1194,0.184900,0.006500,7*0.00000/J=LJ Air Jet
3,0,0.1500,0.0,0.000,0.000,0.000,308.0,1.0,10.0,0.00000,0.23300,0.00000,0.0200,6*0.00000/J=LJ Air Jet
4,3,0.1500,1.2, 16*0.0/  J=1  (Right-axis)
0/NBODY
0/NFINJ
7,60,0.0150,40,0.0150,20,0.0120,20,0.0200,20,0.0400,20,0.0800,10,0.0860/NI,I,X
5,25,0.0050,12,0.0060,10,0.0120,10,0.0300,08,0.0500/NJ,J,Y
2000,0,0.8,-0100,0/   ITEND,ISECS,CFLNO,ISTORE,ISTB
1,1/  ITPRNT,IPRES
'PNT' 'PNT', 'PNT', 'PNT', 'PNT', 'PNT' / N-Scheme- U,V,W, H,Sp,KE
100,100, 100,  100,   100,   100 / No.of Relaxations- U,V, H,  Species
0.9,0.9, 0.99, 0.99, 0.99, 0.99/RELX-U,V,W, H,Sp,K
1.0D-08,1.0D-08, 1.0D-08, 1.0D-08, 1.0D-08, 1.0D-08/Tolerance
1000.0,1.0D+11,10000*1/Rxns.
00,2,0.04,0.08,0.12,0.15/IBEVOL,ISEVOL,NEVOL,(XEVOL(N),N=1,NEVOL)
0,0,6,11,26/IBDRV,NDRV,IDRV(1;10)
0,0/IBDRG,ISDRG
0,10,5,0,00.020,1000.0,01.0,1.0/NOPT,IBINJ,ITINJ,IEINJ,PDIA,PDEN,PTHR,PVEL
1,-10,1,01,0.0,0.100,0.0,0.020,0,2/IBANM,ISANM,KSYM,IPANM,X1,X2,Y1,Y2,NF,KORNT
0,0/NBAVE,NEAVE
'FLAME.DATA'/---- INPUT DATA -----
'FLAMEA.DATA'/---- STORE THE FINAL DATA -----
'TIME.DATA'/----- Time Evolution------
'DRIVE.DATA'/------ Driving History-----
'DRAG.DATA'/------- DRAG Data ---------
'TRACK.DATA'/------ Particle Data-------
'MOVIE.DATA'/------- Movie Data-------------
'FLAVE.DATA'/------- Average Data --------
'output'/---- WRITE THE DATA -----
CCCCCCCCCCCCCCCCCCCCCCCCCCCCCCCCCCCCCCCCCCCCCCCCCCCCCCCCCCCCCCCCCCCCCCCCCCCCCC
```

Fuel now C2H4

Evaluates to Φ = 2

Bibliography

1. Terrence R. Meyer, Sukesh Roy, Thomas N. Anderson, Joseph D. Miller, Viswanath R. Katta, Robert P. Lucht, and James R. Gord. Measurements of OH mole fraction and temperature up to 20 kHz by using a diode-laser-based UV absorption sensor. *Applied Optics*, 44(31):6729–6740, 2005.

2. D. Blunck, S. Basu, Y. Zheng, V. Katta, and J. Gore. Simultaneous water vapor concentration and temperature measurements in unsteady hydrogen flames. *Proceedings of the Combustion Institute*, 32:2527–2534, 2009.

3. John J. Conti. Annual energy outlook 2014 with projections to 2040. Annual report, U.S. Energy Information Administration, 2014.

4. Katharina Kohse-Hoinghaus and Jay B. Jeffries, editors. *Applied Combustion Diagnostics*. Taylor and Francis, 2002.

5. R Mavrodineanu. Bibliography of flame spectrocopy analytical applications. Technical report, National Bureau of Standards, 1967.

6. W. Meier, R. S. Barlow, Y-L. L. Chen, and J-Y. Y. Chen. Raman/Rayleigh/LIF measurements in a turbulent $CH_4/H_2/N_2$ jet diffusion flame: experimental techniques and turbulence-chemistry interactions. *Combustion and Flame*, 123(3):326–343, 2000.

7. Jurgen Wolfrum. Lasers in combustion: From basic theory to practical devices. *Proceedings of the Combustion Institute*, 27:1–41, 1998.

8. David R. Crosley. Laser probes for combustion chemistry. *American Chemical Society Symposium Series*, 134, 1980.

9. S. S. Penner, C. P. Wang, and M. Y. Bahadori. Laser diagnostics applied to combustion systems. *Proceedings of the Combustion Institute*, 20:1149–1176, 1984.

10. A.C. Eckbreth. *Laser Diagnostics for Combustion Temperature and Species*. Combustion Science and Technology Book Series. Gordon and Breach Publishers, 2 edition, 1996.

11. J. W. Daily. Laser induced fluorescence spectroscopy in flames. *Progress in Energy and Combustion Science*, 23(2):133–199, 1997.

12. Katharina Kohse-Hoinghaus. Laser techniques for the quantitative detection of reactive intermediates in combustion systems. *Progress in Energy and Combustion Science*, 20(3):203–279, 1994.

13. Robert J. Cattolica and Thomas G. Mataga. Rotational-level-dependant quenching of OH A $^2\sum$(v'=1) by collisions with H_2O in a low-pressure flame. *Chemical Physics Letters*, 182(6):623–631, 1991.

14. R. A. Copeland, M. J. Dyer, and D.R. Crosley. Rotational-level-dependant quenching of $A^2\Sigma^+$ OH and OD. *Journal of Chemical Physics*, 82(8):4022–4032, 1985.

15. K. J. Rensberger, J. B. Jeffries, R. A. Copeland, K. Kohse-Höinghaus, M. L. Wise, and D.R. Crosley. Laser-induced fluorescence determination of temperatures in low pressure flames. *Applied Optics*, 28(17):3556–3566, 1989.

16. A. Arnold, B. Lange, T. Bouché, T. Heitzmann, G. Schiff, W. Ketterle, P. Monkhouse, and J. Wolfram. Absolute temperature fields in flames by 2D-LIF of OH using excimer laser and CARS spectroscopy. *Berichte der Bunsengesellschaft fur physikalische Chemie*, 96(10):1388–1393, 1992.

17. A. Fried and D. Richter. *Infrared Absorption Spectroscopy, in Analytical Techniques for Atmospheric Measurment.* Blackwell Publishing, 2007.

18. L. S. Rothman, I. E. Gordon, A. Barbe, D. C. Benner, P. F. Bernath, M. Birk, V. Boudon, L. R. Brown, A. Campargue, J. P. Champion, K. Chance, L. H. Coudert, V. Dana, V. M. Devi, S. Fally, J. Flaud, R. R. Gamache, A. Goldman, D. Jacquemart, I. Kleiner, N. Lacome, W. J. Lafferty, J. Mandin, S. T. Massie, S. N. Mikhailenko, C. E. Miller, N. Moazzen-Ahmadi, O. V. Naumenko, A. V. Nikitin, V. I. Orphal, V. I. Perevalov, A. Perrin, A. Predoi-Cross, C. P. Rinsland, M. Rotger, M. Simeckova, M. A. H. Smith, K. Sung, S. A. Tashkun, J. Tennyson, R. A. Toth, A. C. Vandaele, and J. Vander Auwera. The HITRAN 2008 molecular spectroscopic database. *Journal of Quantitative Spectroscopy and Radiative Transfer*, 110:533–572, 2009.

19. L. Ma, C. Weiwei, A. W. Caswell, T. Kraetschmer, S. T. Sanders, S. Roy, and J. R. Gord. Tomographic imaging of temperature and chemical species based on hyperspectral absorption spectroscopy. *Optics Express*, 17(10):8602 – 8613, 2009.

20. Lin Ma and Weiwei Cai. Numerical investigation of hyperspectral tomography for simultaneous temperature and concentration imaging. *Applied Optics*, 47(21):3751–3759, 2008.

21. K. W. Boyack and P. O. Hedman. Dual-Stokes CARS system for simultaneous measurmen of temperature and multiple species in turbulent flames. *Proceedings of the Combustion Institute*, 23:1893–1899, 1990.

22. A. V. Mokhov, H. B. Levinsky, and C. E. van der Meij. Temperature dependance of laser-induced fluorescence of nitric oxide in laminar premixed atmospheric-pressure flames. *Applied Optics*, 36:3233–3243, 1997.

23. J. W. Hahn, S. N. Park, E. S. Lee, C. Rhee, K. T. Kang, S. H. Chung, C. Y. Choi, and Y. D. Huh. Measuring the concentration of minor soecies from the modulation dip of the nonresonate background of broad-band CARS spectra. *Applied Spectroscopy*, 47(6):710 – 714, 1993.

24. A. C. Eckbreth and R. J. Hall. CARS concentration sensitivity with and without non-resonant background suppression. *Combustion Science and Technology*, 25:175 – 192, 1981.

25. K. Robson and M. J. G. Wilson. The stability of laminar diffusion flames of methane. *Combustion and Flame*, 13(6):626–634, 1969.

26. S. H. Chung. Stabilization, propagation and instability of tribrachial triple flames. *Proceedings of the Combustion Institute*, 31:877–892, 2007.

27. W. M. Roquemore, V. R. Katta, S. Stouffer, V. Belovich, R. Pawlik, M. Arstingstall, G. Justinger, J. Gord, A. Lynch, J. Zelina, and S. Roy. Soot studies of laminar diffusion flames with recirculation zones. *Proceedings of the Combustion Institute*, 32:729–736, 2009.

28. Viswanath R. Katta, William M. Roquemore, Scott Stouffer, and David L. Blunck. Dynamic lifed flame in centerbody burner. *Proceedings of the Combustion Institute*, 33:1187–1194, 2010.

29. Natalya Denisova, Pavel Tretyakov, and Andrey Tupikin. Emission tomography in flame diagnostics. *Combustion and Flame*, 160:577–588, 2013.

30. Brent A. Rankin, David L. Blunck, Viswanath R. Katta, Scott D. Stouffer, and Jay P. Gore. Experimental and computational infrared imaging of bluff body stabilized laminar diffusion flames. *Combustion and Flame*, 159:2841–2843, 2012.

31. Brent A. Rankin, David L. Blunck, and Jay P. Gore. Infrared imaging and spatiotemporal radiation properties of a turbulent nonpremixed jet flame and plume. *Journal of Heat Transfer*, 135(2):021201:1–11, 2013.

32. M. G. Mungal and A. Lozano. Some observations of a large, burning jet in crossflow. *Experiments in Fluids*, 21:264–267, 1996.

33. R. Hernandez and J. Ballester. Flame imaging as a diagnostic tool for industrial combustion. *Combustion and Flame*, 155:509–528, 2008.

34. V. Vilimpoc and L. P. Goss. SiC-based thin-filament pyrometry: Theory and thermal properties. *Proceedings of the Combustion Institute*, 22(1):1907–1914, 1989.

35. William M. Pitts, Kermit C. Smyth, and David A. Everest. Effects of finite time response and soot deposition on thin filament pyrometry measurments in time-varying diffusion flames. *Proceedings of the Combustion Institute*, 27:563–569, 1998.

36. W. Grosshandler. Technical note tn1402. Technical report, National Institute of Science and Technology, 1993.

37. R. H. Tourin. *Spectroscopic Gas Temperature Measurments*. Elsevier, 1966.

38. F. S. Simmons, H. Y. Yamada, and C. B. Arnold. Measurment of temperature profiles in hot gases by emission-absorption spectroscopy. Technical Report CR-72491, NASA, 1969.

39. L. E. Brewer and C. C. Limbaugh. Infrared band model technique for combustion diagnostics. *Applied Optics*, 11(5):1200–1204, 1972.

40. P. Vervisch and A. Coppalle. Fire flame radiation. *Combustion and Flame*, 52:127–135, 1983.

41. R. M. Goody. *Atmospheric Radiation.* Clarendon Press, Oxford, 1964.

42. P. R. Solomon, D. G. Hamblen, and R. M. Carangelo. Applications of fourier transform IR spectroscopy in fuel science. *ACS Symposium Series*, 205(4):77, 1982.

43. P. R. Solomon, D. G. Hamblen, R. M. Carangelo, and J. L. Krause. Coal thermal decomposition in an entrained flow reactor: Experiments and theory. *Proceedings of the Combustion Instituteoc*, 19:1139–1149, 1982.

44. P. R. Solomon, R. M. Carangelo, D. G. Hamblen, and P. E. Best. Infrared analysis of particulates by FT-IR emission/transmission spectroscopy. *Applied Spectroscopy*, 40:746, 1986.

45. Peter R. Solomon, Philip E. Best, Robert M. Carangelo, James R. Markham, and Po-Liang Chien. FT-IR emission/transmission spectroscopy for *in situ* combustion diagnostics. *Proceedings of the Combustion Institute*, 21:1763–1771, 1988.

46. P. R. Solomon, P. L. Chien, R. M. Carangelo, P. E. Best, and J. R. Markham. Application of FT-IR emission/transmission (E/T) spectroscopy to study coal combustion phenomena. *Proceedings of the Combustion Institute*, 22:211–221, 1989.

47. D. K. Ottesen and D. A. Stephenson. Fourier transform infrared (FT-IR) measurments in sooting flames. *Combustion and Flame*, 46:95–104, 1982.

48. D. K. Ottesen and L. R. Thorne. Fourier transform infrared (FT-IR) spectroscopic measurments of In-Situ coal combustion. *Proceedings of the 1983 International Conference on Coal Science*, page 621, 1983.

49. J. Butler, P. Maker, T. Korniski, and L. Haack. On-line characterization of vehical emissions by FT-IR and mass spectrometry. *SAE Technical Paper*, (810429), 1981.

50. James W. Butler, Paul D. Maker, Thomas J. Korniski, Larry P. Haack, Fredrick E. McKelvy, and Alex D. Colvin. A system for on-line measuring of multicomponent emissions and engine operating parameters. *SAE Technical Paper*, (851657), 1985.

51. J. R. Markham, Y. P. Zhang, R. M. Carangelo, and P. R. Solomon. FT-IR emission/-transmission tomography of a coal flame. *Proceedings of the Combustion Institute*, 23:1869–1875, 1990.

52. P. E. Best, P. L. Chien, R. M. Carangelo, P. R. Solomon, M. Danchak, and I. Ilovici. Tomographic reconstruction of FT-IR emission and transmission spectra in a sooting laminar diffusion flame: Species concentrations and temperatures. *Combustion and Flame*, 85:309–318, 1991.

53. Matthew J. Hall, Donald Lucas, and Catherine P. Koshland. Measuring chlorinated hydrocarbons in combustion by use of fourier transform infrared spectroscopy. *Environmental Science and Technology*, 25(2):260–267, 1991.

54. Sonnik Clausen and Jimmy Bak. Infrared low resolution emission spectoscopy of hot gases. *Proceedings SPIE*, 3383:133–139, 1998.

55. R. Bourayou, R. Vaillon, and J. F. Sacadura. FTIR low resolution emission spectrometry of a laboratory-scale diffusion flame: experimental set-up. *Experimental Thermal and Fluid Science*, 26:181–187, 2002.

56. E. Lindermeir. Evaluation of infrared emission spectra of aircraft exhaust with the FitFast software. *Annales Geophysicae*, 12(5):417–421, 1994.

57. Moira Hilton, Alan H. Lettington, and Ian M. Mills. Quantitative analysis of remote gas temperatures and concentrations from their infrared emission spectra. *Measurment Science and Technology*, 6(9):1236, 1995.

58. Klaus Schafer, Jorg Heland, Dave H. Lister, Chris W. Wilson, Roger J. Howes, Robert S. Falk, Erwin Lindermeir, Manfred Birk, Georg Wagner, Peter Haschberger, Marc Bernard, Olivier Legras, Peter Wiesen, Ralf Kurtenbach, Klaus J. Brochmann, Volker Kriesche, Moira Hilton, Gary Bishop, Roy Clarke, John Workman, Michael Caola, Rachel Geatches, Roger Burrows, John D. Black, Philippe Herve, and Johanna Vally. Nonintrusive optical measurments of aircraft engine exhaust emissions and comparison with standard intrusive tehcniques. *Applied Optics*, 39(3):441–455, 2000.

59. Sonnik Clausen and Jimmy Bak. FTIR transmission-emission spectroscopy of gases at high temperature: Experimental set-up and analytical procedures. *Journal of Quantitative Spectroscopy and Radiative Transfer*, 61(2):131–141, 1999.

60. L. H. Liu, H. P. Tan, and B. X. Li. Influence of turbulent fluctuation on reconstruction of temperature profile in axisymmetric free flames. *Journal of Quantitative Spectroscopy and Radiative Transfer*, 73:641–648, 2002.

61. Michael F. Modest and Sudarchan P. Bharadwaj. Medium resolution transmission measurments of CO_2 and high temperature. *Journal of Quantitative Spectroscopy and Radiative Transfer*, 73:329–338, 2002.

62. Thomas Flechl, Helmut Jager, and Ingwald Obernberger. Experimental verification of gas spectra calculated from high temperatures using the HIRTAN/HITEMP database. *Journal of Physics D: Applied Physics*, 35:3138–3144, 2002.

63. L. S. Rothman, I. E. Gordon, R. J. Barber, H. Dothe, R. R. Gamache, A. Goldman, V. I. Perevalov, S. A. Tashkun, and J. Tennyson. HITEMP, the high-temperature molecular spectroscopic database. *Journal of Quantitative Spectroscopy and Radiative Transfer*, 111:2139–2150, 2010.

64. Jongmook Lim, Yudaya Sivathanu, Jun Ji, and Jay P. Gore. Estimating scalars from specral radiation measurements in a homogeneous hot gas layers. *Combustion and Flame*, 137:222–229, 2004.

65. Isil Ayranci, Rodolphe Vaillon, Nevin Selcuk, Frederic Andre, and Dany Escudie. Determinatio of soot temperature, volume fraction and refractive index from flame emission spectroscopy. *Journal of Quantitative Spectroscopy and Radiative Transfer*, 104:266–276, 2007.

66. Kevin C. Gross, Kenneth C. Bradley, and Glen P. Perram. Remote identification and quantification of industrial smokestack effluents via imaging fourier-transform spectroscopy. *Environmental Science and Technology*, 44(24):9390 – 9397, 2010.

67. Jacob L. Harley, Brent A. Rankin, David L. Blunck, Jay P. Gore, and Kevin C. Gross. Imaging fourier-transform spectrometer measurements of a turbulent nonpremixed jet flame. *Optics Letters*, 39(8):2350–2353, 2014.

68. Frank M. White. *Viscous Fluid Flow*. McGraw-Hill, 3 edition, 2006.

69. Stephen B. Pope. *Turbulent Flows*. Cambridge, 2000.

70. William M. Roquemore and Viswanath R. Katta. Role of flow visualization in the development of UNICORN. *Journal of Visualization*, 2(3-4):257–272, 2000.

71. Viswanath R. Katta, L. P. Goss, and William M. Roquemore. Numerical investigations of transitional H_2/N_2 jet diffusion flames. *AIAA Journal*, 32(1):84–94, 1994.

72. D. B. Spalding. A novel finite difference formulation for difference expresssions involving both first and second derivatives. *International Journal of Numerical Methods in Engineering*, 4:551, 1972.

73. J. O. Hirschfelder. *Molecular Theory of Gases and Liquids*. John Wiley & Sons, Ltd., New York, 1954.

74. F. A. Williams. *The Fundamentals of Chemically Reacting Flow Systems*. Addison-Wesley Publishings Co., 1985.

75. R. Stephen Berry, Stuart A. Rice, and John Ross. *Physical and Chemical Kinetics*, volume III. Oxford University Press, 2 edition, 2002.

76. Michael F. Modest. *Radiative Heat Transfer*. Academic Press, 2 edition, 2003.

77. Yan Yong, Qiu Tian, Lu Gang, M. M. Hossain, G. Gilabert, and Liu Shi. Recent advances in flame tomography. *Chinese Journal of Chemical Engineering*, 20(2):389–399, 2012.

78. Cameron J. Dash. One-dimensional tomography: A comparison of Abel, onion-peeling, and filtered backprojection methods. *Applied Optics*, 31(8):1146 –1152, 1992.

79. Mahfoud El fagrich and Hassan Chehouani. A simple Able inversion method of interfermetric data for temperature measurment in axisymmetric medium. *Optics and Lasers in Engineering*, 50:336–344, 2012.

80. R. Alvarex, A Rodero, and M. C. Quintero. An Able inversion method for radially resolved measurements in the axial injection torch. *Spectroshimica Acta Part B*, 57:1665–1680, 2002.

81. O. H. Nestor and H. N. Olsen. Numerical methods for reducing line and surface probe data. *SIAM Review*, 2(3):200–207, 1960.

82. Michael R. Rhoby, David L. Blunck, and Kevin C. Gross. Mid-IR hyperspectral imaging of laminar flames for 2-D scalar values. *Optics Express*, 22(18):21600 – 21617, 2014.

83. Kaushik Biswas, Yuan Zheng, Chul Han Kim, and Jay Gore. Stochastic time series analysis of pulsating buoyant pool fires. *Proceedings of the Combustion Institute*, 31(2):2581 – 2588, 2007.

84. Roberto I. Acosta, Kevin C. Gross, Glen P. Perram, Shane Johnson, Ly Dao, David Medina, Robert Roybal, and Paul Black. Gas phase plume from laser irradiated fiberglass reinforced polymers via imaging Fourier-transform spectroscopy. *Applied Spectroscopy*, 68(7), 2014.

85. M. S. Wooldridge, P. V. Torek, M.T. Donovan, D. L. Hall, T. A. Miller, T. R. Palmer, and C. R. Schrock. An experimental investigation of gas-phase combustion synthesis of sio2 nanoparticals using a multi-element diffusion flame burner. *Combustion and Flame*, 131:98–109, 2002.

86. K. C. Gross, P. Tremblay, K. C. Bradley, M. Chamberland, V. Farley, and G. P. Perram. Instrument calibration and lineshape modeling for ultraspectral imagery measurements of industrial smokestack emissions. *Proceedings of SPIE*, 7695(769516), 2010.

87. V. Farley, A. Vallières, M. Chamberland, A. Villemaire, and J. F. Legault. Performance of the FIRST, a longwave infrared hyperspectral imaging sensor. *Proc. SPIE*, 6398(6398T-1), 2006.

185

88. Henry E. Revercomb, H. Buijs, Hugh B. Howell, D. D. LaPorte, William L. Smith, and L. A. Sromovsky. Radiometric calibration of ir fourier transform spectrometers: solution to a problem with the high-resolution interferometer sounder. *Appl. Opt.*, 27(15):3210–3218, 1988.

89. Sumner P. Davis, Mark C. Abrams, and James W. Brault. *Fourier Transform Spectrometry*. Academic Press, 2001.

90. S. A. Tashkun and V. I. Perevalov. CDSD-4000: high-resolution, high-temperature carbon dioxide spectroscopic databank. *Journal of Quantitative Spectroscopy and Radiative Transfer*, 112:1403–1410, 2011.

91. L. S. Rothman, C. P. Rinsland, A. Goldman, S. T. Massie, D. P. Edwards, J.-M. Flaud, A. Perrin, C. Camy-Peyret, V. Dana, J.-Y. Mandin, J. Schroeder, A. Mccann, R. R. Gamache, R. B. Wattson, K. Yoshino, K. V. Chance, K. W. Jucks, L. R. Brown, V. Nemtchinov, and P. Varanasi. The HITRAN molecular spectroscopic database and HAWKS (HITRAN atmospheric workstation): 1996 edition. *Journal of Quantitative Spectroscopy & Radiative Transfer*, 60(5):665–710, 1998.

92. S. Gordon and B. J. McBride. *Computer program for calculation of complex chemical equilibrium compositions and applications, RP-1311*. NASA, 1996.

93. S. Depraz, M. Y. Perrin, Ph. Riviere, and A. Soufiani. Infrared emission spectroscopy of CO_2 at high temperature. Part I: Experimental setup and source characterization. *Journal of Quantitative Spectroscopy and Radiative Transfer*, 113:1–13, 2012.

94. S. Depraz, M. Y. Perrin, Ph. Riviere, and A. Soufiani. Infrared emission spectroscopy of CO_2 at high temperature. Part II: Experimental results and comparisons with spectroscopic databases. *Journal of Quantitative Spectroscopy and Radiative Transfer*, 113:14–25, 2012.

95. Roberto I. Acosta. *Imaging Fourier Transform Spectroscopy Of The Boundary Layer Plume From Laser Irradiated Polymers And Carbon Materials, AFIT-ENP-DS-14-J-8*. PhD thesis, Air Force Institute of Technology, 2014.

96. Stephen Wakefield, Brian Sell, Frederick Schauer, Matthew Fotia, and John Hoke. *Development of a Mid-IR Laser Diagnostic for Combustion Efficiency*. American Institute of Aeronautics and Astronautics, 2014.

97. Katharina Kohse-Hoinghaus and Jay B. Jeffries, editors. *Applied Combustion Diagnostics*. Taylor and Francis, 2002.

98. Chenguang Wang, Anthony M Dean, Huayang Zhu, and Robert J Kee. Model-predicted effects of fuel droplet diameter and O_2 addition in strained, oppposed-flow, non-premixed, multicomponent, hydrocarbon flames. *Combustion and Flame*, 161(8):1998–2007, 2014.

99. Viswanath R. Katta, L. P. Goss, and William M. Roquemore. Effects of nonunity Lewis number and finite-rate chemistry on the dynamics of a hydrogen-air jet diffusion fame. *Combustion and Flame*, 96(1-2):60–74, 1994.

100. V. R. Katta, L. G. Blevins, and W. M. Roquemore. Dynamics of an inverse diffusion flame and its role in polycyclic-aromatic-hydrocarbon and soot formation. *Combustion and Flame*, 142:33–51, 2005.

101. Gregory V. Hartland, Wei Xie, Hai-Lung Dai, Arno Simon, and Michael J. Anderson. Time-resolved Fourier transform spectroscopy with $0.25cm^{-1}$ spectral and $<10^{-7}$s time resolution in the visible region. *Review of Scientific Instruments*, 63(6):3261–3267, 1992.

102. T. J. Johnson, A. Simon, J. M. Weil, and G. W. Harris. Applications of time-resolved step-scan and rapid-scan FT-IR spectroscopy: Dynamics from ten seconds to ten nanoseconds. *Applied Spectroscopy*, 47(9):1376–1381, 1995.

103. V. Saptari. *Fourier Transform Spectroscopy Instrumentation Engineering*. SPIE Press monograph. SPIE Optical Engineering Press, 2004.

104. I. Radu, M. Schleeger, C. Bolwien, and J. Heberle. Time-resolved FT-IR difference spectroscopy and the application to membrane proteins. *Photochemical and Photobiological Sciences*, 8(11):1517–1528, 2009.

105. Donny Magana, Dzmitry Parul, R. Brian Dyer, and Andrew P Shreve. Implementation of time-resolved step-scan Fourier transform infrared (FT-IR) spectroscopy using a kHz repetition rate pump laser. *Applied Spectroscopy*, 65(5):535–542, 2011.

106. William M. Roquemore and Viswanath R. Katta. Role of flow visualization in the development of UNICORN. *Journal of Visualization*, 2(3-4):257–272, 2000.

107. M. Tagawa and Y. Ohta. Two-thermocouple probe for fluctuation temperature measurement in combustion-rational estimation of mean and fluctuation time constants. *Combustion and Flame*, 109(4):549–560, 1997.

108. S. Brohezz, C. Delvosalle, and G. Marlair. A two-thermocouple probe for radiation corrections of measured temperatures in compartment fires. *Fire Safety Journal*, 39(5):399–411, 2004.

109. R. S. Barlow, A. N. Karpetis, J. H. Frank, and J. Y. Chen. Scalar profiles and NO formation in laminar opposed-flow partially premixed methane/air flames. *Combustion and Flame*, 127(3):2102–2118, 2001.

110. R. D. Hancock, K. E. Bertagnolli, and R. P. Lucht. Nitrogen and hydrogen CARS temperature measurements in a hydrogen/air flame using a near-adiabatic flat-flame burner. *Combustion and Flame*, 109:323–331, 1997.

111. Brian J. Kirby and Ronald K. Hanson. Infrared PLIF imaging of CO and CO_2. Number 99-0775, 1999.

112. Brent A. Rankin, David L. Blunck, Viswanath R. Katta, Scott D. Stouffer, and Jay P. Gore. Infrared imaging, computations, and tomography of bluff body stabilized laminar diffusion flames. Number AIAA 2011-690 in 49th AIAA Aerspace Science Meeting Including the New Horizons Frorum and Aerospace Exposition, 2011.

113. D. R. Snelling, K. A. Thomson, G. J. Smallwood, O. L. Gulder, E. J. Weckman, and R. A. Fraser. Spectrally resolved measurement of flame radiation to determine soot temperature and concentration. *AIAA Journal*, 40(9):1789–1795, 2002.

114. Yuan Zheng and Jay P. Gore. Measurements and inverse calculations of spectral radiation intensities of a turbulent ethylene/air jet flame. *Proceedings of the Combustion Institute*, 30:727–734, 2005.

115. George C.-Y. Chan and Gary M. Hieftje. Estimation of confidence intervals for radial emissivity and optimization of data treatment techniques in abel inversion. *Spectrochimica Acta Part B*, 61:31–41, 2006.

116. K. C. Gross, P. Tremblay, and M. Chamberland. IFTS for turbulent flow field diagnostics. *Fourier Transform Spectroscopy, OSA Technical Digest (CD)*, paper(FTuD1), 2011.

117. V. R. Katta and W. M. Roquemore. On the structure of a stretched/compressed laminar flamelet: influence of preferential diffusion. *Combustion and Flame*, 100:61–70, 1995.

118. F. Grisch, B Attal-Tretout, P Bouchardy, V. R. Katta, and W. M. Roquemore. A vortex-flame interaction study using four-wave mixing techniques. *Journal of Nonlinear Optical Physics and Materials*, 5(3):505–526, 1996.

119. S. J. Bowen. Hyperspectral imaging of a turbine engine exhaust plume to determine radiance, temperature, and concentration spatial distribution. Master's thesis, Air Force Institute of Technology, 2009.

120. Kenneth C. Bradley. *Midwave infdrared imaging Fouriter transform spectrometry of combustion plumes.* PhD thesis, Air Force Institute of Technology, 2009.

121. Pierre Tremblay, Kevin C. Gross, Vincent Farley, Martin Chamberland, and A. Villemaire. Understanding and overcoming scene-change artifacts in imaging Fourier-transform spectroscopy of turbulent jet engine exhaust. *Proceedings of SPIE*, 7457:74570F, 2009.

122. Jacob L. Harley, August J. Rolling, Charles F. Wisniewski, and Kevin C. Gross. Spatially resolved infrared spectra of f109 turbofan exhaust, 2012.

123. Martin Chamberland, Vincent Farley, Alexandre Vallieres, Andre Villemaire, Louis Belhumeur, Jean Giroux, and Jean-Francois Legault. High-performance field-portable imaging radiometric spectrometer technology for hyperspectral imaging applications. volume 5994, page 59940N. SPIE, 2005.

124. G. E. Thomas and K. Stamnes. *Radiative Transfer in the Atmospher and Ocean.* Cambridge University Press, 2002.

125. S. A. Clough, M. W. Shephard, E. J. Mlawer, J. S. Delamere, M. J. Iacono, K. Cady-Pereira, S. Boukabara, and P. D. Brown. Atmospheric radiative transfer modeling: A summary of the AER codes. *Journal of Quantitative Spectroscopy and Radiative Transfer,* 91:233–244, 2005.

REPORT DOCUMENTATION PAGE

Form Approved
OMB No. 0704–0188

1. REPORT DATE *(DD–MM–YYYY)*	2. REPORT TYPE	3. DATES COVERED *(From — To)*
16–06–2016	Doctoral Dissertation	June 2012 - June 2016

4. TITLE AND SUBTITLE

Laminar Flame Combustion Diagnostics Using Imaging Fourier Transform Spectroscopy

5a. CONTRACT NUMBER

5b. GRANT NUMBER

5c. PROGRAM ELEMENT NUMBER

6. AUTHOR(S)

Rhoby, Michael R., Mr., Civ.

5d. PROJECT NUMBER

5e. TASK NUMBER

5f. WORK UNIT NUMBER

7. PERFORMING ORGANIZATION NAME(S) AND ADDRESS(ES)

Air Force Institute of Technology
Graduate School of Engineering and Management (AFIT/EN)
2950 Hobson Way
WPAFB OH 45433-7765

8. PERFORMING ORGANIZATION REPORT NUMBER

AFIT-ENP-DS-16-J-018

9. SPONSORING / MONITORING AGENCY NAME(S) AND ADDRESS(ES)

Hypersonic Sciences Branch AFRL/RQHF (Dr. Timothy Ombrello)
High Speed Systems Division
Air Force Research Laboratory, Aerospace Systems Directorate Wright-Patterson Air Force Base, OH 45433-7542
937-656-5950
timothy.ombrello.1@us.af.mil

10. SPONSOR/MONITOR'S ACRONYM(S)

11. SPONSOR/MONITOR'S REPORT NUMBER(S)

12. DISTRIBUTION / AVAILABILITY STATEMENT

APPROVED FOR PUBLIC RELEASE; DISTRIBUTION UNLIMITED.

13. SUPPLEMENTARY NOTES

This material is declared a work of the U.S. Government and is not subject to copyright protection in the United States.

14. ABSTRACT

Laminar flames are an important tool in combustion diagnostics with a host of pre-existing experimental research methods. Currently, however, no method captures time-resolved scalar profile estimates of temperature, and major species concentrations with a single measurement. This work provides IFTS with the capability to measure time-resolved 3D imaging of scalar values in laminar axisymmetric flames. This will make IFTS a useful tool for understanding combustion phenomenon, validating chemical kinetic models, verifying numerical simulations, and system performance estimate. Two algorithms are presented. The first reconstructs spectra as a function of flame period. Through selectively averaging over an ensemble of measurements, interferograms representing the scalar fields at t0 can be created. The second improves on traditional tomographic inversion methods to radially resolve multiple scalar values simultaneously in an axisymmetric flame. The combination of these two algorithms was applied to measurements of an unsteady laminar hydrogen flame. Temperature and water concentrations were successfully resolved radially at eight different "snapshot" times in the period of the flames harmonic motion. Measured results compared favorably with perviously reported values and CFD simulations. Temperatures agree to within 11% and water concentration values agree to within 19%. This work demonstrates the ability of IFTS to make time-resolved 3-D maps of scalar values of harmonic laminar flame.

15. SUBJECT TERMS

Imaging Fourier-transform spectrometer, Combustion, Laminar flame, Tomographic Inversion

16. SECURITY CLASSIFICATION OF:			17. LIMITATION OF ABSTRACT	18. NUMBER OF PAGES	19a. NAME OF RESPONSIBLE PERSON
a. REPORT	b. ABSTRACT	c. THIS PAGE			Dr. Kevin C. Gross, AFIT/ENP
U	U	U	UU	212	19b. TELEPHONE NUMBER *(include area code)* (937) 255-3636 x4558; kevin.gross@afit.edu

Standard Form 298 (Rev. 8–98)
Prescribed by ANSI Std. Z39.18